

Assessing the origin of some representative Archean-Paleoproterozoic porphyry Cu ± Au
deposits

by

Xuyang Meng

A thesis submitted in partial fulfillment
of the requirements for the degree of
Doctor of Philosophy (PhD) in Mineral Deposits and Precambrian Geology

The Faculty of Graduate Studies
Laurentian University
Sudbury, Ontario, Canada

© Xuyang Meng, 2021

THESIS DEFENCE COMMITTEE/COMITÉ DE SOUTENANCE DE THÈSE
Laurentian Université/Université Laurentienne
Faculty of Graduate Studies/Faculté des études supérieures

Title of Thesis Titre de la thèse	Assessing the origin of some representative Archean-Paleoproterozoic porphyry Cu ± Au deposits		
Name of Candidate Nom du candidat	Meng, Xuyang		
Degree Diplôme	Doctor of Philosophy		
Department/Program Département/Programme	Mineral Deposits and Precambrian Geology	Date of Defence Date de la soutenance	June 04, 2021

APPROVED/APPROUVÉ

Thesis Examiners/Examineurs de thèse:

Dr. Daniel Kontak
(Co-Supervisor/Co-directeur(trice) de thèse)

Dr. Pedro Jugo
(Co-Supervisor/Co-directeur(trice) de thèse)

Dr. Ross Sherlock
(Committee member/Membre du comité)

Dr. John H. Dilles
(External Examiner/Examineur externe)

Dr. Michelle DeWolfe
(Internal Examiner/Examineur interne)

Approved for the Office of Graduate Studies
Approuvé pour le Bureau des études supérieures
Tammy Eger, PhD
Vice-President Research
Vice-rectrice à la recherche
Laurentian University / Université Laurentienne

ACCESSIBILITY CLAUSE AND PERMISSION TO USE

I, **Xuyang Meng**, hereby grant to Laurentian University and/or its agents the non-exclusive license to archive and make accessible my thesis, dissertation, or project report in whole or in part in all forms of media, now or for the duration of my copyright ownership. I retain all other ownership rights to the copyright of the thesis, dissertation or project report. I also reserve the right to use in future works (such as articles or books) all or part of this thesis, dissertation, or project report. I further agree that permission for copying of this thesis in any manner, in whole or in part, for scholarly purposes may be granted by the professor or professors who supervised my thesis work or, in their absence, by the Head of the Department in which my thesis work was done. It is understood that any copying or publication or use of this thesis or parts thereof for financial gain shall not be allowed without my written permission. It is also understood that this copy is being made available in this form by the authority of the copyright owner solely for the purpose of private study and research and may not be copied or reproduced except as permitted by the copyright laws without written authority from the copyright owner.

Abstract

Most known porphyry Cu \pm Au deposits are exclusively associated with oxidized and sulfur-rich Phanerozoic arc-related magmas, but Precambrian analogues are rare. The genesis of some rare examples of such deposits (e.g., Tongkuangyu in Trans-North China Orogen) remains debated, and in particular, it remains unclear as to whether similar metallogenic processes that typify the Phanerozoic deposits also operated in the Precambrian. To resolve these issues, three study areas were chosen to variably characterize relevant aspects of these deposits in the context of porphyry-type metallogenies (i.e., the nature of mineralization, the redox states and volatile element abundances of the causative magmas): (1) the \sim 2.1 Ga Tongkuangyu deposit in Trans-North China Craton; (2) the \sim 1.88 Ga Haib porphyry Cu deposit, Southern Namibia; and (3) representative porphyry-type Cu \pm Au deposits (Côté Gold, St-Jude, and Croxall) in the \sim 2.7 Ga Abitibi subprovince.

At the Tongkuangyu deposit, remapping of the distribution of the host rocks, alteration, and mineralization support a porphyry-type model where ore formation occurred at \sim 2.1 Ga. This age is significantly later than the host granodiorite porphyry (\sim 2.18 Ga) and schists (\sim 2.5–2.2 Ga) and indicates that porphyry-type mineralization need not be linked directly to a causative magma exposed at surface. Instead, the latter is interpreted to be represented by subjacent porphyritic stocks and dikes.

At the Haib deposit, the host calc-alkaline plutonic rocks and mineralization are dated to ca. 1886–1881 Ma. Estimations of magmatic fO_2 and S, based on zircon geochemistry, apatite μ -XANES spectra, and apatite S analysis, demonstrate that oxidized, sulfur-rich arc magmas associated with porphyry Cu mineralization already existed in the late Paleoproterozoic. In

addition, zircon Hf-O isotopes and whole-rock geochemistry support magmas of mantle-derivation with minor crustal contributions that experienced amphibole \pm plagioclase fractionation. These features of the Haib magmas are thus similar to those for Phanerozoic porphyry Cu deposits.

For the \sim 2.7 Ga TTG (tonalite-trondhjemite-granodiorite-diorite)-related porphyry-type Cu \pm Au deposits in the Abitibi subprovince, whole-rock geochemistry, zircon Hf-O isotopes, apatite S contents, and multiple oxybarometers suggest that variable magmatic origin and fO_2 for the causative magmas. The rarity of porphyry-type Cu-Au deposits in these older settings may be attributed to either location restriction of these favorable metallogenic conditions and/or preservation, or exploration bias.

Keywords: Porphyry Cu systems, Archean, Paleoproterozoic, Trans-North China Orogen, Richtersveld Magmatic Arc, Abitibi greenstone belt, Tongkuangyu, Haib, Côté Gold, St-Jude, Croxall, Magmatic oxygen fugacity, Zircon, Apatite, S μ -XANES, zircon Hf-O isotopes

Co-Authorship Statement

The Ph.D. thesis includes four manuscripts prepared for publication in peer-reviewed journals based on the original work completed by the candidate (Xuyang Meng) and his collaborators. The candidate completed field work, sample preparation, petrographic observation, data collection, interpretation, and wrote all of the first drafts. The co-authors provide field and analytical assistance, data processing and interpretation, and editorial advice that are deemed sufficiently significant for co-authorships. The candidate prepared all of the samples (particularly for identifying inclusions of apatite and other minerals in zircon grains) and collaborated with Adam Simon, Andrew DuFrane, Jackie Wragie, Jeffrey Marsh, Joseph Petrus, Richard Stern, and Robert Creaser, Simon Tapster in collecting data of apatite μ -XANES spectra, LA-ICP-MS U-Pb-Hf and trace element and SIMS O isotope analyses, molybdenite and pyrite Re-Os dating, CA-ID-TIMS zircon U-Pb dating. The main contributions of the co-authors for each chapter are itemized as follows.

Chapter 2: Jeremy Richards, as the candidate's supervisor, supervised the fieldwork, data collection, and data interpretation, as well as writing. Jingwen Mao supported the fieldwork and part of the analyses and interpreted the data. Huishou Ye joined the fieldwork and contributed to data interpretation. Andrew DuFrane, Jeffrey Marsh, and Joseph Petrus were responsible for LA-ICP-MS data reduction and interpretation. Robert Creaser was responsible for molybdenite and pyrite Re-Os dating and data interpretation.

Chapter 3: Daniel Kontak supervised the candidate in idea development, data interpretation, and writing. Jeremy Richards guided the candidate in sample collection and designed an initial project. Jingwen Mao supervised the candidate in sample collection. Jeffrey Marsh was

responsible for LA-ICP-MS U-Pb-Lu-Hf isotope analyses. All of these co-authors contributed to aspects of data interpretation and have read and edited parts of the manuscript

Chapter 4: Jeremy Richards and the candidate conceived the project, completed field work, and collected the samples. Adam Simon and Jackie Kleinsasser were responsible for the μ -XANES analyses and data processing and interpretation. Simon Tapster was responsible for the CA-ID-TIMS zircon U-Pb dating. Daniel Kontak and Pedro Jugo contribute to the data interpretation. Grant Bybee and Laurence Robb joined the fieldwork and contribute to the data interpretation. Jeffrey Marsh was responsible for LA-ICP-MS U-Pb-Lu-Hf and trace element analyses, and Richard Stern was responsible for zircon O isotope analyses. Jackie Kleinsasser, Adam Simon, Daniel Kontak, and all of the other co-authors contribute to editing the manuscript.

Chapter 5: Jeremy Richards supervised the candidate in designing the project and collecting most of the data. Daniel Kontak supervised the candidate in data interpretation and some of the data collection, as well as editing the manuscript. Adam Simon and Jackie Kleinsasser were responsible for the μ -XANES analyses and data processing and interpretation. Jeffrey Marsh was responsible for LA-ICP-MS U-Pb-Lu-Hf and trace element analyses, and Richard Stern was responsible for zircon O isotope analyses. Pedro Jugo contributed to data interpretation. All of these co-authors have read or edited parts of the manuscript.

Acknowledgments

I would like to express my appreciation to my supervisor, Professor Jeremy Richards, for his advice, education, and incisive criticism that corrected my highly divergent thinking and writing. Without his patience, encouragement, immense knowledge, I could not reach a point to be ready for the challenging time after his sudden passing in June 2019.

I would also like to thank Professor Daniel Kontak for his insightful suggestions to my research and thesis after Jeremy's sudden passing, as well as his encouragement in my career and life aspirations. Great thanks to Professors Pedro Jugo and Ross Sherlock as my supervisory committee members for their constructive comments and invaluable assistance, as well as dealing with some of the paperwork.

Many thanks to my collaborators, Drs. Jingwen Mao, Adam Simon, Simon Tapster, Laurence Robb, Grant Bybee, Jeffrey Marsh, Joseph Petrus, Robert Creaser, Andy DuFrane, Richard Stern, Huishou Ye, and Mrs Jackie Kleinsasser for their great contributions in field work, analyses, data interpretation, and/or writing.

Thanks to Mr. Chunsheng Li and Jianbin Zhang from Zhongtiaooshan Non-Ferrous Metals Group in China and Mr. Pierre Leveille and Vivian Stuart-Williams from Deep South Resources in Canada for the access permission and logistic assistance at Tongkuangyu and Haib, respectively.

Thanks to Mr. Martin von Dollen, Willard Desjardins, Biao Yang, William Zhe, and David Crabtree for their capable assistance with sample preparation and the SEM-EDS and EMPA analyses.

Special thanks to Professor Harold Gibson and some other professors (for those attending my research seminars at Laurentian) for incisive comments on my research. I also wish to thank my colleagues from China and Canada, including Drs. Haidong Zhang, Guiqing Xie, Jingjing Zhu, Hongda Hao, Xin Lin, Dongyang Zhang, Dylan McKeivitt, David Mole, Well-Shen Lee, Ijaz Ahmed, and many other individuals for their helpful discussions about my projects. Thanks to Mrs. Roxane Mehes, Natalie Lafleur-Roy, Courtney Folz, and Mr. Kipp Grose for their logistic assistance during my Ph.D. at Laurentian.

The Ph.D. thesis was funded by Canada First Research Excellence Fund through a Metal Earth thematic project and a Discovery Grant from the Natural Sciences and Engineering Research Council of Canada (RGPIN/5082-2017) to Jeremy Richards, the Natural Science Foundation of China through an International Cooperation and Exchange Project (41820104010) to Jingwen Mao, a China Geological Survey project (DD20160124) to Huishou Ye, as well as three student research grants from the Geological Society of America and the Society of Economic Geologist Canada Foundation. I was also awarded by a Chinese Scholarship Council Ph.D. scholarship.

In particular, I would like to thank my families for their supports and encouragement, and my girlfriend Dr. Boya Geng for her company, support, and love that brings me happiness and confidence in overcoming any difficulties. I cannot persist to finish the Ph.D. without them.

Table of Contents

<i>Abstract</i>	<i>iii</i>
<i>Co-Authorship Statement</i>	<i>v</i>
<i>List of Tables</i>	<i>xv</i>
<i>List of Figures</i>	<i>xvi</i>
<i>Appendix A (Lists of Additional Figures)</i>	<i>xxi</i>
<i>Electronic Supplementay Material (ESM)</i>	<i>xxiii</i>
<i>Chapter 1</i>	<i>1</i>
<i>1 Introduction to the thesis</i>	<i>1</i>
1.1 Introduction.....	1
1.2 Representative Archean to Paleoproterozoic porphyry-type Cu ± Au deposits.....	3
1.3 Research Objectives.....	5
1.4 Structure of Thesis.....	5
1.5 References.....	9
<i>Chapter 2</i>	<i>14</i>
<i>2 The Tongkuangyu Cu deposit, Trans-North China orogen: A metamorphosed Paleoproterozoic porphyry Cu deposit</i>	<i>14</i>
2.1 Abstract.....	14
2.2 Introduction.....	16
2.3 Geological setting of the northern Zhongtiaoshan region.....	17
2.3.1 Tectonic framework of the Zhongtiaoshan region.....	17
2.3.2 Stratigraphy of the northern Zhongtiaoshan region.....	18
2.3.3 Mineral deposits of the northern Zhongtiao region.....	21
2.4 Geology of the Tongkuangyu Cu deposit.....	22
2.4.1 Host rocks.....	23
2.4.2 Hydrothermal alteration.....	24
2.4.3 Copper mineralization.....	26

2.5	Previous geochronological results of the Tongkuangyu Cu deposit.....	29
2.6	Samples	30
2.7	Analytical techniques.....	31
2.7.1	Lithogeochemical analyses.....	31
2.7.2	Zircon, allanite, monazite, and rutile U-Pb dating.....	32
2.7.3	Re-Os dating of molybdenite and pyrite.....	33
2.8	Lithogeochemical results and interpretation.....	34
2.9	Geochronological results	35
2.9.1	Zircon.....	36
2.9.2	Allanite	37
2.9.3	Monazite	37
2.9.4	Rutile.....	38
2.9.5	Molybdenite.....	39
2.9.6	Pyrite.....	39
2.10	Discussion.....	39
2.10.1	Age and origin of the host rocks.....	39
2.10.2	Two stages of hydrothermal activity and their relationships to tectonothermal events	40
2.10.3	Metallogenic implications	41
2.11	Conclusions.....	43
2.12	Acknowledgements.....	44
2.13	References.....	45
2.14	Figures	57
2.15	Tables.....	76
<i>Chapter 3</i>		<i>79</i>
<i>3 Uncovering the missing magmatic link for the Tongkuangyu porphyry Cu deposit, Trans-North China Orogen: Implication for porphyry Cu-deposit model and exploration</i>		<i>79</i>
3.1	Abstract.....	79
3.2	Introduction.....	80
3.3	Geological Setting.....	82
3.3.1	Stratigraphy.....	82

3.3.2	The Tongkuangyu porphyry Cu deposit.....	85
3.4	Reported ~2.1 Ga magmatism in the northern Zhongtiaoshan region.....	86
3.5	Samples.....	88
3.6	Analytical methods.....	89
3.6.1	Whole-rock geochemistry.....	89
3.6.2	Zircon U-Pb isotopic analyses.....	89
3.6.3	Zircon Lu-Hf isotopic analyses.....	90
3.7	Results.....	91
3.7.1	Whole-rock geochemistry.....	91
3.7.2	Zircon U-Pb geochronology.....	91
3.7.3	Zircon Lu-Hf isotopes.....	93
3.8	Discussion.....	94
3.8.1	Absence of ~2.1 Ga magmatic rocks in the Jiangxian Group and Tongkuangyu.....	94
3.8.2	Verification of ~2.1 Ga magmatic events in the Zhongtiao Group.....	95
3.8.3	Original composition of ~2.09 Ga magmatism.....	96
3.8.4	A model for the Tongkuangyu deposit and its implications.....	98
3.9	Conclusions.....	102
3.10	Acknowledgment.....	102
3.11	References.....	103
3.12	Figures.....	111
3.13	Tables.....	118
<i>Chapter 4</i>		<i>121</i>
4	<i>Oxidized sulfur-rich arc magmas formed porphyry Cu deposits by 1.88 Ga</i>	<i>121</i>
4.1	Abstract.....	121
4.2	Introduction.....	122
4.3	Results.....	123
4.3.1	Geological setting.....	123
4.3.2	High-precision U-Pb geochronology.....	124
4.3.4	Relatively oxidized magmas.....	126
4.3.5	Sulfur-rich apatite and melt.....	128

4.4	Discussion and Conclusion.....	129
4.5	Methods	131
4.5.1	Sample preparation	131
4.5.2	Whole-rock geochemistry.....	131
4.5.3	LA-ICP-MS zircon U-Pb isotopes.....	132
4.5.4	CA-ID-TIMS zircon U-Pb isotopes.....	134
4.5.5	Rutile U-Pb isotopes	134
4.5.6	Zircon Lu-Hf isotopes.....	135
4.5.7	Zircon O isotopes.....	136
4.5.8	Electron microprobe analysis	137
4.5.9	Micro X-ray absorption near-edge structure spectroscopy (μ -XANES)	138
4.5.10	Methods in estimating melt sulfur content	141
4.6	Supplementary Information	142
4.6.1	Supplementary Note 1: the Haib porphyry Cu deposit.....	142
4.6.2	Supplementary Note 2: apatite crystallized prior to volatile saturation	146
4.6.3	Supplementary Note 3: P-T correction of magmatic fO_2 from apatite S μ -XANES data	147
4.7	Acknowledgements.....	147
4.8	References.....	149
4.9	Figures	162
<i>Chapter 5</i>		<i>167</i>
<i>5 Variable modes of formation for tonalite-trondhjemite-granodiorite-diorite (TTG)-related porphyry-type Cu \pm Au deposits in the Neoproterozoic southern Abitibi subprovince: Evidence from petrochronology and oxybarometry.....</i>		<i>167</i>
5.1	Abstract.....	167
5.2	Introduction.....	169
5.3	Geological setting of the southern Abitibi subprovince	172
5.3.1	Volcanic and sedimentary stratigraphy	172
5.3.2	Intrusive suites	174
5.3.3	Tectonic interpretation of the southern Abitibi greenstone belt	175
5.3.4	Mineral deposits.....	177
5.4	Porphyry-type Cu \pm Au deposits in the southern Abitibi greenstone belt	178
5.4.1	Côté Gold Au \pm Cu deposit (~2740 Ma)	178

5.4.2	Deposits associated with the ~2700 Ma Flavrian-Powell Intrusion	179
5.4.3	The Croxall Cu ± Mo ± Au deposit (~2689 Ma).....	181
5.5	Samples	182
5.5.1	Whole-rock geochemistry.....	182
5.5.2	Occurrence and features of primary zircon, amphibole, apatite, and Fe-Ti oxides	184
5.6	Analytical methods	185
5.6.1	Whole-rock geochemistry.....	185
5.6.2	Zircon U-Pb-Lu-Hf isotope and trace element analyses.....	186
5.6.3	Zircon O isotopes.....	188
5.6.4	Electron microprobe analyses (EMPA)	188
5.6.5	Micro X-ray absorption near edge structure (μ -XANES) at the S K-edge.....	189
5.7	fO_2 -P-T parameters	190
5.7.1	Oxybarometers.....	190
	<i>Zircon oxybarometer</i>	190
	<i>Amphibole oxybarometer</i>	190
	<i>Sulfur-in-apatite oxybarometer</i>	191
	<i>Magnetite-ilmenite oxybarometer</i>	192
5.7.2	P-T evaluation.....	192
5.8	Results.....	193
5.8.1	Lithochemistry	193
5.8.2	Zircon U-Pb geochronology	195
5.8.3	Zircon Hf-O isotopes	198
5.8.4	Apatite composition.....	199
	<i>Apatite S-Cl contents</i>	199
	<i>Geochemical discrimination of primary versus altered apatites</i>	200
	<i>Preliminary evaluation of pre-degassed melt S content</i>	202
5.8.4	Estimation of magmatic fO_2	203
	<i>Zircon</i>	203
	<i>Amphibole</i>	205
	<i>Sulfur-in-apatite μ-XANES spectra</i>	206
	<i>Magnetite-ilmenite mineral pairs</i>	209
5.9	Discussion.....	209
5.9.1	Geochronology and igneous petrogenesis	209
5.9.2	Oxidation state of the magmas	211
5.9.3	Metallogenic implications	213

5.10	Conclusion	217
5.11	Acknowledgments	218
5.12	Funding	218
5.13	References.....	218
5.14	Figures	232
5.15	Tables.....	253
6	<i>Concluding Statements</i>	255
6.1	Conclusions.....	255
6.2	Future Work.....	258
	<i>Appendix A (Additional Figures)</i>	259

List of Tables

Table 2.1 Summary of new and published geochronological results for volcanic and intrusive rocks and mineralization from the Tongkuangyu district.....	76
Table 2.2 Re-Os dates of molybdenite and pyrite from Tongkuangyu.....	78
Table 3.1. Summary of key features of the host rocks, alteration, and mineralization at Tongkuangyu porphyry Cu deposit, northern Zhongtiaoshan region.....	118
Table 3.2. Summary of new geochronological results for the representative igneous rocks from the northern Zhongtiaoshan region.....	119
Table 3.3. Representative porphyry Cu deposits with hypogene ores hosted mainly by pre-mineralization rocks.....	120
Table 5.1. Locations and descriptions of representative igneous rock samples from the Côté Gold, Flavrian-St-Jude, and Clifford areas in the southern Abitibi subprovince	253
Table 5.2. Summary of zircon U-Pb-Hf-O isotopic and fO_2 -T estimation results for the Côté Gold, Flavrian-St-Jude, and Clifford rocks in the southern Abitibi subprovince.....	254

List of Figures

Figure 2.1. Simplified geological map of the northern Zhongtiaoshan region (modified based on internal document of Shanxi No.6 Geology Engineering Reconnaissance Institute, 2002), with an inset map showing its location within the Trans-North China Orogen (modified from Zhao et al., 2005).	57
Figure 2.2. Lithostratigraphic column with metamorphic and tectonothermal events affecting the northern Zhongtiaoshan region (Bai et al., 1997).	58
Figure 2.3. Simplified geological map of the Tongkuangyu Cu deposit, showing lithological units and geometry of the orebodies, which is modified from internal material from the 214 Geological Group in Zhongtiao Mountain in Shanxi Province (1956).....	59
Figure 2.4. Cross section A-A', showing lithological units and spatial distribution of alteration, mineralization, and orebodies.	60
Figure 2.5. Cross section B-B', showing lithological units and spatial distribution of alteration, mineralization, and orebodies.	61
Figure 2.6. Representative photographs of lithological relationships at the Tongkuangyu Cu deposit.	62
Figure 2.7. Representative photomicrographs of the main lithologies at the Tongkuangyu Cu deposit.	63
Figure 2.8. Photographs and photomicrographs of early disseminated and veinlet alteration and mineralization in granodiorite porphyry from Tongkuangyu.	64
Figure 2.9. Photomicrographs of veinlets and foliated alteration and mineralization in schists from Tongkuangyu.....	65
Figure 2.10. Photomicrographs of syn- and post-deformation alteration and mineralization from Tongkuangyu.	66

Figure 2.11. Vein-type copper mineralization from Tongkuangyu.	67
Figure 2.12. Microphotographs of datable minerals allanite, monzonite, rutile from the Tongkuangyu Cu deposit.	69
Figure 2.13. Zr/TiO ₂ -Nb/Y discrimination diagram (Winchester and Floyd, 1977) for the major lithologies from the Tongkuangyu district.	70
Figure 2.14. Zircon U-Pb concordia diagrams for the major rock phases from Tongkuangyu.	72
Figure 2.15. U-Pb concordia diagrams for hydrothermal allanite, monazite, and rutile samples from Tongkuangyu.	73
Figure 2.16. Re-Os model ages for (A) molybdenite from a deformed quartz - chalcopyrite - molybdenite vein (sample 23-2), and (B) pyrite from an undeformed quartz-pyrite-chalcopyrite vein (sample ZT05).	74
Figure 3.1. (A) Map showing the location of the northern Zhongtiaoshan region within the Trans-North China Orogen. (B) Simplified geological map of the northern Zhongtiaoshan region, which is adapted from Meng et al. (2020) and Shanxi No. 6 Geology Engineering Reconnaissance Institute (unpublished report), 2002.	111
Figure 3.2. Simplified geologic map of the Tongkuangyu porphyry Cu deposit in northern Zhongtiaoshan region, reproduced from Meng et al. (2020) with publication permission from the journal of Economic Geology.	112
Figure 3.3. Photographs of disseminated- and veinlet-type alteration and mineralization in granodiorite, biotite schist, and quartz-sericite schist from the deep levels (in meters above sea level) of the Tongkuangyu Cu deposit.	113
Figure 3.4. Zr/TiO ₂ versus Nb/Y discrimination diagram (Winchester and Floyd, 1977) for the albite-chlorite-sericite schist from the bottom of the Bizigou Formation in the northern Zhongtiaoshan region.	114

Figure 3.5. (A) Primitive mantle-normalized trace element and (B) chondrite-normalized rare-earth element diagrams for samples of the albite-chlorite-sericite schist (i.e., basaltic to andesitic volcanic tuffs) from the bottom of Bizigou Formation in the northern Zhongtiaoshan region. .	115
Figure 3.6. Zircon U-Pb concordia diagrams for the representative samples from the northern Zhongtiaoshan region.....	116
Figure 3.7. Simplified cartoon model (not to scale) illustrating the development of the Tongkuangyu deposit.....	117
Figure 4.1. Simplified geological map of the Haib area showing main lithological units.	162
Figure 4.2. Chondrite-normalized rare-earth element spider diagram for igneous rocks from Haib. The normalization values are from Sun and McDough (1989).....	163
Figure 4.3. Zircon U-Pb-Hf-O and rutile U-Pb isotopes for representative rocks in Haib.....	164
Figure 4.4. Backscattered electron images of inclusions in titanite and zircon, apatite μ -XANES spectra and sulfur contents, and results of magmatic fO_2 estimation.	165
Figure 4.5. Histograms of S concentrations of igneous apatites and melt inclusions from arc magmas, rocks associated with Phanerozoic porphyry Cu systems and the Haib.....	166
Figure 5.1. Temporal correlation between global porphyry Cu deposits, Earth's tectonic regimes, lithologic transition, and ocean-atmospheric evolution through geological time since 3.5 Ga..	232
Figure 5.2. Simplified geologic map of the Abitibi and Pontiac subprovinces, modified from Thurston <i>et al.</i> (2008) and Leclerc <i>et al.</i> (2012). Inset in upper-left showing the location of Figure 4.2 in the Superior province. Abbreviations: PDF = Destor–Porcupine Fault Zone, LLCF = Larder Lake–Cadillac Fault Zone.....	233
Figure 5.3. Geological framework of the southern Abitibi subprovince over geological time. .	234
Figure 5.4. Simplified geologic maps of the (a) Côté Gold, (b) Flavrian-St-Jude, and (c) Clifford area, modified from Katz <i>et al.</i> (2021), Galley (2003), and Piercey <i>et al.</i> (2008).....	235

Figure 5.5. Field photographs for main lithological units from the Côté Gold, Flavrian-St-Jude, and Clifford areas in the southern Abitibi subprovince.	236
Figure 5.6. Microphotographs for the main igneous rock phases from the Côté Gold, Flavrian-St-Jude, and Clifford areas in the southern Abitibi subprovince.	237
Figure 5.7. Representative amphibole and apatite crystals from the main lithological units from Côté Gold, Flavrian-St-Jude, and Clifford in the southern Abitibi subprovince.	239
Figure 5.8. Representative magnetite and ilmenite from the main lithologies from Côté Gold, Flavrian-St-Jude, and Clifford in the southern Abitibi subprovince.	241
Figure 5.9. Primitive mantle-normalized trace element and chondrite-normalized rare earth element diagrams for the major igneous lithologies from Côté Gold, Flavrian-St-Jude, and Clifford in the southern Abitibi subprovince.	242
Figure 5.10. Trace element concentration and ratios for the major igneous lithologies from Côté Gold, Flavrian-St-Jude, and Clifford in the southern Abitibi subprovince.	243
Figure 5.11. Zircon U-Pb concordia diagrams for the major igneous rock phases from Côté Gold, Flavrian-St-Jude, and Clifford in the southern Abitibi subprovince.	245
Figure 5.12. Zircon Hf-O isotopes for the major igneous rock phases from Côté Gold, Flavrian-St-Jude, and Clifford in the southern Abitibi subprovince.	246
Figure 5.13. Plots of apatite volatile compositions for the major igneous rock phases from Côté Gold, Flavrian-St-Jude, and Clifford in the southern Abitibi subprovince.	247
Figure 5.14. Chondrite-normalized rare earth elements for zircons from the major igneous rock phases from the study areas in the southern Abitibi subprovince.	248
Figure 5.15. Histogram and plot of $T-fO_2$ values estimated from zircon geochemistry for the major igneous phases in Côté Gold, Flavrian-St-Jude, and Clifford in the southern Abitibi subprovince.	249

Figure 5.16. Plots for ΔFMQ values versus temperatures and/or pressures, as estimated from amphibole for the major igneous rock phases from Côté Gold and Clifford in the southern Abitibi subprovince..... 250

Figure 5.17. Apatite μ -XANES spectra at S *K*-edge for St-Jude trondhjemite (SJ-08), Clifford tonalite (sample CS-20) and plagioclase-phyric porphyry (sample CS-22).. 251

Figure 5.18. Summary of the interpreted fO_2 -T estimates using zircon, amphibole, apatite, and magnetite-ilmenite oxybarometers for the major igneous rock phases from Côté Gold, Flavrian-St-Jude, and Clifford in the southern Abitibi subprovince. 252

Appendix A (Lists of Additional Figures)

Figure A2.1. Zircon U-Pb data, recalculated from Sun and Hu (1993).....	259
Figure A2.2. Photomicrographs of relatively unaltered quartz-sericite schist collected from outcrops of the Luotuofeng Formation, 5 km northeast of Tongkuangyu.....	260
Figure A2.3. Secondary K-feldspar associated with chalcopyrite overprinting on the albite phenocryst in granodiorite porphyry (sample R3B14); (A) cross-polarized light; (B) plane-polarized light; (C) reflected light; (D) false-color SEM image.....	261
Figure A2.4. Cathodoluminescence images showing zircon grains for U-Pb analyses.....	262
Figure A2.5. Primitive mantle- and chondrite-normalized trace element diagrams for (A–B) quartz-sericite schist, (C–D) biotite schist, and (E–F) granodiorite porphyry. Normalization values are from Sun and McDonough (1989).....	263
Figure A3.1. Zircon U-Pb concordia diagrams for sample ZT91-1 (feldspar porphyry) from the lower part of the Zhongtiao Group, northern Zhongtiaoshan region.....	264
Figure A3.2. Outcrop photograph of layered albite-chlorite-sericite schist rock from the bottom of the Bizigou Formation of the Zhongtiao Group in the northern Zhongtiaoshan region (35°19'37.2''N, 111°37'16.4''E, 700 m).....	265
Figure A3.3. Photomicrographs of the albite-chlorite-sericite schist (i.e., basaltic to andesitic volcanic tuffs) samples collected from the bottom of the Bizigou Formation in the northern Zhongtiaoshan region.....	266
Figure A3.4. Cathodoluminescence (CL) images of the zircon grains analyzed for U-Pb dating from (A) rhyolitic tuff (sample R4B07), (B–D) granodiorite (samples 5159-1, 5S342-2, and Z30), (E, F) albite-chlorite-sericite schist (i.e., basaltic–andesitic volcanic tuffs; samples 19V05 and 19V08).....	267
Figure A4.1. Geological map and cross section of the Haib deposit.....	268

Figure A4.2. Drill core and field photographs of igneous rocks in the Haib area.	270
Figure A4.3. Summary of whole-rock geochemistry of the igneous rocks from Haib and the western Richtersveld Magmatic Arc.....	271
Figure A4.4. Photographs and photomicrographs of alteration and vein types.....	273
Figure A4.5. Zircon U-Pb concordia diagrams for the major rock units from Haib. MSWD represents the mean square of weighted deviates.	275
Figure A4.6. CA-ID-TIMS zircon U-Pb dating results for representative igneous rocks from the Haib deposit. (A and B) Wetherill concordia diagram of CA-ID-TIMS U-Pb isotope analyses..	276
Figure A4.7. LA-ICP-MS U-Pb dating of hydrothermal rutile intergrown with chalcopyrite. ..	277
Figure A4.8. Backscattered electron images of zircons and the apatite inclusions for μ -XANES analyses from Haib, except for image 1 which is in cathodoluminescence.	278
Figure A4.9. Titanite- and zircon-hosted apatite halogen contents.	279
Figure A4.10. Sulfur μ -XANES spectra of apatites and zircon from the main igneous phases in Haib, as well as reference materials.....	280
Figure A5.1. Cathodoluminescence (CL) images of representative zircon grains analyzed for U-Pb-Hf-O isotopes	281
Figure A5.2. X_{Cl}/X_{OH} versus X_F/X_{OH} ratios for altered apatite inclusions in amphibole in sample FLV-32 (Flavrian diorite).	282
Figure A5.3. Zircon Hf and Y contents, and Zr/Hf and Th/U ratios for samples from the Côté Gold, Flavrian-St-Jude, and Clifford intrusions.	283
Figure A5.4. Plots of (A) fO_2 (ΔFMQ , from zircon oxybarometers) and (B) Ti-in-zircon temperatures for representative igneous rocks from the study areas.	284

Electronic Supplementay Material (ESM)

ESM1: Additional Tables for Chapter 2

Table A2.1. Summary of original zircon U-Pb data for samples of meta-rhyolitic tuff and meta-dacitic tuff from the Jiangxian and Zhongtiao Groups, respectively

Table A2.2. Locations and descriptions of samples from the Tongkuangyu ore district

Table A2.3. Sample preparation and instrumental parameters

Table A2.4. LA-ICP-MS U-Pb data of the secondary reference materials for dating zircon, allanite, monazite, and rutile in the three labs (the Radiogenic Isotope Facility of the University of Alberta; the Central Analytical Facility of Laurentian University; Mineral Exploration Research Centre – Isotope Geochemistry Lab, Laurentian University)

Table A2.5. Geochemical data for lithological samples from the Tongkuangyu deposit

Table A2.6. LA-ICP-MS zircon U-Pb data for quartz-sericite schist, biotite schist, and granite porphyry samples at the Tongkuangyu deposit

Table A2.7. LA-ICP-MS U-Pb data for the allanite, monazite, and rutile from the Tongkuangyu deposit

ESM2: Additional Tables for Chapter 3

Table A3.1. LA-ICP-MS zircon U-Pb isotopes for feldspar porphyry sample ZT91-1 from the lower part of the Zhongtiao Group, northern Zhongtiaoshan region

Table A3.2. Whole-rock geochemistry of the meta-basaltic–andesitic tuff from the bottom of the Bizigou Formation in northern Zhongtiaoshan region

Table A3.3. LA-ICP-MS parameters for U-Pb-Lu-Hf isotope analyses

Table A3.4. LA-ICP-MS zircon U-Pb isotope results for representative samples from the northern Zhongtiaoshan region

Table A3.5. LA-ICP-MS zircon Lu-Hf isotope results for one representative basaltic-andesitic tuff sample (19V05) from the bottom of the Bizigou Formation in the northern Zhongtiaoshan region

ESM3: Tables for Chapter 4

Table A4.1. Locations and descriptions of representative igneous rocks from the Haib area

Table A4.2. Whole-rock geochemistry for representative igneous rocks from the Haib area

Table A4.3. Instrumental parameters for LA-ICP-MS U-Pb-Lu-Hf isotope and trace element analyses

Table A4.4. Split stream LA-ICP-MS zircon U-Pb isotope and trace element analyses for representative igneous rocks from the Haib area

Table A4.5. CA-ID-TIMS zircon U-Pb isotope analyses for representative intrusive rocks in the Haib area

Table A4.6. LA-ICP-MS U-Pb isotope analyses of hydrothermal rutile associated with chalcopyrite mineralization in the Haib deposit

Table A4.7. LA-ICP-MS zircon Lu-Hf isotopes for representative igneous rocks from the Haib area

Table A4.8. SIMS zircon O isotopes for representative igneous rocks from the Haib area

Table A4.9. Electron microprobe analyses of zircon/titanite-hosted apatite crystals from the representative igneous rocks from the Haib area

ESM4: Additional Tables for Chapter 5

Table A5.1. Litho-geochemistry for the main lithologies from the Côté Gold, Flavrian-St-Jude, and Clifford areas

Table A5.2. Split-Stream LA-ICP-MS zircon U-Pb isotope and trace element analyses for representative igneous rocks from Côté Gold, Flavrian-St-Jude, and Clifford in the southern Abitibi subprovince

Table A5.3. LA-ICP-MS zircon Lu-Hf isotope analyses for representative igneous rocks from Côté Gold, Flavrian-St-Jude, and Clifford in the southern Abitibi subprovince

Table A5.4. SIMS zircon O isotope analyses for representative igneous rocks from Côté Gold, Flavrian-St-Jude, and Clifford in the southern Abitibi subprovince

Table A5.5. Electron microprobe analyses for representative apatite, amphibole, and magnetite-ilmenite from the Côté Gold, Flavrian-St-Jude, and Clifford areas in the southern Abitibi subprovince

Chapter 1

Introduction to the thesis

1.1 Introduction

A simple formulation of the tectonomagmatic model for porphyry Cu deposit formation is that it requires the emplacement of large volumes ($>100 \text{ km}^3$) of hydrous, moderately oxidized (FMQ+1 to +2), and S-rich magma in a mid- to upper crustal plutonic complex, from which aqueous fluids are exsolved to generate an ore-forming hydrothermal system at shallow (subvolcanic) crustal levels (Cline and Bodnar, 1991; Richards, 2003; Sillitoe, 2010). Such magmas are generated most commonly and reproducibly in Phanerozoic arc settings, as a product of subduction of hydrated and oxidized oceanic lithosphere (Sillitoe, 1972). The associated magmas are typically calc-alkaline to mildly alkaline (potassic), and their moderate oxidation state prevents extensive exsolution of sulfide phases, which would otherwise preferentially deplete the magma in Cu and siderophile elements (Candela, 1992, 1997). The high magmatic water content results in exsolution of an aqueous fluid phase upon ascent into the upper crust, into which these metals will efficiently partition (Candela and Holland, 1984).

Most known porphyry Cu systems formed in the Phanerozoic, but are rare in the Precambrian, which has been ascribed to poor preservation of upper crustal rocks in tectonically active environments, and/or unfavorable tectonomagmatic condition relating to reduced oceanic lithosphere in the Precambrian (Wilkinson and Kesler, 2007; Evans and Tomkins, 2011; Richards and Mumin, 2013). The timing of deep ocean oxygenation has been constrained to 0.5 Ga by a striking increase of the $\text{Fe}^{3+}/\Sigma\text{Fe}$ ratios in hydrothermally altered seafloor basalts

since that time (Stolper and Keller, 2018). The marine sulfate concentration is suggested to have increased gradually from $< 200 \mu\text{M}$ in the Archean, $< 2 \text{ mM}$ until 1.3 Ga, to 7–10 mM in the mid-Neoproterozoic, and shifted to 28 mM in the present. Planavsky et al. (2012) argued that a sharply rising and falling marine oxygen and sulfate levels (ca. 5–20 mM with error) also occurred during a short period from ~ 2.3 to 2.1 Ga. Consequently, ferrous iron and sulfide were thought to be predominant in terrigenous sediments and hydrothermally altered oceanic lithosphere in most of the Precambrian Era. Recycling these materials will release a significant proportion of reduced H_2S to the ‘sub-arc’ mantle, making large amounts of magmatic sulfide retained in the source region, into which chalcophile and siderophile elements will preferentially partition (Evans and Tomkins, 2011). Early sulfide saturation will therefore deplete chalcophile and siderophile elements and limit the fertility of the resultant magma. The more reduced nature of arc-like magmas in the Precambrian is hypothesized to reduce their ability to transport Cu out of the mantle, but they can still transport lithophile elements such as Sn-W-(Mo), and mobilize Au in bisulfide-bearing hydrothermal fluids. Consequently, porphyry Au and Sn-W-Mo deposits occur in both Precambrian and Phanerozoic volcano-plutonic sequences (Douch et al., 1984; Deb and Sarkar, 1990; Sundblad, 1991; Sundblad et al., 1993), but porphyry Cu deposits are almost exclusively restricted to the Phanerozoic.

The hypothesis that the rarity of porphyry $\text{Cu} \pm \text{Au}$ deposits in the Precambrian has been ascribed to poor preservation of tectonically active plate margins and unfavorable tectonomagmatic conditions (Wilkinson and Kesler, 2007; Evans and Tomkins, 2011; Richards and Mumin, 2013) remains poorly constrained, because (1) the genesis of some of these deposits remain debated owing to modification of primary mineralogy and textures by metamorphism, alteration, and deformation; (2) reliable quantitative measurements of the

redox state and volatile element abundances for causative magmas associated with the rare reported Precambrian porphyry Cu deposits are lacking ([Prouteau and Scaillet, 2012](#); [Yang et al., 2014](#)).

1.2 Representative Archean to Paleoproterozoic porphyry-type Cu ± Au deposits

To test the hypothesis, the Ph.D. project focuses on investigating the Archean–Paleoproterozoic deposits that are reported to be porphyry-type (the research objectives are itemized in next section). We choose these oldest deposits because the tectonomagmatic conditions related to redox states of oceanic lithosphere in Archean to Paleoproterozoic are hypothesized to be most likely unfavorable for porphyry Cu ± Au deposit formation.

Only a few porphyry-type Cu ± Au deposits are reported in the Archean to Paleoproterozoic, with the earliest group of deposits associated with ~2.74–2.69 Ga high-Al or low-Al tonalite-trondhjemite-granodiorite-diorite (TTG) in the Abitibi greenstone belt, Superior Province, Canada. The Côté Au-Cu deposit is hosted by the Chester intrusion that consists of tonalite, diorite and quartz diorite, and minor magmatic-hydrothermal breccia in the Swayze greenstone belt, northern Ontario, Canada ([Katz et al., 2017](#)). These rocks have been dated at ~2.74 Ga and display disseminated and veinlet mineralization associated with potassic and sodic alteration. A few porphyry-style breccia-hosted Cu deposits also occur in the volcanoplutonic rocks of the eastern Abitibi greenstone belt. For example, the St. Jude breccia-hosted mineralization and Don Rouyn deposit are associated with different trondhjemite phases in the Flavrian-Powell pluton ([Goldie et al., 1979](#); [Galley and Van Breemen, 2002](#)). The Flavrian-Powell pluton contains diorite, quartz-diorite, and later tonalite and trondhjemite phases

formed at ~2.70 Ga. Similarly, the Croxall breccia-hosted mineralization is associated with the Clifford stock, which intrudes the Ben Nevis volcanic complex. The Clifford stock consists of amphibole-bearing equigranular tonalite to granodiorite that formed at ~2.68 Ga (Piercey et al., 2008). Other reported porphyry-type Cu-Mo-Au deposits, such as those hosted by the Chibougamau pluton, in the northeast Abitibi greenstone belt, have undergone upper greenschist metamorphism and multiple deformation events, such that the original features of the deposit have been modified (Côté-Mantha et al., 2012).

The Paleoproterozoic group includes the ~2.48 Ga Malanjkhanda Cu-Mo deposit associated with peraluminous, calc-alkaline tonalite-granodiorite pluton in the Bhandara Craton, Central India (Sarkar et al., 1996; Stein et al., 2004); the ~2.1 Ga Tongkuangyu porphyry Cu deposit in China (Meng et al., 2020); the ~1.88 Ga Haib Cu deposit in South Namibia (Grumbley, 2015); and the ~1.88 Ga Vaikijaur, Tallberg, Norrbotten, and possibly Aitik deposits in the Fennoscandian shield of northern Sweden (Lundmark et al., 2005). This study will include the Tongkuangyu and Haib deposits, which are described in more detail below.

The Tongkuangyu porphyry Cu deposit is hosted by a metamorphosed Paleoproterozoic granite porphyry and mafic to felsic volcanic rocks in the Zhongtiaoshan region, Trans-North China Block. Early deformed, disseminated and veinlet Cu mineralization (mainly chalcopyrite) is associated with potassic alteration (~2.1 Ga) that postdated the ~2.18 Ga granite porphyry host rock (Liu et al., 2016). The alteration and mineralization are interpreted to be associated with regional ~2.1 Ga magmatism. The Haib Cu deposit is hosted by the Vioolsdrif intrusive suite (~1.86 Ga), which was intruded into the Orange River Group of the Richtersveld magmatic arc of southern Namibia (Grumbley, 2015). The Vioolsdrif stock is a composite intrusion consisting of early andesitic porphyry, two later phases of granodiorite porphyry, and equigranular

granodiorite, gabbro, and aplite. The andesitic porphyry is intruded by potassic granodiorite porphyry and later pale granodiorite porphyry. The alteration assemblages are typical of calc-alkaline porphyry Cu systems with Cu mineralization associated with early stage sodic and potassic alteration.

1.3 Research Objectives

- (1) Identifying whether the rarely reported Archean–Paleoproterozoic Cu ± Au deposits (i.e., Tongkuangyu in the Tran-North China Block in China, Haib in the Richtersveld Arc in South Namibia, those in the Abitibi greenstone belt in Canada) are porphyry-type.
- (2) Constraining the absolute timing of the causative magmas associated with these deposits using high-precision zircon U-Pb geochronology, as well as defining their magmatic origin using whole-rock geochemistry and zircon Hf-O isotopes.
- (3) Estimating the redox state and volatile element abundances of the causative magmas for the mineralization.
- (4) Testing whether metallogenic processes for Phanerozoic porphyry Cu systems operated in the Precambrian, or whether key geodynamic or geochemical differences reduced the fertility of Precambrian magmas.

1.4 Structure of Thesis

The Ph.D. thesis is organized in six chapters, including an introductory chapter (Chapter 1), four journal manuscripts (Chapters 2–5), and a concluding chapter (Chapter 6). The Chapters 2–5 are stand-alone manuscripts prepared for publication in peer-reviewed journals. These chapters focus on resolving different scientific issues as follows.

Chapter 2 focuses on resolving the debate regarding the genesis of the Tongkuangyu Cu deposit in Trans-North China Orogen. The Tongkuangyu copper deposit in the

Zhongtiaoshan region, southern Trans-North China orogen, is hosted by a poorly-constrained sequence of Paleoproterozoic volcano-sedimentary and granitic rocks that have been metamorphosed and deformed. The genesis of this deposit is debated to be porphyry-type or sediment-hosted stratiform-type. In this study, we remapped the distribution of host rocks, alteration, and mineralization, and more accurately constrain the age of ore formation and overprinting. We showed that many features of Tongkuangyu can be fitted by a porphyry-type model.

Published as: Meng, X. Y., Richards, J. P., Mao, J. W., Ye, H. S., DuFrane, S. A., Creaser, R., Marsh, J. & Petrus, J. (2020). The Tongkuangyu Cu Deposit, Trans-North China Orogen: A Metamorphosed Paleoproterozoic Porphyry Cu Deposit. Economic Geology 115, 51–77.

Chapter 3 reports a model for the Tongkuangyu porphyry Cu deposit. Porphyry Cu-Mo ± Au deposits commonly formed by hydrothermal fluids exsolved from a subjacent coeval magma chamber. Chapter 2 shows that the Tongkuangyu porphyry Cu deposit in the northern Zhongtiaoshan region of the Trans-North China Orogen is hosted by ~2.18 Ga granodiorite porphyry and granodiorite and ~2.5–2.2 Ga mafic- to felsic volcanic or subvolcanic rocks, which significantly predate the porphyry-type mineralization by ~80 million years. Chapter 5 refines the extent and absolute timing, as well as the geochemistry of the ~2.1 Ga magmatism in the northern Zhongtiaoshan region. Based on these results, we conclude a causative magma chamber need not in all cases to be immediately subjacent to the mineralized porphyritic stocks and dikes.

Published as: Meng, X. Y., Kontak, D., Richards, J., Mao, J.W., Marsh, J. Uncovering the missing magmatic link for the Tongkuangyu porphyry Cu deposit, Trans-North China Orogen: Implication for porphyry Cu-deposit models and exploration: Society of Economic Geologists Special Publication in tribute to Jeremy P. Richards. In press.

Chapter 4 focuses on constraining the origin of the causative magmas associated with the Paleoproterozoic Haib porphyry Cu deposit in Namibia. To test whether similar metallogenic processes have operated in the Precambrian, we investigated the absolute timing of emplacement of the ore-related calc-alkaline plutonic rocks associated with the Haib porphyry Cu deposit in the Paleoproterozoic Richtersveld Magmatic Arc in southern Namibia. We further constrain the origin, oxidation state, and S contents of the magmas. We show that similar metallogenic processes for Phanerozoic porphyry Cu deposit operated at ~1.88 Ga.

Published as: Meng, X., Kleinsasser, J. M., Richards, J. P., Tapster, S. R., Jugo, P. J., Simon, A. C., Kontak, D. J., Robb, L., Bybee, G. M., Marsh, J. H., and Stern, R. A., 2021, Oxidized sulfur-rich arc magmas formed porphyry Cu deposits by 1.88 Ga: Nature Communications, v. 12, p. 2189.

Chapter 5 focuses on defining the formation modes of TTG (tonalite-trondhjemite-granodiorite-diorite)-related porphyry Cu ± Au deposits in Neoproterozoic Abitibi subprovince. The upper continental crusts in many Archean terranes comprise dominantly of sodium-enriched tonalite-trondhjemite-granodiorite-diorite (TTG) series rocks, which are hypothesized to be relatively reduced or sulfur-poor that prevented porphyry Cu ± Au deposit formation in the Archean. To test the hypothesis, we investigated the nature of the causative magmas for the ~2.7 Ga TTG-related Côté Gold, St-Jude, and Croxall porphyry-type Cu ± Au

deposits reported in the Neoproterozoic southern Abitibi subprovince. We find that these deposits formed from relatively reduced to moderately oxidized magmas and conclude variable formation modes for these deposits. The findings imply that the rarity of porphyry-type Cu-Au deposit in the Archean may be attributed to either local restriction of these favorable metallogenic conditions and/or preservation or exploration bias.

Submitted as: Meng, X. Y., Richards, J., Kontak, D., Simon, A., Kleinsasser, J., Marsh, J., Stern, R., Jugo, P. Variable formation modes of tonalite-trondhjemite-granodiorite-diorite (TTG)-related porphyry-type Cu ± Au deposits in the Neoproterozoic southern Abitibi subprovince (Canada): Evidence from petrochronology and oxybarometry. Journal of Petrology.

1.5 References

- Wilkinson, B. H., and Kesler, S. E., 2007, Tectonism and Exhumation in Convergent Margin Orogens: Insights from Ore Deposits: *The Journal of Geology*, v. 115, p. 611–627.
- Candela, P. A., 1992, Controls on ore metal ratios in granite-related ore systems: an experimental and computational approach: *Earth and Environmental Science Transactions of The Royal Society of Edinburgh*, v. 83, p. 317–326.
- Candela, P. A., 1997, A Review of Shallow, Ore-related Granites: Textures, Volatiles, and Ore Metals: *Journal of Petrology*, v. 38, p. 1619–1633.
- Candela, P. A., and Holland, H. D., 1984, The partitioning of copper and molybdenum between silicate melts and aqueous fluids: *Geochimica et Cosmochimica Acta*, v. 48, p. 373–380.
- Cline, J. S., and Bodnar, R. J., 1991, Can economic porphyry copper mineralization be generated by a typical calc-alkaline melt? : *Journal of Geophysical Research: Solid Earth*, v. 96, p. 8113–8126.
- Côté-Mantha, O., Daigneault, R., Gaboury, D., Chartrand, F., and Pilote, P., 2012, Geology, Alteration, and Origin of Archean Au-Ag-Cu Mineralization Associated with the Synvolcanic Chibougamau Pluton: The Brosman Prospect, Abitibi Greenstone Belt, Canada: *Economic Geology*, v. 107, p. 909–934.
- Deb, M., and Sarkar, S. C., 1990, Proterozoic tectonic evolution and metallogenesis in the Aravalli-Delhi orogenic complex, northwestern India: *Precambrian Research*, v. 46, p. 115–137.

- Douch, C. J., Ramsay, C. R., Hackett, D., Jackson, N. J., and Drysdall, A. R., 1984, Rare element mineralization related to Precambrian alkali granites in the Arabian Shield: *Economic Geology*, v. 79, p. 1366–1377.
- Evans, K. A., and Tomkins, A. G., 2011, The relationship between subduction zone redox budget and arc magma fertility: *Earth and Planetary Science Letters*, v. 308, p. 401–409.
- Galley, A., van Breemen, O., and Franklin, J., 2000, The relationship between intrusion-hosted Cu-Mo mineralization and the VMS deposits of the Archean Sturgeon Lake mining camp, northwestern Ontario: *Economic Geology*, v. 95, p. 1543–1550.
- Galley, A. G., and Van Breemen, O., 2002, Timing of Synvolcanic Magmatism in Relation to Base-metal Mineralization, Rouyn-Noranda, Abitibi, Volcanic Belt, Quebec, Natural Resources Canada, Geological Survey of Canada, p. 1–9.
- Goldie, R., Kotila, B., and Seward, D., 1979, The Don Rouyn Mine: an Archean porphyry copper deposit near Noranda, Quebec: *Economic Geology*, v. 74, p. 1680–1684.
- Grumbley, N. L., 2015, The Geological Evolution of the Haib Cu-Mo Porphyry, Namibia: Unpublished M. Sc. thesis, Dublin, Ireland, Trinity college, the University of Dublin, 175 p.
- Katz, L. R., Kontak, D. J., Dubé, B., and McNicoll, V., 2017, The geology, petrology, and geochronology of the Archean Côté Gold large-tonnage, low-grade intrusion-related Au (–Cu) deposit, Swayze greenstone belt, Ontario, Canada: *Canadian Journal of Earth Sciences*, v. 54, p. 173–202.

- Liu, X., Fan, H. R., Santosh, M., Yang, K. F., Qiu, Z. J., Hu, F. F., and Wen, B. J., 2016, Geological and geochronological constraints on the genesis of the giant Tongkuangyu Cu deposit (Palaeoproterozoic), North China Craton: *International Geology Review*, v. 58, p. 155–170.
- Lundmark, C., Stein, H., and Weihed, P., 2005, The geology and Re–Os geochronology of the Palaeoproterozoic Vaikijaur Cu–Au–(Mo) porphyry-style deposit in the Jokkmokk granitoid, northern Sweden: *Mineralium Deposita*, v. 40, p. 396–408.
- Meng, X. Y., Richards, J. P., Mao, J. W., Ye, H. S., DuFrane, S. A., Creaser, R., Marsh, J. & Petrus, J. (2020). The Tongkuangyu Cu Deposit, Trans-North China Orogen: A Metamorphosed Paleoproterozoic Porphyry Cu Deposit. *Economic Geology* **115**, 51–77.
- Piercey, S. J., Chaloux, E. C., Péroquin, A. S., Hamilton, M. A., and Creaser, R. A., 2008, Synvolcanic and younger plutonic rocks from the Blake River Group: implications for regional metallogenesis: *Economic Geology*, v. 103, p. 1243–1268.
- Planavsky, N. J., Bekker, A., Hofmann, A., Owens, J. D., and Lyons, T. W., 2012, Sulfur record of rising and falling marine oxygen and sulfate levels during the Lomagundi event: *Proceedings of the National Academy of Sciences of the United States of America*, v. 109, p. 18300–18305.
- Prouteau, G., and Scaillet, B., 2012, Experimental constraints on sulphur behaviour in subduction zones: Implications for TTG and adakite production and the global sulphur cycle since the Archean: *Journal of Petrology*, p. 183–213.

- Richards, J. P., 2003, Tectono-magmatic precursors for porphyry Cu-(Mo-Au) deposit formation: *Economic Geology*, v. 98, p. 1515–1533.
- Richards, J. P., and Mumin, A. H., 2013, Magmatic-hydrothermal processes within an evolving Earth: Iron oxide-copper-gold and porphyry Cu \pm Mo \pm Au deposits: *Geology*, v. 41, p. 767–770.
- Sarkar, S. C., Kabiraj, S., Bhattacharya, S., and Pal, A. B., 1996, Nature, origin and evolution of the granitoid-hosted early Proterozoic copper-molybdenum mineralization at Malanjkhand, Central India: *Mineralium Deposita*, v. 31, p. 419–431.
- Sillitoe, R. H., 1972, A plate tectonic model for the origin of porphyry copper deposits: *Economic geology*, v. 67, p. 184–197.
- Sillitoe, R. H., 2010, Porphyry Copper Systems: *Economic Geology*, v. 105, p. 3–41.
- Stolper, D. A., and Keller, C. B., 2018, A record of deep-ocean dissolved O₂ from the oxidation state of iron in submarine basalts: *Nature*, v. 553, p. 323–327.
- Stein, H. J., Hannah, J. L., Zimmerman, A., Markey, R. J., Sarkar, S. C., and Pal, A. B., 2004, A 2.5 Ga porphyry Cu–Mo–Au deposit at Malanjkhand, central India: implications for Late Archean continental assembly: *Precambrian Research*, v. 134, p. 189–226.
- Sundblad, K., 1991, Lead isotopic evidence for the origin of 1.8–1.4 Ga ores and granitoids in the southeastern part of the Fennoscandian Shield: *Precambrian Research*, v. 51, p. 265–281.

Sundblad, K., Ahl, M., and Schöberg, H., 1993, Age and geochemistry of granites associated with Mo mineralizations in western Bergslagen, Sweden: *Precambrian Research*, v. 64, p. 319–335.

Chapter 2

The Tongkuangyu Cu deposit, Trans-North China orogen: A metamorphosed Paleoproterozoic porphyry Cu deposit

2.1 Abstract

The Tongkuangyu copper deposit in the Zhongtiaoshan region, southern Trans-North China Orogen, is hosted by a poorly constrained sequence of Paleoproterozoic volcanosedimentary (quartz-sericite schist and biotite schist) and granitic rocks that have been metamorphosed to lower greenschist facies and variably deformed. The deposit has previously been proposed to be either a porphyry-type or sediment-hosted stratiform Cu deposit, and its age of formation has been debated.

The quartz-sericite schist is interpreted to be a felsic crystal tuff, and consists of angular quartz crystals in a fined-grained sericite-altered matrix. Two quartz-sericite schist samples yielded zircon U-Pb upper concordia intercept ages of 2512 ± 12 Ma (2σ , MSWD = 0.19) and 2335 ± 16 Ma (2σ , MSWD = 0.80). Biotite schist, which is interleaved locally with the quartz-sericite schist and is interpreted to be a basaltic–andesitic sill, yielded a younger zircon U-Pb upper concordia intercept age of 2191 ± 10 Ma (2σ , MSWD = 1.7). Five samples of granodiorite and granodiorite porphyry that intruded the schist sequence yielded similar zircon U-Pb ages, with a weighted mean upper concordia intercept age of 2182 ± 7 Ma (2σ , MSWD = 1.3). These results suggest that the volcanic sequence was deposited between ~ 2.5 – 2.3 Ga, and was intruded by basaltic–andesitic sills and a suite of granodiorite and granodiorite porphyry intrusions at ~ 2.19 – 2.18 Ga.

Two stages of copper mineralization are interpreted to have formed after pervasive sericite alteration of the felsic volcanic rocks. Stage 1 mineralization includes disseminated and

deformed quartz veinlets containing chalcopyrite ± pyrite ± magnetite ± molybdenite associated with biotite ± K-feldspar alteration in granodiorite porphyry and schist. Stage 2 comprises undeformed quartz-chlorite-carbonate veins with bornite ± chalcopyrite ± magnetite associated with local chlorite and silicic alteration. Allanite crystals intergrown with chalcopyrite in the granodiorite porphyry yielded an approximate concordia U-Pb age of 2115 ± 31 Ma (2σ , MSWD = 2.3). Two molybdenite samples in a deformed quartz-chalcopyrite-molybdenite vein yielded Re-Os model ages of 2106 ± 9 Ma and 2089 ± 9 Ma (2σ), consistent with previously published results.

Hydrothermal monazite grains with Cu-Fe-sulfide inclusions in the granodiorite porphyry, quartz-sericite schist, and undeformed chlorite-bornite-quartz veins yielded much younger U-Pb upper concordia intercept ages of 1832 ± 16 Ma (2σ , MSWD = 0.48), 1810 ± 14 Ma (2σ , MSWD = 0.92), and 1809 ± 12 Ma (2σ , MSWD = 0.38), respectively. The results are in agreement with four Re-Os model ages for pyrite mineral separates from undeformed quartz-sulfide veins, which yielded a weighted mean age of 1807 ± 4 Ma (2σ , $n = 4$, MSWD = 0.42). In contrast, hydrothermal rutile crystals in the quartz-sericite schist and biotite schist yielded a range of roughly concordant ages between 2.1 and 1.8 Ga, reflecting isotopic disturbance.

We interpret these results to indicate original copper mineralization at ~ 2.1 Ga that is significantly later than the granodiorite (~ 2.18 Ga) and schists (~ 2.5 – 2.2 Ga), followed by hydrothermal remobilization and metamorphism at ~ 1.8 Ga. The metavolcanic and granodiorite porphyry host rocks, alteration styles, and disseminated and veinlet form of the earlier mineralization are strongly reminiscent of porphyry Cu deposits, and ages of ~ 2.1 Ga have been reported for one intrusion and three volcanic rock samples from the district. The Tongkuangyu

therefore represents one of the oldest known porphyry copper deposits. Remobilization of copper occurred at ~1.8 Ga during the Zhongtiao orogeny.

2.2 Introduction

The Tongkuangyu copper deposit is located in the northern Zhongtiaoshan region of the Trans-North China Orogen, and 370 km southwest of Taiyuan, the capital city of Shanxi province, China (N35°22'0.6'', E111°40'16'', 950 m above sea level). The deposit contains measured and indicated resources plus past production of 453 Mt at a grade of 0.61 % Cu, 0.06 g/t Au, 0.94 g/t Ag, 0.0063 % Co, and 0.0032 % Mo (using a cutoff grade of 0.4 % Cu; [Internal report from Zhongtiaoshan Non-ferrous Metals Group Co., Ltd, 2015](#)). The deposit was first discovered in 1952, but mechanized mining activity did not start until 1989; large-scale block cave mining began in 2001.

The genesis of the deposit has been debated since its discovery, with porphyry-type or sediment-hosted stratiform-type models being proposed ([Geological Group in Zhongtiao Mountain, 1978](#); [Sun et al., 1995](#); [Chen and Li, 1998](#); [Sun et al., 2014](#); [Liu et al., 2016a](#)). Debate arises because metamorphic and hydrothermal overprinting has modified the original form of the Tongkuangyu and the nature of the host rocks, and has disturbed mineralogical and isotopic systems ([Geological Group in Zhongtiao Mountain, 1978](#); [Sun et al., 1995](#); [Chen and Li, 1998](#)). The earliest description of the orebody by [Wang and Wen \(1957\)](#) concluded that the mineralization was hosted in volcanic and subvolcanic rocks, and was genetically linked to the intrusion of the granodiorite porphyry. This view was accepted by [Geological Group in Zhongtiao Mountain \(1979\)](#), [Jiang et al. \(2014\)](#), and [Sun et al. \(2014\)](#). However, others argued that the host rocks are sedimentary in origin and the mineralization is unrelated to the granodiorite porphyry intrusion

(Ji et al., 1992; Chen and Li, 1998; Chen et al., 1998; Sun et al., 1995; Liu et al., 2016a).

Rhenium-osmium dating of molybdenite from the deposit indicates that it formed at ~2.1 Ga (Chen and Li, 1998; Liu et al., 2016a).

To resolve the debate, we have re-mapped the distribution of host rocks, alteration, and mineralization, and tried to distinguish the effects of metamorphism and deformation on the original ore textures. We also aimed to more accurately constrain the ages of ore formation and overprinting. This work was hampered by poor surface exposure, poor preservation of older drill core and logs, and limited access to underground workings (which were either closed or covered with shotcrete). We selected two cross sections through the deposit where drill logs were available to reinterpret the distribution of alteration and mineralization, and carried out localized underground mapping along these sections to validate our interpretations.

2.3 Geological setting of the northern Zhongtiaoshan region

2.3.1 Tectonic framework of the Zhongtiaoshan region

Tongkuangyu is located in the northern Neoproterozoic–Paleoproterozoic Zhongtiaoshan region, which trends SW–NE in the southern part of the Trans-North China Orogen (Fig. 2.1A). The tectonic history of this region is poorly understood, but several tectonothermal events have been recognized, including the Jiangxian movement and the Zhongtiao orogeny (subduction and collision, ~1.9–1.85 Ga; Geological Group in Zhongtiao Mountain, 1978; Sun et al., 1991). The Jiangxian movement represents crustal rifting that is marked by a depositional unconformity, roughly constrained to between 2100 and 2060 Ma (Mei, 1994). Metamorphism during the Zhongtiao orogeny (locally up to 600 °C and 0.7 GPa) variably overprinted earlier fabrics and

textures related to the ~2.1 Ga crustal thinning event (Sun and Hu, 1993; Mei, 1994). The Zhongtiao orogeny is thought to have been caused by final collisional assembly of the eastern and western North China Blocks, which occurred at ~1.85 Ga (Zhai and Liu, 2003; Zhao et al., 2010). It was followed by crustal thickening (1843–1817 Ma; Zhang et al., 2009) and emplacement of syn- and post-collisional granites in the Trans-North China Block (~1832, 1815–1790 Ma; Zhao et al., 2005, 2008).

The northern Zhongtiao region consists of a sequence of Proterozoic volcanic, sedimentary, and intrusive rocks overlying a Neoproterozoic-Paleoproterozoic crystalline basement. The basement was variably metamorphosed from lower greenschist facies to amphibolite facies during the Zhongtiao orogeny (~1.9–1.85 Ga; Geological Group in Zhongtiao Mountain, 1978; Sun et al., 1991).

2.3.2 Stratigraphy of the northern Zhongtiao region

The oldest rocks in north Zhongtiao region belong to the Neoproterozoic-Paleoproterozoic Sushui complex (Sun et al., 1991; Bai et al., 1997; Fig. 2.2). They are overlain unconformably by, in ascending order, the Neoproterozoic-Paleoproterozoic Jiangxian and Zhongtiao Groups, and the Late Paleoproterozoic Danshanshi and Xiyanghe Groups (Sun et al., 1991; Bai et al., 1997; Fig. 2.2).

The Sushui complex consists of tonalite-trondhjemite-granodiorite gneisses (TTG, 2.7–2.3 Ga; Sun et al., 1991; Tian et al., 2006; Yu et al., 2006; Guo et al., 2008; Zhang et al., 2012; Zhu et al., 2013), amphibolites, and mafic dikes. These rocks were metamorphosed to amphibolite facies and subordinate eclogite facies, with the latest metamorphism occurring during the Zhongtiao orogeny at ~1.85 Ga (Fig. 2.2; Xiao et al., 2013).

The Jiangxian Group unconformably overlies the Sushui complex and was variably metamorphosed during the Jiangxian movement and Zhongtiao orogeny, with peak metamorphism at $\sim 1.9\text{--}1.85$ Ga (Sun and Hu, 1993; Mei, 1994; Liu et al., 2007). It is composed of a 2.2 km-thick succession of broadly southeast-younging metasedimentary and metavolcanic rocks intercalated with intrusive rocks. The Lower Jiangxian Group, which crops out in the northwest part of the region and is metamorphosed to lower amphibolite facies, comprises silty and argillaceous schist interlayered with minor amphibolite, and is crosscut by felsic and mafic sills (Mei, 1994). The upper Jiangxian Group crops out to the southeast and is less metamorphosed (lower greenschist facies; Sun and Hu, 1993). This sequence hosts the Tongkuangyu Cu deposit and is composed of the Luotuofeng, Shujinggou, Xijinggou, and Yuantoushan Formations (Fig. 2.2; Bai et al., 1997). These formations comprise folded quartz-sericite schist, biotite schist, and meta-rhyolite, which are interpreted here to be of volcanic and volcanoclastic origin, although their stratigraphic relationships are poorly constrained. This volcanic sequence has been dated between $\sim 2.5\text{--}2.2$ Ga (Sun et al., 1991; Sun and Hu, 1993; Zhang et al., 2012; this study), suggesting a long-lived volcanic succession. One slightly younger weighted mean zircon U-Pb age of 2115 ± 12 Ma (2σ , $n = 14$, MSWD not provided; sensitive high-resolution ion microprobe) was reported by Sun and Hu (1993) for a meta-rhyolitic tuff (sample ZG5002) from the same succession 20 km to the southwest. However, if three highly discordant and reversely discordant analyses are excluded, we calculate an upper concordia intercept age of 2188 ± 83 Ma (2σ , $n = 11$, MSWD = 0.45) from these data, while a single concordant analysis yields a concordia date of 2187 ± 44 Ma (2σ ; Table A2.1, Fig. A2.1A). Although these ages are imprecise, they nevertheless support a lower limit of ~ 2.2 Ga for the Jiangxian Group in this area.

Only one younger zircon U-Pb upper concordia intercept age of 2129 ± 28 Ma (2σ , $n = 18$, $MSWD = 0.66$) is calculated from the original data reported for a quartz-sericite schist sample collected in the Tongkuangyu area (Yang et al. 2015), suggesting presence of a younger but poorly constrained volcanic sequence in this area.

The Middle-Paleoproterozoic Zhongtiao Group (2110–2060 Ma; Sun et al., 1991; Sun and Hu, 1993; Li et al., 2011; Liu, et al., 2012; Liu et al., 2015) unconformably overlies the Jiangxian Group, and consists of clastic sediments, carbonate rocks, and minor mafic to intermediate composition volcanic rocks (Fig. 2.1). This sequence is interpreted to have been deposited in a back-arc basin on the eastern North China Block during the closure of an ocean basin between the eastern and western North China Blocks (Li et al., 2011), but the polarity of the subduction remains debated (Faure et al. 2007; Zhao and Zhai, 2013). These rocks were locally metamorphosed to upper greenschist facies and folded during the Zhongtiao orogeny (Fig. 2.2).

Sun and Hu (1993) reported a weighted mean $^{207}\text{Pb}/^{206}\text{Pb}$ age of 2059 ± 5 Ma (2σ , $MSWD$ not reported; thermal ionization mass spectrometry) for four zircon aliquots (excluding 4 analyses) from a sample of meta-dacitic tuff (sample ZC126) from the Zhongtiao Group, collected ~13 km southwest from Tongkuangyu. However, our recalculation of these data yields a similar $^{207}\text{Pb}/^{206}\text{Pb}$ age but with much larger error (2059 ± 24 Ma, 2σ) and a high $MSWD$ of 8.6, which indicates excess scatter beyond analytical uncertainties. Instead, we have calculated an upper concordia intercept age for these four aliquots of 2096 ± 65 Ma (2σ , $MSWD = 0.91$), and a concordia age of a single concordant aliquot of 2090 ± 20 Ma (2σ), which we interpret to provide a better estimate for the age of this unit at ~2090 Ma (Fig. A2.1B).

Liu et al. (2015) reported an imprecise upper concordia intercept age of 2086 ± 83 Ma (2σ , $n = 18$, MSWD = 16; sensitive high-resolution ion microprobe) for a plagioclase amphibolite (interpreted to be a mafic volcanic rock) interleaved with the Zhongtiao Group. These analyses included one nearly concordant data point with a $^{207}\text{Pb}/^{206}\text{Pb}$ age of 2087 ± 30 (2σ). Taken together, these ages indicate the occurrence of magmatism in the region broadly coeval with ore-formation at Tongkuangyu at ~ 2.1 Ga.

The Late Paleoproterozoic Danshanshi Group overlies the Zhongtiao Group with angular unconformity (Fig. 2.2; Mei, 1994). It consists of molasse-type sub-greenschist facies metaconglomerate and sandstone, with a minimum depositional age of ~ 1.85 Ga (LA-ICP-MS U-Pb dating of detrital zircons; Liu et al., 2012). The Danshanshi Group is in turn unconformably overlain by the unmetamorphosed Xiyanghe Group (Fig. 2.2), which consists of bimodal volcanic rocks erupted between 1.81 and 1.76 Ga during rifting in the Zhongtiaoshan region (Fig. 2.2; ages recalculated from data in Sun and Hu, 1993; Zhao et al., 2004).

2.3.3 Mineral deposits of the northern Zhongtiao region

Several copper deposits occur in the northern Zhongtiaoshan region, and most are considered to be of sediment-hosted stratiform type, hosted in Lower Jiangxian and Zhongtiao Group rocks (Geological Group in Zhongtiao Mountain, 1978). These include the Henglingguan deposit, which is located approximately 5 km west of the Tongkuangyu, and is hosted in mica schist of the Lower Jiangxian Group (Geological Group in Zhongtiao Mountain, 1978; Hu and Sun, 1987). Copper mineralization occurs as disseminations and fabric-controlled quartz veins. Qiu et al. (2017) proposed that copper was leached from the host sedimentary rocks during metamorphism and hydrothermal circulation at ~ 1.87 Ga (monazite U-Pb age), and redeposited

in the quartz veins. Deposits in the Zhongtiao Group (~65 Mt @ 1.21 % Cu in total) are hosted by graphitic schist and dolomitic marble, with copper mineralization occurring as early disseminations, veinlets, and later veins (Sun et al., 1995). Molybdenite from late quartz-sulfide veins in the Tongmugou and Bizigou deposits yielded Re-Os weighted mean ages of 1901 ± 24 Ma and 1919 ± 37 Ma, respectively (Huang et al., 1996; Zhang et al., 2013), but the exact timing of the early mineralization remains unclear.

In contrast, copper mineralization at Tongkuangyu is hosted by what are interpreted here to be meta-volcanic rocks and granitic intrusions, leading some authors to suggest a porphyry-type origin (Wang and Wen, 1957; Geological Group in Zhongtiao Mountain, 1979; Jiang et al., 2014), distinct from the sediment-hosted stratiform deposits that occur elsewhere in the region (Geological Group in Zhongtiao Mountain, 1978; Hu and Sun, 1987; Ji et al., 1992; Sun et al., 1995; and Qiu et al., 2017).

2.4 Geology of the Tongkuangyu Cu deposit

Tongkuangyu is mainly hosted by schists of the Luotuofeng Formation and felsic porphyritic intrusive rocks (granodiorite and granodiorite porphyry; Figs. 2.3–2.5; Geological Group in Zhongtiao Mountain, 1978; Ji et al., 1992; Sun et al., 1995). The granitic rocks intruded the Luotuofeng Formation (Fig. 2.6B) and contain some xenoliths of these rocks (Fig. 2.6C; also reported by Geological Group in Zhongtiao Mountain, 1978). The granitic intrusions and schists are crosscut locally by diabase dikes (Fig. 2.6D).

The host rocks and orebodies are folded along a NW-plunging antiform and NE-plunging synform (Wang et al., 1995; Bai et al., 1997; Fig. 2.3). A postore NW-dipping reverse fault and a

NNW-trending normal fault (dipping 34°–68° to the east) truncated the sequence and the No. V orebody (Fig. 2.3).

2.4.1 Host rocks

The main orebodies at Tongkuangyu are hosted by granodiorite porphyry, biotite schist, and quartz-sericite schist (Figs. 2.3, 2.4A, 2.5A, 2.6). The quartz-sericite schist is variably to strongly foliated, whereas the granodiorite porphyry and biotite schist are less foliated or undeformed except in proximity to sheared lithological contacts. The difference in degree of deformation may reflect rheological contrasts between weak phyllosilicate-rich rocks and stronger more crystalline rocks.

The granodiorite porphyry has previously been interpreted to be of intrusive origin (Geological Group in Zhongtiao Mountain, 1978), a porphyroblast-rich mylonite (Sun et al., 1995), or tuffaceous arkosic quartzite (Chen et al., 1998). Here, we interpret it to be a shallow intrusive phase, as indicated by its porphyritic texture (Fig. 2.7A), embayed quartz phenocrysts (Fig. 2.7B), and the presence of xenoliths of biotite schist (Fig. 2.6C). The granodiorite had intruded the schists locally as small equigranular dikes (Fig. 2.7C). The granodiorite porphyry is coarse-grained and typically contains phenocrysts of quartz (15–30 %), plagioclase (~30 %), and K-feldspar (<5 %), in a groundmass of plagioclase (~30 %) and sericite (~15 %). Microprobe analyses indicate that the plagioclase phenocrysts and groundmass are mostly now albite, probably due to a combination of metamorphism and hydrothermal alteration.

The biotite schist (Fig. 2.7D) was previously interpreted to be either a mafic volcanic or intrusive rock (Geological Group in Zhongtiao Mountain, 1978; Chen et al., 2014) or metapelite (Chen et al., 1998). Most samples are composed of variable amounts of biotite (50–70 %, rarely up to 90

%), plagioclase (15–25 %), quartz (5–10 %), and chlorite (0–10 %). The large amounts of biotite are thought to reflect hydrothermal replacement of original ferromagnesian silicate minerals, and we therefore interpret this rock to be of mafic volcanic or subvolcanic (sill) origin.

The quartz-sericite schist (Fig. 2.7E–G) has previously been interpreted to be either a tuffaceous argillite (Geological Group in Zhongtiao Mountain, 1978), porphyroblastic mylonite (Sun et al., 1995), or metapelite (Chen et al., 1998). It is melanocratic, fine-grained, and comprises 15–25 % quartz (0.05–0.5 mm) and ~0–10 % biotite crystals (0.1–0.5 mm) in a groundmass consisting of sericite and minor quartz. Samples collected ~5 km from the mineralization area contain less or no biotite, suggesting that, where present, this mineral is largely a product of hydrothermal alteration. Here we interpreted this lithology to be a tuffaceous volcanic rock, because the angular quartz crystals are more likely to be derived from a volcanic rather than sedimentary origin. In addition, the presence of magmatic zircons with homogeneous U-Pb isotopic ages supports an igneous origin.

Diabase dikes locally cut the granodiorite porphyry and schists (Figs. 2.3, 2.4A, 2.5A, 2.6D), and are unmineralized and weakly deformed; they could not be dated by the zircon U-Pb method, but are interpreted to be relatively late (post-orogenic). The dikes are composed of sericite-altered plagioclase (~50 %) and chlorite-altered pyroxene (~50 %; Fig. 2.7H).

2.4.2 Hydrothermal alteration

The host rocks to the Tongkuangyu Cu deposit display various types of hydrothermal alteration, but the nature and distribution of this alteration has been obscured by later metamorphism and overprinting by late-stage hydrothermal fluids (Figs. 2.4B, 2.5B). Previous researchers have suggested that the original hydrothermal alteration sequence involved either: early sericite,

scapolite, and chlorite alteration, followed by albite and biotite (\pm K-feldspar) alteration (Geological Group in Zhongtiao Mountain, 1978); early sericite alteration overprinted by albite, biotite (\pm K-feldspar), and chlorite alteration (Ji et al., 1992); or silicic, sericite, and biotite (\pm K-feldspar) alteration overprinted by a second stage of silicic, sericite, and albite alteration (Sun et al., 1995). Scapolite was not observed in this study, but we identified preore sericite and albite alteration, overprinted by ore-associated biotite \pm K-feldspar alteration, followed by late-stage chlorite and minor carbonate alteration (Figs. 2.8–2.10). The distribution and sequence of these alteration types is summarized below.

Pervasive sericite alteration is observed in quartz-sericite schist samples collected 5 km north of Tongkuangyu (Fig. A2.2), outside the limits of hydrothermal alteration associated with the deposit. We conclude that this sericite alteration was caused by low-grade regional metamorphism, which predated and was unrelated to mineralization. Within the orebody, the early sericite alteration was overprinted by albite and biotite \pm K-feldspar alteration (Fig. 2.9A, B).

Albite alteration has not been described previously at Tongkuangyu, and its spatial extent is unknown. However, our observations suggest that it is mainly developed in the granodiorite porphyry and schists within the mineralized zones, and immediately predated mineralization. The alteration is characterized by albite selvages around quartz-biotite-chalcopyrite veins, and extensive fine-grained albite in altered rock matrices (Figs. 2.8D, E; 2.9A, B, F). Most of the plagioclase phenocrysts in the granodiorite porphyry have also been altered to albite (Figs. 2.8D, E; Fig. A2.3).

Biotite \pm K-feldspar alteration is present in the core of the main orebodies (Figs. 2.4B, 2.5B) and is characterized by abundant hydrothermal biotite, locally partially overprinted by chlorite (Fig. 2.8F). Fine-grained anhedral biotite occurs in the granodiorite porphyry, quartz-sericite schist, and biotite schist, with disseminated chalcopyrite, pyrite, and magnetite (Fig. 2.8). Coarser-grained biotite and rare tourmaline also occur in variably deformed quartz-chalcopyrite-pyrite veinlets. Secondary K-feldspar was not previously described in drill logs, but minor amounts were observed in thin section in association with chalcopyrite and magnetite, overprinting albite (Fig. A2.3).

All rocks affected by the early sericite, albite, and mineralization-related biotite \pm K-feldspar alteration have been variably deformed and recrystallized during later metamorphism (Figs. 2.9C–F; 2.10A, B). This metamorphic event appears to have been low-grade (lower greenschist facies), and is mainly characterized by fabric development and new or retrograde crystallization of chlorite (especially replacing biotite; Fig. 2.10C, D). Chlorite alteration is mostly strongly developed around biotite alteration zones and along contacts between different lithological units, presumably where there was higher fluid permeability (Figs. 2.4B, 2.5B). Chlorite alteration was associated with a series of weakly deformed quartz-chlorite-bornite veins with minor chalcopyrite and magnetite (partially oxidized to hematite; Fig. 2.10E, F). Sun et al. (2015) analyzed the chemical composition of chlorite in chlorite-altered quartz-sericite schist and identified it to be Fe-rich ripidolite and pycnochlorite, consistent with its anomalous blue birefringence color. Late, undeformed quartz-pyrite-chalcopyrite \pm carbonate veins with marginal quartz-calcite replacement in the host rocks occur locally in the deposit.

2.4.3 Copper mineralization

Copper mineralization is restricted to the Luotuofeng Formation and granodiorite porphyry intrusions, and occurs in five main orebodies (Nos. I–V). The main orebodies are lens shaped and dip 20° – 67° north or west. The No. I–III orebodies are hosted in biotite schist, but have been mined out and were inaccessible for this study. The largest two orebodies (Nos. IV and V) are mainly hosted in granodiorite porphyry, quartz-sericite schist, and biotite schist, and account for 94 % of the resource (reserves plus past production); they extend to depths of at least 900 m (the limit of drilling).

The No. V orebody crops out at surface (Fig. 2.3) and is up to 171 m thick, extends 1100 m along strike, and has an average grade of 0.62 % Cu. It was folded and then offset by a NNW-trending reverse fault (Fig. 2.3). The western limb of the orebody dips 45° – 58° NW, and the eastern limb dips 35° – 45° NE (Figs. 2.4 and 2.5). The No. IV orebody overlies the No. V orebody, but does not crop out at surface. It is up to 161 m thick, extends ~950 m along strike, and dips $\sim 20^{\circ}$ – 54° NW; it has average grade of 0.53 % Cu.

Hypogene copper mineralization in the main orebodies produced chalcopyrite, bornite, and minor chalcocite, in association with pyrite and magnetite. Sulfide minerals occur as variably deformed disseminations and veinlets, as streaks along the foliation, and in late undeformed quartz-chlorite and quartz-carbonate veins. Mineralization in the central parts of each orebody is characterized by chalcopyrite and pyrite, with bornite and chalcocite locally developed on the margins (Figs. 2.4C, 2.5C). Based on underground observations, hand-lens inspection, and microscopy, two stages of mineralization are recognized: (1) early, deformed, disseminated and veinlet-hosted mineralization, dominated by chalcopyrite, pyrite, and magnetite; and (2) a later stage of undeformed vein-type mineralization dominated by bornite, minor chalcocite, and

magnetite (partially replaced by secondary hematite), which crosscuts and may have remobilized earlier Cu mineralization.

The bulk of the stage 1 mineralization occurs in zones of biotite \pm K-feldspar alteration (Figs. 2.4 and 2.5), and is characterized by disseminated fine-grained chalcopyrite with pyrite and magnetite in the granodiorite porphyry and schists (Fig. 2.8), and in variably folded quartz-biotite-magnetite-(tourmaline-molybdenite) veinlets (Figs. 2.9 and 2.11A). Locally, these sulfides and secondary biotite and sericite are so strongly foliated as to appear stratiform (Fig. 2.9C–F). The $\delta^{34}\text{S}$ values reported by Ji et al. (1992) and Sun et al. (1995) for early disseminated chalcopyrite, molybdenite, and pyrite range from -4.5 to 6.8 ‰ (average = 2.5 ‰).

Stage 2 mineralization produced bornite in and around late crosscutting veins. Two types of late, relatively undeformed cupriferous veins have been identified: (1) horizontal or subhorizontal quartz-chlorite-ankerite-bornite-magnetite veinlets with small amounts of monazite, xenotime, and thorite that have chlorite alteration selvages (replacing biotite; Fig. 2.11B, C); (2) horizontal or steeply dipping ($\sim 50^\circ$ towards NW, striking $\sim 40^\circ$) quartz \pm calcite-pyrite-chalcopyrite veins, with no obvious alteration selvages (Fig. 2.11D–F). Type-1 veins occur locally in the quartz-sericite schist on the margins of the main orebodies, whereas type-2 veins occur in the outer parts of the No. IV orebody. The $\delta^{34}\text{S}$ values of chalcopyrite-pyrite samples from type-2 veins range from -1.4 to 9.6 ‰ (average = 3.3 ‰; Ji et al., 1992; Sun et al., 1995). Crosscutting relationships were not observed between type 1 and 2 veins, so that their relative timing is not known.

Although the volume of this second stage of mineralization is relatively minor, it is important in locally increasing Cu grades by replacement of chalcopyrite with bornite.

Supergene oxidation, leaching, and secondary enrichment of sulfides has resulted in the formation of malachite, limonite, specularite, and minor hematite in the top 100 m of the No. V orebody, and locally down to 300 m below surface (Figs. 2.4C, 2.5C). The supergene enrichment zone accounts for 0.7 % of the total resource (internal material from [the 214 Geological Group in Zhongtiao Mountain in Shanxi Province, 1956](#)).

2.5 Previous geochronological results of the Tongkuangyu Cu deposit

The absolute timing of mineralization at Tongkuangyu was first investigated in the 1970s using the K-Ar method ([Geological Group in Zhongtiao Mountain, 1978](#)), but no reliable results were obtained. A Pb-Pb secondary isochron age of 2132 Ma (error not reported) was later obtained from pyrite and chalcopyrite by [Sun et al. \(1995\)](#). [Chen and Li \(1998\)](#) reported two Re-Os isochron ages of 2108 ± 32 Ma (2σ , $n = 6$, MSWD not reported) and 2947 ± 28 Ma (2σ , $n = 6$, MSWD not reported) from 12 molybdenite samples from Tongkuangyu. It is unclear how these two groups of samples were separated. Furthermore, the older age is substantially older than the host rocks and may reflect decoupling of parent ^{187}Re and daughter-product ^{187}Os ([Stein et al., 2003](#); [Selby and Creaser, 2004](#)). In contrast, [Liu et al. \(2016a\)](#) reported a weighted mean age of 2122 ± 12 Ma (2σ , $n = 6$, MSWD = 0.58) for six samples of molybdenite from Tongkuangyu, which is thought to more accurately date the timing of initial ore formation.

The granodiorite porphyry intrusions at Tongkuangyu have been dated by a number of authors, with dates ranging from ~2222 to 2180 Ma ([Sun et al., 1991](#); [Sun et al., 1995](#); [Li et al., 2013](#); [Liu et al., 2015](#)), and one age of 2121 ± 10 Ma (2σ , MSWD = 1.3) reported by [Li et al. \(2013\)](#). The latter age is of significant interest because it is similar to the age of primary Cu mineralization, but the location of this sample was not reported and could not be verified.

2.6 Samples

Sample locations and descriptions are provided in [Table A2.2](#). Most samples were collected from underground tunnels and surface outcrops in the Tongkuangyu ore district. Four samples of quartz-sericite schist were collected from outcrops of the Luotuofeng Formation 5 km northeast of the ore deposit, outside the main zones of hydrothermal alteration.

Zircons were separated from the quartz-sericite schist, biotite schist, and granodiorite porphyry/granodiorite by traditional magnetic and density methods, and were then manually selected at the Geological Surveying and Mapping Institute of Hebei Province, China. Zircons devoid of cracks and mineral/fluid inclusions were mounted in epoxy and polished to expose their internal structures. Transmitted and reflected light and cathodoluminescence images were used to characterize the interior zoning of zircons. The mounted grains are euhedral and transparent, with oscillatory zoning revealed by cathodoluminescence that suggests they are of magmatic origin ([Fig. A2.4](#)). The crystals range in size from 100–250 μm in granodiorite porphyry, and 50–100 μm in the schists.

Mineralized and altered samples, including veins, were studied petrographically in order to identify minerals that could be used to date these events. Because of the known metamorphic overprinting, dating of K-bearing minerals such as biotite, muscovite, and K-feldspar by the K-Ar and $^{40}\text{Ar}/^{39}\text{Ar}$ methods was not considered. Instead, robust U-bearing accessory minerals with high U-Pb closure temperatures ([Chiaradia et al., 2012](#)) such as allanite, monazite, and rutile, with clear paragenetic relationships to mineralization, were sought. Allanite, monazite, and rutile crystals were identified in polished thin sections using transmitted and reflected light microscopy, as well as backscattered electron imaging using a CAMECA SX100 electron

microprobe at the University of Alberta, and a scanning electron microscope (SEM; JEOL 6400) at Laurentian University.

Allanite was observed to occur with chalcopyrite inclusions in mineralized samples of the granodiorite porphyry (Fig. 2.12A). Monazite grains that enclose allanite or are intergrown with chalcopyrite were also found in the same sample (Fig. 2.12A–C). Trace amounts of monazite with or without chalcopyrite or bornite inclusions were also found in samples of the quartz-sericite schist (Fig. 2.12D–I) and chlorite-bornite-quartz veins (Fig. 2.12J–K). Rutile is associated with bornite, chalcopyrite, chlorite, and titanomagnetite in quartz-sericite schist, where it shows patchy Fe-rich and W-rich zoning in back-scattered electron images (Fig. 2.12L). In contrast, rutile intergrown with hydrothermal biotite in biotite schist (Fig. 2.12M) is fine-grained and free of chemical zoning.

Attempts were also made to date sulfide minerals by the Re-Os method. Ages for molybdenite have been previously reported from Tongkuangyu (Chen and Li, 1998; Liu et al., 2016a), but sampling locations and petrographic descriptions were not provided. We collected molybdenite from an early quartz-chalcopyrite vein in quartz-sericite schist. Samples of coarse-grained pyrite (generally larger than 1–2 cm in diameter, intergrown with chalcopyrite) were also collected from late-stage quartz-pyrite-chalcopyrite veins. Early disseminated pyrite from the mineralized biotite schist were also separated, but the Re content of the pyrite separate is too low (<0.1 ppb), and an age result could not be acquired.

2.7 Analytical techniques

2.7.1 Lithochemical analyses

Powdered samples were obtained by crushing and grinding in an agate disk mill at the Geological Surveying and Mapping Institute of Hebei Province, China. Fifteen samples of quartz-sericite schist, seven samples of biotite schist, and eight samples of granodiorite porphyry were analyzed using X-ray fluorescence (XRF) and inductively coupled plasma-mass spectrometry (ICP-MS) with pre-fusion (lithium metaborate; CCP-PKG03 analytical package) at ALS, Vancouver, Canada. Samples with high copper abundances (>1.0 wt %) were re-analyzed using methods MEOG62 and Cu-OG62.

2.7.2 Zircon, allanite, monazite, and rutile U-Pb dating

U-Pb ages were obtained from sufficiently large zircon, allanite, monazite, and rutile crystals by LA-ICP-MS (laser ablation inductively coupled plasma-mass spectrometer) using various instrumental setups at different laboratories. Equipment included: (i) a New Wave Research Nd:YAG laser ablation system (frequency-quintupled, $\lambda = 213$ nm) coupled with a Nu Plasma MC-ICP-MS (multiple collector inductively coupled plasma-mass spectrometer) at the University of Alberta for zircon samples R1B2, D168-1, D171-4, R2B25, R3B8-1; monazite sample R1B2, and rutile sample ZT11; (ii) a Resonetics Resolution M-50 excimer laser ablation system coupled with a Thermo X Series II ICP-MS (quadrupole mass filter) at Laurentian University for allanite, monazite, and rutile in samples R2B30-1, R2B20, R1B502, and R2B17; and (iii) a Photon Machines Analyte G2 excimer laser ablation system ($\lambda = 193$ nm) coupled with a Thermo Neptune Plus MC-ICP-MS with Jet Interface at the Mineral Exploration Research Centre Isotope Geochemistry Lab, Laurentian University for zircon samples 434-3, 434-6, and 434-12. In-situ analytical techniques were employed following [Simonetti et al. \(2006\)](#) at the University of Alberta, and [Aleinikoff et al. \(2006\)](#), [Zack et al. \(2011\)](#), [Schmitt and Zack \(2012\)](#), and [McFarlane \(2016\)](#) at Laurentian University. The instrument parameters used for the analyses are

summarized in [Table A2.3](#). The beam sizes for laser ablation were 35 μm , 17 μm , 12 μm , and 30 μm (33 μm for the Resonetic Resolution laser) for zircon, allanite, monazite, and rutile, respectively. Each analytical run includes periodic analysis of a primary reference material interspersed through the analytical session, to which the raw data for unknown samples were normalized to correct for instrumental bias and within-run drift. Secondary reference materials were also analyzed and the results are in agreement with standard values ([Table A2.4](#)). An in-house excel spreadsheet and Iolite software ([Paton et al., 2010, 2011; Petrus and Kamber 2012](#)) were used for data reduction in laboratories at the University of Alberta and Laurentian University, respectively.

2.7.3 Re-Os dating of molybdenite and pyrite

Re-Os dating of molybdenite and pyrite were completed at the University of Alberta, using the methods of [Selby and Creaser \(2004\)](#) and [Markey et al. \(2007\)](#). The ^{187}Re and ^{187}Os concentrations in molybdenite were determined by isotope dilution mass spectrometry using Carius-tube, solvent extraction, anion chromatography, and negative thermal ionization mass spectrometry techniques. A mixed double spike containing known amounts of isotopically enriched ^{185}Re , ^{190}Os , and ^{188}Os was used ([Markey et al., 2007](#)). Isotopic analysis used a ThermoScientific Triton mass spectrometer with Faraday collector array. Total procedural blanks for Re and Os are less than 3 and 2 picograms, respectively, which are insignificant in comparison to the Re and Os concentrations in the molybdenite samples. Reference material 8599 Henderson molybdenite ([Markey et al., 2007](#)) was routinely analyzed as a standard over the course of the project and returned an average Re-Os date of 27.73 ± 0.05 Ma ($n = 4$), indistinguishable from the reference age value of 27.66 ± 0.1 Ma ([Wise and Watters, 2011](#)).

Four pyrite aliquots from sample ZT-5 were divided, weighed (~400 mg each), and then transferred to thick-walled, borosilicate glass Carius tubes. Initially, samples were analyzed with a conventional mixed $^{185}\text{Re} + ^{190}\text{Os}$ spike to determine the common Os. Spiked samples were dissolved at 220°C for 48 hours, followed by chemical separation and purification of Os and Re using procedures described by [Shirey and Walker \(1995\)](#), [Cohen and Waters \(1996\)](#), [Birck et al. \(1997\)](#), and [Morelli et al. \(2005\)](#). Total procedural blanks were less than 1 picogram Re and 0.3 picogram Os (< 0.01 picograms ^{187}Os). The decay constant used for ^{187}Re is $\lambda = 1.666\text{e}^{-11}/\text{a}$ following [Smoliar et al. \(1996\)](#), a value which is cross-calibrated to the U-Pb system (^{238}U and ^{235}U) to better than $\sim \pm 0.3\%$ ([Selby et al., 2007](#)). The aliquots of sample ZT-5 were initially analyzed with a conventional spike but yielded low levels of common Os, with radiogenic ^{187}Os comprising > 99 % of the Os inventory in each aliquot. Because the pyrite in sample ZT-5 contains low abundances of common Os, a mixed $^{185}\text{Re} + ^{188}\text{Os} + ^{190}\text{Os}$ spike was used, which allows more accurate mass bias corrections for Os that is purely radiogenic ^{187}Os ([Markey et al., 2007](#)).

2.8 Lithochemical results and interpretation

On an immobile element ratio diagram (Zr/TiO_2 versus Nb/Y ; [Fig. 2.13](#)), the quartz-sericite schist, biotite schist, and granodiorite porphyry samples mostly plot in the dacite–rhyolite, basalt–andesite, and granodiorite fields, respectively. We interpret these rocks to be felsic crystal tuffs, basaltic–andesitic lavas or sills, and shallow porphyritic intrusive rocks, respectively.

The lithochemical results are listed in [Table A2.5](#). The quartz-sericite schist has a wide compositional range ($\text{SiO}_2 = 52\text{--}81$ wt %, total $\text{Fe}_2\text{O}_3 = 1.20\text{--}7.8$ wt %, $\text{MgO} = 0.69\text{--}5.6$ wt %), which likely reflects protolith heterogeneity, as well as hydrothermal alteration. On a primitive

mantle normalized trace element diagram (Fig. A2.5A), the quartz-sericite schist samples are enriched in large-ion-lithophile elements (LILEs: Rb, Th, U, K; some samples are depleted in Th) and depleted in Nb, Ta, Ti. Significant depletions of Sr, P, and Ti likely reflect extensive fractional crystallization of feldspar, apatite, and Fe-Ti oxides. On a chondrite-normalized REE diagram (Fig. A2.5B), all samples have listric-shaped patterns with La/Yb_N of 2.2–23, and distinct negative Eu anomalies.

The biotite schist samples are more mafic than the quartz-sericite schist ($\text{SiO}_2 = 48\text{--}59$ wt %, total $\text{Fe}_2\text{O}_3 = 7.9\text{--}15.8$ wt %, $\text{MgO} = 2.7\text{--}8.3$ wt %) but have similar trace and rare earth element patterns, and La/Yb_N ratios (2.7–15; Fig. A2.5C, D).

The granodiorite porphyry samples have a tighter compositional range ($\text{SiO}_2 = 58\text{--}69$ wt %, total $\text{Fe}_2\text{O}_3 = 2.4\text{--}8.4$ wt %, $\text{MgO} = 0.82\text{--}3.8$ wt %), but have broadly similar trace element compositions to the schists (Fig. A2.5E). Their REE patterns are more steeply sloping ($\text{La}/\text{Yb}_N = 12.8\text{--}66$) and lack significant Eu anomalies (Fig. A2.5F).

2.9 Geochronological results

Geochronological results are illustrated in Figures 2.14, 2.15, and 2.16, and summarized in Table 2.1. Full analytical data are provided in supplemental databases (Tables 2.2 and Tables A2.6–2.7). Upper intercept or concordia U-Pb ages were calculated, and the related $^{206}\text{Pb}/^{238}\text{U}$ - $^{207}\text{Pb}/^{235}\text{U}$ concordia diagrams were plotted using Isoplot version 4.15 (Ludwig, 2011). All results are reported with 2σ uncertainties. Mean square of weighted deviates (MSWD) value is calculated using Isoplot version 4.15 (Ludwig, 2011). The value measures the ratio of the

observed scatter of the points to the predicted scatter by analytical uncertainty, and $MSWD < 1$ suggests that the analytical uncertainty is overestimated (Wendt and Carl, 1991).

2.9.1 Zircon

Twenty analyses of zircon grains from sample R1B2 (chlorite-altered quartz-sericite schist) yielded an upper concordia intercept age of 2512 ± 12 Ma (2σ , $n = 20$, $MSWD = 0.19$; Fig. 2.14A). The tight clustering of data suggests that the zircon grains are of magmatic origin, and supports the interpretation that the protolith was a felsic volcanic rock.

Twenty-seven analyses of zircons from sample D168-1 (quartz-sericite schist) are divided into two groups (Fig. 2.14B): one group defines a well constrained upper concordia intercept age of 2335 ± 16 Ma (2σ , $n = 24$, $MSWD = 0.8$), but three other grains have discordant older ages, and are likely xenocrysts. The main group has a tight age distribution, which again suggests that the protolith is of magmatic, likely volcanic origin.

Thirty-three analyses of zircons from sample 434-3 (biotite schist) yielded an upper concordia intercept age of 2191 ± 10 Ma (2σ , $MSWD = 1.7$; Fig. 2.14C). Three older discordant zircons yielded an upper intercept age of 2519 ± 62 Ma (2σ , $MSWD = 0.014$), and are likely xenocrysts.

A total of 155 zircon grains from five granodiorite and granodiorite porphyry samples were dated and yielded upper concordia intercept ages of 2185 ± 6 Ma (2σ , $n = 32$, $MSWD = 0.90$; sample 434-6; Fig. 2.14D), 2181 ± 7 Ma (2σ , $n = 34$, $MSWD = 0.60$; sample 434-12; Fig. 2.14E), 2186 ± 23 Ma (2σ , $n = 30$, $MSWD = 0.28$; sample D171-4; Fig. 2.14F), 2184 ± 16 Ma (2σ , $n = 29$, $MSWD = 0.19$; sample R2B25; Fig. 2.14G), and 2169 ± 13 Ma (2σ , $n = 30$, $MSWD = 0.20$;

sample R3B8-2; Fig. 2.14H). All of these five dates overlap within error and a weighted mean age of 2182 ± 7 Ma (2σ , MSWD = 1.3) was calculated.

These results suggest that the volcanic country rocks (quartz-sericite schist) were emplaced between ~ 2.5 and 2.3 Ga. They were then intruded by a basaltic–andesitic sill (biotite schist) at ~ 2.19 Ga and granodiorite porphyry and granodiorite at ~ 2.18 Ga.

2.9.2 Allanite

Two angular allanite grains with chalcopyrite inclusions and associated with biotite alteration were identified in a thin section of sample R2B30-1 (granodiorite porphyry closer to late quartz \pm calcite-pyrite-chalcopyrite vein; Fig. 2.12A). Eight laser spot analyses on these two grains yielded an approximate U-Pb concordia age of 2085 ± 25 Ma (2σ , MSWD = 6.1; Fig. 2.15A). However, if two slightly younger analyses (possible Pb-loss) are excluded, a more robust concordia age of 2115 ± 31 Ma (2σ , MSWD = 2.3; Fig. 2.15A) is obtained. We interpret this age to be the time of formation of biotite alteration and early mineralization in the granodiorite porphyry.

2.9.3 Monazite

Two anhedral monazite grains enclosed by chalcopyrite and one grain enclosing allanite were found in sample R2B30-1 (granodiorite porphyry; Fig. 2.12B, C). Twelve analyses of these three grains yielded an upper concordia intercept age of 1832 ± 16 Ma (2σ , $n = 12$, MSWD = 0.48; Fig. 2.15B), which is interpreted to be the timing of a later hydrothermal event in the granodiorite porphyry.

Nineteen analyses of three euhedral to subhedral monazite grains intergrown with chalcopyrite (Fig. 2.12D, E) in sample R2B20 (biotitic quartz-sericite schist close to a late quartz ± calcite-pyrite-chalcopyrite vein) yielded an upper concordia intercept age of 1810 ± 14 Ma (2σ , $n = 19$, MSWD = 0.92; Fig. 2.15C).

Two vein-like monazite aggregates (containing anhedral to subhedral monazite grains, and associated with chlorite alteration; Fig. 2.12F, G), and four euhedral monazite grains were found in sample R1B2 (quartz-sericite schist; Fig. 2.12H, I). Twenty-five analyses of these monazite aggregates yielded an upper intercept age of 1816 ± 10 Ma (2σ , $n = 25$, MSWD = 0.07; Fig. 2.15D). Seventeen analyses of four oscillatory zoned euhedral monazite grains (intergrown with chlorite-altered biotite) yielded an upper concordia intercept age of 1827 ± 17 Ma (2σ , $n = 17$, MSWD = 0.12; Fig. 2.15E).

Four monazite grains with bornite inclusions were found in an undeformed chlorite-bornite-quartz vein cutting quartz-sericite schist in sample R1B502 (Fig. 2.12J, K). Nineteen analyses of these four grains yielded an upper concordia intercept age of 1809 ± 12 Ma (2σ , $n = 19$, MSWD = 0.38; Fig. 2.15F).

Taken together, these various monazite grains record a ~1.8 Ga hydrothermal event that overprinted the ~2.1 Ga Cu mineralization event.

2.9.4 Rutile

Sample ZT11 (quartz-sericite schist) contains a population of rutile intergrown with bornite in the chlorite-altered quartz-sericite schist (Fig. 2.12L), which yielded a range of apparently concordant U-Pb ages from ~2.1–1.8 Ga (Fig. 2.15G). A large number of rutile crystals

intergrown with hydrothermal biotite occur in a folded but unmineralized biotite schist sample (R2B17; Fig. 2.12M). Nineteen rutile crystals were dated and yielded a broad age distribution similar to sample ZT11 (Fig. 2.15H). Taken together, these rutile data likely indicate crystallization as a hydrothermal alteration mineral during the primary mineralization event at ~2.1 Ga, with partial resetting by Pb-loss during metamorphic overprinting at ~1.8 Ga.

2.9.5 Molybdenite

Re-Os analyses of two molybdenite fractions from sample 23-2 (quartz-chalcopyrite-molybdenite vein) yielded two precise model ages of 2106 ± 9 Ma and 2089 ± 9 Ma (2σ), similar to the allanite U-Pb age and previously published molybdenite Re-Os ages (Table 2.1). These results are interpreted to constrain the age of original Cu-(Mo) mineralization at Tongkuangyu at ~2.1 Ga.

2.9.6 Pyrite

The common Os abundances of the four pyrite aliquots (~400 mg per aliquot) are negligible, suggesting that all of the measured ^{187}Os is the radiogenic daughter product of ^{187}Re decay. Four model Re-Os ages overlap within error, yielding a weighted mean age of 1807 ± 4 Ma (2σ , $n = 4$, MSWD = 0.42; Fig. 2.16B). This result is similar to the ages obtained from monazite, and is interpreted to be the best estimate of the age of the late hydrothermal alteration and veining at Tongkuangyu.

2.10 Discussion

2.10.1 Age and origin of the host rocks

The quartz-sericite schist of the Luotuofeng Formation in Tongkuangyu is interpreted to be a crystal tuff of dacitic–rhyolitic composition. However, two samples of this lithology yielded dissimilar zircon U-Pb upper concordia intercept ages of 2512 ± 12 Ma (2σ , MSWD = 0.19) and 2335 ± 16 Ma (2σ , MSWD = 0.80), suggesting that this is not a homogeneous coeval volcanic sequence, but deposition spanned an age range from ~ 2.5 – 2.3 Ga (in agreement with the results of [Sun et al., 1991](#)). Poor surface exposure, lack of correlatable layering, and metamorphic overprinting and deformation prevent a better understanding of this sequence at this time. Biotite schist interleaved with the quartz-sericite schist has a basaltic to andesitic composition, and a significantly younger zircon U-Pb upper concordia intercept age of 2191 ± 10 Ma (2σ , MSWD = 1.7). We interpret this rock unit to be a sill emplaced into the quartz-sericite schist. Four samples of granodiorite porphyry and one sample of granodiorite have a weighted mean age of 2182 ± 7 Ma (2σ , MSWD = 1.3).

2.10.2 Two stages of hydrothermal activity and their relationships to tectonothermal events

The early hydrothermal event is constrained by U-Pb dating of hydrothermal allanite and Re-Os dating of vein-hosted molybdenite at ~ 2.1 Ga, and is associated with biotite \pm K-feldspar alteration and chalcopyrite mineralization. Allanite has a U-Pb closure temperature >750 °C ([Engi, 2017](#)) well above upper greenschist facies, indicating that it would likely have preserved isotopic age information through the lower greenschist facies metamorphism and hydrothermal overprinting evident at Tongkuangyu. Similarly, although with closure temperature above 500 °C indicated ([Suzuko et al., 1996](#)), molybdenite has also been reported to preserve Re-Os age information up to granulite facies metamorphic conditions ([Stein et al., 2001](#)). Thus, in combination, these allanite and molybdenite ages constrain the age of original Cu-(Mo) mineralization and hydrothermal alteration to ~ 2.1 Ga.

The hydrothermal event at ~1.8 Ga caused by local chlorite alteration associated with bornite ± chalcopyrite mineralization, growth of hydrothermal monazite, and deposition of planar quartz ± calcite-pyrite-chalcopyrite veins. Monazite grains from several samples of disseminated and vein-type mineralization yielded upper concordia intercept ages of ~1.8 Ga, similar to a Re-Os age for pyrite from an undeformed quartz-pyrite-chalcopyrite vein. These ages are interpreted to reflect hydrothermal alteration and remobilization of Cu at ~1.8 Ga. In contrast, rutile crystals from hydrothermally altered rocks yielded scattered U-Pb concordia ages between ~2.0 Ga and ~1.8 Ga, and are interpreted to reflect resetting of original ~2.1 Ga-old crystals during the later metamorphic overprint at ~1.8 Ga. Rutile has a lower U-Th-Pb closure temperature (~400 °C; [Mezger et al., 1989](#); [Zack and Kooijman, 2017](#)) compared to allanite, explaining its greater susceptibility to isotopic resetting during metamorphism.

The two stages of hydrothermal activity at Tongkuangyu can be related to crustal rifting at ~2.1 Ga and the Zhongtiao collisional orogeny at ~1.8 Ga, reflecting final collision between the east and west North China Blocks ([Fig. 2.17](#)).

2.10.3 Metallogenic implications

Early chalcopyrite ± pyrite mineralization in the central part of the orebody was closely associated with biotite ± K-feldspar alteration. It has locally been overprinted by chlorite alteration with bornite ± chalcopyrite mineralization on its margin. Previous studies interpreted this mineral zonation to be produced either from a porphyry-type deposit overprinted by metamorphism ([Geological Group in Zhongtiao Mountain, 1978](#)) or chemical reactions of oxidizing fluids with reduced S-rich rocks ([Liu et al. 2016](#)). Our results are more consistent with the first interpretation, in which early chalcopyrite mineralization associated with biotite ± K-

feldspar alteration at ~2.1 Ga was locally overprinted and remobilized to form chlorite-bornite assemblages during a later metamorphic/hydrothermal event at ~1.8 Ga. The $\delta^{34}\text{S}$ isotope data for the early and later sulfides (2.5 ‰ and 3.3 ‰ on average, respectively) were argued to be consistent with a magmatic origin (Ji et al., 1992; Sun et al., 1995). However, our results suggest that, while the early mineralization was indeed likely of magmatic origin, the later sulfide minerals inherited their S isotopic composition by remobilization of the earlier sulfides.

Although Tongkuangyu shows many features similar to porphyry Cu-type deposit (e.g., subvolcanic and/or volcanic host rocks, biotite \pm K-feldspar alteration, disseminated and quartz-sulfide vein mineralization, magmatic-like $\delta^{34}\text{S}$ signatures, and high Re content of molybdenite, Stein et al., 2004), the age of this mineralization event (~2.1 Ga) significantly postdates the granodiorite porphyry host rocks (~2.18 Ga; Fig. 2.17), meaning that these cannot be the causative intrusions. A single age of 2121 ± 10 Ma (2σ , MSWD = 1.3) was reported by Li et al. (2013) for a granodiorite porphyry sample, but no location was provided, and we have not been able to replicate this result. However, if the date is correct and the sample is indeed from the Tongkuangyu mine, then it suggests the presence of intrusive rocks broadly coeval with ore formation. One sample of felsic volcanic rock from the Tongkuangyu area yielded zircon U-Pb upper concordia intercept age of 2129 ± 28 Ma (2σ , MSWD = 0.66, recalculated from data in Yang et al., 2015). Two samples of intermediate and mafic volcanic rocks from the overlying Zhongtiao Group yielded zircon U-Pb upper concordia intercept ages of 2096 ± 65 Ma (2σ , MSWD = 0.91) and 2086 ± 83 Ma (2σ , MSWD = 16), respectively (ages recalculated from data in Sun and Hu, 1993; Liu et al., 2015). Although these ages are not very precise, they provide further evidence for magmatism coeval with ore formation in the area.

These results, taken together, lead us to conclude that Tongkuangyu is indeed a porphyry Cu deposit, formed in association with magmatism at ~ 2.1 Ga, and overprinted by metamorphism at ~ 1.8 Ga.

2.11 Conclusions

Many features of Tongkuangyu resemble porphyry Cu deposits, including alteration and mineralization styles, and volcanic and shallow plutonic host rocks, but the host granodiorite porphyry is too old to be the source intrusion. We were unable to verify a single reported zircon U-Pb age of 2121 ± 10 Ma for a granodiorite porphyry sample reported to be from Tongkuangyu (Li et al., 2013; location unknown), although this result suggests that a coeval pluton may be present. However, sample of quartz-sericite schist from Tongkuangyu yielded zircon U-Pb upper concordia intercept age of 2129 ± 28 Ma, and samples of dacitic tuff and plagioclase amphibolite from the overlying Zhongtiao Group yielded zircon U-Pb upper concordia intercept ages of 2096 ± 65 Ma (2σ , MSWD = 0.91) and 2086 ± 83 Ma (2σ , MSWD = 16; ages recalculated from data in Sun et al., 1991; Sun and Hu, 1993; Liu et al., 2015), suggesting the presence of magmatism coeval with initial ore formation in the Zhongtiao region. We therefore consider that a porphyry-type model best fits the observed features of this old, metamorphosed Cu deposit.

Modification of original features of a deposit by deformation and metamorphism renders identifying the genesis difficult. This study suggests that in Precambrian igneous rocks with low-grade metamorphism (e.g., lower greenschist facies), the alteration and mineralization styles typical of porphyry Cu deposits can be identified. Robust datable minerals, such as zircon, molybdenite, allanite, and monazite, are useful in unraveling regional magmatic, alteration, mineralization, and metamorphic events. The formation of the deposit can therefore be

constrained to be coeval with the host porphyry intrusion or regional magmatism, which best supports a porphyry Cu deposit model.

2.12 Acknowledgements

This research was supported by the China Geological Survey (project No. DD20160124), a Discovery Grant from the Natural Sciences and Engineering Research Council of Canada to Jeremy P. Richards (RGPIN/5082-2017), and student research grants from the Geological Society of America and Society of Economic Geologists to Xuyang Meng. The China Scholarship Council also awarded Xuyang Meng a Ph. D. scholarship in 2016. We thank Andrew Locock for assistance in mineral searching using the electron microprobe and William Zhe for guidance with the scanning electron microscope. We also thank Chunsheng Li and Jianbin Zhang (Zhongtiaoshan Non-ferrous Metals Group, Co., Ltd) for mine access, help from Hongying Li, Minfeng Bi, Wei Jian, Shengsheng Xue, Yanguang Geng, Chenglong Fan, and Mengqi Wang during fieldwork, and editorial comments from Jingjing Zhu on the initial version. We also thank David Cooke, Marc Norman, and an anonymous reviewer for their constructive reviews that have helped focus the work presented here.

2.13 References

214 Geological Group in Zhongtiao Mountain in Shanxi Province, 1956, unpublished internal report, 1 sheet.

Aleinikoff, J. N., Schenck, W. S., Plank, M. O., Srogi, L., Fanning, C. M., Kamo, S. L., & Bosbyshell, H., 2006, Deciphering igneous and metamorphic events in high-grade rocks of the Wilmington Complex, Delaware: Morphology, cathodoluminescence and backscattered electron zoning, and SHRIMP U-Pb geochronology of zircon and monazite: *Geological Society of America Bulletin*, v. 118, p. 39–64.

Bai, J., Yu, Z. X., Yan, Y. Y., and Dai, F. Y., 1997, *The Precambrian geology of Zhongtiao Mountains*, Tianjin Science and Technology Publishing House, 143 p (in Chinese with English abstract).

Birck, J. L., Roy Barman, M., and Capmas, F., 1997, Re-Os isotopic measurements at the femtomole level in natural samples: *Geostandards Newsletter: The Journal of Geostandards and Geoanalysis*, v. 20, p. 19–27.

Chen, W. M., and Li, S. P., 1998, Rhenium-osmium isotopic ages of sulfides from the Tongkuangyu porphyry copper deposit in the Zhongtiao Mountain: *Mineral deposits*, v. 17, p. 224–228 (in Chinese with English abstract).

Chen, W. M., Zhang, C. X., Lu, J. R., Dang, Z. F., Li, S. B., Cui, W. B., Ning, Y., and Cao, Y. J., 1998, Ore-hosted rock of the Zhongtiaoshan metamorphic porphyry copper deposit and its recovery: *Mineral Deposits*, v. 17, p. 523–526 (in Chinese with English abstract).

- Chen, Z. H., Yang, Y. C., Han, S. J., Zhang, G. B., 2014, Geochemical characteristics of ore-bearing rock series and ore genesis of Tongkuangyu copper deposit in Zhongtiao mountains: *Global Geology*, v. 33, p. 348–357 (in Chinese with English abstract).
- Chiaradia, M., Schaltegger, U., Spikings, R., Wotzlav, J. F., and Ovtcharova, M., 2012, How accurately can we date the duration of magmatic-hydrothermal events in porphyry systems?—an invited paper: *Economic Geology*, v. 108, p. 565–584.
- Cohen, A. S., and Waters, F. G., 1996. Separation of osmium from geological materials by solvent extraction for analysis by thermal ionization mass spectrometry: *Analytica Chimica Acta*, v. 332, p. 269–275.
- Engi, M., 2017, Petrochronology based on REE-minerals: monazite, allanite, xenotime, apatite: *Reviews in Mineralogy and Geochemistry*, v. 83, p. 365–418.
- Faure, M., Trap, P., Lin, W., Monié, P., and Bruguier, O., 2007, Polyorogenic evolution of the Paleoproterozoic Trans-North China Belt, new insights from the in Lüliangshan-Hengshan-Wutaishan and Fuping massifs: *Episodes Journal of International Geoscience*, v. 30, p. 95–106.
- Geological Group in Zhongtiao Mountain in Zhongtiao Mountain., 1978, *Geology of the copper deposits in Zhongtiao Mountain*, Geological Publishing House, Beijing, 190 p (in Chinese with English abstract).
- Guo, L. S., Liu, S. W., Liu, Y. L., Tian, W., Yu, S. Q., Li, Q. G., and Lu, Y. J., 2008, Zircon Hf isotopic features of TTG gneisses and formation environment of Precambrian Sushui

- complex in Zhongtiao mountains: *Acta Petrologica Sinica*, v. 24, p. 139–148 (in Chinese with English abstract).
- Huang, D. H., Du, A. D., Wu, C. Y., Liu, L. S., Sun, Y. L., and Zou, X. Q., 1996, Metallochronology of molybdenum (-copper) deposits in the North China Platform: Re-Os age of molybdenite and its geological significance: *Mineral Deposits*, v. 15, p. 365–373 (in Chinese with English abstract).
- Hu, W. X., and Sun, D. Z., 1987, Mineralization and evolution of the early Proterozoic copper deposits in the Zhongtiao Mountains: *Acta Geologica Sinica*, v. 2, p. 152–166 (in Chinese with English abstract).
- Ji, S. K., Li, S. P., Lu, J. R., Fu, Z. R., and Liu, R. L., 1992, Metallogenic and exploration models for copper deposits in Zhongtiao Mountain, Geological Publishing House, 117 p (in Chinese).
- Jiang, Y. H., Niu, H. C., Bao, Z. W., Li, N. B., Shan, Q., and Yang, W. B., 2014, Fluid evolution of the Tongkuangyu porphyry copper deposit in the Zhongtiaoshan region: evidence from fluid inclusions: *Ore Geology Reviews*, v. 63, p. 498–509.
- Li, N. B., Luo, Y., Guo, S. L., Jiang, Y. H., Zeng, L. J., and Niu, H. C., 2013, Zircon U-Pb geochronology and Hf isotope geochemistry of metamorphic quartz-monzonite porphyry from Tongkuangyu area, Zhongtiao Mountain and its geological implications: *Acta Petrologica Sinica*, v. 29, p. 2416–2424 (in Chinese with English abstract).
- Li, Q. G., Liu, S. W., Wang, Z. Q., Shen, Y., Zhang, L., and Zhang, J., 2011, Provenance and

- geotectonic setting of the Palaeoproterozoic Zhongtiao Group and implications for assembly of the North China Craton: whole-rock geochemistry and detrital zircon data: *Journal of the Geological Society*, v. 168, p. 1215–1224.
- Liu, C. H., Zhao, G. C., Sun, M., Zhang, J., and Yin, C. Q., 2012, U–Pb geochronology and Hf isotope geochemistry of detrital zircons from the Zhongtiao Complex: constraints on the tectonic evolution of the Trans-North China Orogen: *Precambrian Research*, v. 222, p. 159–172.
- Liu, S. W., Zhang, C., Liu, C. H., Li, Q. G., Lu, Y. J., Yu, S. Q., Tian, W., and Feng, Y. G., 2007, EMPA Th-U-Pb dating of monazite for Zhongtiao and Lvliang Precambrian metamorphic complexes: *Earth Science Frontiers*, v. 14, p. 64–74.
- Liu, X., Fan, H. R., Qiu, Z. J., Yang, K. F., Hu, F. F., Guo, S. L., and Zhao, F. C., 2015, Formation ages of the Jiangxian and Zhongtiao Groups in the Zhongtiao Mountain region, North China Craton: insights from SIMS U-Pb dating on zircons of intercalated plagioclase amphibolites: *Acta Petrologica Sinica*, v. 31, p. 1564–1572 (in Chinese with English abstract).
- Liu, X., Fan, H. R., Santosh, M., Yang, K. F., Qiu, Z. J., Hu, F. F., and Wen, B. J., 2016a, Geological and geochronological constraints on the genesis of the giant Tongkuangyu Cu deposit (Palaeoproterozoic), North China Craton: *International Geology Review*, v. 58, p. 155–170.
- Liu, X., Fan, H. R., Yang, K. F., Qiu, Z. J., Hu, F. F., and Zhu, X. Y., 2016b, *Geochronology*,

- redox-state and origin of the ore-hosting porphyry in the Tongkuangyu Cu deposit, North China Craton: implications for metallogenesis and tectonic evolution: *Precambrian Research*, v. 276, p. 211–232.
- Ludwig, K. R., 2011, *Isoplot/Ex, Version 4.15: A geochronological toolkit for Microsoft Excel: Geochronology Center Berkeley*, v. 4.
- Markey, R., Stein, H. J., Hannah, J. L., Selby, D., and Creaser, R. A., 2007, Standardizing Re-Os geochronology: a new molybdenite Reference Material (Henderson, USA) and the stoichiometry of Os salts: *Chemical Geology*, v. 244, p. 74–87.
- McFarlane, C. R. M., 2016, Allanite U-Pb geochronology by 193 nm LA ICP-MS using NIST610 glass for external calibration: *Chemical Geology*, v. 438, p. 91–102.
- Mei, H. L., 1994, Metamorphic P-T-t Paths and tectonic evolution of early Proterozoic rocks from the Zhongtiao Mountains, Southern Shanxi: *Geological Review*, v. 40, p. 36–47 (in Chinese with English abstract).
- Mezger, K., Hanson, G. N., and Bohlen, S. R., 1989, High-precision U-Pb ages of metamorphic rutile: application to the cooling history of high-grade terranes: *Earth and Planetary Science Letters*, v. 96, p. 106–118.
- Morelli, R. M., Creaser, R. A., Selby, D., Kontak, D. J., and Horne, R. J., 2005, Rhenium-osmium arsenopyrite geochronology of Meguma Group gold deposits, Meguma Terrane, Nova Scotia, Canada: evidence for multiple gold mineralizing events: *Economic Geology*, v. 100, p. 1229–1242.

- Paton, C., Hellstrom, J., Paul, B., Woodhead, J., and Hergt, J., 2011, Iolite: Freeware for the visualisation and processing of mass spectrometric data: *Journal of Analytical Atomic Spectrometry*, v. 26, p. 2508–2518.
- Paton, C., Woodhead, J.D., Hellstrom, J.C., Hergt, J.M., Greig, A., Maas, R., 2010. Improved laser ablation U–Pb zircon geochronology through robust downhole fractionation correction: *Geochem. Geophys. Geosyst.* v. 11.
- Petrus, J. A., and Kamber, B. S., 2012, VizualAge: A novel approach to laser ablation ICP-MS U-Pb geochronology data reduction: *Geostandards and Geoanalytical Research*, v. 36, p. 247–270.
- Qiu, Z. J., Fan, H. R., Liu, X., Yang, K. F., Hu, F. F., and Cai, Y. C., 2017, Metamorphic P-T-t evolution of Paleoproterozoic schist-hosted Cu deposits in the Zhongtiao Mountains, North China Craton: retrograde ore formation during sluggish exhumation: *Precambrian Research*, v. 300, p. 59–77.
- Schmitt, A. K., and Zack, T., 2012, High-sensitivity U–Pb rutile dating by secondary ion mass spectrometry (SIMS) with an O²⁺ primary beam: *Chemical geology*, v. 332, p. 65–73.
- Selby, D., and Creaser, R. A., 2004, Macroscale NTIMS and microscale LA-MC-ICP-MS Re-Os isotopic analysis of molybdenite: Testing spatial restrictions for reliable Re-Os age determinations, and implications for the decoupling of Re and Os within molybdenite: *Geochimica et Cosmochimica Acta*, v. 68, p. 3897–3908.
- Selby, D., Creaser, R. A., Stein, H. J., Markey, R. J., and Hannah, J. L., 2007, Assessment of the

- ^{187}Re decay constant by cross calibration of the Re-Os molybdenite and U-Pb zircon chronometers in magmatic ore systems: *Geochimica et Cosmochimica Acta*, v. 71, p. 1999–2013.
- Simonetti, A., Heaman, L. M., Chacko, T., and Banerjee, N. R., 2006, In situ petrographic thin section U-Pb dating of zircon, monazite, and titanite using laser ablation-MC-ICP-MS: *International Journal of Mass Spectrometry*, v. 253, p. 87–97.
- Shanxi No.6 Geology Engineering Reconnaissance Institute, 2002, unpublished internal report, 1 sheet.
- Shirey, S. B., and Walker, R.J., 1995, Carius tube digestion for low blank Re-Os analysis: *Analytical Chemistry*, v. 67, p. 2136–2141.
- Smoliar, M. I., Walker, R. J., and Morgan, J. W., 1996, Re-Os ages of group IIA, IIIA, IVA, and IVB iron meteorites: *Science*, v. 271, p. 1099–1102.
- Stein, H.J., Markey, R.J., Morgan, J.W., Hannah, J.L., and Scherstén, A., 2001, The remarkable Re-Os chronometer in molybdenite: how and why it works: *Terra Nova*, v. 13, p. 479–486.
- Stein, H., Scherstén, A., Hannah, J., and Markey, R., 2003, Subgrain-scale decoupling of Re and ^{187}Os and assessment of laser ablation ICP-MS spot dating in molybdenite: *Geochimica et Cosmochimica Acta*, v. 67, p. 3673–3686.
- Stein, H. J., Hannah, J. L., Zimmerman, A., Markey, R. J., Sarkar, S. C., and Pal, A. B., 2004, A 2.5 Ga porphyry Cu–Mo–Au deposit at Malanjkhand, central India: implications for Late

Archean continental assembly: *Precambrian Research*, v. 134, p. 189–226.

Sun, D. Z., and Hu, W. X., 1993, *Precambrian geochronology, chronotectonic framework and model of chronocrustal structure of the Zhongtiao Mountain*: Geological Publishing House, 180 p (in Chinese with English abstract).

Sun, D. Z., Li, H. M., Lin, Y. X., Zhou, H. F., Zhao, F. Q., and Tang, M., 1991, *Precambrian geochronology, chronotectonic framework and model of chronocrustal structure of the Zhongtiao Mountain*: *Acta Geologica Sinica*, v. 3, p. 216–231 (in Chinese with English abstract).

Sun, J. G., Li, H. Y., Liu, X. H., Xie, K. Q., Li, B. L., and Yin, D. W., 2014, *Alteration and mineralization characteristics of Tongkuangyu copper deposit in Zhongtiao Mountain, Shanxi Province*: *Mineral Deposits*, v. 33, p. 1306–1324 (in Chinese with English abstract).

Sun, J. G., Li, H. Y., Liu, X. H., Xie, K. Q., Chen, W., Xue, S. S., and Sun, X. L., 2015, *Characteristics of chlorite from the Tongkuangyu copper deposit in Shanxi Province and their geological implications*: *Bulletin of Mineralogy, Petrology and Geochemistry*, v. 34, p. 1142–1154 (in Chinese with English abstract).

Sun, J. Y., Ji, S. K., and Zhen, Y. Q., 1995, *The copper deposits in the Zhongtiao Rift*, Geological Publishing House, 194 p (in Chinese with English abstract).

Sun, S. S., and McDonough, W. F., 1989, *Chemical and isotopic systematics of oceanic basalts: Implications for mantle composition and processes*: Geological Society, London, Special Publications, v. 42, p. 313–345.

- Suzuki, K., Shimizu, H., and Masuda, A., 1996, Re-Os dating of molybdenites from ore deposits in Japan: Implication for the closure temperature of the Re-Os system for molybdenite and the cooling history of molybdenum ore deposits: *Geochimica et Cosmochimica Acta*, v. 60, p. 3151–3159.
- Tian, W., Liu, S. W., Liu, C. H., Yu, S. Q., Li, Q. G., and Wang, Y. R., 2006, Zircon SHRIMP geochronology and geochemistry of TTG rocks in Sushui Complex from Zhongtiao Mountains with its geological implications: *Progress in Natural Science*, v. 16, p. 492–500.
- Wang, S. A., Bai, J., Li, S. P., Cao, J. S., Chen, W. M., Yu, Z. X., and Fan, C. M., 1995, Ore-forming condition and exploration targeting of Precambrian copper deposits in Zhongtiaoshan region, Shanxi Province: Unpublished internal Report, 183 p (in Chinese).
- Wang, Z., and Wen, G., 1957, Zhongtiaoshan-type porphyry copper deposit: *Acta Geologica Sinica*, v. 37, p. 401–421 (in Chinese with English abstract).
- Wendt, I., and Carl, C., 1991, The statistical distribution of the mean squared weighted deviation: *Chemical Geology: Isotope Geoscience section*, v. 86, p. 275–285.
- Winchester, J. A., and Floyd, P. A., 1977, Geochemical discrimination of different magma series and their differentiation products using immobile elements: *Chemical Geology*, v. 20, p. 325–343.
- Wise, S. A., and Watters, R. L., 2011, Reference Material 8599 Henderson Molybdenite: National Institute of Standards and Technology Report of Investigation, 3 p.

- Xiao, B., Li, Q. G., Liu, S. W., Wang, Z. Q., Yu, T., Zhang, L. F., Zhou, J., and Tu, Y. J., 2013, Muscovite $^{40}\text{Ar}/^{39}\text{Ar}$ dating of the Palaeoproterozoic granitoid gneiss in the Zhongtiao Mountains and its geological significance: *Geological Bulletin of China*, v. 32, p. 706–716.
- Xu, Q. L., Sun, F. Y., Zhang, H., and Huo, L., 2012, Fluid inclusion, zircon U-Pb age and Hf isotope of Tongkuangyu copper deposit in Zhongtiaoshan mountains and its geological significance, Shanxi Province, China: *Journal of Jilin University (Earth Science Edition)*, v. 42, p. 64–80 (in Chinese with English abstract).
- Yang, C. H., Du, L. L., Ren, L. D., Song, H. X., Geng, Y. S., Wang, Y. B., Lu, Z. L., Wang, H., and Li, Y. H., 2015, The age and tectonic setting of metavolcanic rocks in the Tongkuangyu deposit, Zhongtiao Mountain, and their constraints on copper mineralization: *Acta Geoscientica Sinica*, v. 36, p. 613–633 (in Chinese with English abstract).
- Yu, S. Q., Liu, S. W., Tian, W., 2006, SHRIMP zircon U-Pb chronology and geochemistry of the Henglingguan and Beiyu granitoids in the Zhongtiao Mountains, Shanxi Province: *Acta Geologica Sinica—English edition*, v. 80, p. 912–924.
- Zack, T., Stockli, D. F., Luvizotto, G. L., Barth, M. G., Belousova, E., Wolfe, M. R., and Hinton, R. W., 2011, In situ U–Pb rutile dating by LA-ICP-MS: ^{208}Pb correction and prospects for geological applications: *Contributions to Mineralogy and Petrology*, v. 162, p. 515–530.
- Zack, T., and Kooijman, E., 2017, Petrology and geochronology of rutile: *Reviews in Mineralogy and Geochemistry*, v. 83, p. 443–467.

- Zhai, M. G., and Liu, W. J., 2003, Palaeoproterozoic tectonic history of the North China craton: a review: *Precambrian Research*, v. 122, p. 183–199.
- Zhai, M.G., and Santosh, M., 2011, The early Precambrian odyssey of the North China Craton: a synoptic overview: *Gondwana Research*, v. 20, p. 6–25.
- Zhai, M. G., Zhao, Y., and Zhao, T. P., 2016, Main tectonic events and metallogeny of the North China Craton, Springer, 540 p.
- Zhang, H., 2012, Metallogensis of Paleoproterozoic copper deposits in the Northern Zhongtiaoshan Mountains, Shanxi Province: Unpublished Ph.D. thesis, Changchun, China, Jilin University, 155 p (in Chinese with English abstract).
- Zhang, J., Zhao, G. C., Li, S. Z., Sun, M., Wilde, S. A., Liu, S. W., and Yin, C. Q., 2009, Polyphase deformation of the Fuping Complex, Trans-North China Orogen: structures, SHRIMP U-Pb zircon ages and tectonic implications: *Journal of Structural Geology*, v. 31, p. 177–193.
- Zhang, L., Li, B. L., Zhang, H., and Hu, A. X., 2013, Re-Os isotopic dating and its geological significance of molybdenite from Tongmugou copper deposit in Zhongtiaoshan, Shanxi: *Global Geology*, v. 32, p. 740–746 (in Chinese with English abstract).
- Zhang, R. Y., Zhang, C. L., Diwu, C. R., and Sun, Y., 2012, Zircon U-Pb geochronology, geochemistry and its geological implications for the Precambrian granitoids in Zhongtiao Mountain, Shanxi Province: *Acta Petrologica Sinica*, v. 28, p. 3559–3573.
- Zhao, G. C., Sun, M., Wilde, S. A., and Li, S. Z., 2005, Late Archean to Paleoproterozoic

- evolution of the North China Craton: key issues revisited: *Precambrian Research*, v. 136, p. 177–202.
- Zhao, G. C., Wilde, S. A., Sun, M., Li, S. Z., Li, X. P., and Zhang, J., 2008, SHRIMP U–Pb zircon ages of granitoid rocks in the Lüliang Complex: implications for the accretion and evolution of the Trans-North China Orogen: *Precambrian Research*, v. 160, p. 213–226.
- Zhao, G. C., Wilde, S. A., Guo, J. H., Cawood, P. A., Sun, M., and Li, X. P., 2010, Single zircon grains record two Paleoproterozoic collisional events in the North China Craton: *Precambrian Research*, v. 177, p. 266–276.
- Zhao, G. C., and Zhai, M. G., 2013, Lithotectonic elements of Precambrian basement in the North China Craton: Review and tectonic implications: *Gondwana Research*, v. 23, p. 1207–1240.
- Zhao, T. P., Zhai, M. G., Xia, B., Li, H. M., Zhang, Y. X., and Wan, Y. S., 2004, Zircon U–Pb SHRIMP dating for the volcanic rocks of the Xiong'er Group: Constraints on the initial formation age of the cover of the North China Craton: *Chinese Science Bulletin*, v. 49, p. 2495–2502.
- Zhu, X. Y., Zhai, M. G., Chen, F. K., Liu, B., Wang, W., Peng, P., and Hu, B., 2013, ~2.7 Ga crustal growth in the North China Craton: evidence from zircon U–Pb ages and Hf isotopes of the Sushui Complex in the Zhongtiao Terrane: *The Journal of Geology*, v. 121, p. 239–254.

2.14 Figures

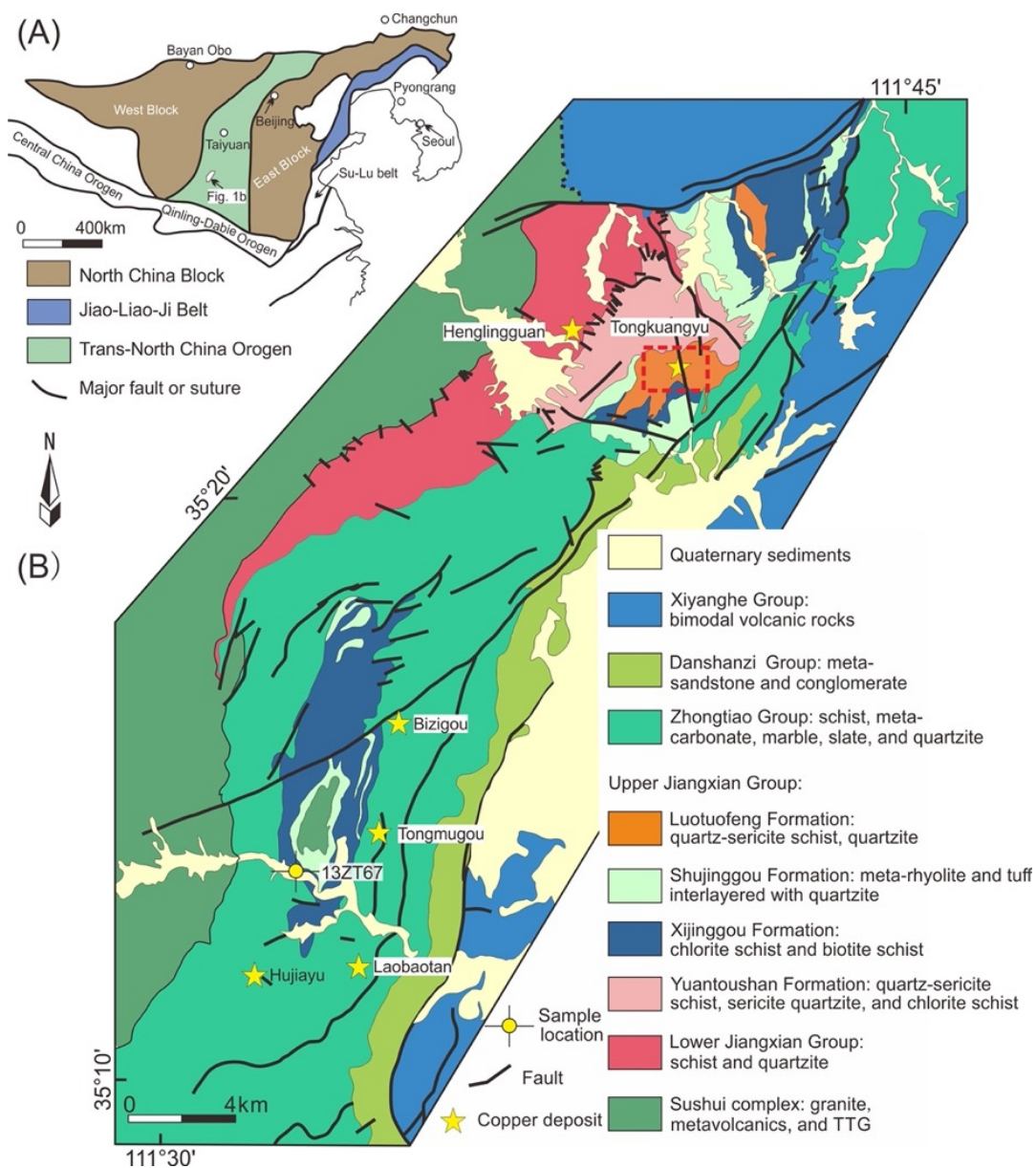


Figure 2.1. Simplified geological map of the northern Zhongtiaoshan region (modified based on internal document of [Shanxi No.6 Geology Engineering Reconnaissance Institute, 2002](#)), with an inset map showing its location within the Trans-North China Orogen (modified from [Zhao et al., 2005](#)).

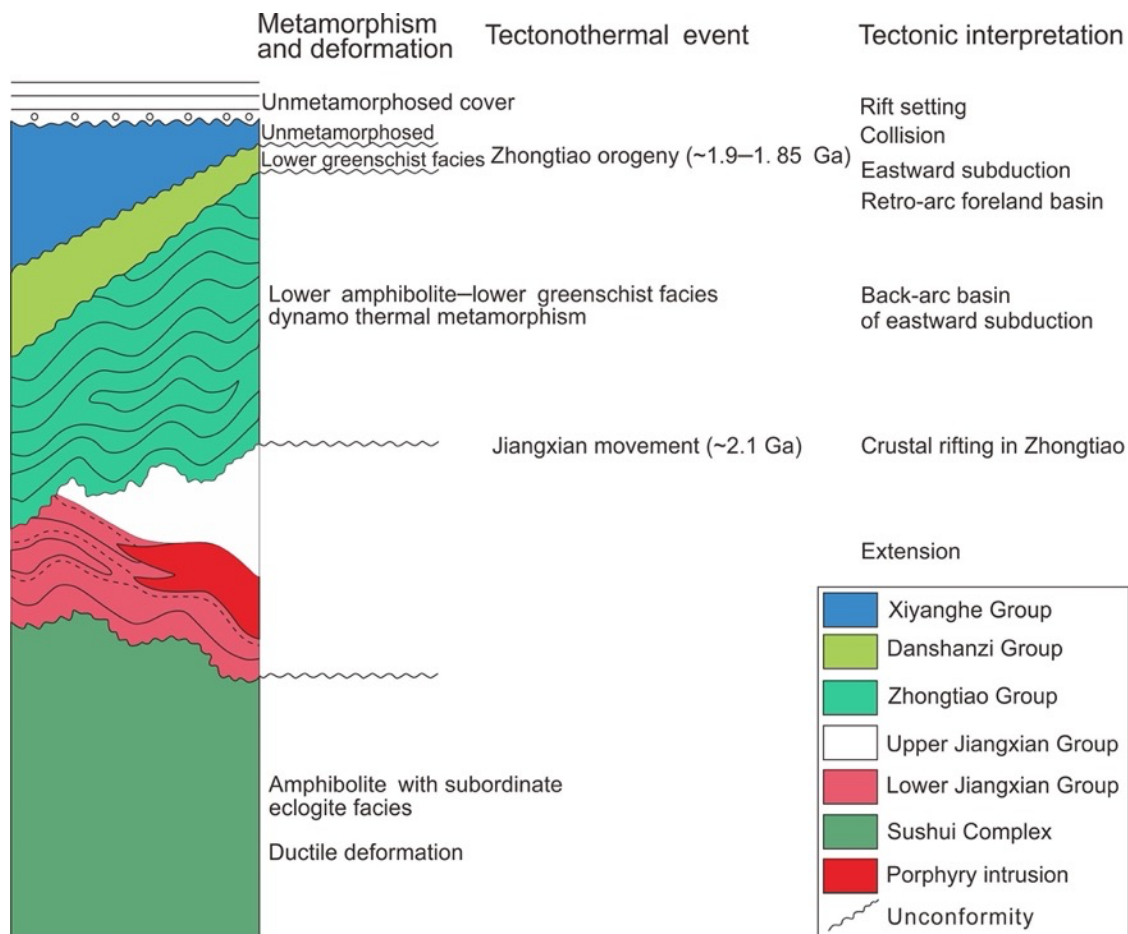


Figure 2.2. Lithostratigraphic column with metamorphic and tectonothermal events affecting the northern Zhongtiaoshan region (Bai et al., 1997). Tectonic interpretations are summarized from Li et al. (2011), Mei (1994), Zhai and Santosh (2011), Zhai et al. (2016), and Zhao et al. (2008).

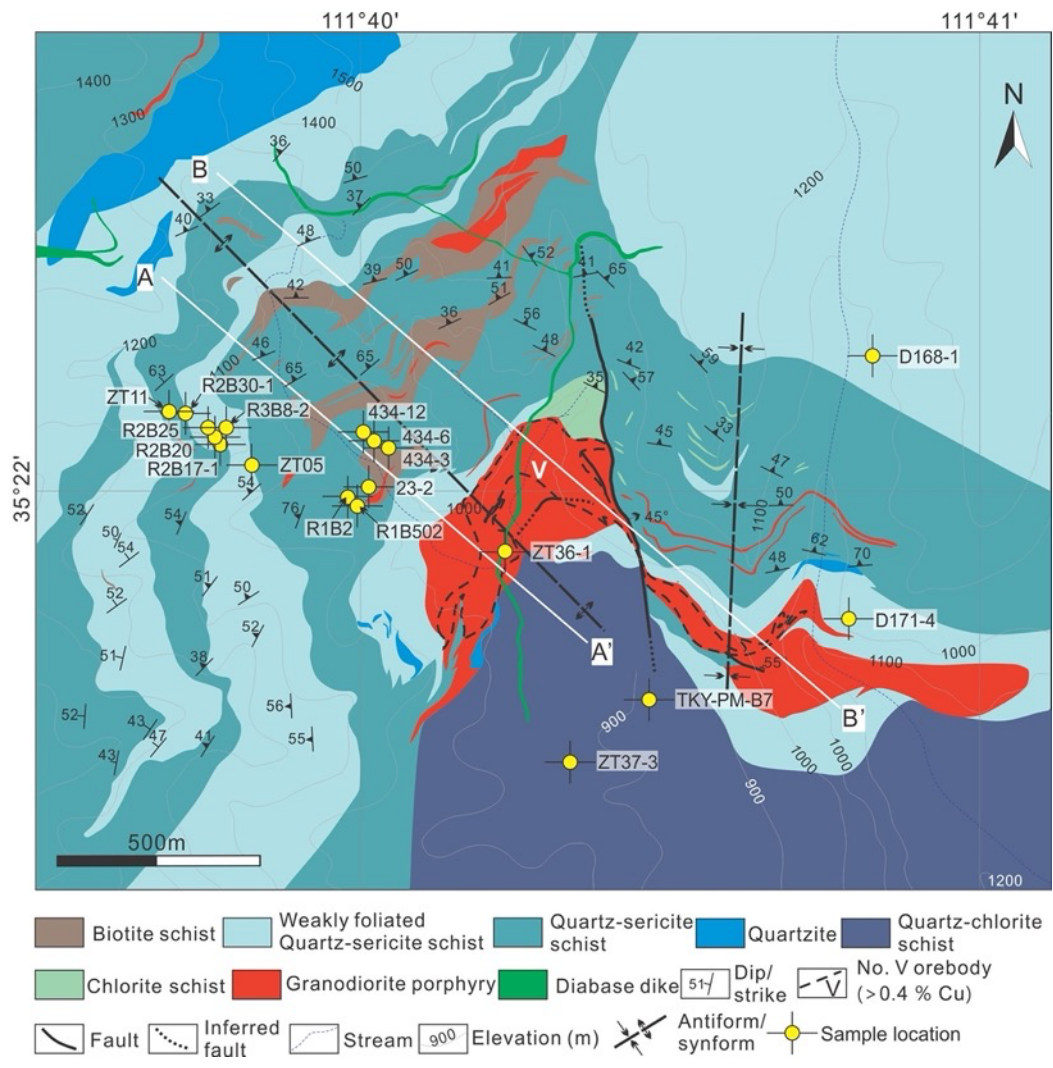


Figure 2.3. Simplified geological map of the Tongkuangyu Cu deposit, showing lithological units and geometry of the orebodies, which is modified from internal material from the [214 Geological Group in Zhongtiao Mountain in Shanxi Province \(1956\)](#).

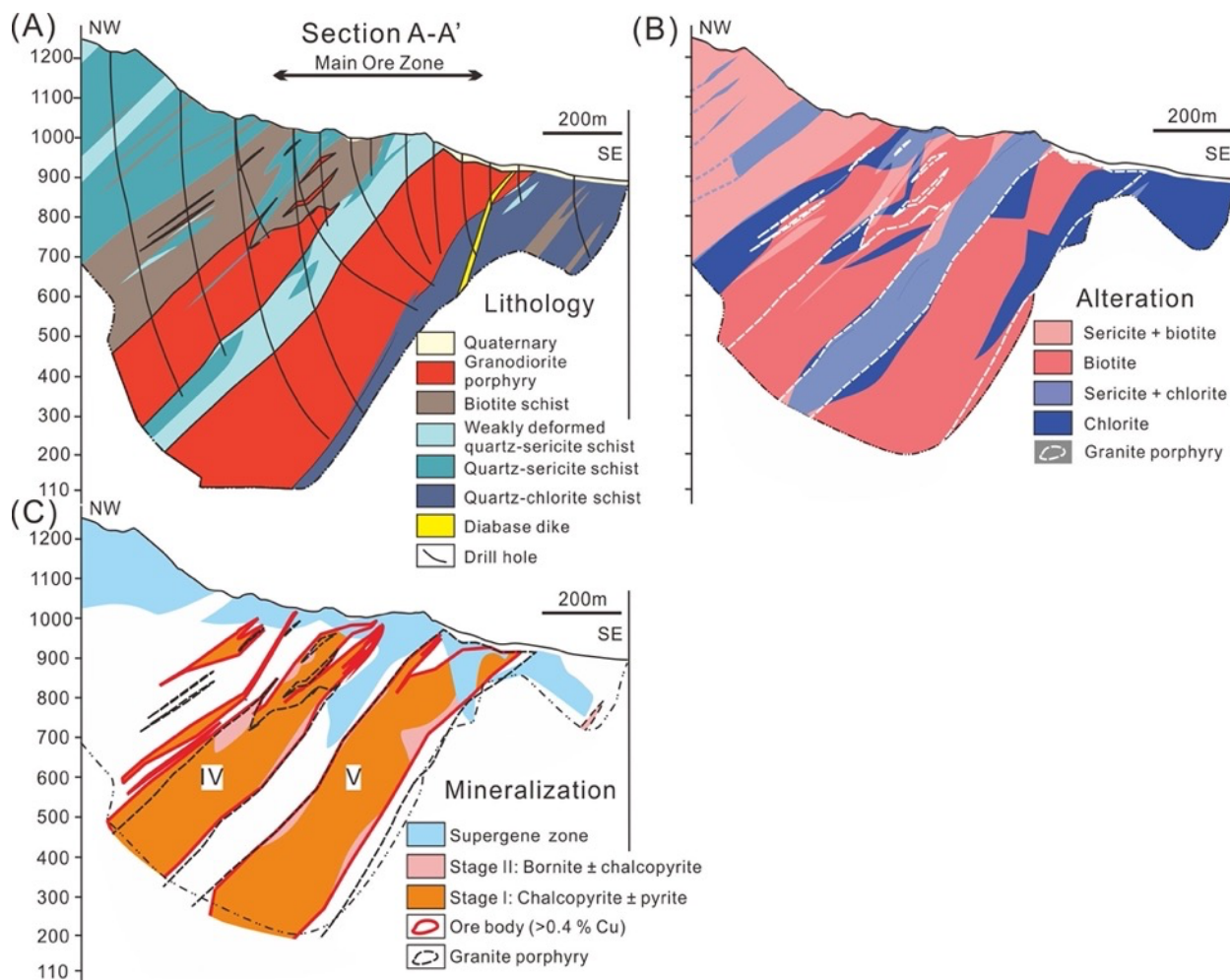


Figure 2.4. Cross section A-A', showing lithological units and spatial distribution of alteration, mineralization, and orebodies. The biotite and chlorite zones are spatially associated with chalcopyrite and bornite ± chalcopyrite mineralization, respectively. Geological cross section in A is modified from internal material from the [214 Geological Group in Zhongtiao Mountain in Shanxi Province \(1956\)](#).

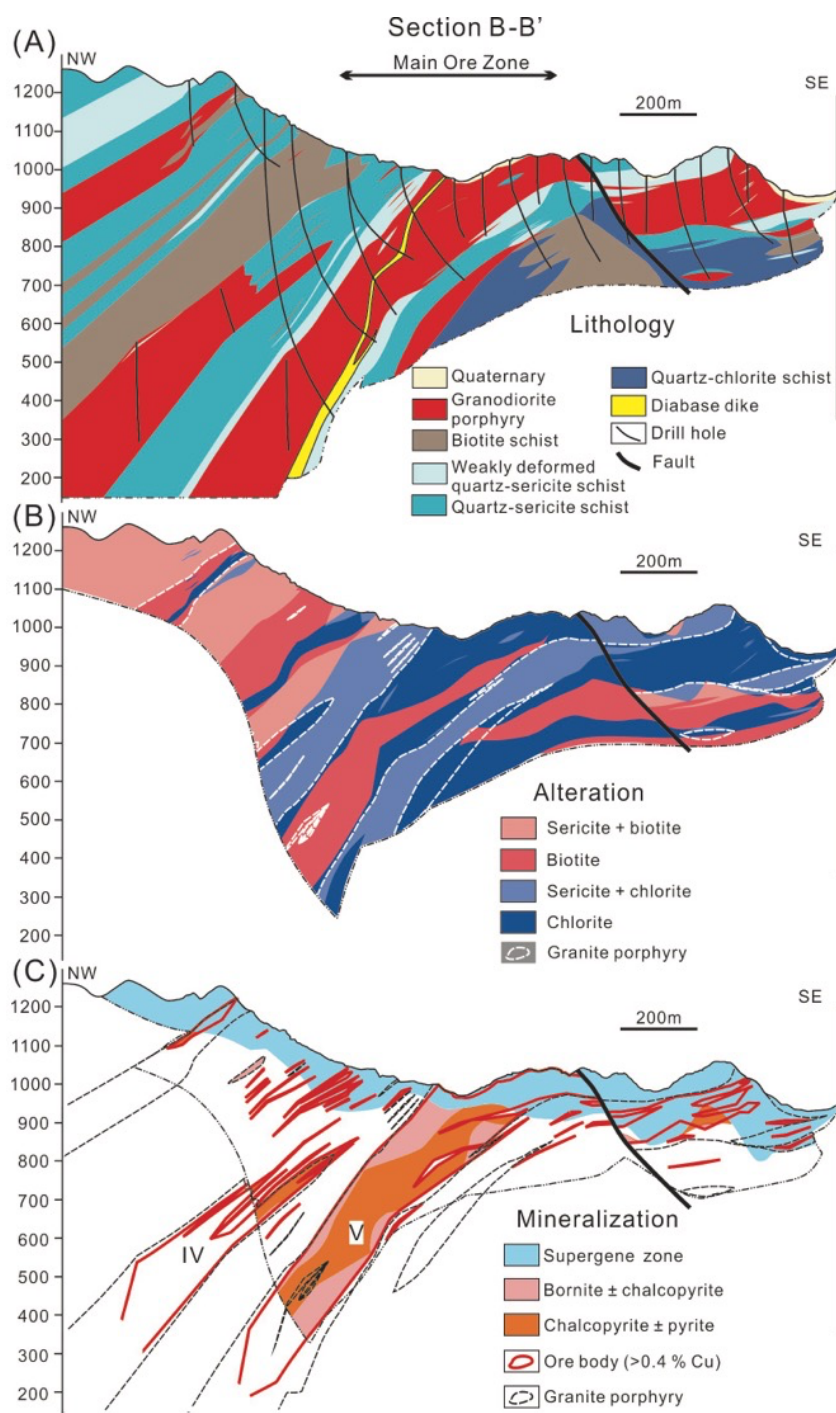


Figure 2.5. Cross section B-B', showing lithological units and spatial distribution of alteration, mineralization, and orebodies. Geological cross section in A is modified from the internal material from the 214 Geological Group in Zhongtiao Mountain in Shanxi Province (1956).

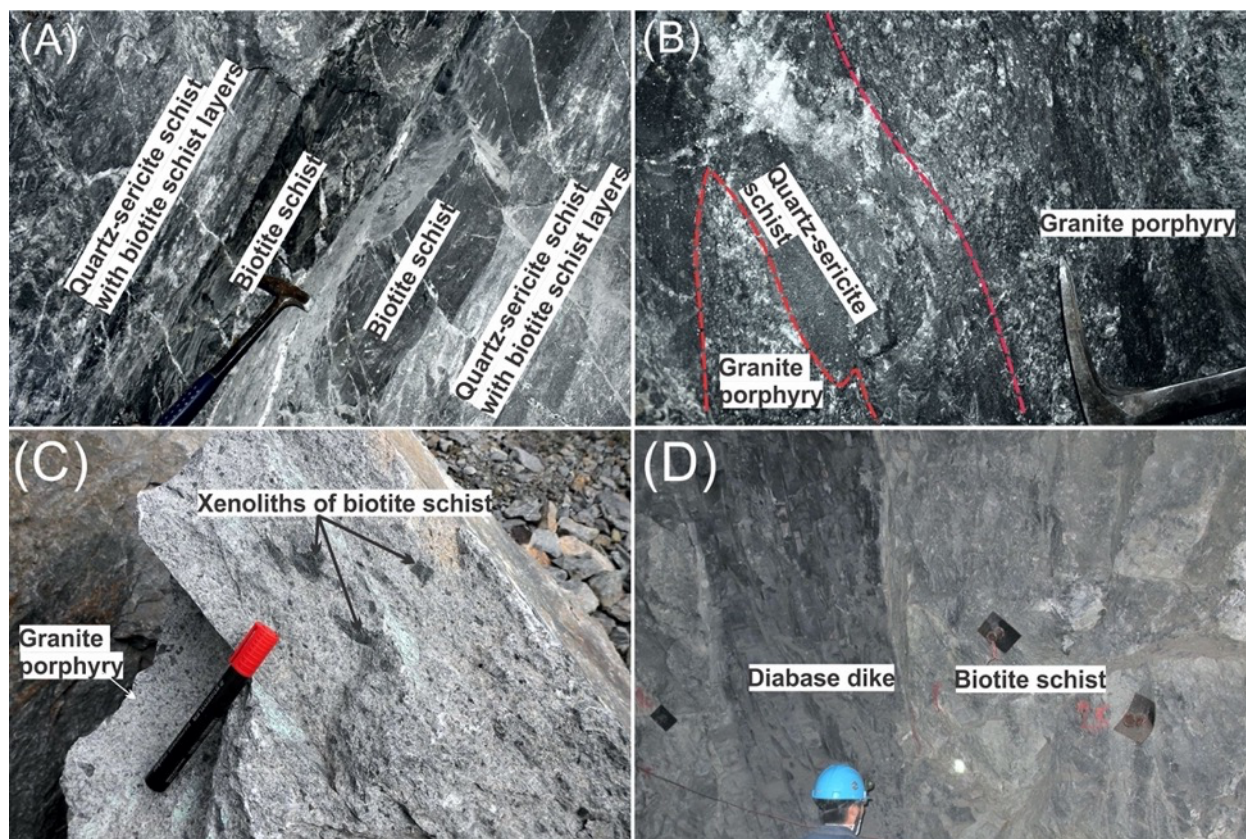


Figure 2.6. Representative photographs of lithological relationships at the Tongkuangyu Cu deposit. (A) concordant relationships between biotite schist and quartz-sericite schist (No. 31 adit of No. IV orebody on 584-m-level); (B) quartz-sericite schist intruded by granodiorite porphyry (No. 33 adit of No. IV orebody on 662-m-level); (C) xenoliths of biotite schist in granodiorite porphyry (N35°21'47.6'', E111°40'47.3''); (D) weakly deformed diabase dike intruded biotite schist (No. 37 adit of No. V orebody on 530-m-level).

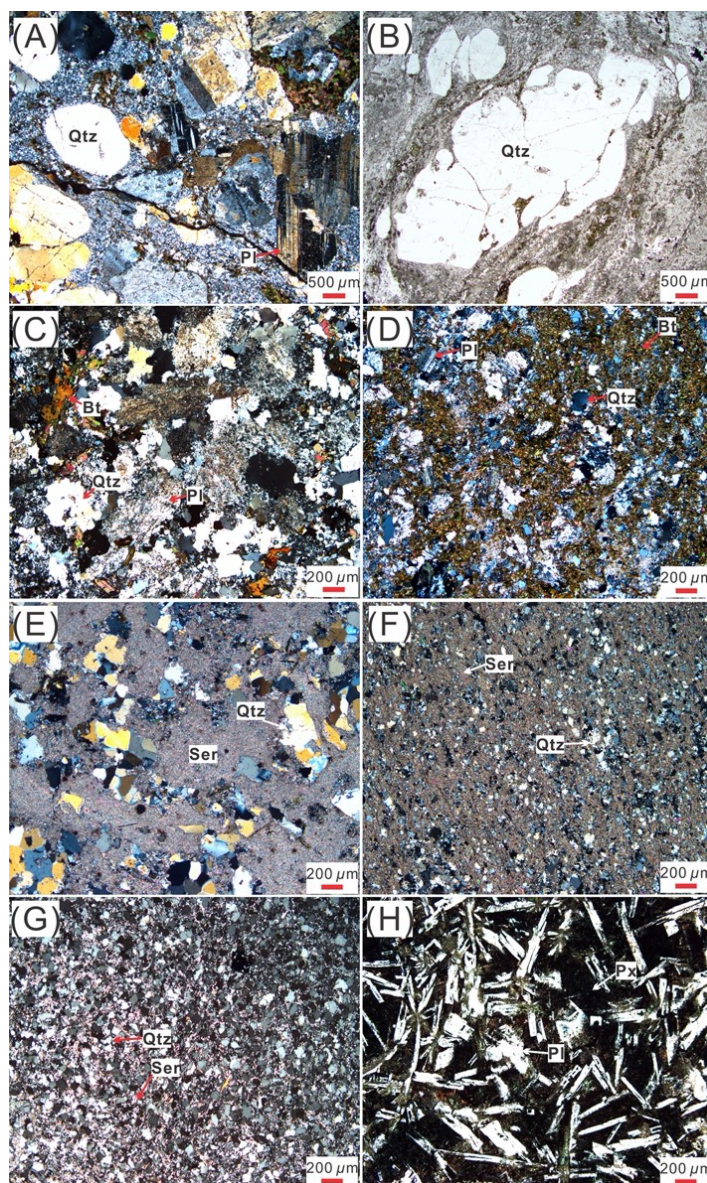


Figure 2.7. Representative photomicrographs of the main lithologies at the Tongkuangyu Cu deposit. (A) granodiorite porphyry (cross-polarized light; sample 434-11); (B) embayed quartz phenocrysts in granodiorite porphyry (plane-polarized light; sample 434-8); (C) granodiorite (cross-polarized light; sample 434-3); (D) biotite schist (cross-polarized light; sample 26-9); (E) quartz-sericite schist with large quartz crystals (cross-polarized light; sample 23-3); (F) quartz-sericite schist with small quartz crystals (cross-polarized light; sample R2B2); (G) quartz-rich quartz-sericite schist (cross-polarized light; sample D168-1); (H) diabase dike (plane-polarized light; sample R2B32). Abbreviations: Bt = biotite, Cp = chalcopyrite, Pl = plagioclase, Px = pyroxene, Qtz = quartz, Ser = sericite. See [Table A2.2](#) for sample locations and descriptions.

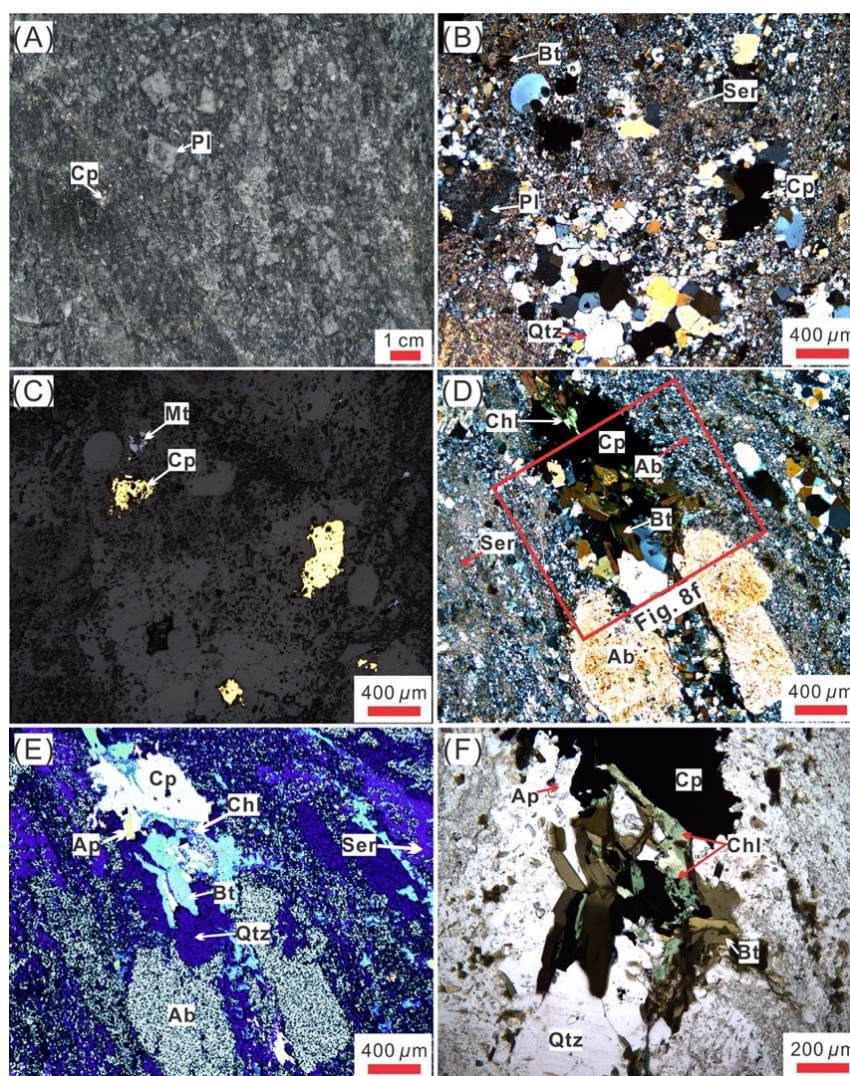


Figure 2.8. Photographs and photomicrographs of early disseminated and veinlet alteration and mineralization in granodiorite porphyry from Tongkuangyu. (A–C) Disseminated chalcopyrite mineralization in granodiorite porphyry (sample 662-7); hand specimen, thin section cross-polarized light, and reflected light. (D–E) Albite-altered granodiorite porphyry crosscut by quartz-biotite vein (overprinted by minor chlorite) containing chalcopyrite (sample 584-3); cross-polarized light and false-color SEM image. (F) Closer view of the relationship between chlorite and biotite; the chlorite is interpreted to have partially overprinted biotite during later metamorphism; plane-polarized light. Abbreviations and colors in (E): Ab = albite (grey), Ap = apatite (yellow), Bt = biotite (light blue), Chl = chlorite (light blue-grey), Cp = chalcopyrite (white), Mt = magnetite, Pl = plagioclase, Qtz = quartz (dark blue), Ser = sericite (sapphire). See [Table A2.2](#) for sample locations and descriptions.

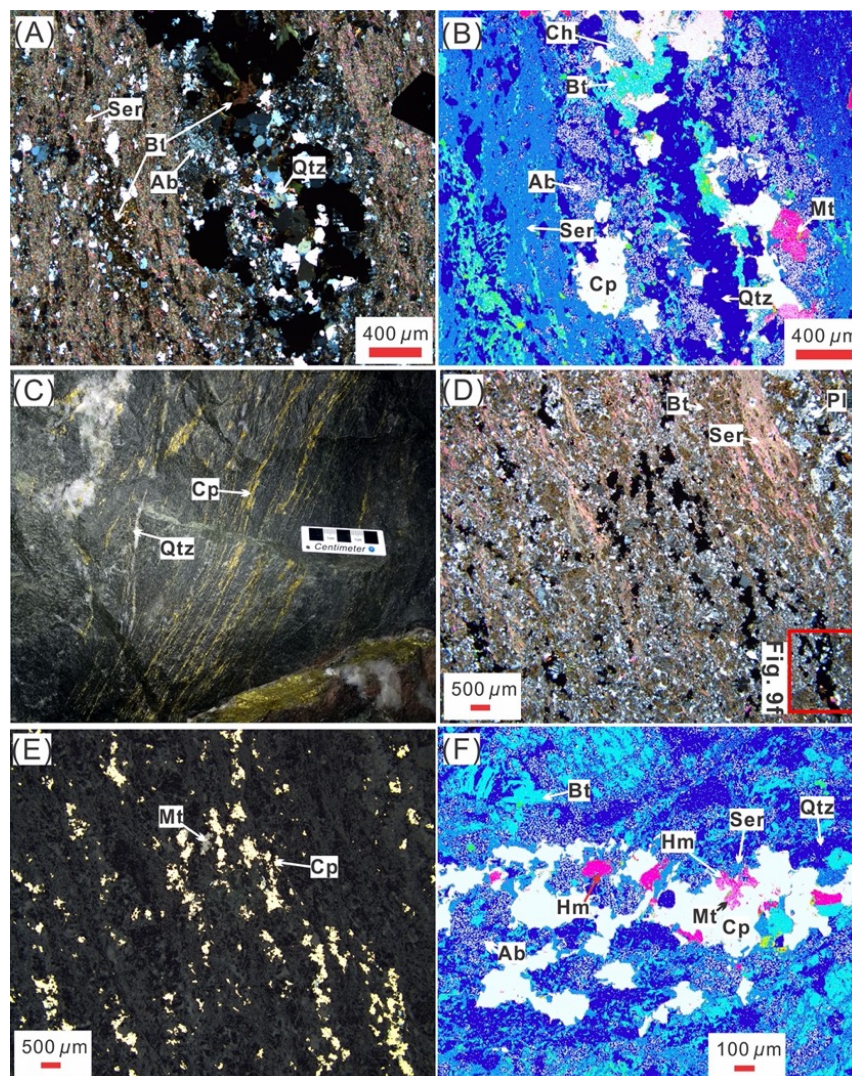


Figure 2.9. Photomicrographs of veinlets and foliated alteration and mineralization in schists from Tongkuangyu. (A–B) Quartz-sericite schist crosscut by quartz-biotite-chalcopyrite-magnetite vein with albite selvage (sample R2B21); cross-polarized light and false-color SEM image. (C) Chalcopyrite along foliation in biotite schist (No. 21 adit of No. IV orebody on 564-m level). (D–E) Chalcopyrite in foliated biotite schist with sericite (sample ZT09); cross-polarized light and reflected light. (F) Closer view of biotite-chalcopyrite alteration in foliated biotite schist, showing that albite-altered plagioclase has been replaced by hydrothermal biotite (sample ZT09); false-color SEM image. Abbreviations and colors in (B, F): Ab = albite (grey), Bt = biotite (light blue), Chl = chlorite (light blue-grey), Cp = chalcopyrite (white), Hm = hematite, Mt = magnetite (magenta), Pl = plagioclase, Qtz = quartz (royal blue), Ser = sericite (sapphire). See [Table A2.2](#) for sample locations and descriptions.

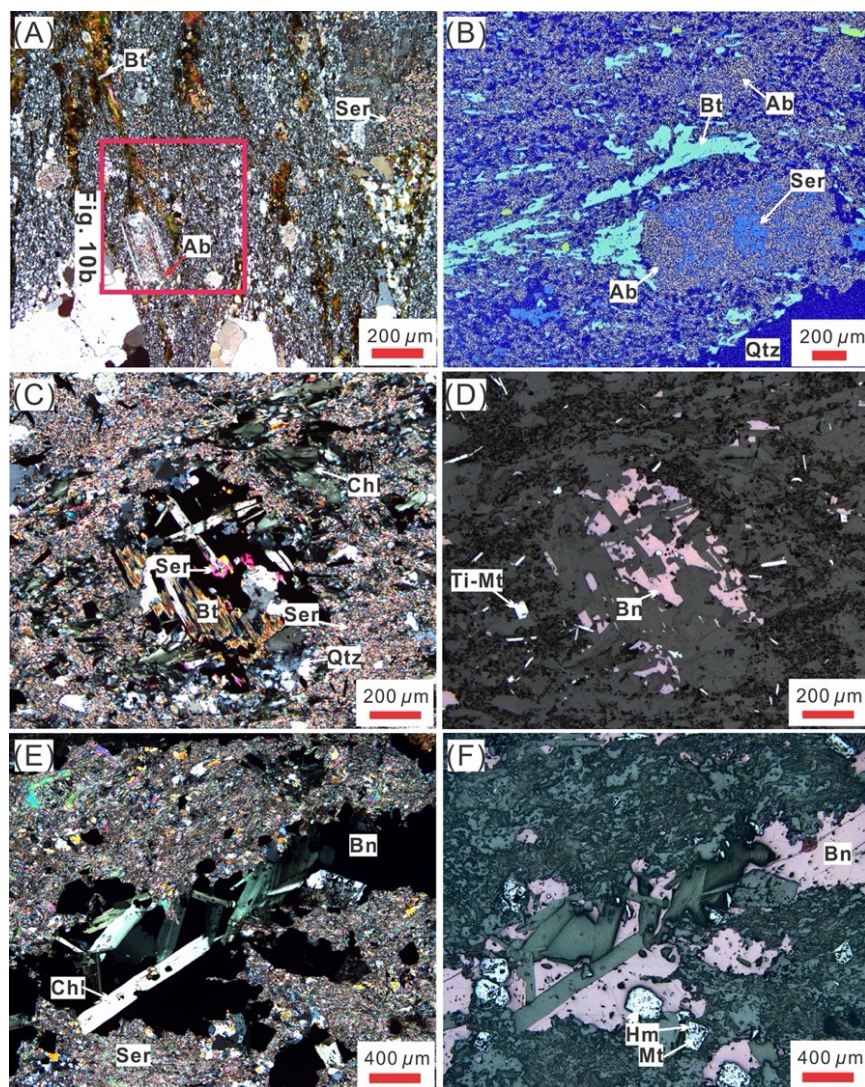


Figure 2.10. Photomicrographs of syn- and post-deformation alteration and mineralization from Tongkuangyu. (A–B) Albite-sericite and biotite alteration in foliated granodiorite porphyry (sample R3B14); cross-polarized light and false-color SEM image. (C–D) Quartz-sericite schist with hydrothermal biotite overprinted by bornite-chlorite alteration, characterized by chlorite altered biotite along cleavage planes and rims (sample ZT-11); cross-polarized light and reflected light. (E–F) quartz-chlorite-bornite-magnetite vein crosscutting quartz-sericite schist; magnetite is partially oxidized to hematite (sample 434-20); cross-polarized light and reflected light. Abbreviations and colors in (B): Ab = albite (grey), Bn = bornite, Bt = biotite (light blue), Chl = chlorite, Hm = hematite, Mt = magnetite, Qtz = quartz (royal blue), Ser = sericite (sapphire), Ti-Mt = titanomagnetite. See [Table A2.2](#) for sample locations and descriptions.

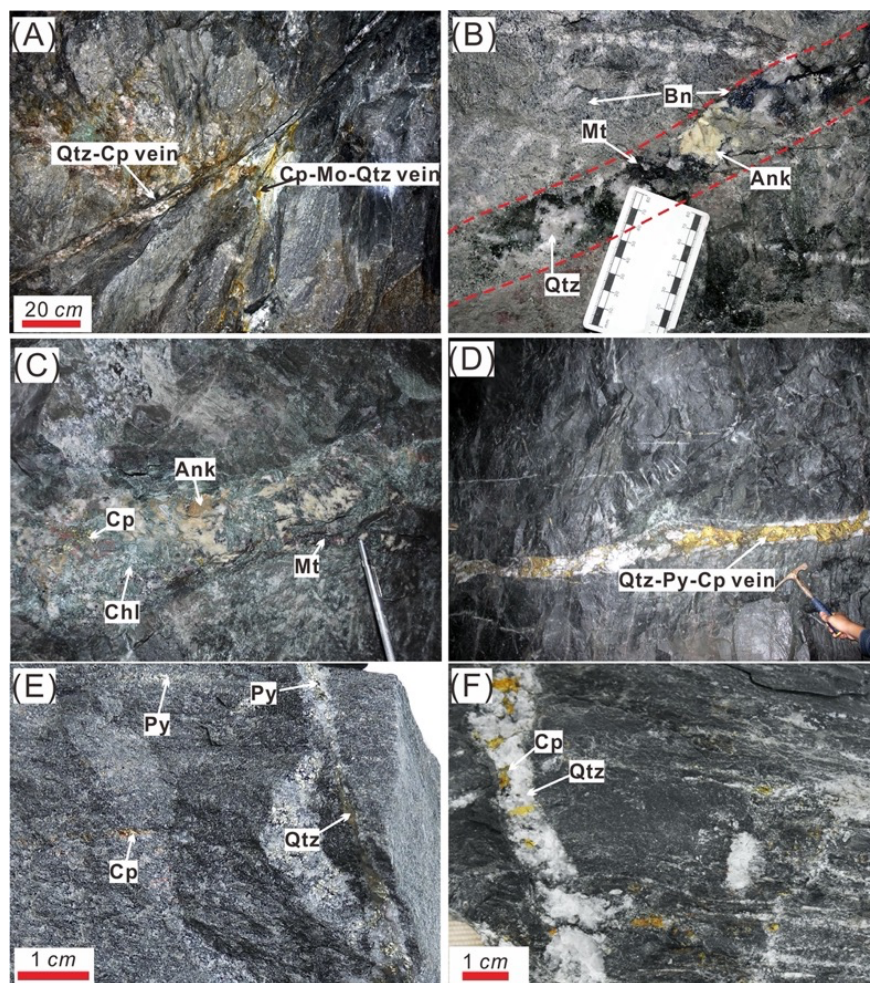


Figure 2.11. Vein-type copper mineralization from Tongkuangyu. (A) Early quartz-chalcopyrite-molybdenite vein crosscut by quartz-pyrite-chalcopyrite vein in quartz-sericite schist (No. 23 adit of No. V orebody on 564-m-level). (B) Late quartz-ankerite-bornite-magnetite vein (outlined in red) cutting chlorite-altered quartz-sericite schist with disseminated bornite \pm chalcopyrite (No. 27 adit of No. V orebody on 564-m-level). (C) Rare late chlorite - ankerite - quartz - chalcopyrite - magnetite vein in quartz-sericite schist (outside of No. 27 adit of No. V orebody on 564-m-level). (D) Late quartz-pyrite-chalcopyrite vein in quartz-sericite schist (No. 37 adit of No. IV orebody on 530-m-level). (E) Late quartz-pyrite \pm chalcopyrite vein in foliated granodiorite porphyry (sample R3B6, No. 20 adit of No. IV orebody on 564-m-level). (F) Late quartz-chalcopyrite \pm pyrite vein in biotite schist (sample 564-26-1, No. 36 adit of No. IV orebody on 564-m-level). Abbreviations: Ank = ankerite, Bn = bornite, Cal = calcite, Chl = chlorite, Cp = chalcopyrite, Mo = molybdenite, Mt = magnetite, Py = pyrite, Qtz = quartz.

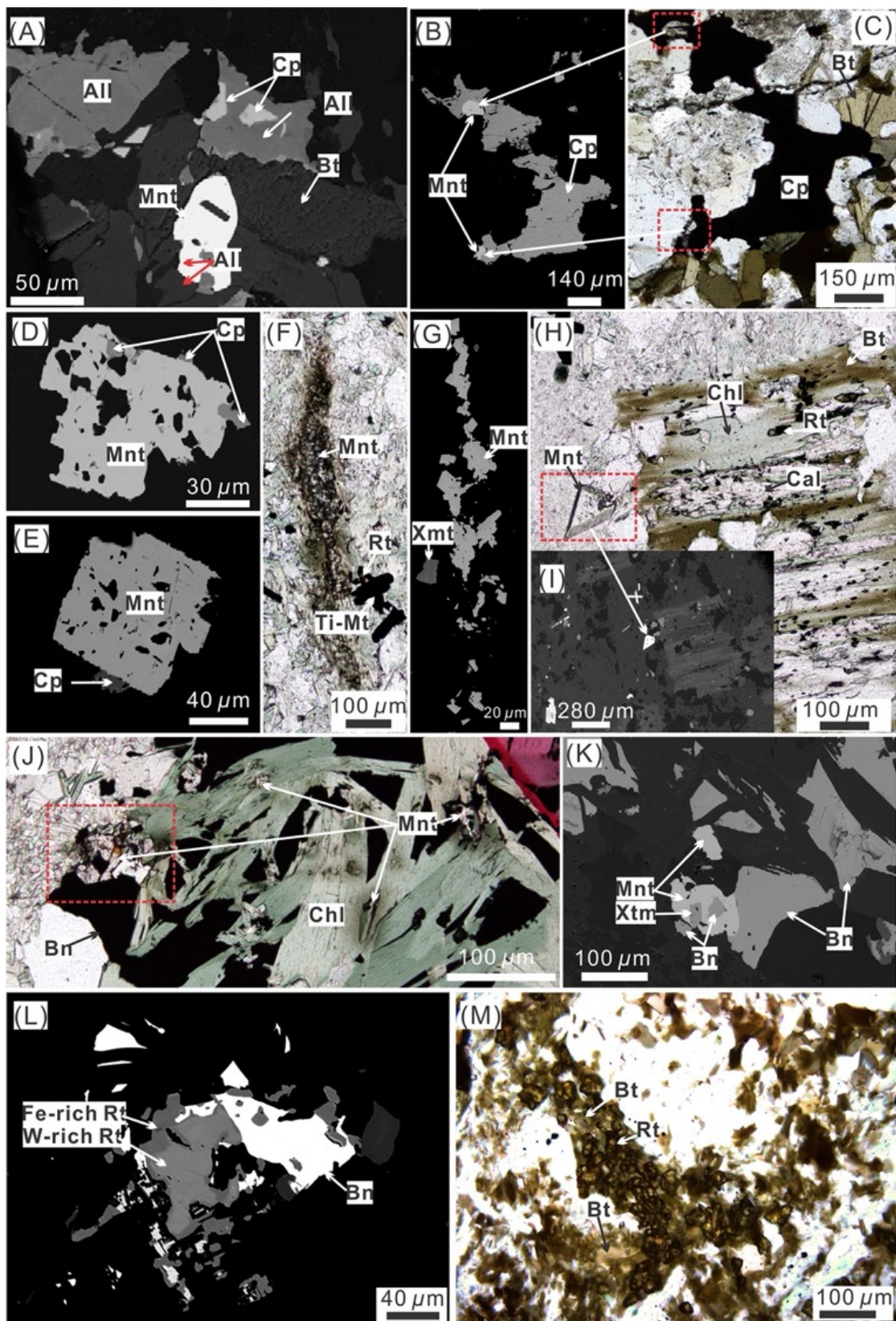


Figure 2.12. Microphotographs of datable minerals allanite, monzonite, rutile from the Tongkuangyu Cu deposit. (A) Angular allanite enclosing chalcopyrite inclusions, and monazite intergrown within hydrothermal biotite and containing allanite in the granodiorite porphyry (sample R2B30-1); BSE. (B–C) Monazite intergrown with chalcopyrite in the granodiorite porphyry (sample R2B30-1); BSE and plane-polarized light. (D–E) Monazite intergrown with chalcopyrite in the quartz-sericite schist (sample R1B2); BSEs. (F–G) Monazite aggregate associated with chlorite alteration in the quartz-sericite schist (sample R1B2); plane-polarized light and BSE. (H–I) Euhedral monazite in quartz-sericite schist (sample R1B502); plane-polarized light and BSE. (J–K) Monazite with bornite and xenotime inclusions in chlorite-bornite-quartz vein (sample R2B20); plane-polarized light and BSE. (L) Rutile with patchy W-rich and Fe-rich zones intergrown with bornite in quartz-sericite schist (sample ZT11); BSE. (M) Folded biotite-rutile vein in biotite schist (sample R2B17); plane-polarized light. Abbreviations: All = allanite, Bn = bornite, Bt = biotite, Cal = calcite, Chl = chlorite, Cp = chalcopyrite, Mnt = monazite, Rt = rutile, Ti-Mt = titanomagnetite, Xtm = xenotime. See [Table A2.2](#) for sample locations and descriptions.

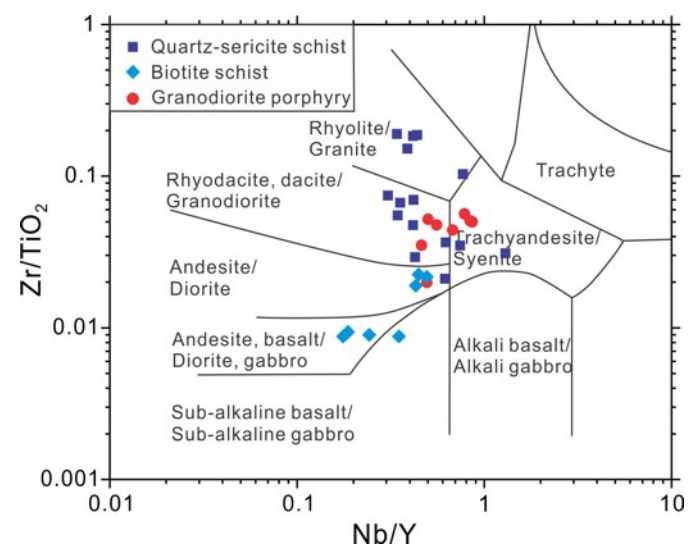


Figure 2.13. Zr/TiO₂-Nb/Y discrimination diagram (Winchester and Floyd, 1977) for the major lithologies from the Tongkuangyu district.

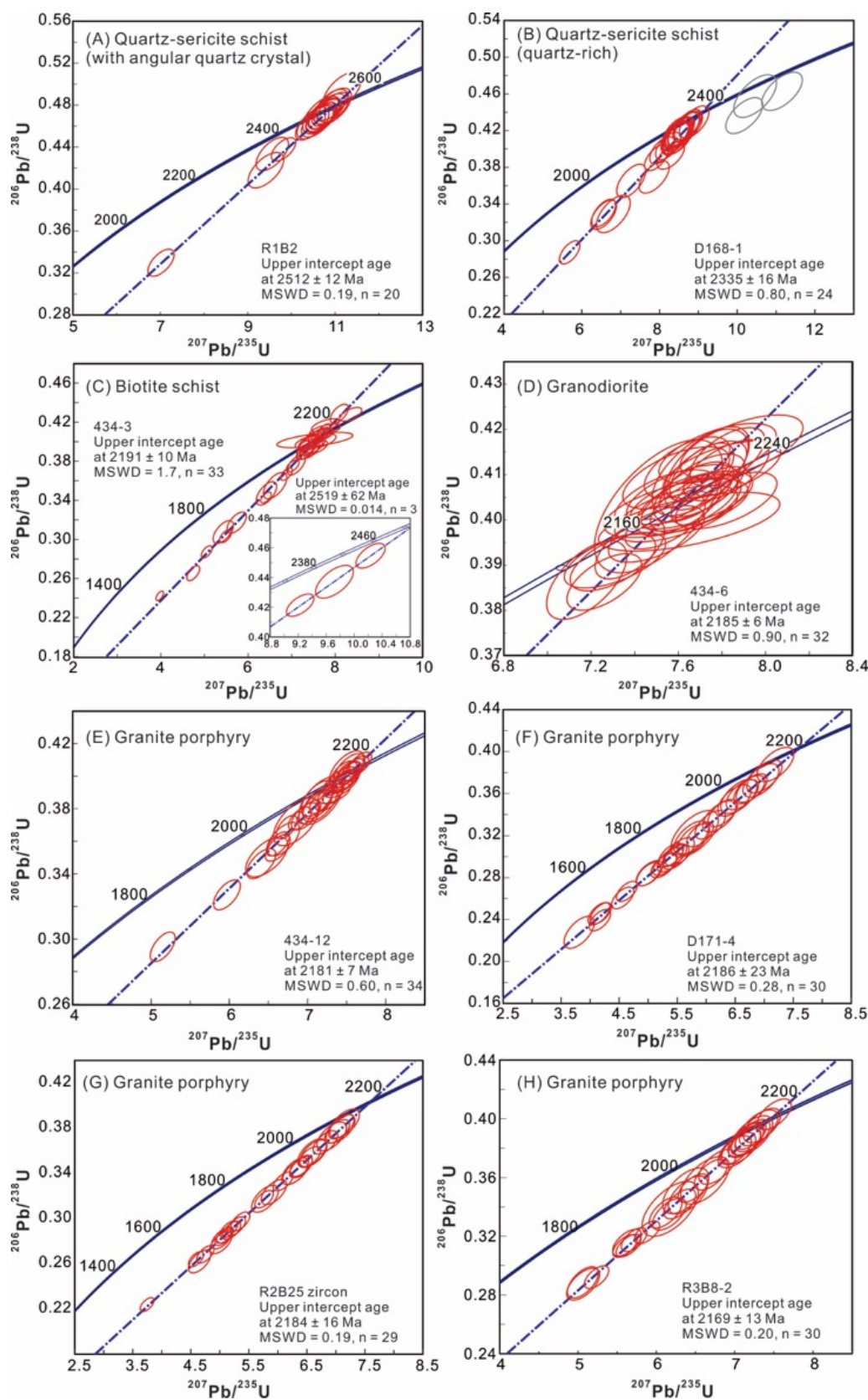


Figure 2.14. Zircon U-Pb concordia diagrams for the major rock phases from Tongkuangyu. Upper intercept ages define the crystallization ages of: (A) quartz-sericite schist (sample R1B2), (B) quartz-rich quartz-sericite schist (sample D168-1; grey error ellipses indicate analyses excluded from regression), (C) biotite schist (sample 434-3), and (D–H) granodiorite and granodiorite porphyry (samples 434-6, 434-12, D171-4, R2B25, and R3B8-2). Cathodoluminescence images for these zircon grains are shown in [Fig. A2.4](#). See [Table A2.2](#) for sample locations and descriptions.

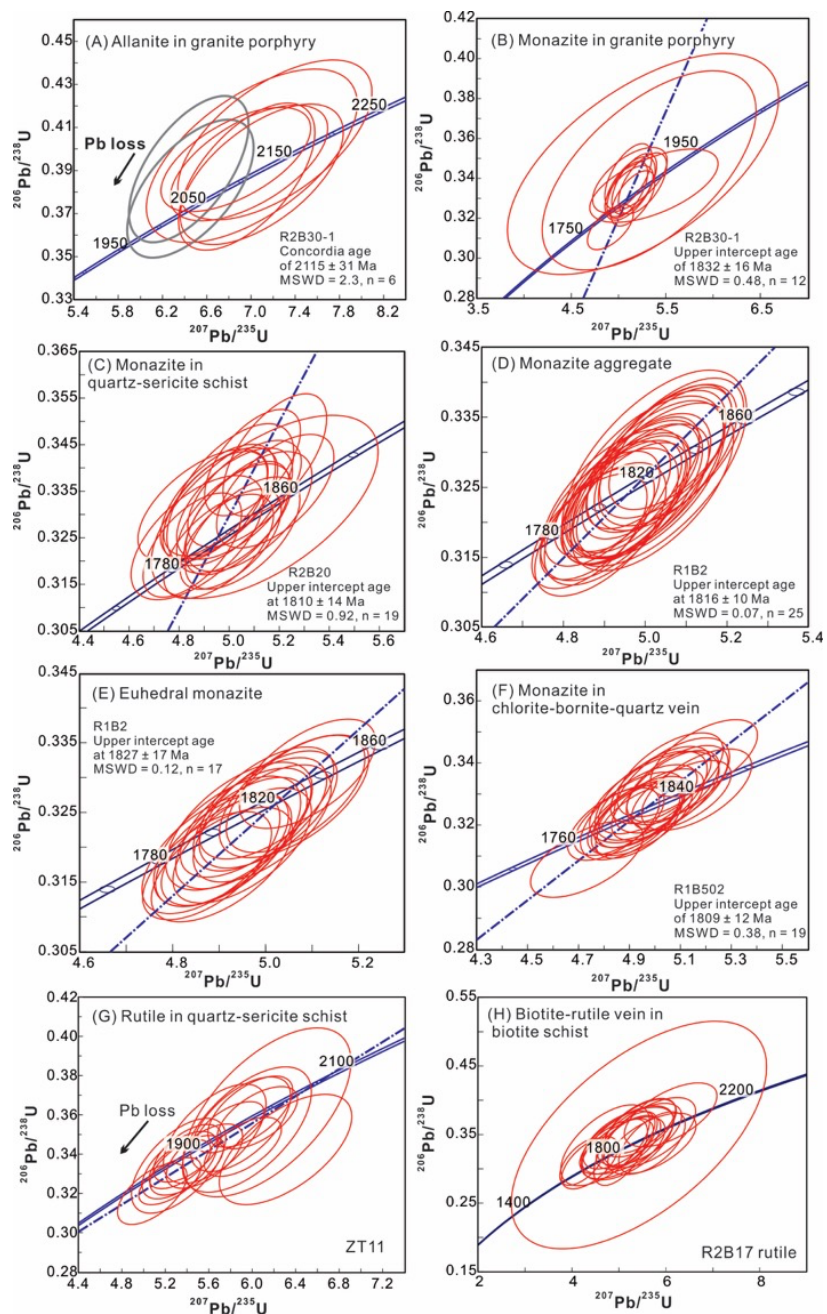


Figure 2.15. U-Pb concordia diagrams for hydrothermal allanite, monazite, and rutile samples from Tongkuangyu. (A) Allanite in sample R2B30-1; two analyses excluded from the concordia age determination are indicated in grey ellipses (Pb-loss). (B) Monazite in sample R2B30-1. (C) Monazite in sample R2B20. (D–E) Monazite in sample R1B2. (F) Monazite in sample R1B502. (G) Rutile in sample ZT11. (H) Rutile in sample R2B17. No ages could be determined for rutile due to apparent isotopic disturbance. See [Table A2.2](#) for sample locations and descriptions.

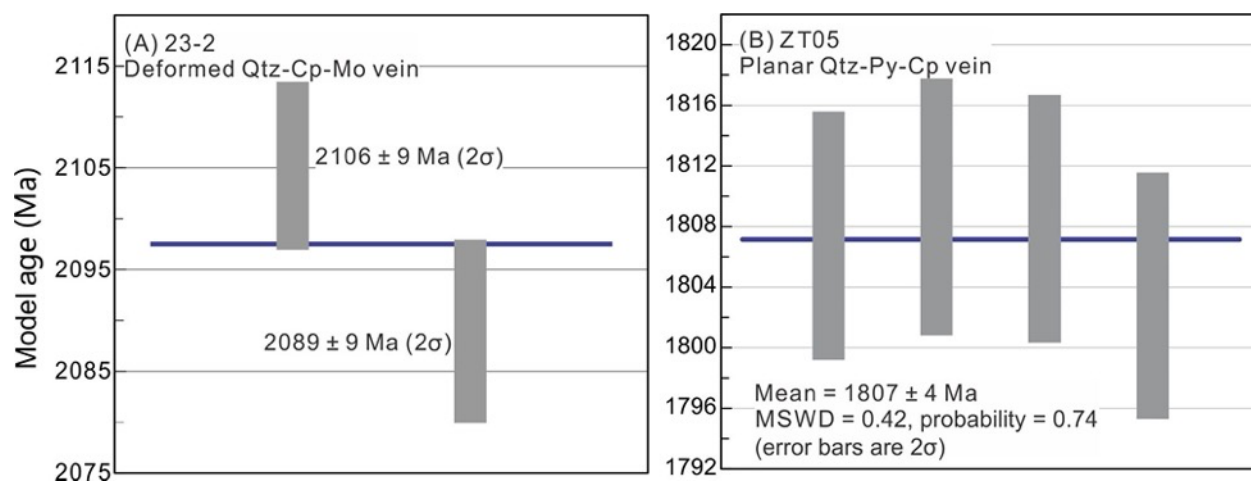


Figure 2.16. Re-Os model ages for (A) molybdenite from a deformed quartz - chalcopyrite - molybdenite vein (sample 23-2), and (B) pyrite from an undeformed quartz-pyrite-chalcopyrite vein (sample ZT05). Abbreviations: Cp = chalcopyrite, Mo = molybdenite, Py = pyrite, Qtz = quartz. See [Table A2.2](#) for sample locations and descriptions.

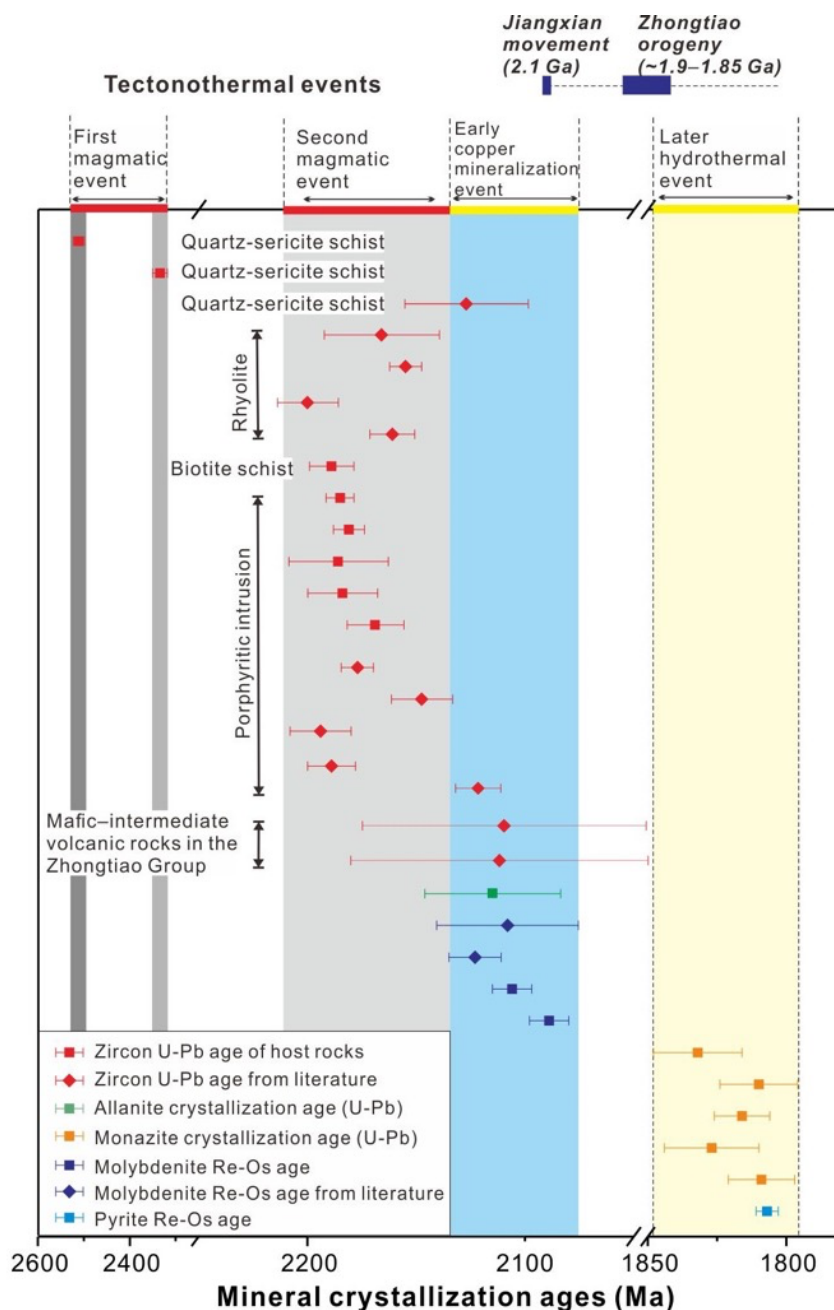


Figure 2.17. Temporal relationships between tectonothermal events, magmatism, and two stages of hydrothermal alteration and mineralization in the Tongkuangyu district. Dating results are compiled from the literature and this study (Table 2.1). The horizontal bars indicate standard errors (2σ ; Tables 2.1–2.2). Significant tectonothermal events are highlighted (Sun et al., 1991).

2.15 Tables

Table 2.1 Summary of new and published geochronological results for volcanic and intrusive rocks and mineralization from the Tongkuangyu district

Sample No.	Host rock	UTM (49S) and elevation	Mineral	Method	Age (Ma)	Reference
Rock type in the Tongkuangyu district						
R1B2	Quartz-sericite schist	560533, 3913894, 564 m	Zircon ¹	LA	2512 ± 12 (2σ, n = 20, MSWD = 0.19)	This study
D168-1	Quartz-sericite schist	561806, 3914335, 1051 m	Zircon ¹	LA	2335 ± 16 (2σ, n = 24, MSWD = 0.80)	This study
ZT37-3	Quartz-sericite schist	561582, 3913113, 873 m	Zircon	SIMS	2129 ± 28 (2σ, n = 18, MSWD = 0.66)	Recalculate data from Yang et al. (2015)
ZT7002	Rhyolite tuff	Not reported	Zircon	TIMS/SIMS	2166 ± 26 / 2155 ± 6	Sun et al. (1991)
ZG5002	Rhyolite tuff	Not reported	Zircon	SIMS	2188 ± 83 (2σ, n = 11, MSWD = 0.45)	Recalculate data from Sun and Hu (1993)
TKY-N2	Rhyolite tuff	Not reported	Zircon	LA	2200 ± 14 (2σ, n = 16, MSWD = 0.28)	Recalculate data from Zhang (2012)
TKY-PM-B7	Rhyolite	561273, 3913299, 913 m	Zircon	LA	2156 ± 10 (2σ, n = 19, MSWD = 0.08)	Recalculate data from Zhang (2012)
434-3	Biotite schist	560622, 3914045, 434 m	Zircon ²	LA	2191 ± 10 (2σ, n = 33, MSWD = 1.7)	This study
434-6	Granodiorite	560598, 3914065, 434 m	Zircon ²	LA	2185 ± 6 (2σ, n = 33, MSWD = 0.90)	This study
434-12	Granodiorite porphyry	560570, 3914088, 434 m	Zircon ²	LA	2181 ± 7 (2σ, n = 34, MSWD = 0.60)	This study
D171-4	Granodiorite porphyry	561759, 3913536, 973 m	Zircon ¹	LA	2186 ± 23 (2σ, n = 30, MSWD = 0.28)	This study
R2B25	Granodiorite porphyry	560189, 3914089, 530 m	Zircon ¹	LA	2184 ± 16 (2σ, n = 22, MSWD = 0.19)	This study
R3B8-2	Granodiorite porphyry	560231, 3914105, 564 m	Zircon ¹	LA	2169 ± 13 (2σ, n = 30, MSWD = 0.30)	This study
13TK01/55/97	Monzonite porphyry	Not reported	Zircon	SIMS	2177 ± 7 (2σ, n = 74, MSWD = 6.6)	Liu et al. (2016b)
TKY-1	Granodiorite porphyry	Not reported	Zircon	LA	2141 ± 14 (2σ, n = 19, MSWD = 0.63)	Recalculate data from Xu et al. (2012)
TKY-2-N1	Granodiorite porphyry	Not reported	Zircon	LA	2195 ± 14 (2σ, n = 20, MSWD = 0.03)	Recalculate data from Zhang (2012)
ZT36-1	Quartz porphyry	560912, 3913737, 962 m	Zircon	SIMS	2191 ± 11 (2σ, n = 17, MSWD = 1.02)	Recalculate data from Yang et al. (2015)
BF6	Quartz monzonite porphyry	Not reported	Zircon	LA	2121 ± 10 (2σ, n = 36, MSWD = 1.3)	Li et al. (2013)
Mafic to intermediate volcanic rocks in the Zhongtiao Group						
ZC126	Dacitic tuff	Not reported	Zircon	TIMS	2096 ± 65 (2σ, n = 4, MSWD = 0.91)	Recalculate data from Sun and Hu (1993)
13ZT67	Plagioclase amphibole	549628, 3898301, 783 m	Zircon	SIMS	2086 ± 68 (2σ, n = 18, MSWD = 16)	Liu et al., 2015

Table 2.1 (Cont.) Summary of new and published geochronological results for volcanic and intrusive rocks and mineralization from the Tongkuangyu district

Sample No.	Host rock	UTM (49S) and elevation	Mineral	Method	Age (Ma)	Reference
Mineralization						
R2B30-1	Granodiorite porphyry	560133, 3914132, 530 m	Allanite ³	LA	2115 ± 31 (2σ, n = 6, MSWD = 2.3)	This study
S528/S602/87-0-5147	Porphyry and quartz-sericite schist	Not reported	Molybdenite	Re-Os	2108 ± 32 (2σ, n = 6, isochron)	Chen and Li (1998)
13TK94	Quartz-sericite schist	Not reported			2122 ± 12 Ma (2σ, n = 6, MSWD = 0.58)	Liu et al. (2016a)
23-2A/B	Quartz-sulfide vein	560584, 3913925, 564 m	Molybdenite ⁴	Re-Os	2106 ± 9 Ma (2σ) / 2089 ± 9 Ma (2σ)	This study
R2B30-1	Granodiorite porphyry	560133, 3914132, 530 m	Monazite ³	LA	1832 ± 16 (2σ, n = 12, MSWD = 0.48)	This study
R2B20	Quartz-sericite schist	560209, 3914071, 530 m	Monazite ³	LA	1810 ± 14 (2σ, n = 19, MSWD = 0.92)	This study
R1B2	Quartz-sericite schist	560533, 3913894, 564 m	Monazite ¹	LA	1816 ± 10 (2σ, n = 25, MSWD = 0.07)	This study
R1B2	Quartz-sericite schist	560533, 3913894, 564 m	Monazite ¹	LA	1827 ± 17 (2σ, n = 17, MSWD = 0.12)	This study
R1B502	Chlorite-bornite-quartz vein	560544, 3913884, 564 m	Monazite ³	LA	1809 ± 12 (2σ, n = 19, MSWD = 0.38)	This study
ZT11	Quartz-sericite schist	560110, 3914136, 530 m	Rutile ¹	LA	2.1–1.8 Ga	This study
R2B17	Biotite schist	560244, 3914048, 530 m	Rutile ³	LA	2.1–1.8 Ga	This study
ZT05	Quartz-sulfide vein	560302, 3913994, 530 m	Pyrite ⁴	Re-Os	1807 ± 4 (2σ, n = 4, MSWD = 0.42)	This study

Notes: Published data were screened using the following criteria: isotopic systems sensitive to metamorphism or hydrothermal remobilization (e.g., Rb-Sr, K-Ar) were excluded; data contradicting geological evidence and without reasonable explanations were excluded. Abbreviations: LA = laser ablation inductively coupled plasma mass spectrometry, TIMS = thermal ionization mass spectrometry, SIMS = secondary-ion-mass spectrometry; MSWD = Mean squares of weighted deviates. For results from this study, the superscripts against the mineral names indicate the laboratory where the analysis was conducted: 1 = Radiogenic Isotope Facility, University of Alberta; 2 = Mineral Exploration Research Centre – Isotope Geochemistry Lab, Laurentian University; 3 = Central Analytical Facility, Laurentian University; 4 = Crustal Re-Os Geochronology Laboratory, University of Alberta.

Table 2.2 Re-Os dates of molybdenite and pyrite from Tongkuangyu

Fraction No.	Description	UTM (49S) and elevation	Re (ppm for Mo / ppb for py)	$\pm 2\sigma$	^{187}Re (ppm for Mo / ppb for py)	$\pm 2\sigma$	^{187}Os (ppb)	$\pm 2\sigma$	Common Os (pg)	Model age (Ma)	$\pm 2\sigma$ with λ (Ma)
23-2-A	Deformed Qtz-Cp-Mo vein that crosscut the chlorite-altered quartz-sericite schist	560584, 3913925, 564 m	286.4	0.8	180	0.5	6427	5	2.2	2106	9
23-2-B	Qtz-Py-Cp crosscut	560302, 3913994, 530 m	216	0.6	135.7	0.4	4807	3	0.9	2089	9
ZT05-A	Qtz-Py-Cp crosscut	560302, 3913994, 530 m	28.85	0.09	18.13	0.05	0.5543	0.0008	0.2	1807.4	8.2
ZT05-B	biotite-altered quartz-sericite schist		27.38	0.08	17.21	0.05	0.5267	0.0011	1.3	1809.5	8.7
ZT05-C			29.96	0.09	18.83	0.05	0.5759	0.0008	0.4	1808.5	8.2
ZT05-D			28.04	0.08	17.63	0.05	0.5376	0.0008	1.3	1803.4	8.1

Note: See sample locations in [Table A2.2](#). Abbreviations: Cp = chalcopyrite, Mo = molybdenite, Py = pyrite, Qtz = quartz.

Chapter 3

Uncovering the missing magmatic link for the Tongkuangyu porphyry Cu deposit, Trans-North China Orogen: Implication for porphyry Cu-deposit model and exploration

3.1 Abstract

The Tongkuangyu porphyry Cu deposit in the northern Zhongtiaoshan region of the Trans-North China Orogen formed at ~2.1 Ga and is much younger than its host ~2.18 Ga porphyritic host rocks that cut basaltic-andesitic sill and rhyolitic tuff of the Jiangxian Group. However, the extent and absolute timing of the syn-mineralization magmatism in the northern Zhongtiaoshan region remains poorly constrained which renders identifying the source of the cupriferous magmatic-hydrothermal fluids for Tongkuangyu difficult.

To resolve this issue, we dated zircon from representative samples from the volcano-plutonic sequences reported to contain poorly constrained ~2.1 Ga igneous rocks using laser ablation multi-collector inductively coupled plasma mass spectrometry. Rhyolitic tuff from the Jiangxian Group, granodiorite from the deepest limit of the mineralized host rocks at Tongkuangyu, and samples from an interpreted basaltic-andesitic tuff sequence in the overlying Zhongtiao Group were collected. The rhyolitic tuff yielded an upper concordia intercept age of 2188 ± 12 Ma (2σ , mean square of weighted deviates [MSWD] = 0.24). Three granodiorite samples yielded upper intercept ages of 2166–2177 Ma. These results do not support the presence of ~2.1 Ga magmatism in the Jiangxian Group and the Tongkuangyu deposit area.

In contrast, two albite-chlorite-sericite schist samples, which are interpreted as basaltic-andesitic tuffs, yielded upper concordia intercept and concordia ages of 2088 ± 16 Ma (2σ , MSWD =

0.05) and 2085 ± 11 Ma (2σ , MSWD = 0.26), which agree within uncertainty to the known age for the porphyry Cu mineralization. Furthermore, a large proportion of ~ 2.18 Ga zircon xenocrysts from the analyzed basaltic- to andesitic tuff samples yielded distinguishable $\epsilon_{\text{Hf}}(t)$ values of 1.3 ± 0.8 (2σ) compared to the ~ 2.09 Ga zircons (5.6 ± 0.6 ; 2σ), but are consistent with the published $\epsilon_{\text{Hf}}(t)$ values for the granodiorite host at Tongkuangyu. These results suggest the ~ 2.09 Ga magmas which fed the volcanic sequence were contaminated by the older regional ~ 2.18 Ga igneous wall rock material.

We interpret the results to indicate the presence of a presently unexposed ~ 2.09 Ga causative magma chamber which exsolved hydrothermal fluids to form the Tongkuangyu deposit. Except for the age discordance between the host rocks and mineralization, Tongkuangyu is comparable in other respects (e.g., vein and stockwork mineralization, alteration) to most Phanerozoic porphyry Cu deposits globally. These results therefore suggest that consolidated but structurally receptive (i.e., permeable) porphyritic and equigranular rocks can trap magmatic-hydrothermal fluids to form porphyry-type alteration and Cu mineralization, which is significant in the context of exploration for such mineralization.

3.2 Introduction

Porphyry Cu \pm Mo \pm Au deposits (hereafter simply porphyry Cu deposits) are commonly in spatial and temporal association with intermediate- to felsic subvolcanic dikes or stocks (at depth of ~ 2 to 5 km) sourced from underlying causative magma chambers (~ 10 km) preferentially formed under transpressional environments in Phanerozoic arc-related settings (Seedorff et al., 2005; Sillitoe, 2010; Richards, 2011). The current consensus is that in such deposits, causative magma chambers exsolve metal-charged hydrothermal fluids which ascend to shallower depths

where, owing to decreasing pressure and temperature (e.g., [Weiss et al. 2012](#); [Hurtig and Williams-Jones, 2015](#)), sulfides precipitate in the earlier formed shallow derivative porphyritic stocks or dikes ([Lowell and Guilbert, 1970](#); [Gustafson and Hunt, 1975](#); [Hedenquist and Lowenstern, 1994](#)). This model accommodates the contemporaneity of magmatic and hydrothermal events well documented in many porphyry Cu deposits.

The Tongkuangyu porphyry Cu deposit contains measured and indicated resources, including past production, of 453 million tonnes grading at 0.61 wt. % Cu, as well as minor Mo and Au ([Zhongtiao Nonferrous Metals Group Co., Ltd., internal report, 2015](#)). It is hosted by ~2.18 Ga granodiorite porphyry and granodiorite and ~2.5–2.2 Ga basaltic- to rhyolitic volcanic or subvolcanic rocks in the northern Zhongtiaoshan region of the Trans-North China Orogen. Of particular note is that earlier work ([Meng et al., 2020](#)) has shown that the porphyry-type disseminated- and veinlet-style mineralization associated with biotite ± K-feldspar alteration is constrained to postdate the host porphyritic rocks by ~80 million years. Thus, its formation is argued to postdate the consolidation of the ~2.18 Ga granodioritic host intrusive complex and instead is genetically related to poorly constrained ~2.1 Ga magmatism in the northern Zhongtiaoshan region ([Meng et al., 2020](#)).

This study aims to refine the extent and absolute timing of the ~2.1 Ga magmatism in the northern Zhongtiaoshan region and explore the plausible controls on the Tongkuangyu mineralization. Data presented here is interpreted to strongly support a ~2.1 Ga, spatially-related basaltic-andesitic volcanic sequence that represents the surface expression of a magma chamber that is temporally related to the exsolved magmatic-hydrothermal metalliferous fluids which formed the Tongkuangyu deposit. Considering the similarity of the geological features of Tongkuangyu, as explored below and discussed in [Meng et al. \(2020\)](#), to many other porphyry

Cu deposits worldwide (e.g., veins, alteration, mineralization), this conclusion is important in two regards: (1) pre-existing, genetically unrelated host rocks can be receptive to mineralizing fluids as long as they are structurally prepared (i.e., permeable) and reactive, such as Fe-rich basic rocks at Tongkuangyu; and (2) the presence of volcanic rocks without a known progenitor can indicate potential porphyry Cu deposits in surrounding basement rocks. The latter point is particularly relevant in older terrains where, due to subsequent deformation, mineralization may be structurally detached from causative intrusions.

3.3 Geological Setting

The Tongkuangyu Cu deposit is situated within the northern Zhongtiaoshan region of the Trans-North China Orogen (Fig. 3.1A). The northern Zhongtiaoshan region consists mainly of Paleoproterozoic volcanic, sedimentary, and intrusive rocks which unconformably overlie and/or intrude the Neoproterozoic-Paleoproterozoic Sushui crystalline basement. The Paleoproterozoic volcano-sedimentary sequences are subdivided in ascending order into the Jiangxian, Zhongtiao, Danshanshi, and Xiyanghe Groups (Fig. 3.1B). The upper Jiangxian and Zhongtiao Groups are of significant interest here because they host the Tongkuangyu deposit and are reported to contain ~2.1 Ga volcanoplutonic sequences.

3.3.1 Stratigraphy

The Sushui complex consists of Neoproterozoic-Paleoproterozoic tonalite-trondhjemite granodiorite gneisses, granite, amphibolite, and mafic dikes. The rocks were variably deformed and metamorphosed to amphibolite facies and locally up to eclogite facies. Three episodes of

Paleoproterozoic granitoids (i.e., ~2.45 Ga, ~2.35 Ga, and ~1.95 Ga) were reported in the Sushui complex, but ~2.1 Ga magmatic rocks are not identified (Zhang et al., 2020).

The lower Jiangxian Group comprises lower amphibolite facies mudstone, sandstone, and volcanic rocks, including garnet-muscovite ± staurolite schists, biotite schist, and minor quartzite and quartz-sericite schist intercalated with amphibolite. The maximum age of the deposition of the clastic rocks from the lower Jiangxian Group is constrained to be ~2.16–2.29 Ga (Li et al., 2008).

The upper Jiangxian Group is composed of lower greenschist facies basaltic- to andesitic and rhyolitic volcanic or volcanoclastic rocks (metamorphosed to biotite schist, quartz-sericite schist, and minor quartz-chlorite schist) that formed mainly at ~2.2 Ga with some of the samples dated at ~2.5–2.3 Ga and were subsequently intruded by ~2.18 Ga granodiorite and granodiorite porphyry stocks that are the host for the Tongkuangyu deposit (Li et al., 2008; Xu et al., 2012; Liu et al., 2016a; Liu et al., 2016b; Meng et al., 2020). However, the chronological sequence of the rhyolitic volcanic or volcanoclastic rocks, which were deformed and metamorphosed to petrographically comparable quartz-sericite schists, remains poorly constrained. One sample of quartz-sericite schist from the upper Jiangxian Group was reported to yield an upper concordia intercept age of 2129 ± 28 Ma (2σ , $n = 18$, $MSWD = 0.66$; recalculated by Meng et al., 2020 from original data reported in Yang et al., 2015), indicating presence of a younger but poorly defined sequence.

The unconformably overlying Zhongtiao Group is composed of clastic and carbonate sedimentary rocks intercalated with a ~100-m-thick basaltic-andesitic volcanic sequence (Fig. 3.1B). These rocks were metamorphosed to upper greenschist facies and locally up to lower

amphibolite facies. The maximum depositional age of the Zhongtiao Group is constrained from two studies via laser ablation-inductively coupled plasma-mass spectrometry (LA-ICP-MS) U-Pb dating of detrital zircons separated from clastic rocks in the lower part of this Group: (1) [Liu et al. \(2012\)](#) constrain a sericitic quartzite sample to 2168 ± 5 Ma based on the weighted mean $^{207}\text{Pb}/^{206}\text{Pb}$ ages for the three youngest zircons (2σ , $n = 3$, $\text{MSWD} = 0.86$); and (2) [Li et al. \(2011\)](#) provide a concordant $^{207}\text{Pb}/^{206}\text{Pb}$ date of 2132 ± 34 Ma (2σ) for a sample of feldspathic quartzite. [Yang et al. \(2018\)](#) recently dated a feldspar porphyry sample (sample ZT91-1; [Fig. 3.1B](#)) from an interpreted felsic volcanic sequence which was reported to be at the bottom of the Bizigou Formation (upper part of the Zhongtiao Group). However, the marked sampling location, if correct, fall within what we interpret to be the lower part of the Zhongtiao Group versus the Bizigou Formation ([Fig. 3.1B](#)). After excluding nine concordant analyses with $^{207}\text{Pb}/^{206}\text{Pb}$ dates of $\sim 2.7\text{--}2.3$ Ga (interpreted as xenocrysts; [Table A3.1](#), [Fig. A3.1](#)), our recalculation of the other 15 analyses yielded an upper concordia intercept age of 2137 ± 16 Ma (2σ , $n = 15$, $\text{MSWD} = 0.70$; [Fig. A3.1B](#)), of which 13 concordant analyses yielded a concordia age of 2140 ± 9 Ma (2σ , $n = 13$, $\text{MSWD} = 0.44$; [Fig. A3.1B](#)), consistent with the weighted mean $^{207}\text{Pb}/^{206}\text{Pb}$ age of 2139 ± 10 Ma (2σ , $n = 13$, $\text{MSWD} = 0.73$) as reported in [Yang et al. \(2018\)](#). These results are interpreted to constrain the maximum depositional age of the lower Zhongtiao Group to $\sim 2.17\text{--}2.14$ Ga.

The Bizigou and Yuyuanxia formations constitute the upper part of the Zhongtiao Group ([Fig. 3.1B](#)). The Bizigou Formation is composed of meta-mudstone and shale, with the $\sim 100\text{-m}$ -thick meta-volcanic sequence at the bottom. The meta-volcanic sequence consists of albite-sericite-chlorite schists which we interpreted here to be basaltic-andesitic volcanic or volcanoclastic rocks that are temporally related to the porphyry Cu mineralization at Tongkuangyu. The Yuyuanxia

Formation comprises mainly dolomitic marble lacking any volcanic sequence. The two Formations and their contacts are host to several medium-size sediment-hosted stratiform Cu deposits (Geological Group, 1978), such as the Bizigou, Tongmugou, Laobaotan, and Hujiayu (Fig. 3.1B).

Unconformably overlying the Zhongtiao Group is the Danshanshi Group which consists of conglomerate and sandstone deposited at ~ 1.85 Ga (Liu et al., 2012). The unconformably overlying Xiyanghe Group unconformably overlies the Danshanshi Group is composed of unmetamorphosed bimodal volcanic rocks erupted between ~ 1.81 Ga and 1.75 Ga (Sun and Hu, 1993; Zhao et al., 2004).

3.3.2 The Tongkuangyu porphyry Cu deposit

The Tongkuangyu deposit is hosted mainly by ~ 2.18 – 2.16 Ga granodiorite porphyry and granodiorite which intrude biotite schist and quartz-sericite schist of the upper Jiangxian Group (Figs. 3.2, 3.3). The biotite schist and quartz sericite schist are interpreted to be basaltic-andesitic volcanic or subvolcanic rocks and clast-rich tuffaceous rocks formed at ~ 2.19 Ga and ~ 2.5 – 2.3 Ga, respectively (Figs. 3.2, 3.3; Meng et al., 2020). Disseminated and veinlet chalcopyrite \pm pyrite \pm magnetite are associated with biotite (\pm K-feldspar) alteration that overprints an earlier albite alteration (Fig. 3.3A–C). The key features of the host rocks, alteration, and mineralization previously reported in Meng et al. (2020) are summarized in Table 3.1. The absolute timing of the porphyry-type biotite (\pm K-feldspar) alteration and Cu mineralization is constrained by Meng et al. (2020) to 2115 ± 31 Ma (2σ , $n = 6$, MSWD = 2.3; sample R2B30-1) based on LA-ICP-MS U-Pb dating of allanite and 2106 ± 9 Ma and 2089 ± 9 Ma (2σ ; sample 23-2) based on Re-Os dating of molybdenite. As Meng et al. (2020) noted, these ages are significantly younger than

previously published zircon U-Pb ages for the host granodiorite porphyry and granodiorite stocks, which precludes these intrusions being the causative magmas for Tongkuangyu mineralization.

The porphyry-type chalcopyrite \pm pyrite veins (locally with albite selvage) and disseminations, which are the dominant forms of the Cu mineralization, were locally overprinted by chlorite alteration and are cut by undeformed quartz-pyrite-chalcopyrite \pm carbonate veins dated to \sim 1.8 Ga (Meng et al., 2020). The chlorite alteration and associated quartz-chlorite-bornite veins with minor chalcopyrite and magnetite formed coincident with the Zhongtiao orogeny at \sim 1.8 Ga, which was a period of final collision between east and west North China blocks.

3.4 Reported \sim 2.1 Ga magmatism in the northern Zhongtiaoshan region

All of the lithological sequences (except for the Xiyanghe Group) and related ore deposits located in the northern Zhongtiaoshan region are variably deformed and record lower greenschist to lower amphibolite facies regional metamorphism as a part of the \sim 1.8 Ga Zhongtiao orogeny (Geological Group, 1978; Sun and Hu, 1993; Mei, 1994; Meng et al., 2020). Thus, the primary mineralogy and textures of all of these rocks have been variably modified in addition to their likely dismemberment and subsequent erosion. These processes have collectively made it challenging to identify the \sim 2.1 Ga magmatic event that relates to the formation of the Tongkuangyu deposit.

Relevant in regard to plausible \sim 2.1 Ga magmatism are the reported LA-ICP-MS zircon U-Pb ages for samples of quartz-sericite schist (ZT37-3) and a quartz monzonite porphyry (BF6,

location not reported) from the northern Zhongtiaoshan region (Fig. 3.1B). The former, from the Jiangxian Group, was interpreted to be rhyolitic tuff and was dated at 2129 ± 28 Ma (2σ , $n = 18$, MSWD = 0.66; Li et al., 2013), whereas the latter yielded an age of 2121 ± 10 Ma (2σ , $n = 36$, MSWD = 1.3; Yang et al., 2015). Two issues are highlighted in regards to these data: (1) this volcano-plutonic complex is neither differentiated petrographically from its host, the Jiangxian Group and Tongkuangyu intrusive stocks; and (2) the results are inconsistent with the maximum depositional age of ~ 2.17 – 2.14 Ga for the overlying Zhongtiao Group, as noted previously.

Additional rocks reported to have formed at ~ 2.1 Ga include the ~ 100 -m-thick mafic- to intermediate volcanic sequence exposed at the bottom of the Bizigou Formation in the Zhongtiao Group (Sun and Hu, 1993). Field observations and petrographic examination of these exposures suggest the layers of these bedded volcanic deposits are metamorphosed and contain mafic or felsic phenocrysts and clasts (Fe-oxides, biotite \pm epidote, and plagioclase; Fig. A3.2). The matrices of samples from these volcanic layers are highly variable (Fig. A3.3) and, based on our petrographic observations, are composed of chlorite (~ 5 – 40 %), sericite (~ 20 – 70 %), albite (~ 2 – 25 %), Fe-Ti oxides (2 – 15 %), epidote (2 – 5 %), and quartz (~ 2 – 5 %). This large range in mineralogical proportions indicates a change in the local bulk composition which may reflect either or both of the effects of alteration or metamorphism of these rocks.

Zircon separates from a dacitic meta-tuff sample of the Bizigou Formation (ZC126) collected ~ 13 km southwest from Tongkuangyu (Fig. 3.1B) yielded an upper concordia intercept age of 2096 ± 65 Ma (2σ , MSWD = 0.91; TIMS, thermal ionization mass spectrometry) which included a concordia age of 2090 ± 20 Ma (2σ) for a single concordant zircon aliquot (Sun and Hu, 1993), as recalculated by Meng et al. (2020). This sample is interpreted based on its litho-geochemistry to be an andesitic tuff (Fig. 3.4). Liu et al. (2015) also reported an upper concordia intercept

zircon U-Pb age of 2086 ± 68 Ma (2σ , MSWD = 16) for a metavolcanic sample (i.e., plagioclase amphibolite), which was also reported to be collected from the mafic- to intermediate volcanic sequence at the bottom of the Bizigou Formation. Because these volcanic rocks overlie the upper Jiangxian Group and are therefore arguably younger, we suggest that this provides evidence for a ~ 2.1 Ga magmatic event in the Tongkuangyu area, but note that the zircon U-Pb ages have large uncertainties.

3.5 Samples

In contrast to the systematic collection and dating of samples from the different stratigraphic sequences in the Zhongtiaoshan region, as conducted by previous studies ([Sun et al., 1991](#); [Sun and Hu, 1993](#)), we targeted samples from the sequence that were reported to contain the poorly constrained ~ 2.1 Ga igneous rocks. Thus, the older rocks of the oldest Sushui plutonic complex, the schist and quartzite rocks of the lower Jiangxian Group, and younger sedimentary and volcanic rocks of the Danshanshi and Xiyanghe Groups, which were less likely to host ~ 2.1 Ga magmatic events, were not the focus of this study. Samples collected for further detailed investigation included: (1) one sample of quartz-sericite schist (rhyolitic meta-tuff) from the upper Jiangxian Group; (2) three samples of granodiorite from the deepest extent of the mineralized stocks exposed by drilling and an underground tunneling project in 2019; and (3) two samples of albite-chlorite-sericite schist (basaltic-andesitic meta-tuff) from the bottom of the Bizigou Formation. Sample locations and descriptions are listed in [Table 3.2](#).

Zircon grains for dating were separated using traditional magnetic and density methods. Clean grains were hand-picked and mounted in epoxy resin, which were subsequently polished to expose their mid-sections. The mounted zircons were imaged in backscattered electron (BSE)

and cathodoluminescence (CL) modes to characterize their internal structures using a Tescan Vega 3 scanning electron microscope (SEM) at the Mineral Exploration Research Centre Isotope Geochemistry Laboratory (MERC-IGL), Laurentian University, Sudbury, Ontario. Zircon grains devoid of mineral and melt inclusions and fractures chosen for analyses varied in size with those from samples R4B07, 5159-1, 5S342-2, and Z30 $>100\ \mu\text{m}$, whereas for samples 19V05 and 19V08 were $\leq 60\ \mu\text{m}$ (Fig. A3.4). For one sample of albite-sericite-chlorite schist (interpreted here to be basaltic-andesitic tuff at $\sim 2.09\ \text{Ga}$), the Lu-Hf isotopes for the zircon separates were determined. Whole-rock geochemistry for four albite-sericite-chlorite schist samples collected in different locations were also analyzed.

3.6 Analytical methods

3.6.1 Whole-rock geochemistry

Four samples of albite-chlorite-sericite schist from the bottom of the Bizigou Formation were crushed and powdered and then analyzed using X-ray fluorescence (XRF) and ICP-MS with pre-fusion by lithium metaborate (following the analytical package CCP-PKG03) at the Australian Laboratory Services (ALS), Vancouver, Canada. The results are reported in Table A3.2.

3.6.2 Zircon U-Pb isotopic analyses

Zircon U-Pb isotopes were analyzed using a 193 nm Photon Machines Analyte G2 laser coupled with a Thermo Neptune Plus MC (multi-collector)-ICP-MS at MERC-IGL, Laurentian University. Detailed instrumental parameters can be seen in Table A3.3. The laser ablation spot size was $35\ \mu\text{m}$, the repetition rate was 7 Hz, and the fluence was $2\ \text{J}/\text{m}^2$. The raw data of

unknowns were normalized to the primary reference material (OG1) which was periodically dispersed (three analyses at the beginning and end, and one analysis between every ten unknown analyses) into the whole analytical session. Secondary reference materials (TanBrA and Grn) were analyzed during the analytical session to monitor the accuracy of the U-Pb isotope ratios. The U-Pb geochronology data reduction scheme in the Iolite software was used for baseline subtraction, instrumental drift, and downhole fractionation corrections. The results of secondary reference material are consistent with the published standard values (Table A3.3).

3.6.3 Zircon Lu-Hf isotopic analyses

The Lu-Hf isotopes of previously dated zircon grains from sample 19V05 (sericite-chlorite schist) were measured using a 193 nm Photon Machines Analyte G2 laser coupled with a Neptune Plus MC-ICP-MS at MERC-IGL, Laurentian University. Instrumental parameters are provided in Table A3.3. The spot size for the laser ablation was 40 μm , the repetition rate was 7 Hz, and the fluence was 6 J/m^2 . The raw Hf isotope data was processed using a modified version of the Hf isotope data reduction scheme in Iolite v. 3.6, with baseline subtraction, instrumental drift, and mass bias corrections. To minimize potential fractionation effects on the data reduction, the 3 second interval in the beginning and 1–2 second interval at the end of the ablation period was excluded. Isotope ratios were normalized to primary zircon reference material Plesovice which was analyzed three times at the beginning and end of the session and periodically dispersed (every ten unknowns) throughout the session. Five secondary reference materials (FC1, MUN1, MUN3, R33, and 91500) were analyzed to monitor the accuracy of the isotope ratios, and the results are consistent with the standard values (Table A3.3). Single-stage Hf model ages and $\varepsilon_{\text{Hf}}(t)$ values were calculated using a ^{176}Lu decay constant of $1.867 \times 10^{-11}/\text{a}$ (Söderlund et al., 2004) and the chondritic parameters from Bouvier et al. (2008).

3.7 Results

3.7.1 Whole-rock geochemistry

Whole-rock major and trace element compositions of the four albite-chlorite-sericite schist samples are listed in [Table A3.2](#). The samples have low- to moderate loss-on-ignition (LOI) values (1.85 to 3.80 wt. %) and a relatively homogeneous composition with SiO₂ content of 49–55 wt. % on a normalized anhydrous basis. Plotting of data on the immobile element-ratio diagram (Zr/TiO₂ versus Nb/Y) suggests the protoliths were volcanic tuffs of basaltic- to andesitic composition ([Fig. 3.4](#)). On a primitive mantle-normalized trace-element diagram ([Fig. 3.5A](#)), the samples display enrichment in large ion lithophile elements (e.g., Rb, Th, U, and K) and depletion in Nb and Ta. The negative Sr and weak negative Eu anomalies are consistent with plagioclase fractionation during magma evolution. On the chondrite-normalized rare earth element (REE) diagram ([Fig. 3.5B](#)), these samples exhibit a flat- to listric-shaped pattern, enrichment of light REE (LREE) relative to the middle and heavy REE (MREE and HREE) with (La/Yb)_N ratio ranging from 4.8 to 6.7. These patterns are consistent with amphibole fractionation and also typical of Phanerozoic hydrous arc magmas hosting PCDs (e.g., [Richards et al., 2003](#)) and are comparable to the ~2.18 Ga rhyolitic tuff in the northern Zhongtiaoshan region except for slightly positive Ti anomaly and different slope of the REE pattern ([Fig. 3.5](#)).

3.7.2 Zircon U-Pb geochronology

The zircon U-Pb dating results are summarized in [Table 3.2](#) and illustrated in [Figure 3.6](#), with complete analytical data provided in [Table A3.4](#). The analyzed zircon grains have oscillatory/sector zonings and Th/U ratios of >0.3, supporting a magmatic origin ([Hoskin and](#)

[Schaltegger, 2003](#)). Most of the analyses for each sample define a slightly discordant linear array, suggesting minor Pb-loss or slight variation in downhole fractionation of the Pb/U ratio relative to the primary reference material (OG1). Thus, in most cases the upper concordia intercept age was used to define the timing of zircon crystallization. In cases where the analyses are largely concordant, a concordia age was calculated. The Wetherill concordia diagrams along with intercept or concordia ages, uncertainties, and related MSWD values, were calculated using Isoplot version 4.15 ([Ludwig, 2012](#)). Uranium decay constant uncertainties were considered in the calculations. The results are reported at 2σ uncertainties.

Zircon for the rhyolitic meta-tuff sample from the upper Jiangxian Group (sample R4B07) yielded an upper concordia intercept age of 2188 ± 12 Ma (2σ , $n = 30$, MSWD = 0.24; [Fig. 3.6A](#)). If excluding two concordant analyses with older $^{207}\text{Pb}/^{206}\text{Pb}$ dates (2215–2222 Ma and interpreted as xenocrystic; [Table A3.4](#)), a similar upper concordia intercept age of 2184 ± 11 Ma (2σ , $n = 28$, MSWD = 0.09; [Fig. 3.6A](#)) is obtained. The tight clustering of the data, in addition to their oscillatory and sector CL ([Fig. A3.4](#)), supports a magmatic origin, hence these results are interpreted to indicate the volcanic rock was deposited at ~ 2.18 Ga.

The three granodiorite samples yielded similar ages within uncertainty, which are summarized as follows: (1) sample 5159-1 yielded an upper concordia intercept age of 2166 ± 17 Ma (2σ , $n = 12$, MSWD = 3.3; [Fig. 3.6B](#)); (2) sample 5S342-2 yielded an upper concordia intercept age of 2177 ± 13 Ma (2σ , $n = 30$, MSWD = 0.16; [Fig. 3.6C](#)); and (3) sample Z30 yielded an upper concordia intercept age of 2176 ± 11 Ma (2σ , $n = 30$, MSWD = 0.19; [Fig. 3.6D](#)). These three dates overlap with uncertainty, and are consistent with previously published zircon U-Pb ages for granodiorite porphyry and granodiorite from Tongkuangyu at ~ 2.18 Ga ([Sun et al., 1991](#); [Liu et al., 2016a](#); [Liu et al., 2016b](#); [Meng et al., 2020](#)).

The two sericite-chlorite schist samples, interpreted to be basaltic-andesite tuffs, yielded two zircon age populations as indicated in Fig. 3.6E and F. For sample 19V05 (sericite-chlorite schist), if excluding two significantly discordant analyses (original data provided in Table A3.4 but not illustrated in the Fig. 3.6E), 25 of the 34 analyses yielded an upper intercept age of 2172 ± 9 Ma (2σ , $n = 25$, MSWD = 1.5; Fig. 3.6E), whereas the other nine analyses yielded a younger upper concordia intercept age of 2088 ± 16 Ma (2σ , $n = 9$, MSWD = 0.05; Fig. 3.6E). For the sample 19V08 (albite-sericite-chlorite), 18 analyses yielded an older upper concordia intercept age of 2175 ± 9 Ma (2σ , $n = 18$, MSWD = 0.13; Fig. 3.6F). If excluding two discordant analyses (i.e., one analysis with Pb loss and one reversely discordant analysis), the remaining 16 analyses yielded a concordia age of 2171 ± 6 Ma (2σ , $n = 16$, MSWD = 0.45; Fig. 3.6F). The remaining data define a second cluster of four concordant analyses with a younger concordia age of 2085 ± 11 Ma (2σ , $n = 4$, MSWD = 0.26; Fig. 3.6F). These results are interpreted to indicate an age of ~ 2.09 Ga for emplacement of the volcanic rocks. The older zircon ages of ~ 2.17 – 2.18 Ga, which reflect inheritance of xenocrystic grains from wall rocks to the magma chamber or during ascent of the magma, are of similar age to the above dated rhyolitic tuff and granodiorite samples.

3.7.3 Zircon Lu-Hf isotopes

Zircon Lu-Hf isotope data for sample 19V05, the interpreted basaltic-andesitic tuff, are provided in Table A3.5. Seven analyses of the ~ 2.09 Ga zircon population yielded $\epsilon_{\text{Hf}}(t)$ values ranging from 5.0 to 5.9 (5.6 ± 0.6 , 2σ , $n = 7$), with two analyses yielding lower values of 2.3 and 4.0. In contrast, the ~ 2.17 – 2.18 Ga zircon population yielded lower $\epsilon_{\text{Hf}}(t)$ values from 1.0 to 2.3 (1.3 ± 0.8 on average; 2σ , $n = 10$). The distinctly different isotopic values for the two zircon age groups indicate: (1) both of them have retained the primary isotopic composition; and (2) the signatures

of the younger zircons indicate a more juvenile melt source compared to magmas from which the older xenocrystic zircons crystallized.

3.8 Discussion

The age results are discussed from oldest to youngest below and integrated with the other geochemical and isotopic data presented, in addition to the earlier work on the Tongkuangyu deposit (Meng et al., 2020).

3.8.1 Absence of ~2.1 Ga magmatic rocks in the Jiangxian Group and Tongkuangyu

The single rhyolitic tuff sample from the Luotuofeng Formation of the upper Jiangxian Group, collected 4 km northeast from the Tongkuangyu deposit, yielded a zircon U-Pb age of 2188 ± 12 Ma. The robustness of the data and the CL zoning, which is typical of that seen in magmatic zircon, strongly suggest these grains have retained their primary chemical features. Thus, the calculated age is interpreted to represent the timing of zircon crystallization and hence eruption of the felsic rocks. The results are comparable to the earlier published zircon U-Pb ages for other rhyolite samples from the upper Jiangxian Group in the northern Zhongtiaoshan region (Sun et al., 1991; Sun and Hu, 1993; Zhang, 2012). These ages are, however, much younger than the LA-ICP-MS zircon U-Pb ages of 2512 ± 12 Ma and 2335 ± 16 Ma for two samples analyzed by Meng et al. (2020) for this unit. These data collectively suggest that the upper Jiangxian Group has a more protracted age history, as concluded in Meng et al. (2020). An alternative interpretation of the younger age for the sample dated here is that it may in fact represent a fine-grained intrusive phase related to the granodiorite discussed next, but with a sericitic overprint. Additional work is required to resolve this issue.

The three granodiorite samples, which come from the deepest extent of the ore zone in the Tongkuangyu deposit at the time of sampling, yielded similar upper concordia intercept zircon U-Pb ages of 2177 ± 13 Ma, 2176 ± 11 Ma, and 2166 ± 17 Ma. These results constrain intrusion and solidification of the granodioritic magma to 2.18–2.16 Ga and are comparable to earlier published zircon U-Pb ages of ca. 2180 Ma for granodiorite and granodiorite porphyry samples collected from the shallower levels of the deposit (Table 3.1; Sun et al., 1991; Liu et al., 2016a; Liu et al., 2016b; Meng et al., 2020). These results suggest all of the dated samples come from the same coalesced intrusive body.

The age results for the above volcanic and intrusive units allow three conclusions to be made. Firstly, the similar ages suggest they may be temporal equivalents formed during a major magmatic event at that time, which is consistent with other age data from the region. Secondly, the results of the granodiorite testify to the absence of ~2.1 Ga intrusive phases at the deepest limit of the currently defined ore zones. Lastly, the new robust age data clearly do not verify the ~2.1 Ga magmatism previously reported in the Luotuofeng Formation and at Tongkuangyu (Li et al., 2013; Yang et al., 2015).

3.8.2 Verification of ~2.1 Ga magmatic events in the Zhongtiao Group

The zircons extracted from the two samples of basaltic-andesitic tuff in the overlying Zhongtiao Group yielded two similar age populations. The older zircons, assigned a xenocrystic origin, apparently dominated the zircon population recovered from both samples (43 of the total 56 grains analyzed, or 77% in proportion). The older age populations of 2172 ± 9 Ma and 2171 ± 6 Ma for the two zircon populations are similar to that for the granodioritic and rhyolitic samples dated (see compilation in Meng et al., 2020 and this study), which strongly suggests they reflect

the same magmatic event in the region. That these ~ 2.18 Ga xenocrystic zircons yielded similar $\varepsilon_{\text{Hf}}(t)$ values to zircons from the granodiorite porphyry samples at Tongkuangyu (Xu et al., 2012; Li et al., 2013; Liu et al., 2016b) also indicates they are co-genetic and likely sourced from the similar protolith.

The apparent absence of ~ 2.12 Ga zircon xenocrysts from the basaltic-andesitic tuff unit suggests that the ~ 2.12 Ga magmatism reported in previous studies (Li et al., 2013; Yang et al., 2015) is either subordinate in the northern Zhongtiaoshan region or that such units were not transected by the conduits which fed the volcanic sequence sampled, hence it was not contaminated by such material.

Instead, the second major but younger zircon age population recovered from the basaltic-andesitic tuff samples yielded identical ages of 2088 ± 16 Ma and 2085 ± 11 Ma. These ages agree, within uncertainties, with age estimates for the biotite \pm K-feldspar alteration and Cu \pm Mo mineralization in the Tongkuangyu deposit (Meng et al., 2020), as constrained, respectively, by LA-ICP-MS U-Pb ages of allanite (2115 ± 31 Ma; 2σ , MSWD = 2.3) and two precise molybdenite Re-Os ages (2106 ± 9 Ma and 2089 ± 9 Ma; 2σ). Thus, the consistency of the age results suggests the volcanic rocks represent the eruptive products of magmatism that is temporally related to the Tongkuangyu mineralization.

3.8.3 Original composition of ~ 2.09 Ga magmatism

The ~ 2.09 Ga zircon population from the basaltic-andesitic tuff unit has a distinctly different, more juvenile $\varepsilon_{\text{Hf}}(t)$ values compared to that of the ~ 2.18 Ga zircon xenocrysts and volcanoplutonic sequence in the Tongkuangyu region. In addition to lacking overgrowth of ~ 2.18 Ga zircons by younger rims (Fig. A3.4E, F), these features reflect crystallization of the

zircons from the mafic magma prior to its extensive interaction with ~2.18 Ga igneous rocks. Because zircon in mafic rocks commonly crystallizes during the late stage of magma crystallization (Shao et al., 2019), the ~2.18 Ga igneous rocks were therefore most likely entrained by explosive eruption at a shallow crustal level. The fact that the proportion of ~2.09 Ga zircon grains are much smaller than the ~2.18 Ga zircon xenocrysts is consistent with the limited zircon yield of mafic magma and/or suggests significant contamination of the ~2.18 Ga igneous rocks.

The four whole-rock samples collected from different locations (presumably different depositional sequences) of the basaltic-andesitic tuff unit are compositionally homogeneous. Compared to the putative ~2.18 Ga granodiorite and rhyolite tuff contaminant (Fig. 3.5), the unit is silica-poor (49–55 wt. % SiO₂ on a normalized anhydrous basis), less fractionated (i.e., lower [La/Yb]_N values), and has a slightly positive versus negative Ti anomaly. If the effect of the contamination of the ~2.18 Ga igneous rocks (interpreted here as ejecta) to the basaltic-andesitic tuff unit was significant, then: (1) the analyzed composition of the ~2.09 Ga units should be more felsic and/or heterogeneous in the different depositional settings, which is contradicted by the geochemical features mentioned above; and (2) to compensate the strong Ti-depletion of the ~2.18 Ga igneous contaminant for making slightly positive Ti anomaly of the basaltic-andesitic tuff unit, the original composition of the ~2.09 Ga magmatism must have had a significantly positive Ti anomaly, which is however not a feature reported for terrestrial basaltic rocks (Farmer et al., 2007; Kelemen et al., 2007). We therefore interpret the above features to indicate that the effect of the contamination from the ~2.18 Ga igneous rocks is insignificant, and the composition of the basaltic-andesitic tuff unit is suggested to be broadly consistent with the original composition of the ~2.1 Ga mafic magma.

The interpretation is relevant since, as noted previously, the ~2.1 Ga mafic magmas, formed contemporaneously with the Tongkuangyu porphyry Cu deposit, has a pattern in the normalized trace and REE plots (Fig. 5.5) that are similar to that for island arc magmas (e.g., Kelemen et al., 2007) and those associated with some of Phanerozoic porphyry Cu deposit globally (e.g., Oyu Tolgoi in southern Mongolia; Wainwright et al., 2011) and the rare Precambrian Haib porphyry Cu deposit in Namibia (Meng et al., 2021). It may further indicate that the porphyry Cu mineralization at the Tongkuangyu deposit plausibly formed in an island-arc-type setting during the middle Paleoproterozoic.

3.8.4 A model for the Tongkuangyu deposit and its implications

Porphyry Cu deposits are characterized by disseminated- and veinlet-type sulfide mineralization (i.e., Cu-Fe-Mo-S phases) that define bell-shaped ore zones that are spatially, temporally and genetically related to their porphyritic igneous host rocks. The porphyritic rocks, composed of variable phenocrystic phases (e.g., amphibole, biotite, plagioclase, and quartz) supported by a fine-grained to glassy groundmass, form from chilling of hydrous magmas commonly emplaced as small plug-like stocks or dikes in the shallower apical part or cupola of magma chambers (Tosdal et al., 2009). Release of the hydrous magma is critical and is suggested to reflect internal processes, such as overpressure of fluids and resultant hydro-fracturing (Candela and Holland, 1984; Shinohara and Hedenquist, 1997; Cloos, 2001), or external processes, such as sudden melt recharge into the magma chamber, volcanic edifice collapse, or mega-earthquake (Fournier, 1999; Sillitoe, 2010; Richards, 2018). Regardless, such triggers result in sudden egress, structural focusing, and upward channeling of a large volume of hot, overpressured, metalliferous fluids which manifests either as bubbly magma or as a separate volatile plume (low- to moderate-

salinity, single-phase brine). These fluids eventually collect in the genetically related cupola of the batholith complex to form porphyry Cu deposits.

Despite the consensus that the porphyritic stocks or dikes are not the source of the fluids (Sillitoe, 2010), the contraction within these rocks may make local tensile stresses and enhance hydraulic fracturing (Fournier, 1999). Focusing the fluid flux by narrow apical channels through the cupola zone of the system is thought to be an effective way to load Cu and Mo ± Au (Shinohara et al., 1995; Shinohara and Hedenquist, 1997; Weiss et al., 2012). This process may become self-organizational once the initial channel ways formed (Richards, 2011). The supercritical magmatic liquids exsolved from depth evolve to immiscible hypersaline brine + vapor fluids through phase separation during ascent (Hedenquist et al., 1998; Heinrich et al., 2004, 2005), and form potassic alteration, radial and concentric veins in the brittle carapace, and an ore shell upon cooling between ~400° and 300 °C, that is at or above the brittle-ductile transition zone (Fournier, 1999; Weiss et al., 2012). This is consistent with the fact that nearly all the mineralization within PCDs immediately follows the emplacement of the subvolcanic stocks (by ≤ 100, 000 yrs) during cooling of the underlying pluton (Cathles et al., 1997; Richards, 2018). This model has been tested to be effective in mineral exploration and is widely accepted (Seedorff et al., 2005; Sillitoe, 2010).

The most significant difference noted here for the Tongkuangyu mineralization setting versus that typifies most other porphyry Cu deposits is the age discordance of ca. 80 Ma between the mineralization and host rocks versus the synchronicity of mineralized host rocks and the causative magmas. We note that the age discordance between host rocks and mineralization have also rarely been reported at Butte, Resolution, Ray deposits in USA, Zaldívar deposit in Chile, and Dexing deposit in China (see the features of these deposits compiled in Table 3.3). For these

previously well-documented deposits, syn-mineralization stocks and/or dikes, which are not the main lithologies host to the mineralization, have been identified or inferred at the deposit or regional scale (Table 3.3). Hence, we argue that the ~2.09 Ga temporally-related volcanic sequence proximal to the Tongkuangyu area implies presence of an ore-forming magma chamber for the porphyry Cu mineralization. The fact that the ore-related intrusive rocks have not been identified may be attributed to either of the following three reasons: (1) they are locally present but petrographically comparable to ~2.18 Ga granodiorite porphyry or granodiorite, rendering discerning them difficult; (2) the batholith or stocks are too deep to be intersected by current drill holes; and/or (3) the batholith or stocks have been tectonically displaced or removed.

Nevertheless, the majority of the currently defined porphyry Cu resources (453 Mt @ 0.61 % Cu) and associated the biotite ± K-feldspar alteration and related Cu mineralization at Tongkuangyu are mainly hosted by a ~2.18–2.16 Ga intrusive complex comprised of granodiorite and granodiorite porphyry that transects basaltic-andesitic sills, interpreted to be subvolcanic in origin, with a broadly similar age of 2191 ± 10 Ma (2σ , $n = 3$; Meng et al., 2020). Both of the rocks intrude a sequence of finer-grained quartz-sericite schist of ~2.5–2.3 Ga, interpreted as a rhyolitic tuff in protolith, which is poorly mineralized except where fractured or where locally mafic minerals are present (Fig. 5.3D; Meng et al., 2020). The fact that the mineralization is preferentially hosted in the more Fe-rich and competent rocks in the granodioritic suite and the basaltic-andesitic sill versus the surrounding less competent and more felsic rocks (e.g., rhyolitic tuff) suggests there was a strong lithological control to the mineralization. The granodiorite unit and basaltic-andesitic sill would have been more reactive given their relatively Fe-rich nature, as reflected by the abundance of biotite (~15 % and ~50–70 %, respectively; Fig. 5.3), in addition to being rheologically more competent thus more prone to

brittle failure and hence structurally receptive to fluid flux. These features together favor the localization of mineralization in porphyry Cu deposit settings (Sillitoe, 2010; Vry et al., 2010).

Here we consider a model whereby a zone of structural anisotropy is what is critical for the fluid flux and ore precipitation. For the Tongkuangyu deposit setting, this anisotropy was a pre-existing zone of weakness in the overlying roof rocks, overlying the magma chamber and its cupola, which subsequently became the focus of fluid egress. In such a setting the effects of far-field seismogenic events (i.e., mega-earthquakes; Richards et al., 2018) might be reactivation of such a structural zone and the resultant depressurization or agitation in the apical zone of the magma chamber where overpressured, sulfurous, and metalliferous fluids have already been stored. The consequence of convergence of these favorable geological factors would be the breaching of the fertile reservoir and the sudden egress of voluminous supercritical magmatic fluids stored in this zone with further draining of volatiles from the underlying magma chamber. In the model of the Tongkuangyu deposit formation, the hydraulic fracturing related to the early 'shake-up' stage of porphyry Cu deposit formation of Richards (2018) is localized to the fractured country rocks to the causative intrusion.

Figure 5.7 summarizes the critical elements of the aforementioned model for the Tongkuangyu deposit which include the presence of a pre-existing structure in the basement rocks into which the hydrothermal fluids from the causative intrusion were focused, and the presence of appropriate volcanic rocks which indicates the presence of the causative intrusion at depth. The model implies that porphyry Cu deposits merely form under a confluence of optimal conditions of fluid exsolution, rock failure, and chemical traps (i.e., reactive rocks noted above), but potentially in variable settings. Thus genetically unrelated but reactive or fractured rocks may also optimal location for porphyry-type disseminated and veinlet Cu mineralization, as supported

by the rare porphyry Cu deposit examples in USA, Chile, and China. This aspect therefore has important additional implications for how such deposits are explored for.

3.9 Conclusions

Our new zircon U-Pb geochronological results presented herein verify the ~2.1 Ga volcanism in the northern Zhongtiaoshan region and suggest the former presence of a deep-seated magma chamber which is interpreted to be the source of the magmatic-hydrothermal fluids responsible for the Tongkuangyu porphyry Cu deposit. Thus, the apparent absence at the deposit site of spatially and genetically related precursor porphyritic dikes emplaced prior to exsolution of metal-charged hydrothermal fluids precludes this as a necessary feature for porphyry Cu deposits. Instead, in the case of the Tongkuangyu, the presence of coeval basaltic-andesitic tuff provides the causative, or in this case, missing link. Existence of such volcanic rocks indicates in itself the presence of a stress field to make conduits for the source magma to access the surface, thereby implying pre-existing favorable structures could be reactivated, possibly due to related contemporaneous seismic activity via [Richards \(2018\)](#) “shake-up model” to form Tongkuangyu.

3.10 Acknowledgment

This research was supported by Canada First Research Excellence Fund through a Metal Earth thematic project to Jeremy P. Richards, Natural Science Foundation of China through an International Cooperation and Exchange Project (41820104010) to Jingwen Mao, and a China Scholarship Council Ph.D. scholarship awarded to Xuyang Meng. We acknowledge mine and drill core access permission from Chunsheng Li and Jianbin Zhang (Zhongtiaoshan Non-Ferrous Metals Group, Co., Ltd) and field assistance of the mine geologists Xiaoming Zhu and Jiaqi

Wang, as well as postgraduate students Chenglong Fan and Chuncheng Cha from China University of Geosciences (Beijing). We appreciate the reviews by the guest editor Ali Sholeh, Richard Tosdal, and an anonymous reviewer for constructive critiques of this manuscript which have helped to improve its quality.

3.11 References

- Bouvier, A., Vervoort, J. D., and Patchett, P. J., 2008, The Lu-Hf and Sm-Nd isotopic composition of CHUR: Constraints from unequilibrated chondrites and implications for the bulk composition of terrestrial planets: *Earth and Planetary Science Letters*, v. 273, p. 48–57.
- Candela, P. A., and Holland, H. D., 1984, The partitioning of copper and molybdenum between silicate melts and aqueous fluids: *Geochimica et Cosmochimica Acta*, v. 48, p. 373–380.
- Cathles, L. M., Erendi, A. H. J., and Barrie, T., 1997, How long can a hydrothermal system be sustained by a single intrusive event?: *Economic Geology*, v. 92, p. 766–771.
- Chen, W. M., and Li, S. P., 1998, Rhenium-Osmium isotopic ages of sulfides from the Tongkuangyu porphyry copper deposit in the Zhongtiao Mountain: *Mineral deposits*, v. 17, p. 224–228 (in Chinese with English abstract).
- Cloos, M., 2001, Bubbling magma chambers, cupolas, and porphyry copper deposits: *International Geology Review*, v. 43, p. 285–311.
- Farmer, G. L., 2007, 3.03 - Continental Basaltic Rocks, in Holland, H. D., and Turekian, K. K., eds., *Treatise on Geochemistry*: Oxford, Pergamon, p. 1–39.
- Fournier, R. O., 1999, Hydrothermal processes related to movement of fluid from plastic into brittle rock in the magmatic-epithermal environment: *Economic Geology*, v. 94, p. 1193–

1211.

Geological Group, i. Z. M., 1978, Geology of the copper deposits in Zhongtiao Mountain:

Geological Publishing House, Beijing, p. 1–190.

Gustafson, L. B., and Hunt, J. P., 1975, The porphyry copper deposit at El Salvador, Chile:

Economic Geology, v. 70, p. 857–912.

Hedenquist, J. W., Arribas, A., and Reynolds, T. J., 1998, Evolution of an intrusion-centered

hydrothermal system: Far Southeast-Lepanto porphyry and epithermal Cu-Au deposits,

Philippines: Economic Geology, v. 93, p. 373–404.

Hedenquist, J. W., and Lowenstern, J. B., 1994, The role of magmas in the formation of

hydrothermal ore deposits: Nature, v. 370, p. 519–527.

Hehnke, C., Ballantyne, G., Martin, H., Hart, W., Schwarz, A., and Stein, H., 2012, Geology and

exploration progress at the Resolution porphyry Cu-Mo deposit, Arizona: Geology and

exploration progress at the Resolution porphyry Cu-Mo deposit, Arizona, p. 147–166.

Heinrich, C. A., Driesner, T., Stefansson, A., and Seward, T. M., 2004, Magmatic vapor

contraction and the transport of gold from the porphyry environment to epithermal ore

deposits: Geology, v. 32, p. 761–764.

Heinrich, C. A., Halter, W., Landtwing, M. R., and Pettke, T., 2005, The formation of economic

porphyry copper (-gold) deposits: constraints from microanalysis of fluid and melt

inclusions: Geological Society, London, Special Publications, v. 248, p. 247–263.

Hoskin, P. W. O., and Schaltegger, U., 2003, The composition of zircon and igneous and

metamorphic petrogenesis. In: Hanchar, J. M. & Hoskin, P. W. O. (eds) Zircon: Reviews

in Mineralogy and Geochemistry, p. 27–62.

Hurtig, N. C., and Williams-Jones, A. E., 2015, Porphyry-epithermal Au-Ag-Mo ore formation

- by vapor-like fluids: New insights from geochemical modeling: *Geology*, v. 43, p. 587–590.
- Kelemen, P. B., Hanghøj, K., and Greene, A. R., 2007, 3.18 - One View of the Geochemistry of subduction-related magmatic arcs, with an emphasis on primitive andesite and lower crust, in Holland, H. D., and Turekian, K. K., eds., *Treatise on Geochemistry*: Oxford, Pergamon, p. 1–70.
- Li, N. B., Luo, Y., Guo, S. L., Jiang, Y. H., Zeng, L. J., and Niu, H. C., 2013, Zircon U-Pb geochronology and Hf isotope geochemistry of metamorphic quartz-monzonite porphyry from Tongkuangyu area, Zhongtiao Mountain and its geological implications: *Acta Petrologica Sinica*, v. 29, p. 2416–2424 (in Chinese with English abstract).
- Li, Q., Liu, S., Wang, Z., Shen, Y., Zhang, L., and Zhang, J., 2011, Provenance and geotectonic setting of the Palaeoproterozoic Zhongtiao Group and implications for assembly of the North China Craton: Whole-rock geochemistry and detrital zircon data: *Journal of the Geological Society*, v. 168, p. 1215–1224.
- Li, Q. G., Liu, S. W., Wang, Z. Q., Zhang, F., Chen, Y. Z., and Wang, T., 2008, LA-ICP-MS geochronology of the detrital zircons from the Jiangxian Group in the Zhongtiao Mountain and its tectonic significance: *Acta Petrologica Sinica*, v. 24, p. 1359–1368 (in Chinese with English abstract).
- Liu, C. H., Zhao, G. C., Sun, M., Zhang, J., and Yin, C. Q., 2012, U–Pb geochronology and Hf isotope geochemistry of detrital zircons from the Zhongtiao Complex: constraints on the tectonic evolution of the Trans-North China Orogen: *Precambrian Research*, v. 222, p. 159–172.
- Liu, X., Fan, H. R., Qiu, Z. J., Yang, K. F., Hu, F. F., Guo, S. L., and Zhao, F. C., 2015,

- Formation ages of the Jiangxian and Zhongtiao groups in the Zhongtiao Mountain region, North China Craton: Insights from SIMS U-Pb dating on zircons of intercalated plagioclase amphibolites: *Acta Petrologica Sinica*, v. 31, p. 1564–1572 (in Chinese with English abstract).
- Liu, X., Fan, H. R., Santosh, M., Yang, K. F., Qiu, Z. J., Hu, F. F., and Wen, B. J., 2016a, Geological and geochronological constraints on the genesis of the giant Tongkuangyu Cu deposit (Palaeoproterozoic), North China Craton: *International Geology Review*, v. 58, p. 155–170.
- Liu, X., Fan, H. R., Yang, K. F., Qiu, Z. J., Hu, F. F., and Zhu, X. Y., 2016b, Geochronology, redox-state and origin of the ore-hosting porphyry in the Tongkuangyu Cu deposit, North China Craton: Implications for metallogensis and tectonic evolution: *Precambrian Research*, v. 276, p. 211–232.
- Lowell, J. D., and Guilbert, J. M., 1970, Lateral and vertical alteration-mineralization zoning in porphyry ore deposits: *Economic Geology*, v. 65, p. 373–408.
- Ludwig, K. R., 2012, User's manual for Isoplot version 3.75–4.15: a geochronological toolkit for Microsoft: Excel Berkley Geochronological Center Special Publication.
- Mao, J. W., Zhang, J. D., Pirajno, F., Ishiyama, D., Su, H. M., Guo, C. L., and Chen, Y. C., 2011, Porphyry Cu–Au–Mo–epithermal Ag–Pb–Zn–distal hydrothermal Au deposits in the Dexing area, Jiangxi province, East China—a linked ore system: *Ore Geology Reviews*, v. 43, p. 203–216.
- Mei, H. L., 1994, Metamorphic P-T-t paths and tectonic evolution of early Proterozoic rocks from the Zhongtiao Mountains, Southern Shanxi: *Geological Review*, v. 40, p. 36–47 (in Chinese with English abstract).

- Meng, X., Richards, J. P., Mao, J. W., Ye, H. S., DuFrane, S. A., Creaser, R., Marsh, J., and Petrus, J., 2020, The Tongkuangyu Cu Deposit, Trans-North China Orogen: A Metamorphosed Paleoproterozoic Porphyry Cu Deposit: *Economic Geology*, v. 115, p. 51–77.
- Meng, X., Kleinsasser, J. M., Richards, J. P., Tapster, S. R., Jugo, P. J., Simon, A. C., Kontak, D. J., Robb, L., Bybee, G. M., Marsh, J. H., and Stern, R. A., 2021, Oxidized sulfur-rich arc magmas formed porphyry Cu deposits by 1.88 Ga: *Nature Communications*, v. 12, p. 2189.
- Mercer, C. N., and Reed, M. H., 2013, Porphyry Cu-Mo Stockwork Formation by Dynamic, Transient Hydrothermal Pulses: Mineralogic Insights from the Deposit at Butte, Montana: *Economic Geology*, v. 108, p. 1347–1377.
- Perelló, J., González, A., and Monroy, C., 2018, Geologic Controls on Hypogene Mineralization at the Zaldívar Porphyry Copper-Gold-Molybdenum Deposit, Escondida District, Northern Chile, *in* Arribas R, A. M., and Mauk, J. L., eds., *Metals, Minerals, and Society*, 21, Society of Economic Geologists (SEG), p. 271–292.
- Phillips, C., Gambell, N., and Fountain, D., 1974, Hydrothermal alteration, mineralization, and zoning in the Ray deposit: *Economic Geology*, v. 69, p. 1237–1250.
- Richards, J. P., 2011, Magmatic to hydrothermal metal fluxes in convergent and collided margins: *Ore Geology Reviews*, v. 40, p. 1–26.
- Richards, J. P., 2018, A Shake-Up in the Porphyry World?: *Economic Geology*, v. 113, p. 1225–1233.
- Seedorff, E., 2005, Porphyry deposits: characteristics and origin of hypogene Features. Society of economist Geologists, Inc: *Economic Geology 100th Anniversary Volume*, p. 251–

298.

- Shao, T., Xia, Y., Ding, X., Cai, Y., and Song, M., 2019, Zircon saturation in terrestrial basaltic melts and its geological implications: *Solid Earth Sciences*, v. 4, p. 27–42.
- Shinohara, H., and Hedenquist, J. W., 1997, Constraints on magma degassing beneath the Far Southeast porphyry Cu-Au deposit, Philippines: *Journal of Petrology*, v. 38, p. 1741–1752.
- Shinohara, H., Kazahaya, K., and Lowenstern, J. B., 1995, Volatile transport in a convecting magma column: Implications for porphyry Mo mineralization: *Geology*, v. 23, p. 1091–1094.
- Sillitoe, R. H., 2010, Porphyry copper systems: *Economic Geology*, v. 105, p. 3–41.
- Söderlund, U., Patchett, P. J., Vervoort, J. D., and Isachsen, C. E., 2004, The ^{176}Lu decay constant determined by Lu-Hf and U-Pb isotope systematics of Precambrian mafic intrusions: *Earth and Planetary Science Letters*, v. 219, p. 311–324.
- Sun, D. Z., and Hu, W. X., 1993, Precambrian geochronology, chronotectonic framework and model of chronocrustal structure of the Zhongtiao Mountain, Geological publishing house, 1–180 p (In Chinese).
- Sun, D. Z., Li, H. M., Lin, Y. X., Zhou, H. F., Zhao, F. Q., and Tang, M., 1991, Precambrian geochronology, chronotectonic framework and model of chronocrustal structure of the Zhongtiao Mountain: *Acta Geologica Sinica*, v. 3, p. 216–231 (in Chinese with English abstract).
- Sun, S. S., and McDonough, W. F., 1989, Chemical and isotopic systematics of oceanic basalts: implications for mantle composition and processes: Geological Society, London, Special Publications, v. 42, p. 313–345.

- Tosdal, R. M., Dilles, J. H., and Cooke, D. R., 2009, From source to sinks in auriferous magmatic-hydrothermal porphyry and epithermal deposits: *Elements*, v. 5, p. 289–295.
- Vry, V. H., Wilkinson, J. J., Seguel, J., and Millán, J., 2010, Multistage intrusion, brecciation, and veining at El Teniente, Chile: Evolution of a nested porphyry system: *Economic Geology*, v. 105, p. 119–153.
- Wainwright, A., J., Tosdal, R. M., Wooden, J. L., Mazdab, F. K., and Friedman, R. M., 2011, U–Pb (zircon) and geochemical constraints on the age, origin, and evolution of Paleozoic arc magmas in the Oyu Tolgoi porphyry Cu–Au district, southern Mongolia: *Gondwana Research*, v. 19, p. 764–787.
- Weis, P., Driesner, T., and Heinrich, C. A., 2012, Porphyry-copper ore shells form at stable pressure-temperature fronts within dynamic fluid plumes: *Science*, v. 338, p. 1613–1618.
- Winchester, J. A., and Floyd, P. A., 1977, Geochemical discrimination of different magma series and their differentiation products using immobile elements: *Chemical Geology*, v. 20, p. 325–343.
- Xu, Q. L., Sun, F. Y., Zhang, H., and Huo, L., 2012, Fluid inclusion, zircon U-Pb age and Hf isotope of Tongkuangyu copper deposit in Zhongtiaoshan mountains and its geological significance, Shanxi Province, China: *Journal of Jilin University (Earth Science Edition)*, v. 42, p. 64–80.
- Yang, C. H., Du, L. L., Ren, L. D., Song, H. X., Geng, Y. S., Wang, Y. B., Lu, Z. L., Wang, H., and Li, Y. H., 2015, The age and tectonic setting of metavolcanic rocks in the Tongkuangyu deposit, Zhongtiao Mountain, and their constraints on copper mineralization: *Acta Geoscientica Sinica*, v. 36, p. 613–633 (in Chinese with English abstract).

- Yang, C. H., Du, L. L., Song, H. X., Ren, L. D., Miao, P. S., and Lu, Z. L., 2018, Stratigraphic division and correlation of the Paleoproterozoic strata in the North China Craton: A review: *Acta Petrologica Sinica*, v. 34, p. 1019–1057 (in Chinese with English abstract).
- Zhang, H., 2012, Metallogenesis of Paleoproterozoic copper deposits in the Northern Zhongtiaoshan Mountains, Shanxi Province: Doctoral thesis, Jilin University, 1–155 p. (in Chinese with English abstract).
- Zhao, G. C., Sun, M., Wilde, S. A., and Li, S. Z., 2004, A Paleo-Mesoproterozoic supercontinent: assembly, growth and breakup: *Earth-Science Reviews*, v. 67, p. 91–123.
- Zhang, R., Sun, Y., and Zhang, S., 2020, Early Precambrian geological events in the Zhongtiao Mountain, China: implication for the evolution of Neoproterozoic to Paleoproterozoic crust in the southern segment of North China Craton: *International Geology Review*, p. 1–21.

3.12 Figures

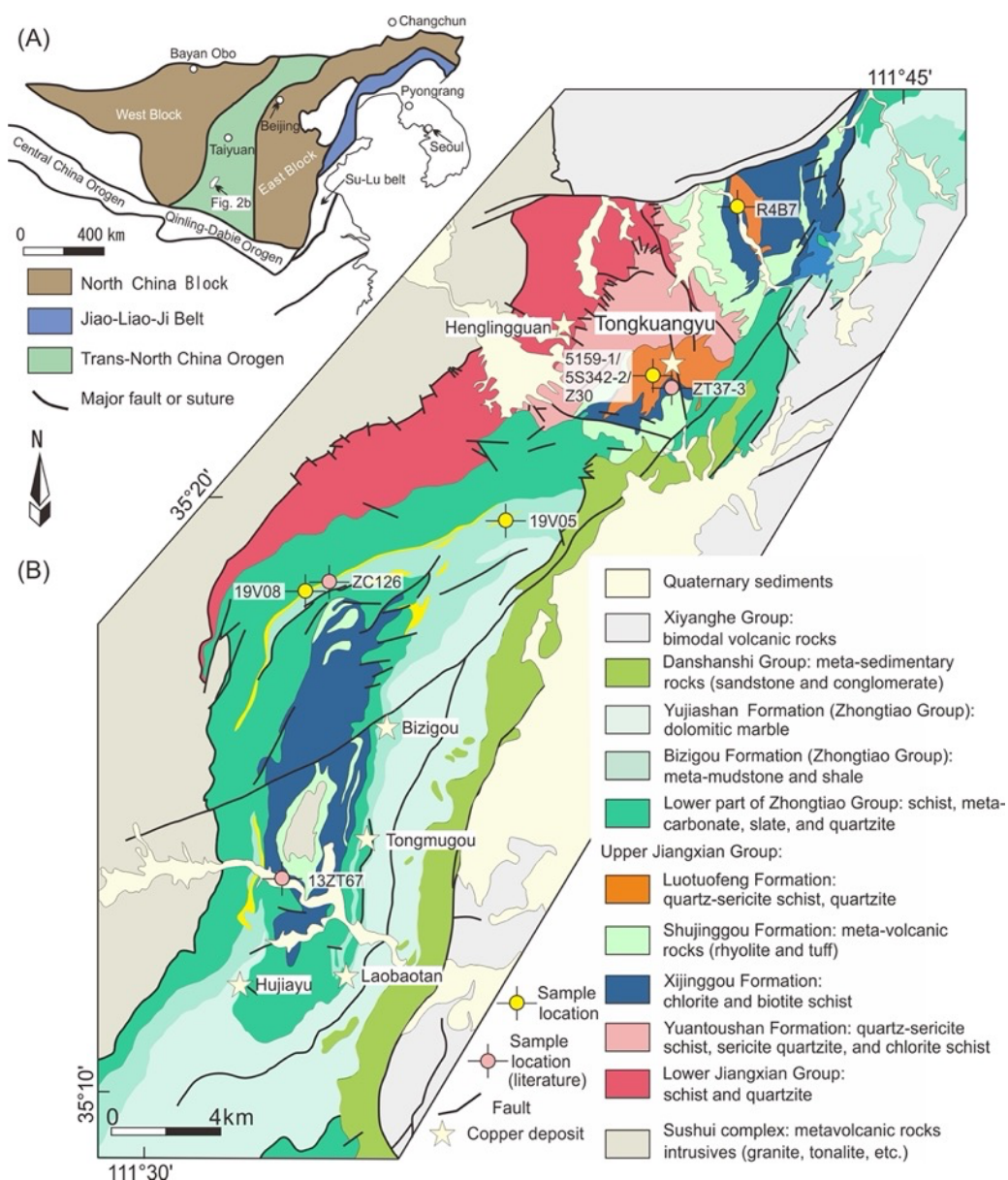


Figure 3.1. (A) Map showing the location of the northern Zhongtiaoshan region within the Trans-North China Orogen. The figure is reproduced from Figure 1A in Meng et al. (2020). (B) Simplified geological map of the northern Zhongtiaoshan region, which is adapted from Meng et al. (2020) and Shanxi No. 6 Geology Engineering Reconnaissance Institute (unpublished report), 2002. Note the locations of samples referred to in the text and used in this study.

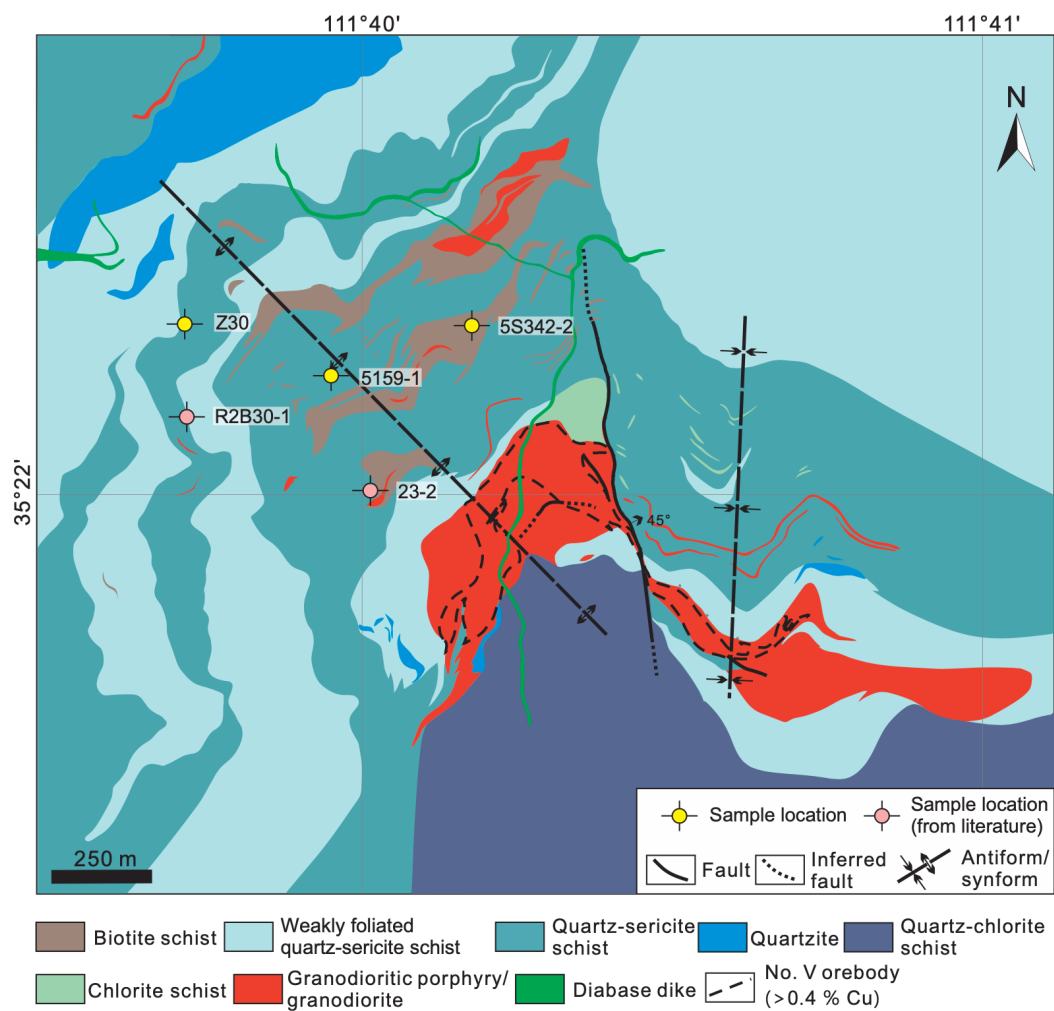


Figure 3.2. Simplified geologic map of the Tongkuangyu porphyry Cu deposit in northern Zhongtiaoshan region, reproduced from Meng et al. (2020) with publication permission from the journal of Economic Geology. The original map was from the 214 Geological Group in Zhongtiao Mountain in Shanxi Province (unpublished report, 1956).

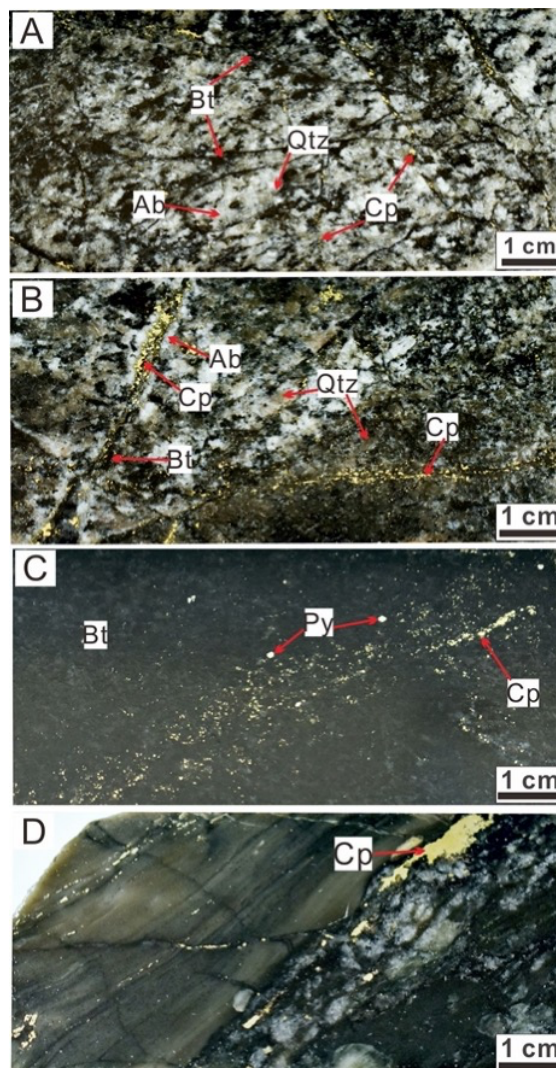


Figure 3.3. Photographs of disseminated- and veinlet-type alteration and mineralization in granodiorite, biotite schist, and quartz-sericite schist from the deep levels (in meters above sea level) of the Tongkuangyu Cu deposit. (A) Albite-altered granodiorite crosscut by biotite ± chalcopyrite vein (sample 5S342-2; N35°22'15.8''; E111°40'10.7'', 270 m; WGS84 datum). (B) Biotite ± chalcopyrite ± quartz vein with albite selvage in granodiorite (sample 5S342-3; N35°22'15.8''; E111°40'10.7'', 136 m). (C) Biotite ± chalcopyrite ± pyrite vein in biotite schist (sample 5S342-1; N35°22'15.8''; E111°40'10.7'', 216 m), which is interpreted to be a basaltic-andesitic sill. (D) Chalcopyrite mineralization in highly strained sample of granodiorite porphyry and quartz-sericite schist (sample Z37; N35°22'16.1''; E111°39'42.8'', 267 m). Abbreviations: Ab = albite, Bt = biotite, Cp = chalcopyrite, Qtz = quartz.

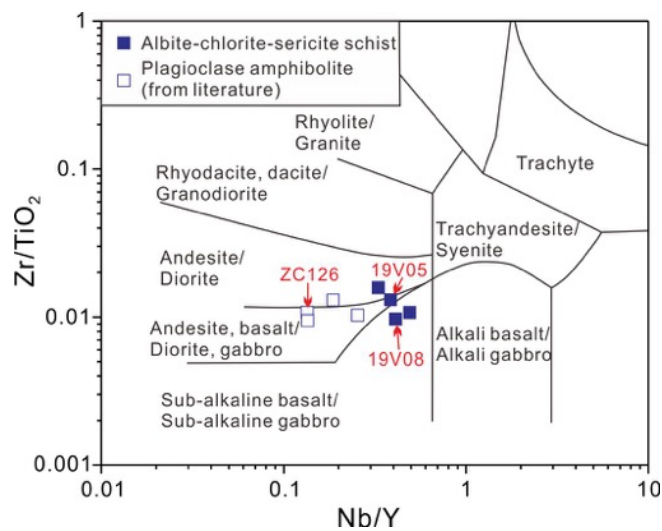


Figure 3.4. Zr/TiO₂ versus Nb/Y discrimination diagram (Winchester and Floyd, 1977) for the albite-chlorite-sericite schist from the bottom of the Bizigou Formation in the northern Zhongtiaoshan region.

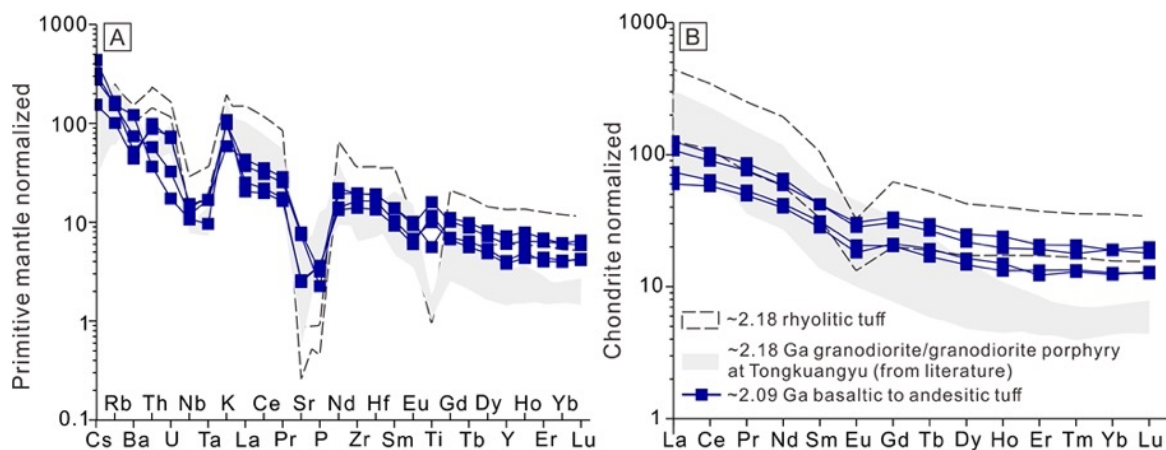


Figure 3.5. (A) Primitive mantle-normalized trace element and (B) chondrite-normalized rare-earth element diagrams for samples of the albite-chlorite-sericite schist (i.e., basaltic to andesitic volcanic tuffs) from the bottom of Bizigou Formation in the northern Zhongtiaoshan region. Dashed red ellipses in (F) indicate Pb-loss or reversely concordant analyses. See [Table 3.2](#) for sample locations and descriptions.

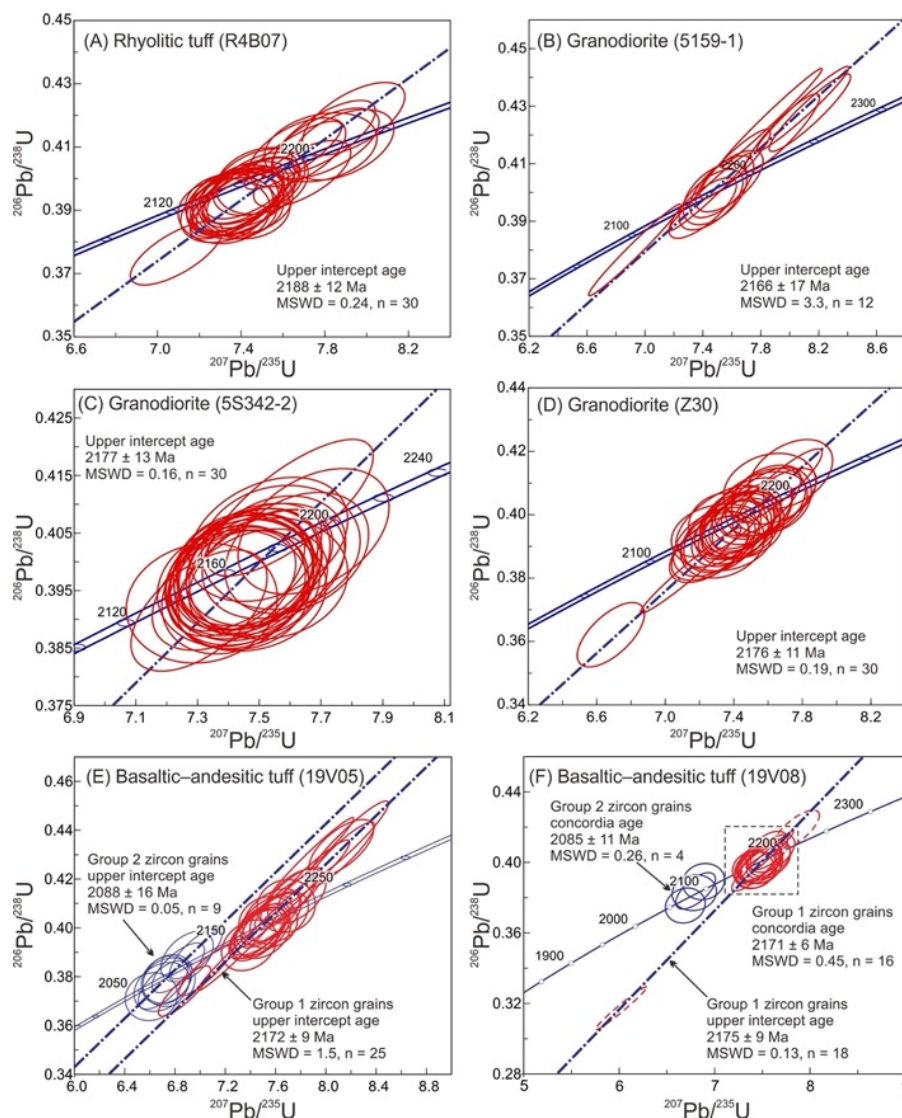


Figure 3.6. Zircon U-Pb concordia diagrams for the representative samples from the northern Zhongtiaoshan region. Error ellipses are shown at 2σ . (A) Rhyolitic tuff (sample R4B07), (B–D) granodiorite (samples 5159-1, 5S342-2, and Z30), (E–F) albite-chlorite-sericite schist (i.e., basaltic-andesitic tuffs; samples 19V05 and 19V08).

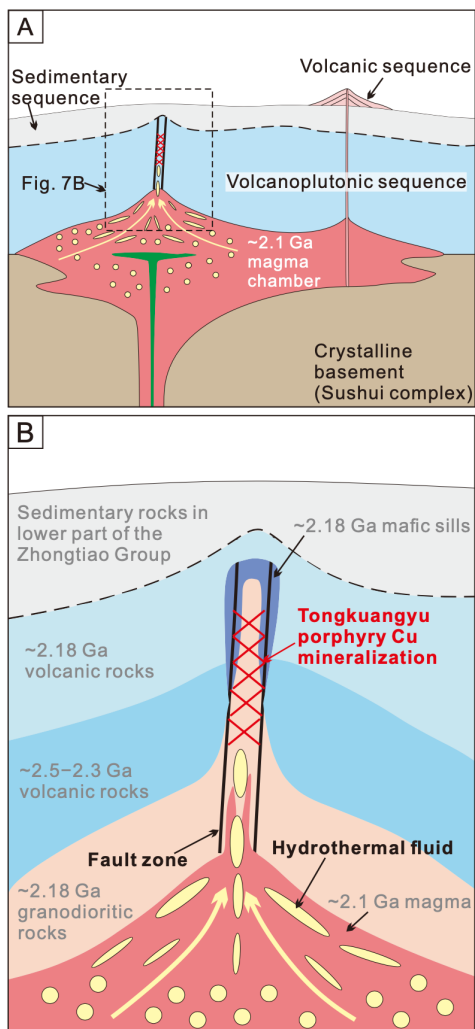


Figure 3.7. Simplified cartoon model (not to scale) illustrating the development of the Tongkuangyu deposit. (A) Thick, impermeable volcano-sedimentary sequences maintain high fluid pressures of the magma chamber. External processes proposed by Richards (2018) trigger exsolution and venting of hydrothermal fluids into a zone of structural weakness (i.e., pre-existing fractures) in the granodioritic suite and basaltic-andesitic sill. Minor volcanism related to the causative intrusion erupted along the narrow conduit to form the thin basaltic-andesitic tuff sequence (~2.1 Ga) at the bottom of the Zhongtiao Group. (B) Focusing of sulfurous metalliferous fluids along structural zone into the permeable, reactive granodioritic suite and basaltic-andesitic sill rocks (simply two stocks at Tongkuangyu into one). Reaction of the hydrothermal fluids with the Fe-rich rocks produces biotite \pm K-feldspar alteration and precipitates sulfide minerals. See the location of panel B in section A.

3.13 Tables

Table 3.1. Summary of key features of the host rocks, alteration, and mineralization at Tongkuangyu porphyry Cu deposit, northern Zhongtiaoshan region

Deposit geology	Description	Ages	References for ages
<i>Host rocks</i>			
Quartz-sericite schist	Melanocratic, fine-grained, consists of 15–25 % Qtz and ~0–10 % Bt crystals in groundmass of Ser and minor Qtz. Interpreted to be tuffaceous volcanic rocks	2.51–2.33 Ga (LA/Zrn/U-Pb)	Meng et al. (2020)
Biotite schist	Bt (50–70 %, rarely up to 90 %), Pl (15–25 %), Qtz (5–10 %), Chl (0–10 %). Interpreted to be basaltic-andesitic sill	~2.19 Ga (LA/Zrn/U-Pb)	Meng et al. (2020)
Granodiorite porphyry	Porphyritic, coarse-grained. Phenocrysts of Qtz (15–30 %), Pl (~30 %), and Kfs (<5 %) in groundmass of Pl (~30 %) and Ser (~15 %)	~2.18–2.16 Ga (LA/Zrn/U-Pb)	This study , Meng et al. (2020) and reference therein
Granodiorite	Equigranular. Pl (partially sericitized, 45–55 %), Qtz (20–25 %), ~10 % Kfs, 5–15 % Bt	~2.18–2.16 Ga (LA/Zrn/U-Pb)	
<i>Alteration</i>			
Sericite	Pervasive in quartz-sericite schist and is overprinted by Ab and Bt ± Kfs alteration. Unrelated to mineralization	N/A	
Albite	Unknown spatial extent, mainly in granodiorite porphyry, granodiorite, and schists within the mineralization zones	N/A	
Biotite ± K-feldspar	Immediately postdating the albite alteration and is associated with Cp ± Py ± Mt. Mainly develops in the core of the orebodies and occurs in granodiorite porphyry, granodiorite, biotite schist, and quartz-sericite schist	2115 ± 31 Ma (2σ; LA/All/U-Pb)	Meng et al. (2020)
Chlorite	Developed around Bt alteration zones and along the lithological contacts along the fractures. Associated with largely undeformed Qtz-Chl-Bn veins	~1.8 Ga (LA/Mnt/U-Pb)	Meng et al. (2020)
Quartz	Local planar Qtz-Calc-Cp-Py vein	1807 ± 4 Ma (2σ; N-TIMS/Py/Re-Os)	Meng et al. (2020)
<i>Mineralization</i>			
Stage-I (porphyry)	Dominant form of mineralization at Tongkuangyu. Disseminated Cp-Py-Mt and in variably deformed Qtz-Bt-Mt-(Tour-Mo) veins	2106 ± 9/2089 ± 9 Ma (2σ; N-TIMS/Mo/Re-Os) 2108 ± 32 Ma (2σ; ICP/Mo/Re-Os) 2122 ± 12 Ma (2σ; ICP/Mo/Re-Os)	Meng et al. (2020) Chen et al. (1998) Liu et al. (2016a)
Stage-II (overprinting)	Local. In and around late undeformed crosscutting Qtz-Chl-Bn and Qtz-Calc-Cp-Py veins	~1.8 Ga (LA/Mnt/U-Pb)	Meng et al. (2020)

Abbreviations:

Minerals: Ab = albite, All = allanite, Bn = bornite, Bt = biotite, Calc = calcite, Chl = chlorite, Cp = chalcopyrite, Ep = epidote, Kfs = K-feldspar, Mnt = monazite, Mol = molybdenite, Mt = magnetite, Pl = plagioclase, Py = pyrite, Qtz = quartz, Ser = sericite, Tour = tourmaline, Zrn = zircon. Methods: ICP = Inductively coupled plasma mass spectrometry, LA = laser ablation inductively coupled plasma mass spectrometry, N-TIMS = negative thermal ion mass spectrometry.

Table 3.2. Summary of new geochronological results for the representative igneous rocks from the northern Zhongtiaoshan region

Sample	Rock type	Latitude / Longitude	Elevation	Mineralogy (approximated volume)	Zircon U-Pb age (Ma, 2 σ)
R4B7	Quartz-sericite schist	N35°24'50.0'', E111°41'38.8''	1063 m	Clast of 5 % angular Qtz in groundmass of Ser (90 %) and minor Qtz (5 %).	2188 ± 12 (n = 30, MSWD = 0.24)
5159-1	Granodiorite	N35°22'10.9'', E111°39'57.0''	413 m	Equigranular texture. 45 % Pl (partially sericitized), 10 % Kfs, 25 % Qtz, 15 % Bt. Minor Cp, Mt.	2166 ± 17 (n = 12, MSWD = 3.3)
5S342-2*	Granodiorite	N35°22'15.8'', E111°40'10.7''	270 m	Equigranular texture. 50 % Pl (partially sericitized), 10 % Kfs, 20 % Qtz, and 15 % Bt. Minor Cp, Mt.	2177 ± 13 Ma (n = 30, MSWD = 0.16)
Z30*	Granodiorite	N35°22'16.1'', E111°39'42.8''	352 m	Equigranular texture. 50–55 % Pl (partially sericitized), 20 % Kfs, 20 % Qtz, and 5 % Bt. Minor Cp, Mt	2176 ± 11 Ma (n = 30, MSWD = 0.19)
19V05	Sericite-chlorite schist	N35°19'34.9'', E111°37'09.1''	772 m	Clast of 10 % Mt in groundmass of Chl (40 %), Ser (40 %), Qtz (5 %), Ab (2 %).	2088 ± 16 Ma (n = 9, MSWD = 0.05)
19V08	albite-sericite schist	N35°18'24.5'', E111°33'11.9''	952 m	Clasts of 5 % Mt, 15 % Bt, and 5 % Ep in groundmass of 25–30 % Ab, 20 % Ser, 15 % Mt, 5 % Chl, and 2–5 % Qtz.	2085 ± 11 Ma (n = 4, MSWD = 0.26)

Abbreviations: Ab = albite, Bt = biotite, Chl = chlorite, Cp = chalcopyrite, Ep = epidote, Kfs = K-feldspar, Mt = magnetite, Pl = plagioclase, Qtz = quartz, Ser = sericite. Symbol * represents drill core sample.

Table 3.3. Representative porphyry Cu deposits with hypogene ores hosted mainly by pre-mineralization rocks

Deposit ¹	Butte	Resolution	Ray	Zaldívar	Dexing	Tongkuangyu
Location	Montana, USA	Arizona, USA	Arizona, USA	Escondida, Chile	Jiangxi, China	Shanxi, China
Cu ore tonnage /grade ²	5220 Mt @ 0.67 % (in total)	1624 Mt @ 1.47 % Cu	1583 Mt @ 0.68 % Cu	~1000 Mt @ 0.27 % Cu	1825 Mt @ 0.46 % Cu	453 Mt @ 0.61 % Cu
Age	66–64 Ma	65–64 Ma	~69 Ma	~39–37 Ma	~170 Ma	~2.1 Ga
Main host lithology ³	77–75 Ma Butte Granite	1.1 Ga diabase sills, Proterozoic and Paleozoic quartzite and carbonate, and Cretaceous sandstone, volcanoclastic rocks, and tuff	1.14 Ga mafic diabase 1.7 Ga Qtz-Mus-Chl schist.	~290 Ma granodioritic porphyry and andesitic country rocks.	Neoproterozoic metasedimentary phyllite, and minor in granodiorite porphyry stock	~2.18 Ga granodiorite porphyry and granodiorite; ~2.19 Ga basaltic-andesitic sill
Main ore-related alteration	Bt ± Kfs	Qtz ± Ser; Bt ± Kfs ± Anh	Bt and rare Kfs	Bt ± Kfs ± Ab	Qtz-Ser in phyllite and Kfs in granodiorite porphyry	Bt ± Kfs
Major mineralization types	Disseminated and stockwork veinlet Cp ± Mo	Disseminated and veinlet Cp ± Mo ± Bn ± Cc ± Dg	Stockwork veinlet Cp and minor Bn, with minor disseminations.	Disseminated and veinlet Cp ± Bn ± Mt	Disseminated, stockwork, and veinlet Cp ± Mo	Disseminated and veinlet Cp ± Mt
Main vein types ⁴	EDM, PGS	Qtz-Anh-Py-Cp vein with Ser selvage to shallower Cc-Bn-Dg-Py veins with Ser selvage	Qtz-Cp-Py vein with Bt selvage, Qtz-Mt vein	A-, B-,	D-	Mainly Qtz-Bt-Mt-Cp vein
Causative magmatism	Inferred beneath the mineralization zone	Not reported	Not reported	Dacitic porphyry dikes	Granodiorite porphyry stock	Not reported
Syn-ore magmatism	dikes identified	Regional intrusive complex	Not reported	Yes	Yes	basaltic-andesitic volcanic sequence
References	Mercer and Reed, 2013	Hehnke et al., 2012	Phillips et al., 1974	Perelló et al., 2018	Mao et al., 2011	Meng et al., 2020 and this study

Notes:

- Information for hydrothermal overprinting of some of the deposits, such as Butte and Tongkuangyu, are not included.
- The ore tonnages and grades of the deposits are from the cited references or the USGS website (<https://www.usgs.gov/energy-and-minerals/mineral-resources-program>).
- The alteration-, mineralization-, and vein-types described below are for the main lithologies hosting the porphyry Cu mineralization.
- See definition of vein types (A-, B-, D-) in [Sillitoe et al. \(2020\)](#). EDM = early dark micaceous vein, PGS = quartz-chalcocopyrite-magnetite vein with pale-green sericitic envelope.

Abbreviations: Ab = albite, Anh = anhydrite, Bn = bornite, Bt = biotite, Cc = chalcocite, Cp = chalcopyrite, Dg = digenite, Kfs = K-feldspar, Mo = molybdenite, Mt = magnetite, Mus = muscovite, Py = pyrite, Qtz= quartz, Ser = sericite.

Chapter 4

Oxidized sulfur-rich arc magmas formed porphyry Cu deposits by 1.88 Ga

4.1 Abstract

Most known porphyry Cu deposits formed in the Phanerozoic and are exclusively associated with moderately oxidized, sulfur-rich, hydrous arc-related magmas derived from partial melting of the asthenospheric mantle metasomatized by slab-derived fluids. Yet, whether similar metallogenic processes also operated in the Precambrian remains obscure. Here we address the issue by investigating calc-alkaline plutonic rocks associated with the Haib porphyry Cu deposit in the Paleoproterozoic Richtersveld Magmatic Arc (southern Namibia), an interpreted mature island arc setting. High-precision uranium-lead geochronology constrains the emplacement of these plutonic rocks to ca. 1886–1881 Ma. Narrow ranges of Hf and O isotopes for magmatic zircons support a mantle-dominated source with minor crustal contributions and limited crustal assimilation during magma ascent. Estimation of fO_2 using independent oxybarometers based on zircon geochemistry and sulfur micro X-ray absorption near edge structure (S μ -XANES) spectroscopy of apatite inclusions in zircon reveal that the magmas were relatively oxidized ($\Delta FMQ+1-2$ log units). The relatively high S contents (up to 0.2 wt. %) of the apatite inclusions in zircon and titanite attest to high magmatic sulfur contents. These results indicate that moderately oxidized, sulfur-rich arc magma associated with porphyry Cu mineralization already existed in the late Paleoproterozoic, probably as a result of recycling of sulfate-rich seawater or sediments from the subducted oceanic lithosphere at that time.

4.2 Introduction

Porphyry Cu systems presently contribute ~75 % of the world's Cu production and of the known deposits most formed in Phanerozoic arc-related settings (Sinclair, 2007; Sillitoe, 2010). The arc-related calc-alkaline, intermediate magmas responsible for most known porphyry Cu deposit formation are hydrous, moderately oxidized ($\Delta\text{FMQ}+1$ to $+2$; where ΔFMQ is $f\text{O}_2$ in log units relative to the fayalite-magnetite-quartz mineral redox buffer), and sulfur-rich, reflecting partial melting of the asthenospheric mantle metasomatized by slab-derived oxidized fluids (Kelley and Cottrell, 2009; Zellmer et al., 2015; Richards, 2015). Chalcophile metals (e.g., Cu) behave as incompatible elements in moderately oxidized magma and are transported to upper crustal levels where they partition efficiently into exsolving S- and Cl-bearing magmatic-hydrothermal ore fluids to form economic deposits under optimal ore-formation conditions (Sillitoe, 2010, Richards, 2015).

The apparent rarity of porphyry Cu deposits in the Precambrian is attributed to poor preservation of upper crustal rocks in tectonically active environments, and/or unfavorable tectonomagmatic conditions which precluded their formation (Wilkinson and Kesler, 2007; Richards and Mumin, 2013). The predominance of ferrous iron and sulfide in terrigenous sediments, anoxic ocean water, and hydrothermally altered reduced submarine basalts during the Precambrian (Shields-Zhou and Och, 2011; Fakhraee et al., 2019; Stolper and Keller, 2018) suggest that a significant proportion of H_2S would have been released to the sub-arc mantle in subduction zones, thus maintaining stability of mantle sulfides during partial melting in the source region of arc magmas (Evans and Tomkin, 2011; Richards and Mumin, 2013; Stolper and Bucholz, 2019), depleting

juvenile silicate melts of chalcophile metals, and limiting the ore-forming potential of ascending magma (Candela, 1992, 1997).

The hypothesis that tectonomagmatic conditions in the Precambrian are unfavorable for porphyry Cu deposit formation remains poorly constrained because pervasive metamorphism, deformation, and alteration in Precambrian terrains have variably modified the primary mineralogy and textures of old rocks, rendering estimation of magmatic conditions and original composition difficult. Haib represents one of the largest and best-preserved Paleoproterozoic porphyry Cu deposits (indicated resource of 456.9 million tonnes at a Cu grade of 0.31 %, using a cut-off grade of 0.25 %, and minor Mo; <https://www.deepsouthresources.com/>) and only records minimal deformation and relatively low-grade metamorphism. Here we investigate the absolute timing of emplacement of the ore-related magmas at Haib using high-precision geochronology, and constrain the origin, and, in particular, the oxidation states and S contents of the magmas. Mineral inclusions in robust zircon and titanite were sought out to minimize potential effects of alteration and metamorphism. Contrary to previous knowledge (Richards and Mumin, 2013; Evans and Tomkin, 2011), our findings demonstrate that similar metallogenic processes for Phanerozoic porphyry Cu deposits operated at ~1.88 Ga, a period of rapid crustal growth, oxygenation of Earth's atmosphere and oceans, and sulfur cycling in subduction zones.

4.3 Results

4.3.1 Geological setting

The Haib deposit is hosted mainly by the high-K calc-alkaline intrusions of the Vioolsdrif Suite and subaerial volcanic rocks of the Orange River Group along the western part of the Paleoproterozoic Richtersveld Magmatic Arc (RMA) of southern Namibia (Minnitt, 1986; Reid

et al., 1987; Grumbley, 2015; Macey et al., 2017; Fig. 4.1, Supplementary Note 1 and Figs. A4.1, A4.2), which formed in a mature island-arc setting at 1.85–1.91 Ga (Reid et al., 1987; Macey et al., 2017). The pre-mineralization Orange River Group mainly contains plagioclase-phyric andesite porphyry and interleaved rhyolitic tuff (Fig. 4.1, Fig. A4.2). The Vioolsdrif Suite mainly comprises equigranular granodiorite, with quartz-monzonite enclaves, and diorite succeeded by shallower syn-ore granodiorite porphyry and leucocratic granodiorite porphyry crosscut by poorly mineralized and carbonate-altered aplite dikes (Fig. 4.1, Figs. A4.2, 4.3). Rocks in the RMA, including the Haib deposit, evolved along a fractionation trend controlled by amphibole and minor plagioclase as indicated by listric-shaped rare-earth element (REE) patterns, moderate negative Eu anomalies (Macey et al., 2017), and a negative relationship between Dy/Yb ratios and SiO₂ contents (Fig. 4.2).

Disseminated and veinlet chalcopyrite mineralization with minor magnetite is associated with biotite ± K-feldspar ± epidote ± anhydrite ± titanite ± rutile alteration locally overprinted by chlorite and sericite alteration (Figs. A4.1, 4.4; Minnitt, 1986, Grumbley, 2015). Early dark micaceous veins are more common than A-, B-, and D-type veins (Fig. A4.4; see terminology for the various vein types in Seedorff, 2005), which reflects relatively deep levels of exposure of the system. Emplacement pressure for the plutonic host rocks and mineralization is estimated at ~200–300 MPa (Minnitt, 1986), which is comparable to deeper parts of typical Phanerozoic porphyry Cu systems. The area underwent metamorphism of up to greenschist facies and localized intense shearing in the volcanic rocks during the ~1.1 Ga Namaqua orogeny (Jacobs et al., 2008).

4.3.2 High-precision U-Pb geochronology

Zircon U-Pb geochronology by laser ablation multi-collector inductively coupled plasma mass spectrometry (LA-MC-ICP-MS) and chemical abrasion isotope dilution thermal ionization mass spectrometry (CA-ID-TIMS) constrains the absolute timing of the crystallization of the igneous rocks and related mineralization. Zircons from two samples of andesite porphyry and one sample of rhyolitic tuff yielded LA-MC-ICP-MS upper concordia intercept ages of 1912 ± 10 Ma, 1892 ± 9 Ma, and 1892 ± 6 Ma, respectively (Fig. 4.3A, Fig. A4.5). Zircon from equigranular granodiorite, quartz monzonite enclave, and diorite of the Vioolsdrif Suite yielded LA-MC-ICP-MS upper concordia intercept ages of 1887 ± 7 Ma, 1886 ± 5 Ma, and 1875 ± 10 Ma, respectively (Fig. 4.3A, Fig. A4.5). These ages are consistent with ages for other rocks in the RMA (Grumbley, 2015; Macey et al., 2017).

Mitigation of Pb-loss in zircons from samples of mineralized granodiorite porphyry and leucocratic granodiorite porphyry, and aplite was accomplished using chemical abrasion, and the CA-ID-TIMS U-Pb isotopic system provides the most precise dates (Fig. 4.3A, Fig. A4.6). These three samples yielded weighted mean $^{207}\text{Pb}/^{206}\text{Pb}$ ages (Th-corrected) of 1885.47 ± 0.93 Ma, 1886.0 ± 1.6 Ma, and 1881.02 ± 0.71 Ma, respectively (Fig. 4.3A, Fig. A4.6). Mild chemical abrasion of six small zircon grains ($< 30 \mu\text{m}$) from one carbonate-altered aplite dike from the ore zone partially mitigated Pb loss, with five of the six grains yielding a weighted mean $^{207}\text{Pb}/^{206}\text{Pb}$ age (Th-corrected) of 1881.8 ± 1.2 Ma (Fig. 4.3A, Fig. A4.6). These results are interpreted to best constrain the emplacement age of the Vioolsdrif Suite and are consistent with the LA-ICP-MS zircon U-Pb age data (Fig. 4.3A). The age range between the granodiorite porphyry and the carbonate-altered aplite brackets the mineralization to 1883.6 ± 1.8 Ma, which broadly agrees, within uncertainty, with the LA-ICP-MS upper concordia intercept U-Pb age of 1891 ± 34 Ma for hydrothermal rutile associated with chalcopyrite mineralization (Fig. 4.3A, Fig. A4.7).

4.3.3 Zircon Hf-O isotopes

Xenocrysts are rare in zircons from the igneous rocks sampled. Some petrographically distinct cores identified as antecrysts yielded LA-ICP-MS $^{207}\text{Pb}/^{206}\text{Pb}$ dates that are indistinguishable from ages of the host rocks (Fig. A4.5). Zircons from these rocks yielded initial ϵ_{Hf} values of -2.6 ± 0.6 to -1.0 ± 0.9 (2σ , $n = 99$, -2.0 ± 1.6 on average) and $\delta^{18}\text{O}$ values of 5.56 ± 0.64 ‰ to 7.10 ± 0.39 ‰ (2σ , $n = 102$, 6.14 ± 1.19 ‰ on average; Fig. 4.3B, C). Considering the rarity of zircon inheritance, the narrow ranges of the isotope ratios for the igneous rocks are consistent with homogenized primary arc magma variably contaminated with recycled upper crustal materials (e.g., from an earlier arc nearby RMA; Macey et al., 2017) in its source region. The elevated zircon $\delta^{18}\text{O}$ values for the volcanic and porphyritic rocks compared to the equigranular rocks (Fig. 4.3C) indicate more contamination from the recycled upper crustal materials that had undergone low-temperature alteration (Valley et al., 2005). The near-constant Hf isotope ratios among the samples (Fig. 4.3B) suggest a limited effect of the crustal contaminants on the Hf isotopic systematics of the source and also support insignificant crustal assimilation during magma ascent.

4.3.4 Relatively oxidized magmas

The $f\text{O}_2$ of the causative Haib magmas, from which the mineralizing ore fluid evolved, is estimated using three independent oxybarometers (see methods in Wones, 1989; Dilles, 1987; Konecke et al., 2019; Loucks et al., 2020, Fig. 4.4A–C). Magmatic $f\text{O}_2$ is estimated using synchrotron-based micro X-ray absorption near-edge structure spectroscopy (μ -XANES) at the S K -edge to measure the $\text{S}^{6+}/\Sigma\text{S}$ ratios of zircon-hosted F-rich apatite inclusions remote from fractures (Figs. 4.4A, Fig. A4.8). Because most zircons yielded concordant U-Pb dates indicating closed system behavior (Figs. A4.5, 4.6), analysis of apatite inclusions in the zircons eliminates

the effects of post-crystallization metamorphism and/or alteration. The equant to sub-equant morphology of these monophase apatite inclusions and absence of other coeval silicate mineral inclusions are consistent with crystallization as early mineral phases under near-equilibrium, near-liquidus conditions (Fig. 4.4A, B). Based on thermodynamic models in Stock et al. (2018) that predict apatite halogen compositions evolve along different trajectories during volatile-undersaturated and water-saturated crystallization, these fluorapatite inclusions are interpreted to have crystallized prior to the melt reaching volatile saturation (Supplementary Note 2, Fig. A4.9). The μ -XANES data reveal that sulfur in apatite is dominantly S^{6+} (Fig. 4.4D, Fig. A4.10), and integrated $S^{6+}/\Sigma S$ peak area ratios (Fig. 4.4E) yield fO_2 values that range from $\Delta FMQ+0.85 \pm 0.08$ to $\Delta FMQ+1.07 \pm 0.11$ (1σ , $\Delta FMQ+0.89 \pm 0.04$ on average) based on the apatite oxybarometer experimentally calibrated at 1000 °C and 300 MPa (Konecke et al., 2019). Changes in temperature and pressure are reported to shift the sulfide-sulfate transition in fO_2 space for silicate glasses (Matjuschkin et al., 2016; Nash et al., 2019). Thus if we consider that the effect of temperature and pressure on silicate glasses is proportional to the effect of sulfur incorporation into apatite (Konecke et al., 2019), the P-T-corrected fO_2 values for the Haib plutonic and volcanic rocks are $\Delta FMQ+1.24 \pm 0.01$ and $\Delta FMQ+1.37 \pm 0.02$ (1σ), respectively (Fig. 4.4F; Supplementary Note 3). The results for the plutonic rocks are interpreted to provide the best estimate of the pre-degassed redox state of the ore-forming magmas.

The Ce, Ti, and age-corrected initial U concentrations in zircon from the syn-ore plutonic rocks (the diorite, granodiorite and quartz monzonite, granodiorite porphyries) yield magmatic fO_2 values ranging from $\Delta FMQ+1.3 \pm 0.3$ to $\Delta FMQ+2.1 \pm 0.6$ (1σ , $\Delta FMQ +1.9 \pm 0.6$ on average) using a new empirical oxybarometer (Loucks et al., 2020; see screening criteria of zircon geochemistry data in notes in Table A4.5). These results are consistent with the titanite +

magnetite + quartz assemblage in the diorite which constrains the redox state of the melt to be $>\Delta\text{FMQ}+0.7 \pm 0.1$ at 768 ± 23 °C (Wones, 1989; Dilles, 1987; Ferry and Watson, 2007; 1σ , temperature calculated using titanium-in-zircon thermometer; Fig. 4.2C, F), although the result is interpreted to be less reliable because of the difficulty in finding credible equilibrated mineral assemblage.

4.3.5 Sulfur-rich apatite and melt

Magmatic apatite inclusions in zircon and titanite from the Haib system contain relatively high S contents ranging from 0.11 ± 0.04 to 0.19 ± 0.08 wt. %; Fig. 4.4E, Table A4.9), which are comparable to those reported for basaltic-andesitic to rhyolitic arc magmas and igneous rocks associated with Phanerozoic porphyry Cu systems (Fig. 4.5A). Recent studies suggest that the partition coefficient for S between apatite and silicate melt ($D_{\text{S}^{\text{ap/m}}}$) varies with magmatic $f\text{O}_2$ and temperature and is not significantly affected by melt composition (Peng et al., 1997; Parat et al., 2011; Konecke et al., 2019). Because a $D_{\text{S}^{\text{ap/m}}}$ model involving all these parameters is not currently available, we developed a method based on published experimental results (Method 1) and used a published thermodynamic method (Method 2) to determine partition coefficients for S between apatite and silicate melt (see details in ‘Methods’ section), which in turn were used to estimate melt S contents for the Haib samples that range from 0.07 ± 0.03 to 0.17 ± 0.08 wt. % S (1σ , 0.11 ± 0.06 wt. % on average), and 0.02 ± 0.001 to 0.08 ± 0.04 wt. % S (1σ , 0.04 ± 0.03 wt. % on average), respectively. The two independent estimates of melt S content agree within one order of magnitude and are broadly similar to S concentrations in many Phanerozoic arc melts ($\text{SiO}_2 \geq 52$ wt. %, with limited degassing; Fig. 4.5B) and those associated with Phanerozoic porphyry Cu systems.

4.4 Discussion and Conclusion

The calc-alkaline arc-type magmas, from which the mineralizing fluid evolved, formed at ~1886–1881 Ma, thus coinciding with a period of rapid crustal growth (Condie, 1998) and supercontinent assembly in Earth history. Pervasive hydrothermal anhydrite, part of the potassic alteration stage, is associated with chalcopyrite mineralization in the Haib deposit and indicates the hydrothermal system was relatively oxidized and consistent with exsolution of hydrothermal fluids from a relatively oxidized ore-related magma. The pre-degassed magmas were moderately oxidized ($\Delta\text{FMQ}+1-2$) and sulfur-rich, which are salient characteristics for Phanerozoic arc magmatism.

The elevated magmatic $f\text{O}_2$ values of the Haib magmas relative to mid-oceanic ridge basalts (MORB; $\Delta\text{FMQ}-2-0$; Carmichael, 1991) are strongly reminiscent of Phanerozoic oxidized island arc magmas that are generally thought to originate from the oxidized sub-arc mantle (Ballhaus et al., 1990; Wood et al., 1990; Parkinson and Arculus, 1999; Kelley and Cottrell, 2009; Evans and Tomkin, 2011; Zellmer et al., 2015; Brounce et al., 2015; Benard et al., 2018; Bucholz and Kelemen, 2019; Stolper and Bucholz, 2019). Deep crustal garnet fractionation has recently been hypothesized to auto-oxidize magma for porphyry Cu deposit formation (Tang et al., 2018; Lee and Tang, 2020). However, the Haib rocks have listric REE patterns and moderately negative Eu anomalies which indicate low-pressure differentiation with amphibole \pm plagioclase fractionation (Fig. 4.2). Amphibole preferentially incorporates middle REEs over heavy REEs and garnet incorporates heavy REEs relative to light REEs, thus amphibole fractionation will decrease, but garnet fractionation will increase, residue melts of Dy/Yb ratios (Macpherson et al., 2006; Davidson et al., 2007). The decreasing Dy/Yb ratios with increasing SiO_2 content (Fig. 4.2)

support amphibole-dominated fractionation without or with minimal garnet influence, leading us to discount the possibility that the elevated magmatic fO_2 of the Haib magmas is a result of garnet fractionation. In addition, the narrow ranges of zircon Hf and O isotopic compositions combined with the rarity of zircon inheritance (i.e., xenocrysts) in the Haib plutonic rocks suggest that modification of the magmatic fO_2 by crustal contamination during magma ascent is insignificant.

Considering that modern plate tectonics or its equivalent may have, at least on a local scale, operated since 1.8–1.9 Ga or earlier (Möller et al., 1995; Weller and St-Onge, 2017; Francois et al., 2018; Yin et al., 2019), we argue that the Haib magmas are more likely derived from partial melting of the asthenospheric mantle (or mantle lithosphere) that was modified by oxidized slab-derived fluids in the Paleoproterozoic. This is consistent with the recent findings that thick layers of evaporites and an abrupt elevation of marine sulfate content (up to at least 10 mmol/kg, compared to modern seawater sulfate content of 28 mmol/kg) occurred at ~2.0 Ga (Lyons and Gill, 2010; Planavsky et al., 2012; Blättler et al., 2018; Steadman et al., 2020), which supports the hypothesis that surface sulfate would have been available to be recycled into the mantle since the middle Paleoproterozoic. Although the hydrothermally altered oceanic basalt at that time is considered to be relatively reduced (Stolper and Keller, 2018), the sulfate-rich fluid released from the oxidized sediments in the subducted oceanic lithosphere may have been able to oxidize the sub-arc mantle without direct addition of Fe^{3+} (de Hoog et al., 2001; Kelley and Cottrell, 2009), culminating in the formation of relatively oxidized and sulfur-rich magmas.

The oxidized and sulfur-rich features of the derivative basaltic to dacitic magma can delay high-volume sulfide saturation and deep-crustal loss of chalcophile metals, which is the first-order control required for the magma to form the preserved Paleoproterozoic porphyry Cu deposit

upon its emplacement in the upper crust (Streck and Dilles, 1998; Richards, 2003). Our findings suggest similar metallogenic processes for Phanerozoic porphyry Cu deposits have operated much earlier than generally considered, as recently suggested by others (Richards and Mumin, 2013; Evans and Tomkin, 2011).

4.5 Methods

4.5.1 Sample preparation

Sixty-two samples of volcanic and intrusive igneous rocks, including a minority of altered and vein-type samples, were collected from drill core and outcrops in October 2018. To investigate the nature of the magmatism, least-altered samples were targeted for collection, but most of the drill core samples are variably altered owing to proximity to the ore deposit. Nineteen of the petrographically least altered samples were chosen for analytical work (Table A4.1).

Zircons were separated from representative samples of the major igneous phases by traditional magnetic and density methods after electric-pulse disaggregation at Overburden Drilling Management Inc., Ottawa, Canada. Zircon grains devoid of cracks and mineral and/or fluid inclusions as well as inclusion-rich grains were hand-picked and mounted in separate sets of epoxy pucks and polished to expose their middle-sections. Magmatic zircon and titanite crystals, and contained mineral inclusions, as well as hydrothermal rutile, were characterized using a Tescan Vega 3 scanning electron microscope (SEM) with backscattered electron (BSE) imaging, cathodoluminescence (CL), and Bruker energy-dispersive spectroscopy (EDS) at Laurentian University.

4.5.2 Whole-rock geochemistry

Eighteen of the least altered samples collected from drill cores and outcrops from Haib were crushed and ground at Australian Laboratory Services (ALS), Sudbury, Canada for whole-rock geochemical analyses. The powdered samples were analyzed using X-ray fluorescence (XRF) and inductively coupled plasma-mass spectrometry (ICP-MS) with pre-fusion (lithium metaborate; CCP-PKG01 analytical package) at ALS, Vancouver, Canada. One secondary reference sample LK-NIP-1 (Nipissing diabase, https://www.mndm.gov.on.ca/sites/default/files/2018_geo_labs_brochure.pdf) was analyzed as an unknown to verify the analytical quality during the analytical session, and the results are consistent with standard values (see [Table A4.2](#)). Some elements of samples HB-23, HB-51, and HB-61 were duplicated. The results are reported in [Table A4.2](#).

4.5.3 LA-ICP-MS zircon U-Pb isotopes

Zircon uranium-lead (U-Pb) isotope and trace element analyses were conducted in the Mineral Exploration Research Centre – Isotope Geochemistry Laboratory (MERC–IGL) at Laurentian University. A 193 nm Photon Machines Analyte G2 ArF excimer laser equipped with a two-volume Helix II laser cell was used to ablate the zircons. To minimize the common lead contamination from surface material prior to ablation, the samples were polished using alumina powder, put in an ultrasonic bath with milli-Q water, and cleaned with ethanol by Kim wipe. The detailed instrumental parameters of laser ablation and ICP-MS, as well as data processing, for these analyses are listed in [Table A4.3](#).

The parameters for the laser were a fluence of 2 J/cm², a repetition rate of 7 Hz, and a spot size of 35 μm. Ablation duration was 10 seconds, leaving an estimated ablation pit depth of < 5 μm. The ablated aerosol downstream of the sample cell was split into two mass spectrometers for measuring the U-Pb isotope ratios and trace element abundances simultaneously ([Kylander-Clark](#)

[et al., 2013](#)). Uranium-lead isotopic ratios, and U, Th, and Pb concentrations were measured on a Thermo Scientific Neptune Plus multi-collector ICP-MS equipped with a Jet interface and nine Faraday cups, whereas trace elements were analyzed on a Thermo Scientific iCap triple-quadrupole (TQ) ICP-MS in single quad mode to ensure maximum sensitivity on low to intermediate mass range. Sixty seconds of background were measured at the beginning and end of each analytical session, with 30 seconds of background measured between each analysis.

Correction of laser-induced element fractionation, instrumental drift, and downhole fractionation was performed with the U-Pb Geochronology data reduction scheme implemented within Iolite v. 3.6 software ([Paton et al., 2010](#); [Paton et al., 2011](#)), with U-Pb isotope ratios normalized to the zircon primary reference material OGC-01 that was periodically dispersed into the analytical sessions. The secondary reference materials TanBrA and Grn were analyzed to monitor the accuracy and reproducibility of the unknown analyses, with results consistent with standard values ([Table A4.4](#)). Within-run variance in the measured ratios for OGC-01 was propagated into the 2SE uncertainty for all unknowns. No additional uncertainty propagation was applied to the $^{207}\text{Pb}/^{206}\text{Pb}$ ratios of the unknown analyses because long-term variance of $^{207}\text{Pb}/^{206}\text{Pb}$ ratios of the verification reference materials across all sessions is limited with statically acceptable MSWD (mean square of weighted deviates; that is, ~ 1). Concordia age calculation and data plotting were completed using Isoplot v. 4.15 ([Ludwig, 2012](#)), in which uranium decay constant uncertainties were not considered. The MSWD of the dates are statistically acceptable for population sizes at the 95 % confidence interval. Trace element data were processed using the internal standard data reduction scheme within Iolite v. 3.6 and normalized to the synthetic glass NIST610. The stoichiometric concentration of Si in zircon was assumed to be 15.284 wt. %.

synthetic glass NIST612 and zircon 91500 were used to verify the accuracy of the analyses. The results are reported in [Table A4.4](#).

4.5.4 CA-ID-TIMS zircon U-Pb isotopes

Chemical abrasion isotope dilution thermal ionization mass spectrometry (CA-ID-TIMS) U-Pb geochronology of single zircon crystals and fragments was undertaken at the Geochronology and Tracers Facility, British Geological Survey, Keyworth, the UK. Chemical abrasion was undertaken at 190 °C for 12 hours for samples HB-18, HB-29, and HB-51, within the exception of sample HB-20 that was leached at 180°C following the method in [Mattinson, 2005](#). The methodology for all other analytical procedures, instrumental conditions, corrections and data reduction follows that outlined in detail in [Tapster et al., 2016](#) using the ET2535 tracers ([McLean et al., 2015](#); [Condon et al., 2015](#)). Isotope ratio measurements were made using a Thermo Triton thermal ionization mass-spectrometer (TIMS), with the U decay constants of [Jaffey et al. \(1971\)](#), the $^{238}\text{U}/^{235}\text{U}$ ratio of ([Hiess et al., 2012](#)), and the ^{230}Th decay constants of [Cheng et al., 2000](#). The $^{206}\text{Pb}/^{238}\text{U}$ and $^{207}\text{Pb}/^{206}\text{Pb}$ dates were corrected for initial ^{230}Th disequilibrium ([Schärer, 1984](#)) using a value of $\text{Th}/\text{U} [\text{magma}] = 3.5$. The results are reported in [Table A4.5](#).

The best estimate of emplacement age was selected from the population of concordant data where the $^{207}\text{Pb}/^{206}\text{Pb}$ weighted mean date had a statistically acceptable MSWD for the given population size at 95 % confidence interval. For zircons from sample HB-20, the Pb loss has not been completely mitigated, we report the weighted mean $^{207}\text{Pb}/^{206}\text{Pb}$ age with acceptable MSWD of 0.15. All uncertainties are reported at 2σ level considering analytical and tracer calibration uncertainty but excluding the contribution from uncertainties of decay constants.

4.5.5 Rutile U-Pb isotopes

In-situ U-Pb isotopes of rutile in thin section were measured using the Thermo Neptune Plus MC-ICP-MS coupled to a 193 nm Photon Machines Analyte G2 laser equipped with a two-volume Helex II laser cell in MERC-IGL at Laurentian University. The laser ablation was carried out with a fluence of 2–3 J·cm⁻², a repetition rate of 7 Hz, and a spot size of 35 μm. Each analysis lasted for 35 s. Primary reference material was R10 (1095 ± 4.7 Ma; [Luvizotto et al., 2009](#)) and secondary materials were R19 (489.5 ± 0.9 Ma; [Zack et al., 2011](#)) and Sugluk (1723 ± 6.8 Ma; [Bracciali et al., 2013](#)), which were periodically analyzed throughout the analytical run. The detailed instrumental parameters of laser ablation and ICP-MS, as well as data processing, are listed in [Table A4.3](#). The results for secondary reference materials of rutile are reported in [Table A4.6](#) and are in agreement with the published standard values. Results for unknown analyses are also reported in [Table A4.6](#).

4.5.6 Zircon Lu-Hf isotopes

Lu-Hf isotopes were measured on the same spots as O isotopes and some of the zircon U-Pb isotope and trace element analyses. The same analytical equipment as for the U-Pb analyses were used. Laser ablation was carried out with a fluence of 6 J·cm⁻², a repetition rate of 7 Hz, and a spot size of 40 μm. Ablation duration was 60 s, leaving an estimated ablation pit depth of ~30 μm. One primary and five secondary reference standards (Plesovice; 91500, R33, FC1, OGC, MUN1, and MUN3) were periodically analyzed during the analytical runs. The details for the instrumental parameters of laser ablation and ICP-MS, as well as data processing, for these analyses are listed in [Table A4.3](#).

The raw Hf isotope data were processed in Iolite v.3.6, with baseline subtraction, instrumental drift, and mass bias corrections performed with a modified version of the Hf isotope data reduction scheme. Within-run variance in the measured ratios for Plesovice was propagated into

the 2SE uncertainty for all unknowns. Similar to the U-Pb isotopic analyses, no additional uncertainty propagation was applied to the Hf isotope ratios for the unknown analyses. Instrumental mass bias and interference correction factors were determined within the session through the iterative calculation of the effective $^{176}\text{Yb}/^{173}\text{Yb}$ ratio required to yield identical $^{176}\text{Hf}/^{177}\text{Hf}$ ratios of MUN1 and MUN3. The effective (mass bias-corrected) within-session $^{176}\text{Yb}/^{173}\text{Yb}$ was then applied in the interference correction for all analyses as part of the data reduction scheme. The corrected $^{176}\text{Hf}/^{177}\text{Hf}$ ratios are 0.282309 ± 30 (2σ , $n = 13$) for 91500, 0.282750 ± 22 (2σ , $n = 13$) for R33, 0.282184 ± 31 (2σ , $n = 13$) for FC1, 0.280558 ± 54 (2σ , $n = 13$) for OGC, and 0.282127 ± 19 (2σ , $n = 10$) for MUN. These results are identical to the published values within uncertainties (Wiedenbeck et al., 1995; Fisher et al., 2014; Kemp et al., 2017). The initial $^{176}\text{Hf}/^{177}\text{Hf}$ ratios and $\epsilon_{\text{Hf}}(t)$ values are calculated using a ^{176}Lu decay constant of $1.867 \times 10^{-11}/\text{a}$ (Söderlund, 2004) and the chondritic parameters from Bouvier et al. (2008). The results are reported in Table A4.7.

4.5.7 Zircon O isotopes

Oxygen isotopes (^{18}O and ^{16}O) in zircon were analyzed using a Cameca IMS 1280 multi-collector ion microprobe in the Canadian Centre for Isotopic Microanalysis at the University of Alberta. Most of the samples were analyzed in session IP19029 prior to U-Pb-Lu-Hf isotope analyses, except for samples HB-30 and HB-33 which were analyzed in session IP20013 and the analyses were conducted on different sets of grains for U-Pb-Lu-Hf isotopes. Counts of $^{16}\text{O}^1\text{H}/^{16}\text{O}$ for zircons in the session IP19029, in which some of the samples were collected from the ore deposit, were simultaneously analyzed with the O isotopes to monitor the effect of hydrothermal alteration. Most of the analyses yielded low $^{16}\text{O}^1\text{H}/^{16}\text{O}$, and only a few analyses having significantly higher values than the standards ($\Delta \text{OH} > 40 \%$) were excluded.

The zircons were analyzed using a 20 keV $^{133}\text{Cs}^+$ primary beam with a spot size of $\sim 10\ \mu\text{m}$. Detailed instrumental parameters have been described by [Rezeau et al. \(2016\)](#). Instrumental mass fractionation was monitored by repeated analysis of the zircon primary reference material (S0081, $\delta^{18}\text{O}_{\text{VSMOW}} = +4.87$; [R. Stern, unpublished laser fluorination data, University of Oregon](#)) after every four unknown analyses. The $^{18}\text{O}/^{16}\text{O}$ - dataset for S0081 was processed collectively for two analytical sessions ($n = 64$ and 12), yielding standard deviations of $0.12\ \text{‰}$ and $0.09\ \text{‰}$, respectively, following correction for a systematic within-session drift of $\leq 0.4\ \text{‰}$. Zircon secondary reference material TEM2 was analyzed following every eight unknown analyses. Multiple spots on different TEM2 grains yielded weighted mean $\delta^{18}\text{O}_{\text{VSMOW}}$ values of $+8.23 \pm 0.12\ \text{‰}$ (SD, $n = 42$, MSWD = 1.07) for session IP19029 and $+8.27 \pm 0.09\ \text{‰}$ (SD, $n = 23$, MSWD = 0.74) for session IP20013, which is consistent with the published standard $\delta^{18}\text{O}_{\text{VSMOW}}$ value of $+8.2\ \text{‰}$ ([Black et al., 2004](#)). The individual spot uncertainties of $\delta^{18}\text{O}_{\text{VSMOW}}$ for unknowns in the two sessions have medians of $\pm 0.25\ \text{‰}$ and $\pm 0.20\ \text{‰}$ at 95% confidence, which includes errors relating to within-spot counting statistics, geometric effects, and correction for instrumental mass fractionation. The results are reported in [Table A4.8](#).

4.5.8 Electron microprobe analysis

Major and minor element compositions of apatite were acquired using a Cameca SX100 electron microprobe analyzer with wavelength-dispersive spectroscopy (WDS) at Ontario Geosciences Laboratory, with results reported in [Table A4.9](#). An accelerating voltage of 15 keV, a beam current of 10 nA, and rastered beam sizes of 2 or 5 μm (depending on the apatite grain size) were used for all element analyses. X-ray lines, analyzing crystals, and counting times (for both peak and background measurements) were as follows: P $K\alpha$, LPET5, 15s; Si $K\alpha$, LTAP2, 20s; Al $K\alpha$, LTAP2, 20s; Mg $K\alpha$, LTAP2, 20s; Ca $K\alpha$, LPET5, 15s; Mn $K\alpha$, LiF4, 40s; Fe $K\alpha$, LiF4, 40s; Sr

Lα, LPET5, 30s; Na *Kα*, LTAP2, 20s; K *Kα*, PET3, 20s; S *Kα*, LPET3, 60s; F *Kα*, PCO, 20s; Cl *Kα*, LPET5, 20s; Zr *Lα*, LPET5, 5s. The detection limits for these elements were calculated to be as follows: P₂O₅, 680 ppm; SiO₂, 130 ppm; Al₂O₃, 140 ppm; MgO, 140 ppm; CaO, 340 ppm; MnO, 520 ppm; FeO, 520 ppm; SrO, 850 ppm; Na₂O, 170 ppm; K₂O, 140 ppm; SO₃, 270 ppm; F, 880 ppm; and Cl, 190 ppm.

Due to the small size of the apatites analyzed, zirconium concentrations were measured to monitor the contamination from the host zircon crystal. Analyses with ZrO₂ > 1 % were excluded. The decomposition of apatite caused by electron beam damage (Stormer et al., 1993; Goldoff et al., 2012) under the conditions used for this study was also tested (see Table A4.9). The compositions of the test samples (beam size of 2 μm) typically show, with analytical time: (1) an increase or decrease in F count rate; (2) slightly decrease in Cl count rate; and (3) a nearly constant S count rate. The test demonstrates that the S and Cl abundances are reliable and the F concentrations might not be well constrained. Beam damage of apatite obtained at a larger beam size of 5 μm can be minimized, particularly for apatite grains with c-axis perpendicular to the electron beam.

4.5.9 Micro X-ray absorption near-edge structure spectroscopy (μ-XANES)

To measure the sulfur oxidation states of the pristine apatite inclusions (i.e., previously not analyzed by electron microprobe), micro X-ray absorption near-edge structure spectroscopy at the sulfur K-edge (S μ-XANES) was conducted at the Advanced Photon Source (APS) of the Argonne National Laboratory in Chicago, IL, USA, and at the Swiss Light Source (SLS) of the Paul Scherrer Institute in Villigen, Switzerland. The analyses at the APS were performed at the GSECARS X-ray microprobe beamline on sector 13-ID-E and those at the SLS were performed at the PHOENIX X07MA/B tender X-ray microspectroscopy beamline. The APS beamline has

an energy range of 2.3–28 keV, whereas the SLS beamline has an energy range of 0.35–8 keV. Both beamlines use undulator X-ray sources to provide photons for μ -XANES measurements and employ double crystal (silicon 111) monochromators to generate monochromatic radiation focused with a Kirkpatrick-Baez (KB) mirror system. The monochromatic beam was focused down to a size of $2 \times 2 \mu\text{m}$ at APS and $3 \mu\text{m}$ diameter at SLS. The energy at both beamlines was calibrated to the ~ 2482 eV white line of sulfate, using clear double-sided sticky tape at APS (2481.8 eV) and powdered CaSO_4 at SLS (2482 eV). Differences in the calibration are attributed to slight differences in monochromator calibration and setup.

To minimize the Compton and Rayleigh scattering contribution, the polished surface of the samples was positioned at 45° from the incoming beam. We followed the collection and processing procedures described in [Konecke et al. \(2017, 2019\)](#). X-ray fluorescence maps were acquired at the beamlines immediately preceding spectra collection to locate the apatite inclusions in zircon. The incoming energy for maps was fixed at 2482 eV and measured fluorescence lines of S, Si, P, and Al to discriminate different phases in the maps (e.g., zircon, apatite, and epoxy). The dwell time of the detector was set at 1 sec for each $3 \times 3 \mu\text{m}$ pixel at SLS and 0.02 sec for each $2 \times 2 \mu\text{m}$ pixel at APS. At both beamlines sulfur fluorescence spectra were collected using four-element silicon drift diode detector arrays positioned at an angle of 90° to the incident beam and corrected for detector dead time.

The S μ -XANES spectra were collected by scanning the incident beam energy from 2440 to 2550 eV using a slightly different setup at each beamline, but all scans were divided into the same three energy regions: i) a pre-edge region from 2440–2460 eV, ii) the edge region from 2460–2500 eV, and iii) a post-edge region from 2500–2550 eV. At APS, step sizes of 1 eV, 0.3 eV, and 2 eV were used in the pre-edge, edge, and post-edge regions, respectively, while at SLS

step sizes of 2 eV, 0.3 eV, and 2 eV were used. The counting duration for all regions at APS was 3 seconds and at SLS was 1 second per step in the pre- and post-edge regions and 2 seconds per edge step. The total scan duration was ~9 minutes at APS and ~12 minutes at SLS, with differences in beamline mechanics and scan setup resulting in different scan durations. The European Synchrotron Radiation Facility S K-edge XANES spectra database was used to identify the S^{6+} (~2482 eV; anhydrite), S^{4+} (~2478 eV; sodium sulfite), and S^{2-} (~2470 eV; pyrrhotite) peak energy position for the unknowns. Spectra of pyrrhotite ($Fe_{1-x}S$) and anhydrite powder ($CaSO_4$) are shown in [Fig. A4.10A](#) to illustrate the differences in S^{2-} from S^{6+} spectra.

Two scans were collected at each point to improve counting statistics and monitor for beam damage caused by irradiation of the focused X-ray beam and contribution from other phases (e.g., host zircon, epoxy). Beam damage manifests as the growth or shrinkage of absorption peaks from the first to second scan and can easily be identified. Beam damage was not observed in any apatite spectra collected here, which is consistent with previous observations that apatite is robust and does not easily incur beam damage at the energies used for S μ -XANES, even after more than one hour of beam exposure ([Konecke et al., 2017, 2019](#)). However, contribution from the host zircon was observed, most severely on relatively small apatite grains (~4 μm or less in diameter). Zircon contribution to the spectra was characterized by an intense peak that begins ~2540 eV in the post-edge region, corresponding to the Zr $L\gamma_2$ transition ([Fig. A4.10B](#)). The intensity of the Zr peak was less than half the intensity of the S^{6+} peak in apatite in spectra collected on large apatite grains (> 10 μm diameter) and the spectra was discarded if the Zr peak intensity surpassed and drowned out the S^{6+} signal, illustrated in [Fig. A4.10B](#). Scans collected on host zircon showed very low sulfur counts and no characteristic edge step, therefore any contribution from zircon to the sulfur spectra is considered insignificant. Following the criteria

described in [Konecke et al. \(2019\)](#), S μ -XANES spectra were monitored for contribution of sulfur-bearing epoxy. Any spectra exhibiting contribution from other phases were discarded.

S μ -XANES spectra collected from the same apatite grain were normalized against the incident flux (I_0), the pre- and post-edge set to 0 and 1, respectively, and were merged using the XAS software analysis package Athena or Iffeffit ([Ravel et al., 2005](#)). Peak positions and areas were then fitted and calculated using the Fityk software version 1.3.1 ([Wojdyr 2010](#)), from which the integrated $S^{6+}/\Sigma S$ peak area ratios were calculated and input to the calibration equation in [Konecke et al. \(2019\)](#) to calculate the values of $\log fO_2$ relative to FMQ.

4.5.10 Methods in estimating melt sulfur content

Method 1 uses experimental $D_S^{ap/m}$ calculated for a mafic melt varying with $\log fO_2$ at a temperature of ~ 1000 °C and pressure of ~ 300 MPa ([Konecke et al., 2019](#)). The effect of temperature (from ~ 1000 °C to the calculated *model* apatite saturation temperature; [Piccoli and Candela, 1994](#)) was evaluated using the $D_S^{ap/m}(T)$ from [Parat and Holtz \(2004\)](#) that was derived for an oxidized rhyolitic melt. Although [Peng et al. \(1997\)](#) also reported an equation relating the $D_S^{ap/m}$ with temperature ($\ln(D_S^{ap/m}) = 21330/T(K) - 16.2$), the equation does not consider the effects of depleting phosphate concentration in the melt following apatite saturation with decreasing temperature ([Streck and Dilles, 1998](#)) and the experiment in ([Konecke et al., 2019](#)) conducted at ~ 800 °C may not represent the equilibrium S content because of early apatite crystallization from melt during annealing ([Parat and Holtz, 2004](#)). We therefore chose not to use it. The combined equation can be expressed as:

$$S_{ap} = D_S^{ap/m}(fO_2) \times S_{melt} \times [D_S^{ap/m}(AST) / D_S^{ap/m}(1000\text{ °C})]$$

The values of $D_{S^{ap/m}}^{(fO_2)}$ are 0.85 and 1 for plutonic and volcanic rocks at FMQ + 1.24 and +1.37, whereas $D_{S^{ap/m}}^{(AST)}$ are estimated to be 10.2, 13.3 ± 0.2 , and 10.7 at temperatures of 867 °C (HB-24, andesite porphyry), 914 ± 4 °C (HB-18 and HB-51, granodiorite porphyries; HB-32, granodiorite; and HB-30, diorite), and 951 °C (HB-33; quartz monzonite enclaves), respectively.

Method 2 to calculate the partition coefficient of S between apatite and melt is derived from [Streck and Dilles \(1998\)](#) and involves activities of phosphate, sulfate, and silica, as well as percentages of crystals, and is sensitive to the apatite saturation temperature (see details in [Streck and Dilles, 1998](#)). We followed the method of the linear negative relationship between $D_{S^{ap/m}}$ and temperature and assumed $D_{S^{ap/m}}^{(AST)} = 3.91$ at 930 °C ([Peng et al., 1997](#)). The $D_{S^{ap/m}}$ are estimated to be 7.7, 4.9 ± 0.2 , and 2.7 at temperatures of 867 °C (HB-24, andesite porphyry), 914 ± 4 °C (HB-18 and HB-51, granodiorite porphyries; HB-32, granodiorite; and HB-30, diorite), and 951 °C (HB-33, quartz monzonite enclave), respectively.

4.6 Supplementary Information

4.6.1 Supplementary Note 1: the Haib porphyry Cu deposit

The Haib porphyry Cu deposit is located in the western Richtersveld Magmatic Arc of southern Namibia, where the arc assemblage mainly comprises the greenschist facies Orange River Volcanic Group and underlying younger Vioolsdrif Plutonic Suite ([Fig. 4.1](#)). In Haib, the Vioolsdrif Plutonic Suite is remarkably undeformed compared to the localized intense deformation of the Orange River Volcanic Group along the NW-trending shear zones ([Fig. 4.1](#)), which may reflect rheological contrasts between strong crystalline plutonic rocks and the weaker phyllosilicate-rich volcanic rocks. General lack of deformation in the volcanic rocks within Haib

and near contacts with the granodiorite intrusions may indicate local induration by contact metamorphism prior to the regional deformation. Metamorphism to greenschist grade occurs during the ~1.1 Ga Namaqua Orogeny (Jacobs et al., 2008) and has variably affected the rocks in Haib.

Lithology

The rocks in the Haib deposit include pre-mineralization plagioclase-phyric andesite porphyry and interleaved rhyolitic tuff, syn-mineralization granodiorite porphyry and leucocratic granodiorite porphyry, and post-mineralization aplite dikes (Figs. A4.1–4.3). The rocks in the regional batholith (i.e., Vioolsdrif Plutonic Suite) mainly include unmineralized equigranular granodiorite, diorite, and aplite (Figs. A4.1, A4.2). The petrographic descriptions for the samples studied are listed in Table A4.1.

The granodiorite porphyry locally contains xenoliths of plagioclase-phyric andesite porphyry and is intruded with a sharp contact by leucocratic granodiorite porphyry dikes, as observed in drill core (Fig. A4.2C–E). Granodiorite in the batholith locally contains quartz monzonite enclaves (Fig. A4.2F). Aplite dikes cut the granodiorite porphyry and intrude equigranular granodiorite of the batholith (Fig. A.4.2H and I). The dike is poorly mineralized and is crosscut by late quartz-ankerite veins, which is interpreted to have formed later than the main porphyry Cu-mineralization stage.

Note that the plagioclase-phyric andesite porphyry, granodiorite porphyry, and leucocratic granodiorite porphyry are formerly referred to as feldspar porphyry, quartz-feldspar porphyry, and quartz-feldspar porphyry II (Minnitt, 1986; Grumbley, 2015), and reports from the Deep Resources, Inc. A phase of quartz biotite porphyry is also identified, but its geochronology and

lithogeochemical composition are comparable to the granodiorite porphyry (Grumbley, 2015). We therefore argue that petrographic differences may reflect various degrees of alteration. A mineralized dioritic feldspar porphyry dike containing granodiorite porphyry xenolith is identified (Fig. A4.1B), which is interpreted to be a breccia (Grumbley, 2015) and is not studied here.

Alteration

Alteration at Haib has been described in detail in Minnitt (1986) and Grumbley (2015), and the noted alteration assemblages are comparable to Phanerozoic porphyry Cu systems (Lowell and Guilbert, 1970; Sillitoe, 2010), which include early potassic alteration with local overprinting by albite, chlorite, and sericite alteration types (Fig. A4.1C). Pervasive biotite and minor K-feldspar alteration are commonly associated with epidote, anhydrite, muscovite, and minor tourmaline, titanite, and rutile (Fig. A4.4A–F). Epidote is rarely associated with potassic alteration and mineralization in typical Phanerozoic porphyry Cu systems, and its presence in Haib may reflect the hydrothermal fluid being more calcic. Local K-feldspar selvages are seen around veins, and most of this alteration has associated minor molybdenite mineralization.

Albite alteration is rare and was only identified in the granodiorite porphyry at a depth of ~780 m in drill hole TCDH-10 (Fig. A4.1C). It is characterized by replacement of K-feldspar with albite and is associated with low-Cu grades.

Chlorite alteration is mainly observed in the plagioclase-phyric andesite porphyry (Fig. A4.2A) and part of the granodiorite porphyry intrusion (Fig. A4.2H). Two stages of epidote-chlorite alteration are identified in the plagioclase-phyric andesite porphyry (Figs. A4.2A, 4.4G), which

may be associated with thermal metamorphism of this unit during intrusion of the granodiorite porphyry and later hydrothermal alteration (Grumbley, 2015).

Sericite alteration is locally seen in drill core and mainly replaces plagioclase and biotite (Fig. A4.4H). At the property surface, which is considered as the shallow levels of the system, the potassic alteration is locally overprinted by sericite alteration whereby sericite completely replaces plagioclase.

Regional metamorphism during Namaqua Orogeny (Jacobs et al., 2008) is mainly characterized by the presence of epidote, sericite, and minor chlorite, and has variably affected all of the rock types in the area.

Veining and mineralization

The deposit contains disseminated and veinlet chalcopyrite ± pyrite mineralization mainly associated with biotite ± K-feldspar ± anhydrite ± titanite ± rutile ± epidote alteration. Magnetite is exceptionally rare. The early dark micaceous (EDM) alteration selvages contain biotite ± epidote ± muscovite ± K-feldspar ± albite ± titanite ± rutile which are crosscut by sinuous and milky quartz A veins (Fig. A4.4D, E).

The sinuous quartz A veins, with granular textures, contain relatively minor amounts of sulfide minerals, mainly chalcopyrite, and are in equilibrium with potassic alteration in the wall rock, but also locally have narrow K-feldspar alteration halos (Fig. A4.4F).

Quartz ± molybdenite ± chalcopyrite ± pyrite B veins are rarely found and pyritic D veins are minor. The D veins with chlorite-sericite (in the plagioclase-phyric andesite porphyry) or feldspar-destructive sericite (in the granodiorite porphyry) alteration halos follow the main stage

of Cu mineralization (Fig. A4.4G, H). The lack of widespread sericite alteration and B and D veins may reflect the relatively deeper level of the system. The localized quartz-tourmaline veins seem to have not introduced significant sulfide mineralization (Fig. A4.4J). Carbonate veins crosscut the quartz-tourmaline veins and are similarly barren.

4.6.2 Supplementary Note 2: apatite crystallized prior to volatile saturation

Thermodynamic models in Stock et al. (2018) predict that apatite halogen compositions evolve along different trajectories during volatile-undersaturated and water-saturated crystallization. (1) During volatile-undersaturated crystallization, the X_F/X_{OH} ratio decreases while the X_{Cl}/X_{OH} ratio (X_{Cl} , X_F , and X_{OH} are mole fractions of Cl, F, and OH in apatite) varies depending on the exact values of the partition coefficients for F, Cl, and OH between apatite and melt. (2) Because the partition coefficient for Cl in the fluid is much higher than for F (Webster et al., 2009; Borodulin et al., 2019), during water-saturated crystallization the apatite X_{Cl}/X_{OH} ratio sharply decreases with constant or slightly increasing X_F/X_{OH} ratio.

To evaluate the relative timing of crystallization of titanite/zircon-hosted apatite to volatile saturation in parent melt for Haib, we plot apatite halogen compositions in Fig. A4.9. We restrict the plotting to analyses containing Cl content above the detection limit (190 ppm), and these analyses are mainly for samples HB-30 (diorite) and HB-51 (leucocratic granodiorite porphyry). One single analysis is also available for granodiorite (sample HB-34) but cannot form a trend in itself, and is therefore not included. The c-axis of most of the apatite grains are perpendicular to the electron beam, so that beam damages are interpreted to have been minimized (see the ‘Methods’ section in the main text’).

The apatite X_F/X_{OH} ratio decreases with decreasing X_{Cl}/X_{OH} ratio, which is consistent with the modeling result for apatite crystallized in a volatile-undersaturated environment in [Stock et al. \(2018\)](#), suggesting that the apatites crystallized earlier than magmatic degassing. This is also consistent with the fact that apatite from individual samples yielded limited compositional variability ([Table A4.9](#)) and lacks zoning ([Fig. A4.9](#)).

4.6.3 Supplementary Note 3: P-T correction of magmatic fO_2 from apatite S μ -XANES data

In silicate glasses, it has been demonstrated that a decrease in temperature of 100 °C and a decrease in pressure of 300 MPa may result in an approximate deviation of $\Delta FMQ + 0.5$ and -0.2 , respectively ([Matjuschkin et al., 2016](#); [Nash et al., 2019](#)). Given that apatite may crystallize as a near-liquidus phase, we use the *model* apatite saturation temperature (AST; [Piccoli and Candela, 1994](#)) to constrain the temperature at which the majority of the zircon-hosted apatite crystallized. The P-T-corrected magmatic fO_2 for the plutonic rocks ($n = 4$, $AST = 914 \pm 4$ °C for granodiorite and diorite emplaced at ~ 200 – 300 MPa ([Minnitt, 1986](#)); samples HB-18, HB-30, HB-32, and HB-51) yielded a narrow range of $\Delta FMQ + 1.22$ to $+1.25$ (1σ , 1.24 ± 0.01 on average). For subaerial volcanism, which presumably erupted at near-atmospheric pressure, results yielded an AST of 868 ± 1 °C ($n = 2$), the average $\log fO_2$ values for samples HB-24 (plagioclase-phyric andesite porphyry) and HB-28 (rhyolitic tuff) are $\Delta FMQ + 1.37 \pm 0.02$ (1σ).

4.7 Acknowledgements

The research was supported by Natural Sciences and Engineering Research Council of Canada Discovery Grant (RGPIN/5082-2017) and Canada First Research Excellence Fund through a Metal Earth thematic project to J. P. Richards, as well as a student research grant from the Geological Society of America and a China Scholarship Council award to X. Y. Meng. We

acknowledge the access permission to the drill cores and exploration database, and the logistic assistance from P. Leveille and V. Stuart-Williams at the Deep-South Resources Inc. We appreciate the assistance from D. Crabtree at Ontario GeoLabs on electron microprobe analyses. We acknowledge the Paul Scherrer Institut, Villigen, Switzerland at beamline X07MB for provision of synchrotron radiation beamtime and we thank Drs. Thomas Huthwelker and Camelia Borca for assistance. This research also used synchrotron resources of the Advanced Photon Source, a U.S. Department of Energy (DOE) Office of Science User Facility operated for the DOE Office of Science by Argonne National Laboratory under Contract No. DE-AC02-06CH11357. We thank Drs. Antonio Lanzirotti and Matthew Newville of Sector 13-ID-E of APS. S.R.T. and L.R. acknowledge financial support from NERC FAMOS NE/P01724X/1 grant and DSI-NRF Centre of Excellence, University of Johannesburg, respectively.

4.8 References

- Ballhaus, C., Berry, R. F., and Green, D. H., 1990, Oxygen fugacity controls in the Earth's upper mantle. *Nature*, v. 348, p. 437–439.
- Benard, A., Klimm, K., Woodland, A. B., Arculus, R. J., Wilke, M., Botcharnikov, R. E., Shimizu, N., Nebel, O., Rivard, C., and Ionov, D. A., 2018, Oxidising agents in sub-arc mantle melts link slab devolatilisation and arc magmas: *Nature Communications*, v. 9, p. 3500.
- Black, L. P., Kamo, S. L., Allen, C. M., Davis, D. W., Aleinikoff, J. N., Valley, J. W., Mundil, R., Campbell, I. H., Korsch, R. J., and Williams, I. S., 2004, Improved $^{206}\text{Pb}/^{238}\text{U}$ microprobe geochronology by the monitoring of a trace-element-related matrix effect; SHRIMP, ID-TIMS, ELA-ICP-MS and oxygen isotope documentation for a series of zircon standards: *Chemical Geology*, v. 205, p. 115–140.
- Blättler, C. L., Claire, M. W., Prave, A. R., Kirsimäe, K., Higgins, J. A., Medvedev, P. V., Romashkin, A. E., Rychanchik, D. V., Zerkle, A. L., Paiste, K., Kreitsmann, T., Millar, I. L., Hayles, J. A., Bao, H., Turchyn, A. V., Warke, M. R., and Lepland, A., 2018, Two-billion-year-old evaporites capture Earth's great oxidation: *Science*, v. 360, p. 320–323.
- Borodulin, G. P., Chevychelov, V. Y., and Zaraysky, G. P., 2009, Experimental study of partitioning of tantalum, niobium, manganese, and fluorine between aqueous fluoride fluid and granitic and alkaline melts: *Doklady Earth Sciences*, 2009, p. 868–873.
- Bouvier, A., Vervoort, J. D., and Patchett, P. J., 2008, The Lu–Hf and Sm–Nd isotopic composition of CHUR: Constraints from unequilibrated chondrites and implications for the

- bulk composition of terrestrial planets: *Earth and Planetary Science Letters*, v. 273, p. 48–57.
- Bracciali, L., Parrish, R. R., Horstwood, M. S. A., Condon, D. J., and Najman, Y., 2013, UPb LA-(MC)-ICP-MS dating of rutile: New reference materials and applications to sedimentary provenance: *Chemical Geology*, v. 347, p. 82–101.
- Brounce, M., Kelley, K. A., Cottrell, E., and Reagan, M. K., 2015, Temporal evolution of mantle wedge oxygen fugacity during subduction initiation: *Geology*, v. 43, p. 775–778.
- Bucholz, C. E., and Kelemen, P. B., 2019, Oxygen fugacity at the base of the Talkeetna arc, Alaska: *Contributions to Mineralogy and Petrology*, v. 174, p. 79.
- Candela, P. A., 1997, A Review of Shallow, Ore-related Granites: Textures, Volatiles, and Ore Metals: *Journal of Petrology*, v. 38, p. 1619–1633.
- Candela, P. A., 1992, Controls on ore metal ratios in granite-related ore systems: an experimental and computational approach: *Earth and Environmental Science Transactions of The Royal Society of Edinburgh*, v. 83, p. 317–326.
- Carmichael, I. S. E., 1991, The redox states of basic and silicic magmas: a reflection of their source regions?: *Contributions to Mineralogy and Petrology*, v. 106, p. 129–141.
- Cheng, H., Edwards, R. L., Hoff, J., Gallup, C. D., Richards, D. A., and Asmerom, Y., 2000, The half-lives of uranium-234 and thorium-230: *Chemical Geology*, v. 169, p. 17–33.
- Condie, K. C., 1998, Episodic continental growth and supercontinents: a mantle avalanche connection?: *Earth and Planetary Science Letters*, v. 163, p. 97–108.

- Condon, D. J., Schoene, B., McLean, N. M., Bowring, S. A., and Parrish, R. R., 2015, Metrology and traceability of U–Pb isotope dilution geochronology (EARTHTIME Tracer Calibration Part I): *Geochimica et Cosmochimica Acta*, v. 164, p. 464–480.
- Davidson, J., Turner, S., Handley, H., Macpherson, C., and Dosseto, A., 2007, Amphibole “sponge” in arc crust?: *Geology*, v. 35, p. 787–790.
- Dilles, J. H., 1987, Petrology of the Yerington Batholith, Nevada; evidence for evolution of porphyry copper ore fluids: *Economic Geology*, v. 82, p. 1750–1789.
- de Hoog, J. C. M., Mason, P. R. D., and van Bergen, M. J., 2001, Sulfur and chalcophile elements in subduction zones: constraints from a laser ablation ICP-MS study of melt inclusions from Galunggung Volcano, Indonesia: *Geochimica et Cosmochimica Acta*, v. 65, p. 3147–3164.
- Evans, K. A., and Tomkins, A. G., 2011, The relationship between subduction zone redox budget and arc magma fertility: *Earth and Planetary Science Letters*, v. 308, p. 401–409.
- Fakraee, M., Hancisse, O., Canfield, D. E., Crowe, S. A., and Katsev, S., 2019, Proterozoic seawater sulfate scarcity and the evolution of ocean–atmosphere chemistry: *Nature Geoscience*, v. 12, p. 375–380.
- Ferry, J. M., and Watson, E. B., 2007, New thermodynamic models and revised calibrations for the Ti-in-zircon and Zr-in-rutile thermometers: *Contributions to Mineralogy and Petrology*, v. 154, p. 429–437.
- Fisher, C. M., Hanchar, J. M., Samson, S. D., Dhuime, B., Blichert-Toft, J., Vervoort, J. D., and Lam, R., 2011, Synthetic zircon doped with hafnium and rare earth elements: A reference material for in situ hafnium isotope analysis: *Chemical Geology*, v. 286, p. 32–47.

- Francois, C., Debaille, V., Paquette, J. L., Baudet, D., and Javaux, E. J., 2018, The earliest evidence for modern-style plate tectonics recorded by HP-LT metamorphism in the Paleoproterozoic of the Democratic Republic of the Congo: *Sci Rep*, v. 8, p. 15452.
- Goldoff, B., Webster, J. D., and Harlov, D. E., 2012, Characterization of fluor-chlorapatites by electron probe microanalysis with a focus on time-dependent intensity variation of halogens: *American Mineralogist*, v. 97, p. 1103–1115.
- Grondahl, C., and Zajacz, Z., 2017, Magmatic controls on the genesis of porphyry Cu–Mo–Au deposits: The Bingham Canyon example: *Earth and Planetary Science Letters*, v. 480, p. 53–65.
- Grumbley, N. L., 2015, *The Geological Evolution of the Haib Cu-Mo Porphyry, Namibia*, Trinity College Dublin, 1–175 p.
- Hiess, J., Condon, D. J., McLean, N., and Noble, S. R., 2012, $^{238}\text{U}/^{235}\text{U}$ systematics in terrestrial uranium-bearing minerals: *Science*, v. 335, p. 1610–1614.
- Imai, A., 2001, Generation and evolution of ore fluids for porphyry Cu-Au mineralization of the Santo Tomas II (Philex) deposit, Philippines: *Resource Geology*, v. 51, p. 71–96.
- Imai, A., 2002, Metallogenesis of porphyry Cu deposits of the western Luzon arc, Philippines: K-Ar ages, SO_3 contents of microphenocrystic apatite and significance of intrusive rocks: *Resource Geology*, v. 52, p. 147–161.
- Imai, A., 2004, Variation of Cl and SO_3 contents of microphenocrystic apatite in intermediate to silicic igneous rocks of Cenozoic Japanese island arcs: Implications for porphyry Cu metallogenesis in the Western Pacific Island arcs: *Resource Geology*, v. 54, p. 357–372.

- Irvine, T. N. J., and Baragar, W. R. A., 1971, A guide to the chemical classification of the common volcanic rocks: *Canadian journal of earth sciences*, v. 8, p. 523–548.
- Jacobs, J., Pisarevsky, S., Thomas, R. J., and Becker, T., 2008, The Kalahari Craton during the assembly and dispersal of Rodinia: *Precambrian Research*, v. 160, p. 142–158.
- Jaffey, A. H., Flynn, K. F., Glendenin, L. E., Bentley, W. C., and Essling, A. M., 1971, Precision measurement of half-lives and specific activities of ^{235}U and ^{238}U : *Physical review C*, v. 4, p. 1889.
- Kelley, K. A., and Cottrell, E., 2009, Water and the oxidation state of subduction zone magmas: *Science*, v. 325, p. 605–607.
- Kelley, K. A., Plank, T., Newman, S., Stolper, E. M., Grove, T. L., Parman, S., and Hauri, E. H., 2010, Mantle melting as a function of water content beneath the Mariana Arc: *Journal of Petrology*, v. 51, p. 1711–1738.
- Kemp, A. I. S., Vervoort, J. D., Bjorkman, K. E., and Iaccheri, L. M., 2017, Hafnium Isotope Characteristics of Palaeoarchaeon Zircon OG1/OGC from the Owens Gully Diorite, Pilbara Craton, Western Australia: *Geostandards and Geoanalytical Research*, v. 41, p. 659–673.
- Konecke, B. A., Fiege, A., Simon, A. C., Linsler, S., and Holtz, F., 2019, An experimental calibration of a sulfur-in-apatite oxybarometer for mafic systems: *Geochimica et Cosmochimica Acta*, v. 265, p. 242–258.
- Konecke, B. A., Fiege, A., Simon, A. C., Parat, F., and Stechern, A., 2017, Co-variability of S^{6+} , S^{4+} , and S^{2-} in apatite as a function of oxidation state: Implications for a new oxybarometer: *American Mineralogist*, v. 102, p. 548–557.

- Kylander-Clark, A. R. C., Hacker, B. R., and Cottle, J. M., 2013, Laser-ablation split-stream ICP petrochronology: *Chemical Geology*, v. 345, p. 99–112.
- Le Maitre, R. W., 1989, A classification of igneous rocks and glossary of terms: Recommendations of the international union of geological sciences subcommission on the systematics of igneous rocks, v. 193.
- Lee, C. T. A., and Tang, M., 2020, How to make porphyry copper deposits: *Earth and Planetary Science Letters*, v. 529, p. 115868.
- Loucks, R. R., Fiorentini, M. L., and Henríquez, G. J., 2020, New magmatic oxybarometer using trace elements in zircon: *Journal of Petrology*, v. 61, p. 1–30.
- Lowell, J. D., and Guilbert, J. M., 1970, Lateral and vertical alteration-mineralization zoning in porphyry ore deposits: *Economic Geology*, v. 65, p. 373–408.
- Ludwig, K. R., 2012, User's manual for Isoplot version 3.75–4.15: a geochronological toolkit for Microsoft: Excel Berkley Geochronological Center Special Publication.
- Luvizotto, G. L., Zack, T., Meyer, H. P., Ludwig, T., Triebold, S., Kronz, A., Münker, C., Stockli, D. F., Prowatke, S., Klemme, S., Jacob, D. E., and von Eynatten, H., 2009, Rutile crystals as potential trace element and isotope mineral standards for microanalysis: *Chemical Geology*, v. 261, p. 346–369.
- Lyons, T. W., and Gill, B. C., 2010, Ancient Sulfur Cycling and Oxygenation of the Early Biosphere: *Elements*, v. 6, p. 93–99.
- Macey, P. H., Thomas, R. J., Minnaar, H. M., Gresse, P. G., Lambert, C. W., Groenewald, C. A., Miller, J. A., Indongo, J., Angombe, M., Shifotoka, G., Frei, D., Diener, J. F. A., Kisters, A. F. M., Dhansay, T., Smith, H., Doggart, S., Le Roux, P., Hartnady, M. I., and Tinguely,

- C., 2017, Origin and evolution of the ~1.9Ga Richtersveld Magmatic Arc, SW Africa: *Precambrian Research*, v. 292, p. 417–451.
- Macpherson, C. G., Dreher, S. T., and Thirlwall, M. F., 2006, Adakites without slab melting: High pressure differentiation of island arc magma, Mindanao, the Philippines: *Earth and Planetary Science Letters*, v. 243, p. 581–593.
- Matjuschkin, V., Blundy, J. D., and Brooker, R. A., 2016, The effect of pressure on sulphur speciation in mid- to deep-crustal arc magmas and implications for the formation of porphyry copper deposits: *Contributions to Mineralogy and Petrology*, v. 171, p. 66.
- Mattinson, J. M., 2005, Zircon U–Pb chemical abrasion (“CA-TIMS”) method: Combined annealing and multi-step partial dissolution analysis for improved precision and accuracy of zircon ages: *Chemical Geology*, v. 220, p. 47–66.
- McLean, N. M., Condon, D. J., Schoene, B., and Bowring, S. A., 2015, Evaluating uncertainties in the calibration of isotopic reference materials and multi-element isotopic tracers (EARTHTIME Tracer Calibration Part II): *Geochimica et Cosmochimica Acta*, v. 164, p. 481–501.
- Minnitt, R. C. A., 1986, Porphyry copper-molybdenum mineralization at Haib River, South West Africa/Namibia: *Mineral deposits of southern Africa*, 1986, p. 1567–1585.
- Minnitt, R. C. A., 1979, The geological setting of porphyry-type copper mineralization in the Haib River area, South West Africa., University of the Witwatersrand, 1–366 p.
- Möller, A., Appel, P., Mezger, K., and Schenk, V., 1995, Evidence for a 2 Ga subduction zone: Eclogites in the Usagaran belt of Tanzania: *Geology*, v. 23, p. 1067–1070.

- Nash, W. M., Smythe, D. J., and Wood, B. J., 2019, Compositional and temperature effects on sulfur speciation and solubility in silicate melts: *Earth and Planetary Science Letters*, v. 507, p. 187–198.
- Parat, F., and Holtz, F., 2004, Sulfur partitioning between apatite and melt and effect of sulfur on apatite solubility at oxidizing conditions: *Contributions to Mineralogy and Petrology*, v. 147, p. 201–212.
- Parat, F., Holtz, F., and Streck, M. J., 2011, Sulfur-bearing Magmatic Accessory Minerals: *Sulfur in Magmas and Melts: Its Importance for Natural and Technical Processes*, v. 73, p. 285–314.
- Parkinson, I. J., and Arculus, R. J., 1999, The redox state of subduction zones: insights from arc-peridotites: *Chemical Geology*, v. 160, p. 409–423.
- Paton, C., Woodhead, J. D., Hellstrom, J. C., Hergt, J. M., Greig, A., and Maas, R., 2010, Improved laser ablation U-Pb zircon geochronology through robust downhole fractionation correction: *Geochemistry, Geophysics, Geosystems*, v. 11.
- Paton, C., Hellstrom, J., Paul, B., Woodhead, J., and Hergt, J., 2011, Iolite: Freeware for the visualisation and processing of mass spectrometric data: *Journal of Analytical Atomic Spectrometry*, v. 26, p. 2508–2518.
- Peng, G. Y., Luhr, J. F., and McGee, J. J., 1997, Factors controlling sulfur concentrations in volcanic apatite: *American Mineralogist*, v. 82, p. 1210–1224.
- Piccoli, P., and Candela, P., 1994, Apatite in felsic rocks: a model for the estimation of initial halogen concentrations in the Bishop Tuff (Long Valley) and Tuolumne Intrusive Suite (Sierra Nevada Batholith) magmas: *American Journal of Science*, v. 294, p. 92–135.

- Planavsky, N. J., Bekker, A., Hofmann, A., Owens, J. D., and Lyons, T. W., 2012, Sulfur record of rising and falling marine oxygen and sulfate levels during the Lomagundi event: *Proc Natl Acad Sci U S A*, v. 109, p. 18300–18305.
- Ravel, B., and Newville, M., 2005, ATHENA, ARTEMIS, HEPHAESTUS: data analysis for X-ray absorption spectroscopy using IFEFFIT: *Journal of synchrotron radiation*, v. 12, p. 537–541.
- Reid, D. L., Erlank, A. J., Welke, H. J., and Moyes, A., 1987, The Orange River Group: a Major Proterozoic Cal-calkaline Volcanic Belt in the Western Namaqua Province, Southern Africa: Geological Society, London, Special Publications, v. 33, p. 327–346.
- Rezeau, H., Moritz, R., Wotzlaw, J. F., Tayan, R., Melkonyan, R., Ulianov, A., Selby, D., d'Abzac, F. X., and Stern, R. A., 2016, Temporal and genetic link between incremental pluton assembly and pulsed porphyry Cu-Mo formation in accretionary orogens: *Geology*, v. 44, p. 627–630.
- Richards, J. P., and Mumin, A. H., 2013, Magmatic-hydrothermal processes within an evolving Earth: Iron oxide-copper-gold and porphyry Cu \pm Mo \pm Au deposits: *Geology*, v. 41, p. 767–770.
- Richards, J. P., López, G. P., Zhu, J. J., Creaser, R. A., Locock, A. J., and Mumin, A. H., 2017, Contrasting Tectonic Settings and Sulfur Contents of Magmas Associated with Cretaceous Porphyry Cu \pm Mo \pm Au and Intrusion-Related Iron Oxide Cu-Au Deposits in Northern Chile: *Economic Geology*, v. 112, p. 295–318.
- Richards, J. P., 2003, Tectono-magmatic precursors for porphyry Cu-(Mo-Au) deposit formation: *Economic Geology*, v. 98, p. 1515–1533.

- Richards, J. P., 2015, The oxidation state, and sulfur and Cu contents of arc magmas: implications for metallogeny: *Lithos*, v. 233, p. 27–45.
- Schärer, U., 1984, The effect of initial ^{230}Th disequilibrium on young U-Pb ages: the Makalu case, Himalaya: *Earth and Planetary Science Letters*, v. 67, p. 191–204.
- Seedorff, E., 2005, Porphyry deposits: characteristics and origin of hypogene Features. Society of economist Geologists, Inc: *Economic Geology 100th Anniversary Volume*. Canada.
- Shields-Zhou, G., and Och, L., 2011, The case for a Neoproterozoic oxygenation event: geochemical evidence and biological consequences: *GSA Today*, v. 21, p. 4–11.
- Sillitoe, R. H., 2010, Porphyry Copper Systems: *Economic Geology*, v. 105, p. 3–41.
- Sinclair, W. D., 2007, Porphyry deposits: Mineral deposits of Canada: A synthesis of major deposit-types, district metallogeny, the evolution of geological provinces, and exploration methods: Geological Association of Canada, Mineral Deposits Division, Special Publication, v. 5, p. 223–243.
- Söderlund, U., Patchett, P. J., Vervoort, J. D., and Isachsen, C. E., 2004, The ^{176}Lu decay constant determined by Lu–Hf and U–Pb isotope systematics of Precambrian mafic intrusions: *Earth and Planetary Science Letters*, v. 219, p. 311–324.
- Steadman, J., Large, R., Blamey, N., Mukherjee, I., Corkrey, R., Danyushevsky, L., Maslennikov, V., Hollings, P., Garven, G., and Brand, U., 2020, Evidence for elevated and variable atmospheric oxygen in the Precambrian: *Precambrian Research*, p. 105722.
- Stock, M. J., Humphreys, M. C. S., Smith, V. C., Isaia, R., Brooker, R. A., and Pyle, D. M., 2018, Tracking Volatile Behaviour in Sub-volcanic Plumbing Systems Using Apatite and

- Glass: Insights into Pre-eruptive Processes at Campi Flegrei, Italy: *Journal of Petrology*, v. 59, p. 2463–2492.
- Stolper, D. A., and Bucholz, C. E., 2019, Neoproterozoic to early Phanerozoic rise in island arc redox state due to deep ocean oxygenation and increased marine sulfate levels: *Proceedings of the National Academy of Sciences*, v. 116, p. 8746–8755.
- Stolper, D. A., and Keller, C. B., 2018, A record of deep-ocean dissolved O₂ from the oxidation state of iron in submarine basalts: *Nature*, v. 553, p. 323–327.
- Stormer, J. C., Pierson, M. L., and Tacker, R. C., 1993, Variation of F-X-Ray and Cl-X-Ray Intensity Due to Anisotropic Diffusion in Apatite during Electron-Microprobe Analysis: *American Mineralogist*, v. 78, p. 641–648.
- Streck, M. J., and Dilles, J. H., 1998, Sulfur evolution of oxidized arc magmas as recorded in apatite from a porphyry copper batholith: *Geology*, v. 26, p. 523–526.
- Sun, S. S., and McDonough, W. F., 1989, Chemical and isotopic systematics of oceanic basalts: implications for mantle composition and processes: Geological Society, London, Special Publications, v. 42, p. 313–345.
- Tang, M., Erdman, M., Eldridge, G., and Lee, C. T. A., 2018, The redox “filter” beneath magmatic orogens and the formation of continental crust: *Science Advances*, v. 4, p. eaar4444.
- Tapster, S., Condon, D. J., Naden, J., Noble, S. R., Petterson, M. G., Roberts, N. M. W., Saunders, A. D., and Smith, D. J., 2016, Rapid thermal rejuvenation of high-crystallinity magma linked to porphyry copper deposit formation; evidence from the Koloula Porphyry Prospect, Solomon Islands: *Earth and Planetary Science Letters*, v. 442, p. 206–217.

- Valley, J. W., Lackey, J. S., Cavosie, A. J., Clechenko, C. C., Spicuzza, M. J., Basei, M. A. S., Bindeman, I. N., Ferreira, V. P., Sial, A. N., and King, E. M., 2005, 4.4 billion years of crustal maturation: oxygen isotope ratios of magmatic zircon: *Contributions to Mineralogy and Petrology*, v. 150, p. 561–580.
- Valley, J. W., Kinny, P. D., Schulze, D. J., and Spicuzza, M. J., 1998, Zircon megacrysts from kimberlite: oxygen isotope variability among mantle melts: *Contributions to Mineralogy and Petrology*, v. 133, p. 1–11.
- Webster, J. D., Tappen, C. M., and Mandeville, C. W., 2009, Partitioning behavior of chlorine and fluorine in the system apatite–melt–fluid. II: Felsic silicate systems at 200MPa: *Geochimica et Cosmochimica Acta*, v. 73, p. 559–581.
- Weller, O. M., and St-Onge, M. R., 2017, Record of modern-style plate tectonics in the Palaeoproterozoic Trans-Hudson orogen: *Nature Geoscience*, v. 10, p. 305–311.
- Wiedenbeck, M., Alle, P., Corfu, F., Griffin, W. L., Meier, M., Oberli, F., Von Quadt, A., Roddick, J. C., and Spiegel, W., 1995, Three natural zircon standards for U-Th-Pb, Lu-Hf, trace element and REE analyses: *Geostandards newsletter*, v. 19, p. 1–23.
- Wilkinson, B. H., and Kesler, S. E., 2007, Tectonism and Exhumation in Convergent Margin Orogens: Insights from Ore Deposits: *The Journal of Geology*, v. 115, p. 611–627.
- Winchester, J. A., and Floyd, P. A., 1977, Geochemical discrimination of different magma series and their differentiation products using immobile elements: *Chemical Geology*, v. 20, p. 325–343.
- Wojdyr, M., 2010, Fityk: a general-purpose peak fitting program: *Journal of Applied Crystallography*, v. 43, p. 1126–1128.

- Wones, D. R., 1989, Significance of the assemblage titanite+magnetite+quartz in granitic rocks*: *American Mineralogist*, v. 74, p. 744–749.
- Wood, B. J., Bryndzia, L. T., and Johnson, K. E., 1990, Mantle oxidation state and its relationship to tectonic environment and fluid speciation: *Science*, v. 248, p. 337–345.
- Yin, A., Brandl, G., and Kröner, A., 2019, Plate-tectonic processes at ca. 2.0 Ga: Evidence from >600 km of plate convergence: *Geology*, v. 48, p. 103–107.
- Zack, T., Stockli, D. F., Luvizotto, G. L., Barth, M. G., Belousova, E., Wolfe, M. R., and Hinton, R. W., 2011, In situ U–Pb rutile dating by LA-ICP-MS: ^{208}Pb correction and prospects for geological applications: *Contributions to Mineralogy and Petrology*, v. 162, p. 515–530.
- Zajacz, Z., and Halter, W., 2009, Copper transport by high temperature, sulfur-rich magmatic vapor: Evidence from silicate melt and vapor inclusions in a basaltic andesite from the Villarrica volcano (Chile): *Earth and Planetary Science Letters*, v. 282, p. 115–121.
- Zellmer, G. F., Edmonds, M., and Straub, S. M., 2015, Volatiles in subduction zone magmatism: Geological Society, London, Special Publications, v. 410, p. 1–17.
- Zhang, D. H., and Audétat, A., 2017, What Caused the Formation of the Giant Bingham Canyon Porphyry Cu-Mo-Au Deposit? Insights from Melt Inclusions and Magmatic Sulfides: *Economic Geology*, v. 112, p. 221–244.
- Zhu, J. J., Richards, J. P., Rees, C., Creaser, R., DuFrane, S. A., Locock, A., Petrus, J. A., and Lang, J., 2018, Elevated Magmatic Sulfur and Chlorine Contents in Ore-Forming Magmas at the Red Chris Porphyry Cu-Au Deposit, Northern British Columbia, Canada: *Economic Geology*, v. 113, p. 1047–1075.

4.9 Figures

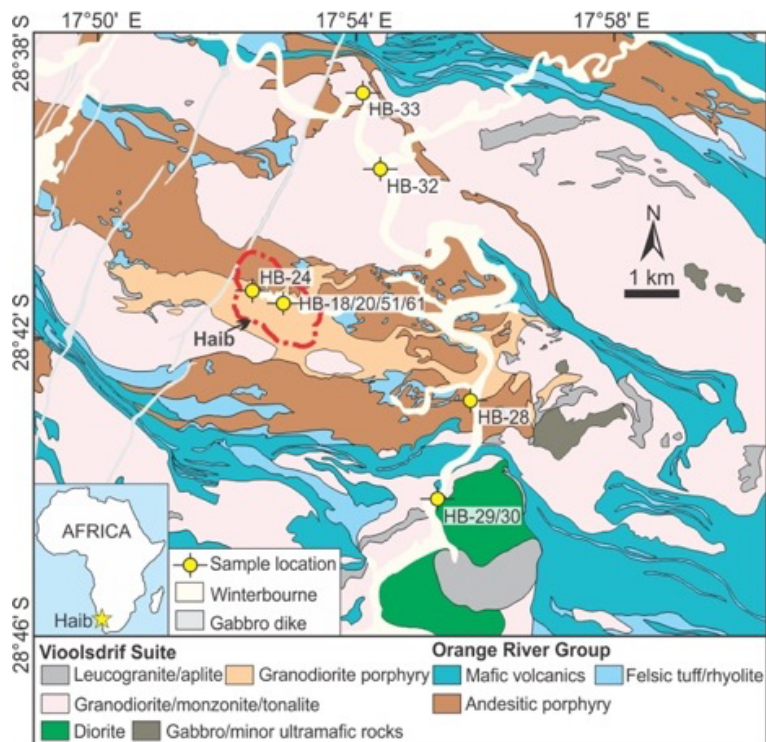


Figure 4.1. Simplified geological map of the Haib area showing main lithological units. The map is modified from Minnitt (1979). The red dashed line represents the defined mineralization zone for Haib (report from Deep South Resources, Inc.).

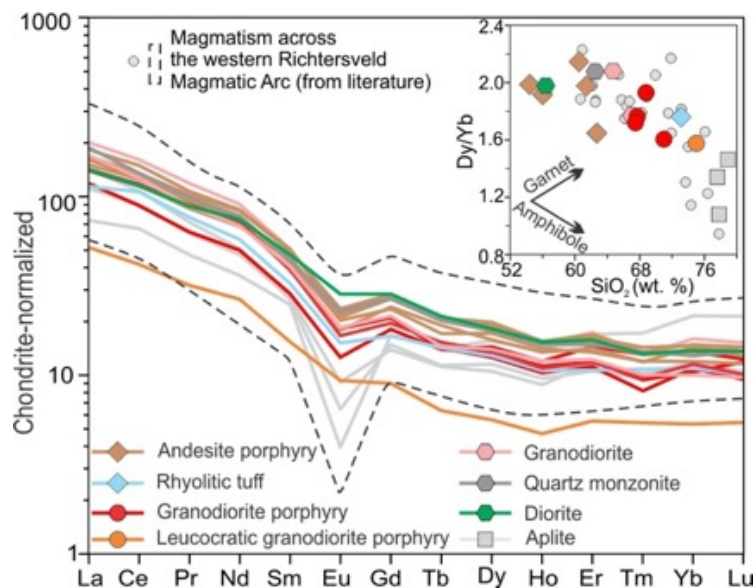


Figure 4.2. Chondrite-normalized rare-earth element spider diagram for igneous rocks from Haib. The normalization values are from [Sun and McDough \(1989\)](#).

Inset is Dy/Yb versus SiO₂ diagram, and the fractionation trends of amphibole and garnet are from [Davidson et al. \(2007\)](#). Data for the igneous rocks (LOI ≤ 2 wt. %) from the western Richtersveld Magmatic Arc were compiled in [Macey et al. \(2017\)](#).

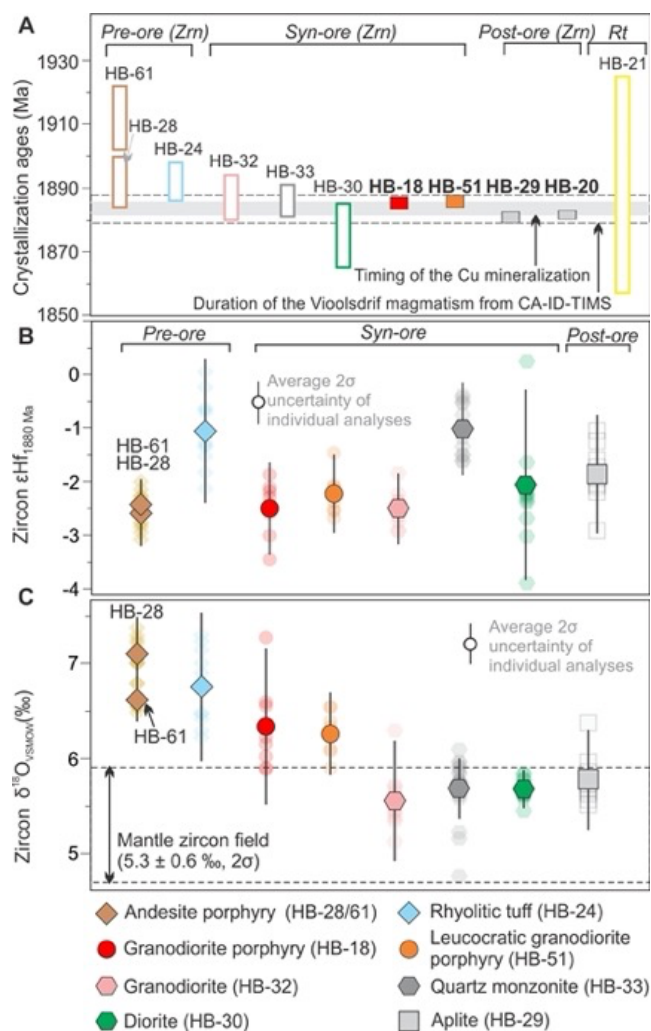


Figure 4.3. Zircon U-Pb-Hf-O and rutile U-Pb isotopes for representative rocks in Haib. (A) Crystallization ages of magmatic zircons from ten pre-, syn-, and post-ore igneous rocks (identified from cross-cutting relationship, details in [Supplementary Note 1](#)) and a hydrothermal rutile (sample HB-21, syn-ore granodiorite porphyry) associated with chalcopyrite mineralization in Haib, dated using LA-ICP-MS (samples HB-61, HB-28, HB-24, HB-32, HB-33, and HB30) and CA-ID-TIMS (sample numbers in bold; samples HB-18, HB-51, HB-29, and HB-20) methods. (B) Zircon Hf isotopic composition (as ϵ_{Hf} calculated at 1880 Ma). (C) Zircon $\delta^{18}\text{O}$ ratios for representative igneous samples. Filled symbols in (B) and (C) are average values for each sample; smaller pale symbols represent individual analyses. Mantle zircon field in (C) is from [Valley et al. \(1998\)](#). Error bars indicate 2σ uncertainties. See [Table A3.1](#) for sample locations and descriptions.

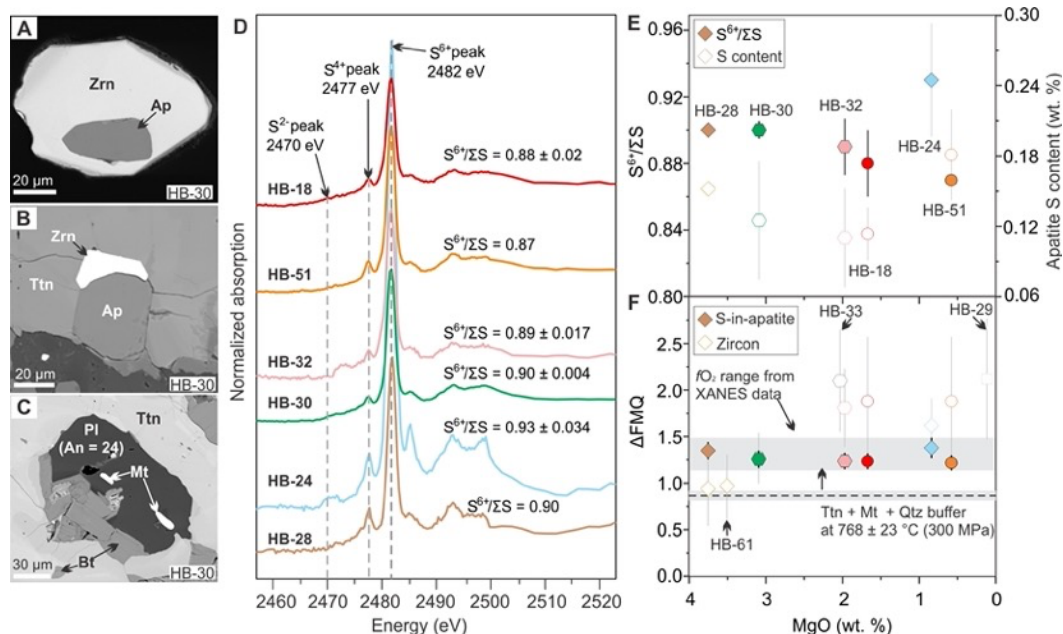


Figure 4.4. Backscattered electron images of inclusions in titanite and zircon, apatite μ -XANES spectra and sulfur contents, and results of magmatic fO_2 estimation.

(A) Representative apatite inclusion in zircon from sample HB-30; BSE. (B) Zircon overgrowth on apatite with both hosted in magmatic titanite from sample HB-30; BSE. (C) Biotite, plagioclase (An number = 24, calculated from energy dispersive X-ray analysis), and magnetite in titanite from diorite sample HB-30; BSE. (D) Normalized μ -XANES spectra at the S K -edge of apatite in zircons for representative igneous rocks from Haib. Spectra for only one apatite inclusion ($n = 1$) were obtained for samples HB-28 and HB-51, respectively, while the others represent averaged spectra of a number of apatite inclusions (HB-18, $n = 4$; HB-24, $n = 2$; HB-30, $n = 3$; HB-32, $n = 3$). Peak positions for S^{2-} , S^{4+} , and S^{6+} are at 2470 eV, 2477 eV, and 2482 eV, respectively, and are shown as dotted grey lines. The average $S^{6+}/\Sigma S$ ratios (1σ) are calculated from the merged spectra following Konecke et al. (2019). (E) Plot of apatite $S^{6+}/\Sigma S$ ratios and S contents versus MgO for the representative samples. (F) ΔFMQ values versus MgO for the representative samples. Error bars in (E) and (F) represent 1σ uncertainties. Abbreviations: An = anorthite, Ap = apatite, Mt = magnetite, Pl = plagioclase, Ttn = titanite, Zrn = zircon. Symbols and colors are the same as in Fig. 4.3.

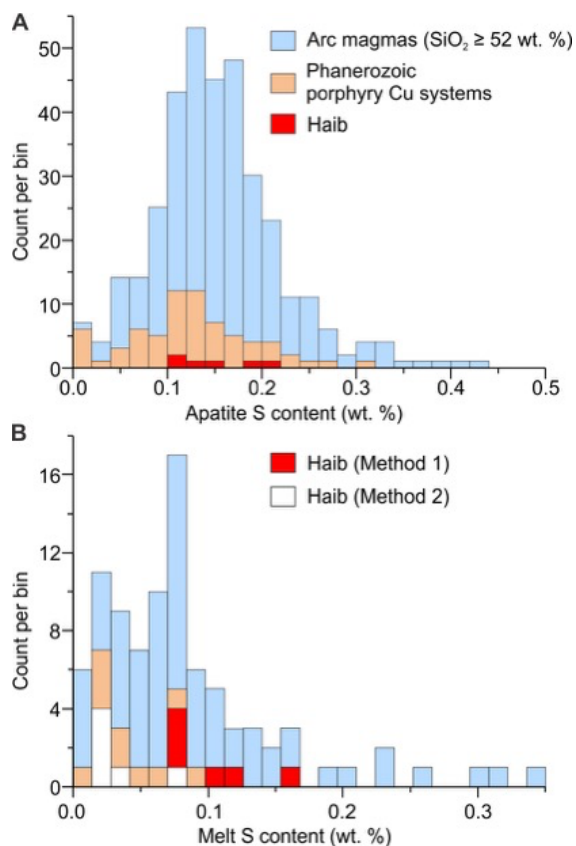


Figure 4.5. Histograms of S concentrations of igneous apatites and melt inclusions from arc magmas, rocks associated with Phanerozoic porphyry Cu systems and the Haib.

(A) Igneous apatites from intermediate to felsic arc magmas (0.15 ± 0.07 wt. % S on average; 1σ , $n = 349$, basaltic-andesitic to rhyolitic composition with SiO_2 presumably ≥ 52 wt. %; most of them are from the Circum-Pacific volcanic arcs) and a subset from those associated with Phanerozoic porphyry Cu systems (0.12 ± 0.065 wt. % S on average; 1σ , $n = 64$; data from GEOROC database; Imai, 2001, 2002, 2004; Richards et al., 2017; Zhu et al., 2018) and Haib ($n = 6$). **(B) Measured S concentrations of melt inclusions in olivine and minor pyroxene in arc rocks (0.09 ± 0.07 wt. % on average; 1σ , $n = 69$; $\text{SiO}_2 \geq 52$ wt. %; data from GEOROC database; Grondahl and Zajacz, 2017; Zajacz and Halter, 2009; Zhang and Audétat, 2017) and in rocks associated with Phanerozoic porphyry Cu systems, as well as those estimated using apatite-melt partition coefficients for S from the Haib igneous apatites. The melt inclusion data for arc rocks were filtered using $\text{CO}_2 \geq 50$ ppm to identify those with limited degassing (see Kelley et al. 2010). N represents numbers of samples or groups of apatites and melt inclusions.**

Chapter 5

Variable modes of formation for tonalite-trondhjemite-granodiorite-diorite (TTG)-related porphyry-type Cu ± Au deposits in the Neoproterozoic southern Abitibi subprovince: Evidence from petrochronology and oxybarometry

5.1 Abstract

Most known porphyry Cu ± Au deposits are associated with moderately oxidized and sulfur-rich calc-alkaline to mildly alkalic arc-related magmas in the Phanerozoic. In contrast, sodium-enriched tonalite-trondhjemite-granodiorite-diorite (TTG) magmas predominant in the Archean are hypothesized to be unoxidized and sulfur-poor, which together preclude porphyry Cu deposit formation. Here we test this hypothesis by interrogating the causative magmas for the ~2.7 Ga TTG-related Côté Gold, St-Jude, and Croxall porphyry-type Cu ± Au deposits reported in the Neoproterozoic southern Abitibi subprovince. The dioritic and trondhjemitic magmas associated with Côté Gold and St-Jude evolved along a plagioclase-dominated fractionation trend, in contrast to amphibole-dominated fractionation for tonalitic magma at Croxall. Analyses of zircon grains from the Côté Gold, St-Jude, and Croxall rocks yielded $\varepsilon_{\text{Hf}}(t) \pm \text{SD}$ values of 4.5 ± 0.3 , 4.2 ± 0.6 , and 4.3 ± 0.4 , and $\delta^{18}\text{O} \pm \text{SD}$ values of 5.40 ± 0.11 ‰, 3.91 ± 0.13 ‰, and 4.83 ± 0.12 ‰, respectively. These isotopic signatures indicate that whereas the magmas in all three locations are mantle-sourced with minimal crustal contamination, for the St-Jude and Croxall settings the magmas or their sources may have undergone variable alteration by heated seawater or meteoric fluids.

Primary barometric minerals (i.e., zircon, amphibole, apatite, and magnetite-ilmenite) that survived variable alteration and metamorphism (up to greenschist facies) were identified for

estimating fO_2 of the causative magmas. Estimation of magmatic fO_2 values using zircon geochemistry shows the magmas associated with St-Jude, Côte Gold, and Croxall yielded increasing magmatic fO_2 values from $\Delta FMQ -0.3 \pm 0.6$, $\Delta FMQ +0.8 \pm 0.4$, to $\Delta FMQ +1.2 \pm 0.4$, respectively. In contrast, amphibole chemistry yielded systematically higher fO_2 values of $\Delta FMQ +1.6 \pm 0.3$ and $\Delta FMQ +2.6 \pm 0.1$ for Côte Gold and Croxall, respectively, which is consistent with previous studies that indicate amphibole may overestimate fO_2 of intrusive rocks by up to one log unit. Micro X-ray absorption near edge structure (μ -XANES) spectrometry of primary apatite yielded $>\Delta FMQ -0.3$ and $\Delta FMQ +1.4$ – 1.8 for the St-Jude and Croxall, respectively. The magnetite-ilmenite mineral pairs from the Croxall tonalite yielded $\Delta FMQ +3.3 \pm 1.3$ at equilibrium temperatures of 634 ± 21 °C, recording the redox state of the late stage of magma crystallization. Electron microprobe analyses show that the Croxall igneous apatites are richer in S (up to 0.1 wt. %) than those of Côte Gold and St-Jude (below the detection limit), which is attributed to either relatively oxidized or sulfur-rich features of the Croxall tonalite.

We interpret these results to indicate the Côte Gold and Croxall deposits formed from mildly ($\sim \Delta FMQ +0.6$ – 0.7) to moderately ($\sim \Delta FMQ +1.5$) oxidized magmas where voluminous early sulfide saturation was probably limited, whereas the St-Jude deposit represents a rare case whereby the ingress of externally derived heated seawater facilitated metal fertility in a relatively reduced magma chamber ($\sim \Delta FMQ +0$). Furthermore, we conclude that variable modes of formation for these deposits and, in addition, the apparent rarity of porphyry-type Cu-Au deposits in the Archean may be attributed to either local restriction of favorable metallogenic conditions and/or preservation or an exploration bias.

5.2 Introduction

Porphyry Cu \pm Au deposits predominantly occur at shallow crustal levels (i.e., < 5 km below the paleosurface) in Phanerozoic arc-related settings. In active orogens (e.g., arc-related settings), the susceptibility of shallow porphyry Cu \pm Au deposits to erosion during rapid uplift has been considered as a relevant factor for the rarity of these deposits in Precambrian terranes (Groves *et al.*, 2005, Wilkinson & Kesler, 2007). However, the thick (~250 to 350 km), refractory, and buoyant subcontinental lithospheric mantle roots underlying Archean cratons make the cratons resistant to reworking by younger orogenic cycles, thus leading to the preservation of many Archean volcanoplutonic terranes (Kerrick *et al.*, 2005). The fact that these volcanoplutonic terranes have been preserved suggests that the rarity of porphyry Cu \pm Au deposits in the Archean may not reflect erosion (Richards & Kerrich, 2007), but may instead be attributed to unfavorable tectonomagmatic settings and related geochemical features (Evans & Tomkins, 2011, Richards & Mumin, 2013).

Most known porphyry Cu \pm Au deposits are of Phanerozoic age and are exclusively associated with moderately oxidized ($\Delta\text{FMQ} +1$ to $+2$; where ΔFMQ is the log unit of $f\text{O}_2$ relative to the fayalite-magnetite-quartz mineral redox buffer), sulfur-rich, and hydrous magmas of calc-alkaline to mildly alkalic affinity derived from partial melting of the mantle wedge previously metasomatized by slab-derived fluids (Richards, 2011). In contrast, intrusive rocks in many Archean terranes are dominated by sodium-rich tonalite-trondhjemite-granodiorite-diorite suites (abbreviated as TTG hereafter; Fig. 5.1). The origin of the TTG magmas remains highly contentious, but are generally attributed to processes including melting of thickened mafic crust or subducted oceanic crust, crystal fractionation of hydrous arc basalts, or upper crustal

differentiation of magmas from the melting of basalt (Kleinhanns *et al.*, 2003, Nagel *et al.*, 2012, Jagoutz *et al.*, 2013, Martin *et al.*, 2014, Hastie *et al.*, 2016, Johnson *et al.*, 2017, Laurent *et al.*, 2020). The rarity of porphyry Cu \pm Au deposits in the Archean could therefore be attributed to the absence of modern-style plate tectonics (Fig. 5.1), particularly prior to 3.0 Ga (Moyen & van Hunen, 2012, Bédard, 2018, Johnson *et al.*, 2019), and/or predominance of relatively reduced hydrothermally altered seafloor basalts and sulfate-poor (< 200 μ M) seawater (Fig. 5.1; Habicht *et al.*, 2002, Jamieson *et al.*, 2013, Crowe *et al.*, 2014, Stolper & Keller, 2018). Neither of the aforementioned factors allows for the recycling of oxidized materials from the Earth's surface to the mantle, thus rendering the sodium-rich TTG magmas in the Archean either reduced or sulfur-poor (Prouteau & Scaillet, 2012, Jagoutz *et al.*, 2013). Such reduced magmas would however favor formation of magmatic sulfides, either retained in the source region or during magma ascent by assimilation of the overriding reduced lithosphere, which would therefore deplete the silicate melts of their chalcophile element contents (Candela & Holland, 1984, Evans & Tomkins, 2011, Audétat & Simon, 2012) and thus limit the Cu \pm Au potential of the evolved magmas to form porphyry Cu deposits upon emplacement in the upper crust (Richards, 2011; Simon and Ripley, 2011).

However, there are currently few constraints on the magmatic fO_2 and volatile contents of sodic TTG magmas (based mainly on zircon geochemistry; e.g., Yang *et al.*, 2014, Madon *et al.*, 2020, Mole *et al.*, 2021), particularly for those associated with porphyry-type Cu \pm Au deposits in the Neoarchean. Given the general lack of constraint of the intensive parameters (e.g., fO_2) and presence of some, albeit rare, significant porphyry-type Cu \pm Au mineralization (e.g., Côté Gold Au \pm Cu deposit in the Abitibi greenstone belt, with ~10 Moz Au and geochemically significant but undefined Cu resource; Kontak *et al.*, 2013, Katz *et al.*, 2017,

2021), it remains unclear as to whether the metallogenic processes of Phanerozoic porphyry Cu systems are necessary to form the same type of deposits in the Archean. The issue is also relevant for identifying the actual cause of the apparent rarity of porphyry-type Cu \pm Au deposits in the Archean.

To address the issue, three porphyry-type Cu \pm Au deposit settings (i.e., Côté Gold, St-Jude, and Croxall) previously reported in the well-mapped \sim 2.7 Ga southern Abitibi subprovince, Canada, were selected for study. These settings were chosen because they: (1) are host to disseminated- and veinlet-type mineralization associated with potassic alteration, thus resembling aspects of Phanerozoic porphyry Cu systems (Sillitoe, 2010); (2) are well characterized and their absolute timing of emplacement is constrained by high-precision U-Pb geochronology (Galley & Van Breemen, 2002, Piercey *et al.*, 2008, Kontak *et al.*, 2013, Katz *et al.*, 2017, 2021); and (3) are among the earliest known cluster of TTG-related porphyry-type Cu \pm Au deposits worldwide (Singer *et al.*, 2008).

Specifically, the goal of this study is to estimate the magmatic fO_2 conditions of the causative magmas for these deposits using the chemistry of primary mineral phases, which can be hindered by variable, post-emplacement modification of such old rocks owing to alteration, deformation, and metamorphism (e.g., Madon *et al.*, 2020; Meng *et al.*, 2021). Where analysis of apatite composition was possible, the magma S contents were also evaluated. Whole-rock geochemistry and zircon U-Pb-Hf-O isotopes were also analyzed, and used in combination with previously published results, to constrain the crystallization ages and geochemical processes, as well as sources of these magmas. The findings of this pilot study demonstrate that the three studied Archean porphyry-type Cu \pm Au deposits formed from magmas with variable

fO_2 ($\sim\Delta FMQ +0$ to $+1.5$) and petrogenesis, suggesting complex magmatic conditions for these porphyry-type Cu \pm Au deposits.

5.3 Geological setting of the southern Abitibi subprovince

The three porphyry-type Cu \pm Au deposits studied are located in the southern part of the Neoproterozoic Abitibi greenstone belt (abbreviated as AGB hereafter) of the southeastern Superior Province, Canada. The AGB is bounded to the north and south by sedimentary rocks of the Opatica and Pontiac subprovinces, respectively, and is separated from the Wawa subprovince to the west by the northeast-trending, west-dipping Kapuskasing thrust zone (Fig. 5.2). The AGB is comprised primarily of ~ 2.70 – 2.75 Ga east-trending volcanic assemblages and unconformably overlying fluvial siliciclastic sedimentary sequences with rare alkaline volcanic rocks, as well as ~ 2.70 – 2.75 Ga TTG rocks and younger (< 2.68 Ga) granite-monzonite-syenite-dominated intrusions (Figs. 5.2, 5.3; Feng & Kerrich, 1992; Beakhouse, 2011; Mathieu *et al.*, 2020).

5.3.1 Volcanic and sedimentary stratigraphy

Six semi-continuous submarine volcanic assemblages have been defined based on rock types and high-precision zircon U-Pb geochronology, including four dominantly tholeiitic \pm komatiitic assemblages (i.e., Pacaud, Stoughton-Roquemaure, Kidd-Munro, and Tisdale) and two calc-alkaline-dominated assemblages (i.e., Delore and Blake River groups; Figs. 5.2, 5.3; Ayer *et al.*, 2002, Thurston *et al.*, 2008). Thurston *et al.* (2008) showed that most of the six volcanic assemblages are locally separated by ~ 200 m-thick chemical sedimentary layers such as iron formation (Fig. 5.3). The Porcupine and Timiskaming sedimentary assemblages unconformably overlie these six volcanic assemblages (Fig. 5.3).

The ages and distribution of the volcanic and sedimentary assemblages, which are summarized in [Figures 5.2 and 5.3](#), are briefly described below. The earliest of these assemblages, the Pacaud, is mainly composed of komatiites, tholeiites, and calc-alkaline intermediate to felsic volcanic rocks deposited from 2747 to 2735 Ma. It underlies the Delore assemblage (2734–2724 Ma) composed of calc-alkaline mafic- to felsic volcanic rocks interbedded locally with tholeiitic mafic volcanic rocks. The Stoughton-Roquemaure assemblage, deposited during a short period of 2723–2720 Ma, mainly consists of tholeiitic basalts with lesser komatiitic- and rhyolitic volcanic rocks. The conformably overlying Kidd-Munro assemblage (2720–2710 Ma) is composed of a mixture of various volcanic sequences that includes calc-alkaline intermediate to felsic volcanic rocks, tholeiitic basalts and komatiites, local felsic volcanic rocks, and graphitic metasedimentary rocks. The younger Tisdale assemblage (2710–2704 Ma) is composed of tholeiitic komatiites with local tholeiitic- to calc-alkaline rhyolitic volcanic rocks and overlying calc-alkaline, intermediate- to felsic volcanoclastic units. The Blake River Group (2704–2695 Ma) is the youngest volcanic assemblage and voluminously outcrops in the southern AGB. It comprises, in ascending order, thin layers of clastic metasedimentary rocks, Fe-Mg-rich tholeiitic volcanic rocks with minor tholeiitic intermediate- to felsic volcanic rocks (2704–2701 Ma), and tholeiitic- to calc-alkaline, mafic- to felsic volcanic rocks and volcanoclastic rocks (2701–2695 Ma).

Two sedimentary-dominated sequences (i.e., Porcupine and Timiskaming) overlie the volcanic-dominated successions. The older Porcupine assemblage (≤ 2690 – ≤ 2685 Ma) mainly includes fine-grained, deep-water deposited, flysch-like clastic sedimentary rocks that unconformably overlie the submarine volcanic assemblages noted above ([Fig. 5.2, 5.3](#)). These clastic rocks include greywacke and mudstone, which are locally intercalated with conglomerate, banded iron formation, and calc-alkaline rhyodacitic volcanoclastic deposits ([Bleeker, 2015](#)). Detrital zircons

from greywackes yielded ages of 2750–2690 Ma, with some having Mesoarchean ages, and thus consistent with the age spectrum of the putative sources such as pre-Porcupine igneous rocks of the AGB (Ayer *et al.*, 2005, Frieman *et al.*, 2017). The younger sedimentary sequence is the molasse-like Timiskaming assemblage (≤ 2679 – ≤ 2669 Ma), which accumulated in extensional basins, unconformably overlies folded Porcupine and older volcanic assemblages, and consists mainly of subaerial alluvial-fluvial conglomerates and sandstone with lesser subaerial alkaline volcanic rocks (Bleeker, 2015).

5.3.2 Intrusive suites

Five stages or suites of intrusive rocks are present in the southern AGB based on rock type as well as relative timing with respect to the volcanic assemblages and regional tectonic deformation (e.g., Feng & Kerrich, 1992, Beakhouse, 2011, Mathieu *et al.*, 2020).

(1) ~2750–2695 Ma: this earliest group includes syn-volcanic, high-Al and minor low-Al tonalite (see definition in Barker and Arth, 1976), trondhjemite, and diorite of the well-known TTG clan.

(2) 2695–2685 Ma: syn-deformational granodioritic and tonalitic intrusion and high-level porphyritic stocks formed synchronously with deposition of the Porcupine assemblage. The extent of the extrusive equivalents remains unclear (e.g., MacDonald and Piercy, 2019).

(3) 2685–2679 Ma: a younger, late syn-deformational suite of granodioritic and quartz monzonitic intrusions emplaced between the termination of the Porcupine sedimentation and the start of the Timiskaming sedimentation.

(4) 2679–2660 Ma: an alkalic intrusive suite comprising diorite, monzonite, quartz syenite, syenite and granite emplaced during and immediately after the Timiskaming sedimentation.

(5) <2660 Ma: peraluminous granitic intrusions formed during crustal exhumation of the southern AGB that intrude the metamorphosed volcanic and sedimentary assemblages as mentioned before.

These types of intrusive rocks reflect a broadly evolutionary pattern with time comparable to those in many other Archean cratons globally, which may be attributed to evolving geodynamic processes in the early Earth (e.g., cooling; [Laurent *et al.*, 2014](#)).

5.3.3 Tectonic interpretation of the southern Abitibi greenstone belt

Pre-2.70 Ga

The autochthonous process for the formation of the southern AGB is supported by the broadly correlated volcanic stratigraphy and intrusive rocks across the belt ([Ayer *et al.*, 2002](#)). The recurring tholeiitic and calc-alkaline volcanic assemblages over ~50 million years prior to ~2.70 Ga are interpreted to indicate either episodic short-term plate tectonics ([Moyen & van Hunen, 2012](#)) or ‘plume-arc’ interaction ([Ayer *et al.*, 2002](#), [Sproule *et al.*, 2002](#), [Wyman *et al.*, 2002](#)) under a broadly extensional environment ([Fig. 5.3](#)). Based on an interpretation of the LITHOPROBE seismic reflection profiles suggesting subduction zone scars are present within the sub-Opatoca lithosphere ([Calvert & Ludden, 1999](#)), the model of the plume-arc interaction in the AGB was extended by [Benn and Moyen \(2008\)](#) to suggest that an ocean basin was subducted beneath an active and partially differentiated oceanic plateau. However, [Bédard *et al.* \(2013\)](#) instead argued that the calc-alkaline volcanic rocks formed due to the intermittent melting at the base of the thickened basaltic crust (e.g., in vertical tectonics or a sagduction model).

Post-2.70 Ga

Tectonic shortening of the southern AGB postdating ~ 2.70 Ga was interpreted to be a consequence of subduction-like processes (Daigneault *et al.*, 2002). The syn-deformational granodiorite and tonalite plutonic suites are thought to be more likely derived from melting of subducted flat slab versus accreted oceanic crust or thickened plateau crust (Feng & Kerrich, 1992; Sutcliffe *et al.*, 1993, Wyman *et al.*, 2002). Crustal thickening in the southern AGB starting at ≤ 2690 Ma was followed by the Porcupine sedimentation and deformation of the previously formed volcanic and intrusive rocks (Monecke *et al.*, 2017). The intrusion of the late syn-deformational quartz syenite-quartz monzonite-granite suites (sanukitoid *sensu lato*) are interpreted to have been derived from a combination of metasomatized hydrous mantle sources and adakite-type sources (Wyman *et al.*, 2002).

Large-scale folding and thrusting, commensurate with a second stage of tectonic deformation, occurred prior to the Timiskaming sedimentation (i.e., before ~ 2679 Ma). This event was succeeded by emplacement of post-deformational shoshonitic trachytic and alkali-feldspar syenitic magmas localized to trans-lithospheric strike-slip structures. These magmas are related to the partial melting of refractory 'sub-arc' mantle fertilized by alkali-rich fluids or melts (Feng & Kerrich, 1992, Wyman *et al.*, 2002). Lastly, crustal melting and exhumation after ~ 2669 Ma was associated with formation of peraluminous granite (Daigneault *et al.*, 2002).

The southern AGB mainly experienced prehnite-pumpellyite to greenschist facies metamorphism during 2677–2643 Ma, but locally up to amphibolite facies metamorphism in the contact aureoles of plutons (Powell *et al.*, 1995, Ayer *et al.*, 2002). In contrast to the greenschist to amphibolite facies metamorphism of rocks in the northern AGB, the generally lower metamorphic grade now observed in outcropping rocks of the southern AGB (Fig. 5.2) may

reflect the shallower levels of exposure of the supracrustal rocks because of differential uplift (Benn & Moyen, 2008).

5.3.4 Mineral deposits

The main mineral deposit types and their exploited resources in the AGB include volcano-hosted massive sulfide (Cu, Zn, Au), komatiite-hosted magmatic Ni-Cu-PGE, banded iron formation, and mesothermal and intrusion-related Au deposits, as well as the unusual Chibougamau-type Cu-Au veins (see Monecke *et al.*, 2017 for a review). The intrusion-related Au deposits are reported to be associated with quartz-carbonate-albite alteration hosted in the late- to post-deformational felsic intrusions (Robert, 2001, Bigot & Jébrak, 2015), thus not comparable to either the Phanerozoic porphyry Cu-Au deposits (Sillitoe, 2010) or the reduced intrusion-related gold deposits (e.g., Thompson *et al.*, 1999, Hart, 2007). As the associated rock types with the intrusion-related Au deposits are not sodic TTG, they are therefore not the focus of this study.

Only a few porphyry-type Cu \pm Au deposits are reported for the southern AGB. This includes the Côté Gold and St-Jude deposits, both associated with low-pressure syn-volcanic TTG suites formed at \sim 2.74 Ga and \sim 2.70 Ga, respectively, and the Croxall deposit associated with \sim 2.69 Ga syn-deformational medium-pressure tonalite-granodiorite (Goldie *et al.*, 1979, Galley & Van Breemen, 2002, Piercey *et al.*, 2008, Katz *et al.*, 2017, 2021). Each of these deposits consists dominantly of breccia-hosted mineralization that is mainly associated with potassic (biotite \pm K-feldspar) alteration.

5.4 Porphyry-type Cu \pm Au deposits in the southern Abitibi greenstone belt

The salient features of four mineralized magmatic-hydrothermal settings (i.e., Côté Gold, St-Jude, Don-Rouyn, and Croxall) in the AGB are summarized below. Of particular relevance to this study is that these deposits are constrained using high-precision geochronology to have formed at three different times: the Côté Gold Au \pm Cu deposit of \sim 2.74 Ga, the St-Jude and Don-Rouyn Cu-Mo deposits related to the \sim 2.70 Ga Flavrian-Powell intrusive complex, and the Croxall Cu \pm Mo \pm Au deposit of \sim 2.69 Ga.

5.4.1 Côté Gold Au \pm Cu deposit (\sim 2740 Ma)

The Côté Gold Cu \pm Au deposit is located in the Swayze greenstone belt, an interpreted southwest extension of the AGB (Fig. 5.2). The deposit is hosted by the \sim 2.74 Ga Chester Intrusive Complex, a composite tonalite, diorite, and quartz diorite suite that is cut by magmatic and hydrothermal breccia bodies (Figs. 5.4A, 5.5A–B). The tectonic regime is generally thought to have been a back-arc-like setting based on the geochemistry of synchronous massive- and pillowed mafic volcanic rocks of the Arbutus Formation, which is part of the Pacaud assemblage noted above (Fig. 5.3; Katz *et al.*, 2017).

The deposit contains an indicated ore resource of 355.4 Mt at 0.87 g/t Au or 9.97 Moz Au (Katz *et al.*, 2021) with an associated but undefined amount of Cu (Kontak *et al.*, 2013, Katz, 2016, Katz *et al.*, 2021). The intrusive bodies, in particular the hydrothermal breccia, host sheeted-, stockwork-, disseminated-, and veinlet-types of mineralization associated mainly with biotite alteration overprinted by albite and sericite alteration. Four molybdenite separates from

mineralized quartz veins yielded a weighted mean Re-Os age of 2740.2 ± 5.6 Ma (2σ , $n = 4$, mean square of weighted deviates [MSWD] = 0.73), which is consistent with the isotope dilution-thermal ionization mass spectrometry (ID-TIMS) zircon U-Pb ages of the intrusive phases in the Chester Intrusive Complex (Kontak *et al.*, 2013, Katz *et al.*, 2017, 2021). The diorite is interpreted to be the causative magma for the Cu \pm Au mineralization (Kontak *et al.*, 2013, Katz, 2016, Katz *et al.* 2021). The area was overprinted by lower greenschist facies metamorphism related to later (i.e., <2.7 Ga) deformation (Katz *et al.*, 2017) and was cut by a series of later dike rocks of variable type, with the most dominant being the ~2.45–2.5 Ga Matachewan swarm (Fig. 5.4A).

5.4.2 Deposits associated with the ~2700 Ma Flavrian-Powell Intrusion

The St-Jude and Don-Rouyn porphyry-type are reported to be associated with the ~2.70 Ga Flavrian-Powell intrusive complex (Fig. 5.4B) estimated to have been emplaced at a pressure of 90–150 MPa (Feng & Kerrich, 1990). The complex intruded intermediate- to felsic volcanic rocks of the synchronous Blake River Group, which hosts many massive sulphide deposits (Monecke *et al.*, 2017) and formed during cauldron subsidence or early rifting in an arc- to the back-arc basin setting (Goldie *et al.*, 1979, Laflèche *et al.*, 1992, Galley & Van Breemen, 2002). The Flavrian pluton comprises diorite (Fig. 5.5C), tonalite, two phases of low-Al trondhjemite (phases I and II; Fig. 5.5D, E), and a late-stage quartz diorite (Galley, 2003). The high-level pluton has a wide contact aureole (<1 km) developed in the enveloping and synchronous volcanic rocks that reflects extensive convection of circulated seawater (Hannington *et al.*, 2003). The volcanic and plutonic rocks record the effects of later overprinting greenschist facies metamorphism.

The St-Jude deposit consists of porphyry-type Cu ± Mo ± Au mineralization hosted in a trondhjemite stock (Figs. 5.4B, 5.5F), which is interpreted to be genetically related to the Flavrian amphibole-bearing trondhjemite phase II (Fig. 5.5E; Goldie *et al.*, 1979, Galley & Van Breemen, 2002). The ~600 m diameter magmatic-hydrothermal breccia pipe (inset in Fig. 5.4B) hosts disseminated- and veinlet-type Cu ± Mo ± Au mineralization associated with a core of biotite alteration and outer biotite-sericite alteration where the altered rocks are crosscut by aplite dikes (Galley & Van Breemen, 2002). The lower limit of the age for the breccia-hosted mineralization is constrained by an ID-TIMS zircon U-Pb age of 2697 ± 2 Ma for the aplite dike (Galley & Van Breemen, 2002), which is temporally consistent with the Blake River Group volcanic rocks (Péloquin *et al.*, 2008 and references therein) and with the laser ablation-inductively coupled plasma-mass spectrometry (LA-ICP-MS) U-Pb zircon ages for the trondhjemite (see the section of 'Zircon U-Pb geochronology'). We interpret the trondhjemite in the core of the breccia body to be the causative magma for the mineralization.

In contrast to the St-Jude deposit, the Don Rouyn Cu-Mo deposit is hosted by the Powell intrusion that is interpreted to be structurally offset from its Flavrian counterpart (Fig. 5.4B). The deposit area is extensively fractured and overprinted by retrograde metamorphic chlorite that renders identifying the original mineralogy difficult. It is reported to be a porphyry-type deposit with disseminated- and veinlet-type mineralization and zoned in Cu with a chalcopyrite-bornite core to chalcopyrite outer zone having grades from <0.1 wt. % to >0.25 wt. %, respectively (Goldie *et al.*, 1979). According to Galley (2003), the associated alteration includes a silicic core, a biotite-rich halo, and outer zone of pervasively chlorite-altered host rock, which resemble the features of porphyry Cu deposit. However, limited access to the formerly mined area prevented verifying the causative magma, leading us not to consider the deposit as part of this study.

5.4.3 The Croxall Cu ± Mo ± Au deposit (~2689 Ma)

The porphyry-type Cu ± Mo ± Au mineralized Croxall breccia pipe (~40 m in diameter) is hosted by the Ben Nevis volcanic complex of the ~2701–2694 Ma Blake River Group (Péloquin *et al.*, 2008) and is one of several mineralized breccia bodies in this area. The Croxall pipe, well described by Chaloux (2005) and Piercey *et al.* (2008), has a core of andesitic breccia cemented by quartz and sulfide that grades outwards to a marginal “milled” breccia enriched in quartz, pyrite, and chalcopyrite with elevated Au, Ag, and Mo abundances. The pipe contains silicification and disseminated pyrite, whereas the wall rocks contain a network of mm- to cm-size veins of quartz, epidote, K-feldspar, hematite, and calcite (± sericite). The sulfide mineralization of the dark gray quartz veins with pyrite, chalcopyrite and molybdenite (± gold) is cut by hematite-calcite ± K-feldspar veins, which is similar to “J veins” in porphyry systems due to their jasperoidal appearance, as noted by Piercey *et al.* (2008).

A molybdenite separate from a quartz-pyrite-molybdenite vein yielded a Re-Os model age of 2682 ± 8 Ma, which overlaps with the ID-TIMS weighted mean zircon $^{207}\text{Pb}/^{206}\text{Pb}$ ages of 2689 ± 2 Ma and 2687 ± 1 Ma (2σ ; MSWD = 0.6 and 0.47, respectively; uranium decay constant uncertainties not considered) for the plagioclase-phyric porphyry and tonalite from the Croxall breccia, respectively (Piercey *et al.*, 2008). The porphyry-type mineralization is therefore interpreted to be genetically related to the subvolcanic Clifford stock composed mainly of tonalite, with minor granodiorite (Fig. 5.5G; Piercey *et al.*, 2008), and quartz diorite. The stock is surrounded by a number of quartz-feldspar porphyritic (Fig. 5.5H) and mafic dikes. The limited extent of an albite-epidote-magnetite alteration zone defines a pseudo-contact aureole in the enveloping basaltic to andesitic volcanic rocks (Fig. 5.4C) and has been interpreted to be related

to syn-intrusion high-temperature fluid circulation (Hannington *et al.*, 2003, Piercey *et al.*, 2008).

The area experienced prehnite-pumpellyite facies metamorphism.

5.5 Samples

5.5.1 Whole-rock geochemistry

The petrographic features of the major igneous phases from Côté Gold, Flavrian-St-Jude, and Clifford have been described in detail by Katz *et al.* (2017), Galley (2003), and Piercey *et al.* (2008), respectively. Representative samples from the different phases of these intrusions were collected for petrological characterization. Locations and petrographic descriptions of the representative samples are provided in Table 5.1. Heavy minerals from nine representative samples were separated using a Wilfley table after electric-pulse disaggregation at Overburden Drilling Management Inc., Ottawa, Canada. Zircon grains were hand-picked using a binocular microscope and were mounted in epoxy pucks, which were then polished to their mid-section using diamond grits (final grit size was $\sim 0.25 \mu\text{m}$). Petrographic features of the mounted zircons, including both the zircons and their inclusions, were characterized using a microscope and a Tescan Vega 3 scanning electron microscope (SEM) equipped with a Bruker energy dispersive spectrometer (EDS) and cathodoluminescence (CL) detector at Laurentian University.

Despite most samples having LOI (loss on ignition) values $< 2 \text{ wt. } \%$ ($< 2.5 \text{ wt. } \%$ for all), variable metamorphic effects are indicated by petrographic features (Fig. 5.6). In order to constrain magmatic $f\text{O}_2$ of the causative magmas for the mineralization, analyses were limited to the primary igneous minerals (i.e., zircon, amphibole, apatite, and magnetite-ilmenite pairs) that are demonstrated to have preserved magmatic features such as twinning or zoning, or to be

enclosed as inclusions in fresh coarser phases (i.e., amphibole and plagioclase) and in robust zircon hosts.

We focused initially on identifying primary mineral inclusions hosted in zircons, preparing ~300–500 grains for each sample except for the samples FLV-22 and CS-22 that had poor zircon yields. Zircon grains were mounted and polished to identify mineral inclusions, in particular for inclusions remote from fractures because they are known to have most likely preserved primary compositions (e.g., Bell, 2016). However, the exposed number of mineral inclusions varied considerably among zircon samples, which we consider to probably reflect the intrinsic abundances of inclusions and/or an unintentional bias towards selective cutting (i.e., along a single plane) of the zircon grains. Following on this, we also attempted to identify primary minerals in some of the polished thin sections of the selected samples.

The abundance of apatite inclusions in zircon grains most likely reflects the relative timing of apatite versus zircon crystallization (Bell *et al.*, 2018). If zircon crystallized earlier than apatite, which is manifested as elevated or nearly identical Ti-in-zircon temperature ($T_{\text{Ti-Zr}}$) relative to the apatite saturation temperature (AST), the chance of finding apatite inclusions in zircon is much reduced, and *vice versa*. For samples yielding elevated or close $T_{\text{Ti-Zr}}$ compared to AST (e.g., diorite sample Z10896 from Côte Gold with $T_{\text{Ti-Zr}}$ of 815 ± 30 °C and lower AST of 668 °C; tonalite sample CS-20 from Clifford with $T_{\text{Ti-Zr}}$ of 810 ± 27 °C and close AST of 865 °C), so that zircon-hosted apatite inclusions are rarely identified, efforts were made to seek apatite inclusions protected by other mineral phases or in the matrices. We scanned the thin sections of these samples using CL and BSE modes of the SEM to identify the apatite grains and examine their chemical zoning and textures.

5.5.2 Occurrence and features of primary zircon, amphibole, apatite, and Fe-Ti oxides

Zircon grains have crystal sizes that vary from 50–250 μm and typically exhibit oscillatory or sector zoning, as revealed by CL imaging (Fig. A5.1), which is consistent with a magmatic origin (e.g., Corfu *et al.*, 2003). The presence of mineral inclusions, as summarized in Table 5.1, varied and included apatite, K-feldspar, plagioclase, quartz, and minor biotite, rutile, titanite, and Fe-Ti oxides. Amphibole inclusions were not found in any of the zircon grain, and zircon grains from Côté Gold diorite sample, of which several hundred polished grains were examined, were completely devoid of mineral inclusions.

The nature of amphibole in the different intrusion varies considerably. Most of the amphiboles in the studied Côté Gold diorite samples record actinolitic alteration (Fig. 5.6B), although rarely less altered samples were identified and analyzed (Katz *et al.*, 2017). In contrast, the trondhjemite-II phase from the Flavrian intrusion contains amphibole (edenitic variety; Figs. 5.6E, 5.7A), which is not present in the trondhjemite from the St-Jude breccia (Fig. 5.6F). For the Clifford stock, the calcic amphiboles are common in the equigranular tonalite (Figs. 5.6G, 5.7B) and are also rarely found as phenocrysts in the plagioclase-phyric porphyry dike (Figs. 5.6H, 5.7C) proximal to the Clifford stock (Fig. 5.4C). Of particular note is that a plagioclase-phyric porphyry sample that was found to contain an amphibole glomerocryst with two optically different zones of similar magnesio-hornblende – the core and overgrowth areas are noted as Amp-I and Amp-II, respectively (Figs. 5.6H, 5.7C).

The number of exposed apatite inclusions in the studied zircons varies for Côté Gold, Flavrian-St-Jude, and Clifford (Fig. 5.7D, F–I). For diorite sample Z10896 from Côté Gold, one large interstitial equant apatite grain in the matrix having sector and oscillatory zoning was identified

(Fig. 5.7E), whereas other smaller apatite grains with fractures and patchy zonings, likely reflecting the effect of metamorphism, were noted. A few apatite grains have been found in zircons from sample CS-20 (tonalite) collected from the Clifford stock (Fig. 5.7H, I), and apatite grains hosted by amphibole in the matrix were identified with most having a patchy/mosaic CL response indicative of metamorphism and alteration (e.g., Fig. 5.7K). Apatite grains of sufficiently large size ($> 2 \mu\text{m}$) for analysis have not been identified in zircons from sample CS-22 (plagioclase-phyric porphyry), but one large grain with a faint magmatic zoning hosted in an amphibole phenocryst (Amp-I, Fig. 5.7J) was identified.

Primary magnetite and ilmenite are rare, but a single magnetite inclusion was found in a zircon grain from the Côte Gold tonalite (Fig. 5.8A) and an ilmenite inclusion was found in a zircon from a trondhjemite sample from the St-Jude breccia (sample SJ-04; Fig. 5.8B). Subhedral inclusions forming a primary magnetite-ilmenite pair showing textural equilibrium were identified in primary plagioclase (andesine with polysynthetic twinning) from the Clifford tonalite (samples CS-03 and CS-07; Fig. 5.8C–F), but some of the magnetite grains are pitted and may reflect alteration (Fig. 5.8G–J).

5.6 Analytical methods

5.6.1 Whole-rock geochemistry

Seventeen least-altered igneous rock samples were collected from outcrops in three study areas (i.e., Côte Gold, Flavrian-St-Jude, Clifford) for whole-rock geochemistry. Weathered and altered surfaces were removed from samples using a rock saw prior to crushing and grinding at ALS, Sudbury, Canada. The powdered samples were analyzed using X-ray fluorescence (XRF) and

ICP-MS with pre-fusion (lithium metaborate; CCP-PKG01 analytical package) at the Australian Laboratory Services (ALS) laboratory, Vancouver, Canada. To monitor the data accuracy, one secondary reference sample LK-NIP-1 (Nipissing diabase) was included in the submitted samples for analysis and the results are consistent with published values (https://www.mndm.gov.on.ca/sites/default/files/2018_geo_labs_brochure.pdf). Some elements in samples Z10896 and FLV-08 were duplicated. The results for the secondary reference (LK-NIP-1) and the unknown samples are reported in [Table A5.1](#).

5.6.2 Zircon U-Pb-Lu-Hf isotope and trace element analyses

All zircon samples were imaged using CL and BSE to characterize their internal textures, and to ensure they were devoid of mineral inclusions and cracks prior to ablation and analyses. To minimize the common lead contamination from surface contamination, all samples were polished with alumina powder and cleaned with ethanol-saturated kimwipes prior to analyses.

Zircon U-Pb-Lu-Hf isotope and trace element analyses were conducted in the Mineral Exploration Research Centre – Isotope Geochemistry Laboratory (MERC-IGL) at Laurentian University, Sudbury, Ontario, Canada. A 193 nm Photon Machines Analyte G2 laser equipped with a two-volume Helex II laser cell was used to ablate the zircons with a fluence of 2 J/cm², a repetition rate of 7 Hz, and a spot size of 35 µm. Each analysis lasted 10 seconds. Sixty seconds of background were measured at the beginning and end of the analytical session, with 30 seconds of background measurement between each ablation. The ablated aerosol was split into two mass spectrometers for simultaneous measurement of the U-Pb isotopic ratios and trace element abundances. The U-Pb isotopic ratios, and U, Th, and Pb concentrations were measured on a Thermo Neptune Plus multiple collector ICP-MS, whereas trace elements were analyzed on an

iCap TQ triple-quadrupole ICP-MS. The detailed instrumental parameters of laser ablation and ICP-MS, details of data processing and standards incorporated in the analytical protocol are identical to that provided in [Meng *et al.* \(2021\)](#). The results for the unknown samples and standard materials are reported in [Table A5.2](#).

The $^{206}\text{Pb}/^{238}\text{U}$ - $^{207}\text{Pb}/^{235}\text{U}$ concordia diagrams for the U-Pb isotope analyses were plotted using Isoplot version 4.15, with upper concordia intercept or concordia ages (reported with 2σ uncertainties), as well as the MSWD values calculated ([Ludwig, 2011](#)). Uranium decay constant uncertainties were not considered given that only U-Pb ages are being compared in this study. A small number of analyses with La content >1 ppm, which reflects contamination of subsurface REE-rich inclusions, were excluded for the calculation and plotting.

The Lu-Hf isotope analysis were measured on the same spot area previously used for O isotopes and some of the zircon U-Pb and trace element analyses. The laser ablation used a fluence of $6 \text{ J}\cdot\text{cm}^{-2}$, a repetition rate of 7 Hz, and a spot size of 40 μm . Ablation lasted 60 seconds for each analysis. Sixty seconds of background were measured at the beginning and end of the analytical session, with 30 seconds of background measurement between each ablation. One primary and five secondary reference standards (Pleosovice; 91500, R33, FC1, OGC, and MUN1/3) were periodically analyzed during the analytical runs. Readers are referred to [Meng *et al.*, 2021](#) for detailed information for instrumental parameters and data processing. The results for the unknown samples and standard materials are reported in [Table A5.3](#). The results for the secondary reference materials are identical to the published values ([Wiedenbeck *et al.*, 1995](#), [Fisher *et al.*, 2014](#), [Kemp *et al.*, 2017](#)). Single-stage Hf model ages and $\varepsilon_{\text{Hf}}(t)$ values are calculated using a ^{176}Lu decay constant of $1.867 \times 10^{-11}/\text{a}$ ([Söderlund *et al.*, 2004](#)) and the chondritic parameters from [Bouvier *et al.* \(2008\)](#).

5.6.3 Zircon O isotopes

Zircon oxygen isotope analyses were carried out prior to in-situ U-Pb-Lu-Hf isotope analyses using a Cameca IMS 1280 multi-collector ion microprobe housed in the Canadian Centre for Isotopic Microanalysis at the University of Alberta, Edmonton, Canada. Oxygen isotopes (^{18}O and ^{16}O) and counts of $^{16}\text{O}^1\text{H}/^{16}\text{O}$ in zircon were analyzed using a 20 keV $^{133}\text{Cs}^+$ primary beam ($\sim 10\ \mu\text{m}$ width) with a beam current of $\sim 2\ \text{nA}$. A minor group of analyses with $\Delta\text{OH} > 40\ \%$ were excluded, in which ΔOH represents the deviation of $^{16}\text{O}^1\text{H}/^{16}\text{O}$ ratios of the unknown from that of the standard (S0081). Details of sample preparation, instrumental parameters, and instrument mass fractionation are provided in [Meng *et al.* \(2021\)](#). The results for the unknown samples and standard materials are reported in [Table A5.4](#). Multiple analyses on different TEM2 grains (standard materials) yielded a weighted mean $\delta^{18}\text{O}_{\text{VSMOW}}$ value of $+8.23 \pm 0.12\ \%$ (2σ , $n = 42$, $\text{MSWD} = 1.07$), which is consistent with the published standard $\delta^{18}\text{O}_{\text{VSMOW}}$ value of $+8.20\ \%$ ([Black *et al.*, 2004](#)).

5.6.4 Electron microprobe analyses (EMPA)

Compositional data of apatite and amphibole were acquired with a Cameca SX100 EMPA operated using the wavelength-dispersive spectrometry (WDS) method at the Ontario Geoscience Laboratories (GeoLabs, Sudbury) and the Expert Process Solutions Laboratories (XPS, Falconbridge, Sudbury) in Ontario, Canada, respectively. For the magnetite and ilmenite grains, analyses were conducted using a JEOL JXA-8230 electron probe micro-analyzer at the University of Ottawa, Canada.

For the apatite analysis, fourteen elements (P, Si, Al, Mg, Ca, Mn, Fe, Sr, Na, K, S, F, Cl, Zr) were measured using the following conditions: 15-kV accelerating voltage, 10-nA beam current,

and 2- or 5- μm raster beam sizes. Zirconium concentrations were measured to monitor potential contamination of the apatite by the host zircon; analysis >1 wt. % ZrO_2 were excluded. As apatite is prone to decomposition due to electron beam damage, the resultant effect on halogen contents was tested. The test results, as reported in [Meng *et al.* \(2021\)](#), show that the S and Cl contents are reliable, but F content in apatite may be compromised by decomposition using a 2 μm beam. Damage of apatite using a beam size of 5 μm can be minimized, particularly for apatite grains with *c*-axis perpendicular to the electron beam. The test results were taken into account for analysis and data screening. The mole fractions of F, Cl, and OH (X_{F} , X_{Cl} , and X_{OH}) in apatite were calculated using a spreadsheet provided in [Zhang *et al.* \(2012\)](#).

For amphibole, thirteen elements (Si, Ti, S, Al, Fe, Mg, Ca, Cr, Mn, K, Na, Cl, F) were analyzed using conditions of 15-kV accelerating voltage, 10-nA beam current, and 5- μm beam size. For magnetite and ilmenite twelve elements (Si, Ti, Al, Cr, Fe, Mn, Mg, Ca, Zn, V, Ni, and Nb) were analyzed using the following conditions: 15-kV accelerating voltage, 20-nA beam current, and focused beam size. X-ray lines, analyzing crystals, and counting times (for both peak and background measurements), and detection limits for the elements of the minerals at the different settings are listed in [Table A5.5](#). The results are also reported in [Table A5.5](#).

5.6.5 Micro X-ray absorption near edge structure (μ -XANES) at the S *K*-edge

Micro X-ray absorption near-edge structure spectroscopy at the sulfur *K*-edge (S μ -XANES) was conducted to measure the sulfur oxidation states of apatite inclusions at the Advanced Photon Source (APS) of the Argonne National Laboratory in Chicago, IL, USA, and at the Swiss Light Source (SLS) of the Paul Scherrer Institute in Villigen, Switzerland. The μ -XANES analyses were conducted on representative apatite crystals unaffected by prior electron microprobe beam

analysis. Two scans were collected at each point to improve counting statistics and to monitor for beam damage caused by irradiation of the focused X-ray beam and contribution from other phases (e.g., the host zircon, epoxy). Beam damage was not observed in any apatite spectra collected in this study. Details of the method are referred to [Meng *et al.* \(2021\)](#).

5.7 fO_2 -P-T parameters

5.7.1 Oxybarometers

Zircon oxybarometer

[Smythe and Brenan \(2016\)](#) and [Loucks *et al.* \(2020\)](#) have recently calibrated two different methods to quantify magmatic fO_2 using zircon geochemistry. The method of [Smythe and Brenan \(2016\)](#) requires the use of zircon trace element abundances and the known melt composition, as approximated by the whole-rock composition of the sample, in addition to melt water content and activities of SiO_2 and TiO_2 . The sensitivity of the method to water content can introduce large uncertainties (i.e., variation of the H_2O content by 1 wt. % can produce a deviation of about 0.5 log unit of fO_2) because accurate estimation of melt water content is difficult owing to the lack of reliable hydrometers. Thus, we have instead used the method of [Loucks *et al.* \(2020\)](#) which only involves the measured zircon Ti, Ce, and age-corrected initial U content. The method is applicable to volcanoplutonic rocks with a broad range of composition, including calc-alkaline, tholeiitic, adakitic, shoshonitic, metaluminous to mildly peraluminous and mildly peralkaline having fO_2 values of ΔFMQ ranging from -4.9 to $\Delta FMQ +2.9$. The method yields a standard error of $\sim \pm 0.6$ log unit.

Amphibole oxybarometer

Ridolfi *et al.* (2010) retrieved empirical oxybarometric formulations suitable for calc-alkaline volcanic rocks with crystallization conditions in the range of 550 to 1120 °C, <1200 MPa, and $-1 \leq \Delta\text{NNO} \leq +5$ (ΔNNO represents $f\text{O}_2$ in log units relative to the nickel-nickel-oxide buffer), with estimated uncertainty of ± 0.22 log unit. The method can be as reliable as the magnetite-ilmenite oxybarometer for volcanic rocks (Ridolfi *et al.*, 2010), but it may systematically overestimate the $f\text{O}_2$ by one log unit for intrusive rocks (Wang *et al.*, 2014). Nevertheless, we can use the oxybarometer to semi-quantitatively constrain $f\text{O}_2$ values for internal comparison between different intrusive rocks.

Sulfur-in-apatite oxybarometer

Apatite has traditionally been inferred to incorporate sulfur only as S^{6+} (Peng *et al.*, 1997, Tepper & Kuehner, 1999, Parat *et al.*, 2011) until Konecke *et al.* (2017) recently detected varying proportion of S^{6+} , S^{4+} , and S^{2-} as a function of $f\text{O}_2$ in natural apatite samples using μ -XANES at the S K -edge. The observation was corroborated by ab-initio calculations of the energetics and geometry of the different sulfur species in the apatite structure (Kim *et al.*, 2017). Konecke *et al.* (2019) further refined a Boltzmann-type sigmoidal, experimental correlation between the apatite $\text{S}^{6+}/\Sigma\text{S}$ ratio and $f\text{O}_2$ for mafic silicate melts having P-T crystallization conditions of 300 MPa and 1000°C. The oxybarometer is sensitive to the redox range of $\Delta\text{FMQ} +0$ to $+1.2$ and can also provide first-order $f\text{O}_2$ constraints on relatively reduced ($< \text{FMQ}$) and moderately to highly oxidized ($\Delta\text{FMQ} > 1.2$) magmatic systems. If considering that the P-T or compositional effect on silicate glasses may be proportional to apatite, the S-in-apatite calibration curve therefore needs correction (Konecke *et al.*, 2019). The P-T conditions at the time of apatite crystallization are therefore evaluated (see methods below).

Magnetite-ilmenite oxybarometer

The magnetite-ilmenite oxybarometer is well developed to estimate magmatic fO_2 based on an assumption of equilibrium between the Fe-Ti oxides (Buddington & Lindsley, 1964, Ghiorso & Sack, 1991, Sack & Ghiorso, 1991, Ghiorso & Evans, 2008). Because Fe-Ti oxide minerals are prone to hydrothermal alteration and sub-solidus re-equilibration during slow cooling in plutonic rocks (Anderson & Thomas, 1985, Anderson *et al.*, 2008), we restrict the calculation to those igneous magnetite and ilmenite showing textural equilibrium, as demonstrated by their intergrowth relationship. Grains with exsolution of ilmenite/magnetite lamellae or martitization that formed during subsolidus cooling or hydrothermal alteration were excluded. The ILMAT spreadsheet from Lepage (2003) is used to calculate the equilibrium temperature and fO_2 . The results of T and fO_2 yielded 2σ uncertainties of $\sim 10\text{--}30$ °C and $0.1\text{--}0.2$ log fO_2 units, respectively (Spencer & Lindsley, 1981).

5.7.2 P-T evaluation

The emplacement pressure of the Flavrian intrusion has been estimated by Feng & Kerrich (1990) to be 90–150 MPa (~ 120 MPa on average). The emplacement pressure of the Clifford stock is estimated from amphibole composition using the method of Mutch *et al.* (2016) in order to correct sulfur-in-apatite oxybarometer (such estimation is not required for samples from Côte Gold because μ -XANES spectra was not obtained). The Al-in-hornblende geobarometer is suitable for tonalitic to granodioritic rocks containing amphibole, biotite, plagioclase (An_{15-80}), quartz, alkali-feldspar, apatite, titanite, and zircon, which are broadly consistent with the mineral assemblage identified in the Clifford tonalite and plagioclase-phyric porphyry (biotite has locally been found).

Crystallization temperatures of zircon, amphibole, apatite, and Fe-Ti oxides are calculated using the following thermometers: Ti-in-zircon (Ferry & Watson, 2007), amphibole (Ridolfi *et al.*, 2010), *model* apatite saturation (Piccoli & Candela, 1994), and magnetite-ilmenite (Lepage, 2003). For the Ti-in-zircon thermometer, based on the presence of quartz and Ti-bearing minerals (e.g., titanite and ilmenite) in the studied samples, the activities of SiO₂ and TiO₂ are assumed to be 1 and 0.5, respectively (Schiller & Finger, 2019). The *model* AST (apatite saturation temperature) is calculated to represent the temperature at which apatite began to crystallize from the metaluminous magmas [molar Al₂O₃/(CaO + Na₂O + K₂O) ≤ 1.0 and Al₂O₃/(Na₂O + K₂O) ≤ 1.0] (Piccoli & Candela, 1994). We assume that the whole-rock SiO₂ and P₂O₅ abundances approximate the concentration of these oxides in the melt at the time of apatite crystallization.

5.8 Results

5.8.1 Lithochemistry

In addition to the analyses presented here for the selected seventeen samples, which includes diorite and tonalite at Côté Gold, diorite and trondhjemite at Flavrian-St-Jude, and tonalite and plagioclase-phyric porphyry at Clifford (Table A5.1), previously published whole-rock major and trace element data (filtered by LOI < 2.5 wt. %) for forty-seven samples of similar phases are compiled in Table A5.1 from Galley (2003), Piercey *et al.* (2008), and Katz (2016). The major elements and Cu contents are reported for those samples lacking noted alteration with LOI < 2.0 wt. %. The major elements were recalculated on a normalized anhydrous basis.

The Côté Gold diorite samples have $K_2O/Na_2O = 0.04\text{--}0.57$, total $Fe_2O_3 = 5.1\text{--}13.7$ wt. %, $MgO = 1.5\text{--}6.1$ wt. %, and $Mg\#$ (molar $Mg/[Mg + Fe]*100$) = $28\text{--}48$ (0.21 ± 0.14 , 9.7 ± 2.5 wt. %, 4.2 ± 1.2 wt. %, and 41 ± 6 on average, respectively; 1σ , $n = 22$). The least altered samples yielded an average Cu content of 39 ± 21 ppm (1σ). On a primitive mantle normalized trace element diagram, most of the samples are enriched in large ion lithophile elements (LILEs: Rb, Th, U, and K; some other samples are depleted in Rb or K) and depleted in Nb, Ta, and Ti (Fig. 5.9A). On a chondrite-normalized rare earth element (abbreviated as REE hereafter) diagram, the samples display a concave pattern (Fig. 5.9B) with low La/Yb ratios of $0.7\text{--}9.0$ and moderate to significant negative Eu anomalies ($0.25\text{--}1.10$, 0.70 ± 0.19 on average; 1σ , $n = 32$). Moderate depletion of Sr, P, and Ti, as well as the negative Eu anomalies, reflects minor fractionation of apatite and Fe-Ti oxides and moderate fractionation of plagioclase.

One diorite sample from the Flavrian intrusion yielded flat trace and rare element patterns and has $K_2O/Na_2O = 0.08$, total $Fe_2O_3 = 10.1$ wt. %, $MgO = 4.3$ wt. %, and $Mg\# = 41$. In contrast, the Flavrian and St-Jude trondhjemite samples have $K_2O/Na_2O = 0.03\text{--}0.33$, total $Fe_2O_3 = 0.8\text{--}8.3$ wt. %, $MgO = 0.2\text{--}2.7$ wt. %, and $Mg\# = 4\text{--}60$ (0.12 ± 0.07 , 3.8 ± 2.3 wt. %, 0.7 ± 0.4 wt. %, and 22 ± 15 on average, respectively; 1σ , $n = 14$). In the primitive mantle normalized trace element diagram, these samples are seen to be depleted in Nb, Ta, Sr, P, and Ti (Fig. 5.9C), whereas in the chondrite-normalized REE diagram, they show slight enrichment of light REE but a flat heavy REE profile (Fig. 5.9D) with La/Yb ratios of $1.9\text{--}7.4$ (3.6 ± 1.7 on average; 1σ , $n = 15$) and negative Eu anomalies of $0.42\text{--}0.97$ (0.70 ± 0.21 on average; 1σ , $n = 15$). These features suggest moderate to significant fractionation of plagioclase, apatite, and Fe-Ti oxides during magma evolution. The least altered trondhjemite samples yielded an average Cu content of 11 ± 9 ppm (1σ , $n = 14$).

The Clifford tonalite and plagioclase-phyric porphyry samples have $K_2O/Na_2O = 0.21\text{--}0.23$, total $Fe_2O_3 = 4.5\text{--}4.9$ wt. %, $MgO = 2.2\text{--}2.8$ wt. %, and $Mg\# = 44\text{--}50$ (0.22 ± 0.01 , 4.7 ± 0.2 wt. %, 2.5 ± 0.4 wt. %, and 44 ± 5 on average, respectively; 1σ , $n = 2$). The two samples contain an average Cu content of 36 ± 18 ppm (1σ , $n = 2$). These samples yielded noticeably different trace and rare earth element patterns and lower REE contents in comparison to the Côté Gold and Flavrian samples. In the primitive mantle normalized trace element diagram, they show enrichment in fluid-mobile LILEs (Rb, Ba, Th, U, K, and Sr) and light REEs, and are depleted in Nb, Ta, and minor Ti (Fig. 5.9E). Their REE_{CN} profile shows a strongly fractionated pattern with high La/Yb ratios (9.7–15.3, 12.4 ± 1.6 ; 1σ , $n = 13$), and weak negative to positive Eu anomalies (1.09 ± 0.27 on average, 1σ , $n = 13$; Fig. 5.9F). These samples also have high Sr/Y (20–45, 31 ± 7 on average, $n = 13$; Fig. 5.10A) and V/Sc (13.1 ± 0.8 ; 1σ , $n = 3$) ratios. These features suggest fractionation of amphibole and Fe-Ti oxides, but the lack of plagioclase fractionation. The amphibole-dominated fractionation trend is also supported by broadly decreasing Dy/Yb ratios with SiO_2 in Figure 5.10B (Davidson *et al.*, 2007).

5.8.2 Zircon U-Pb geochronology

The LA-ICP-MS zircon U-Pb ages for the samples are summarized in Figure 5.11 and Table 5.2, with the complete database provided in Table A5.2. The major intrusive phases in each of the studied areas have previously been dated with ID-TIMS (Galley & Van Breemen, 2002, Piercey *et al.*, 2008, Kontak *et al.*, 2013, Katz *et al.*, 2017). The new data for Côté Gold provide further age constraints on previously dated phases (diorite and tonalite), and this study also supplement the published data for the St-Jude and Clifford areas with five new intrusive samples including three samples of the two trondhjemite phases from the Flavrian intrusion, the trondhjemite from the St-Jude breccia, and one each of the tonalite and plagioclase-phyric porphyry from the

Clifford stock. Representative zircon grains from the previously dated diorite and tonalite were also incorporated into the analytical session to monitor zircon inheritance and post-crystallization possible Pb loss.

The diorite and tonalite samples from Côte Gold previously dated using CA-ID-TIMS method were analyzed. Thirty-five analyses of zircon grains from sample Z10896 (diorite) yielded an upper concordia intercept age of 2736 ± 6 Ma (2σ , $n = 35$, MSWD = 0.01; Fig. 5.11A). Thirty-one analyses of zircon grains from sample Z10993 (tonalite) yielded an upper concordia intercept age of 2736 ± 4 Ma (2σ , $n = 31$, MSWD = 0.13; Fig. 5.11B). These results agree within uncertainty with the published CA-ID-TIMS ages of 2741.5 ± 0.7 Ma and 2741.4 ± 0.9 Ma for the samples Z10896 and Z10993, respectively, reported by Katz *et al.* (2017), as well as an age of 2741.1 ± 0.9 Ma for a tonalite sample reported in Kontak *et al.*, 2013. These new and published results constrain the emplacement age of the Côte Gold intrusions to ~ 2.74 Ga.

For the Flavrian intrusive complex four trondhjemite samples were dated. Thirty-five analyses of zircon grains from sample FLV-22 (trondhjemite phase I) yielded an upper concordia intercept age of 2691 ± 9 Ma (2σ , $n = 35$, MSWD = 0.31; Fig. 5.11C). If four analyses are excluded, two each with Pb-loss or reverse discordance (grey ellipses in Fig. 5.11C), a concordia intercept age of 2700 ± 9 Ma (2σ , $n = 31$, MSWD = 0.7; Fig. 5.11C) is defined. Thirty-two analyses of zircon grains from sample FLV-28 (trondhjemite phase I) yielded an upper concordia intercept age of 2689 ± 6 Ma (2σ , $n = 32$, MSWD = 0.23; Fig. 5.11D). If the single analysis with Pb-loss is excluded, this yields a concordia age of 2692 ± 6 Ma (2σ , $n = 31$, MSWD = 1.18). Forty-three analyses of zircon grains from sample FLV-04 (trondhjemite phase II) yielded an upper concordia intercept age of 2694 ± 8 Ma (2σ , $n = 43$, MSWD = 0.26; Fig. 5.11E), which agrees within uncertainty to the previously published CA-ID-TIMS age of $2700 +3/-2$ Ma (2σ , MSWD

= 0.62; Galley & Van Breemen, 2002). Twenty-two analyses of zircon grains from sample SJ-04 (St-Jude trondhjemite) yielded similar upper concordia intercept age of 2697 ± 13 Ma (2σ , $n = 22$, MSWD = 2.6; Fig. 5.11F), with two other analyses not shown in the plot yielding similar discordant older ages ($^{207}\text{Pb}/^{206}\text{Pb}$ ages of 2882 ± 38 Ma and 2847 ± 7 Ma; Table A5.2) and thus likely reflecting xenocrysts. All four of the LA-ICP-MS U-Pb dates are consistent within uncertainty and yield a calculated weighted mean age of 2695 ± 5 Ma (2σ , $n = 4$, MSWD = 1.11). Thus these dates constrain the emplacement age of the Flavrian-St-Jude trondhjemite phases to ~ 2.70 Ga.

For the Clifford stock, two samples with tonalitic composition were dated. For sample CS-20 (tonalite), thirty-six analyses of zircon grains yielded an upper concordia intercept age of 2690 ± 7 Ma (2σ , $n = 36$, MSWD = 0.78; Fig. 5.11G). Twenty-nine analyses of zircon grains from sample CS-22 (plagioclase-phyric porphyry) yielded an upper concordia intercept age of 2694 ± 12 Ma (2σ , $n = 29$, MSWD = 0.61; Fig. 5.11H). These two dates overlap within uncertainty, a weighted mean age of 2692 ± 8 Ma (2σ , $n = 2$, MSWD = 0.05) was calculated. These dates overlap within uncertainty with the previously published ID-TIMS zircon weighted mean $^{207}\text{Pb}/^{206}\text{Pb}$ ages of 2687 ± 1 Ma and 2689 ± 2 Ma (Piercey *et al.*, 2008), constraining the formation of tonalite and plagioclase-phyric porphyry to ~ 2.69 Ga.

The age results are consistent within the uncertainty of previously published ID-TIMS zircon U-Pb age results, although the new ages reported here have relatively poorer precision. Of particular interest and relevance to this study is that most of the zircon analyses for each sample yielded concordant data that are consistent with closed system behavior despite variable degrees of post-crystallization tectonic disturbance in the study areas.

5.8.3 Zircon Hf-O isotopes

The zircon Hf-O isotopic data are summarized in [Figure 5.12](#) and [Table 5.2](#), with the full dataset reported in [Tables A5.3–5.4](#). Zircon $\varepsilon_{\text{Hf}}(t)$ values of 113 analyses for all of the samples range from 2.4 to 5.3 (4.3 ± 0.4 on average; 1σ). These values are consistent with melt extraction to form new crust at ~ 2.69 – 2.74 Ga ([Fig. 5.12](#); [Dhuime et al., 2011](#)) and suggest juvenile sources with minimal crustal contribution. In contrast to the indistinguishable $\varepsilon_{\text{Hf}}(t)$ values among the samples, the zircon $\delta^{18}\text{O}$ values decrease from 4.88–5.59 ‰ (5.29 ± 0.18 ‰ on average; 1σ , $n = 24$) for the Côte Gold diorite and tonalite, 4.01–5.10 ‰ (4.71 ± 0.23 ‰ on average; 1σ , $n = 27$) for the Clifford tonalite and plagioclase-phyric porphyry, and to 3.98–4.89 ‰ (4.53 ± 0.20 ‰ on average; 1σ , $n = 53$) for the Flavrian trondhjemite. Zircons from the St-Jude trondhjemite yielded the lowest $\delta^{18}\text{O}$ values of 3.72 to 4.13 ‰ (3.91 ± 0.13 ‰ on average; 1σ , $n = 8$), with a xenocrystic zircon grain yielding a similar $\delta^{18}\text{O}$ value of 4.16 ± 0.29 ‰ (2se). The low- $\delta^{18}\text{O}$ zircons from the Clifford and Flavrian-St-Jude intrusions have low OH/O ratios which are comparable to those of the measured reference zircons in the analytical session, we therefore suggest that the apparent $\delta^{18}\text{O}$ depletions are intrinsic features of the protolith rather than as a result of post-crystallization modification due to fluid-mediated alteration.

We interpret these results to indicate that the Côte Gold magmas were derived from a mantle source, whereas the protoliths (also with juvenile mantle-derived sources) for the Flavrian, St-Jude, and Clifford magmas experienced variable degrees of high-temperature hydrothermal alteration comparable to low $\delta^{18}\text{O}$ magmas (e.g., [Valley et al., 2005](#), [Bindeman & Simakin, 2014](#), [Hammerli et al., 2018](#), and references therein). Note that the scattered and broadly lower $\delta^{18}\text{O}$ zircon values for the plagioclase-phyric porphyry versus the tonalite in the Clifford stock

may indicate preferential assimilation of altered volcanic supracrustal rocks of the Blake River Group (reported to locally have a relatively depleted $\delta^{18}\text{O}$ signature; Cathles, 1993) during the magma ascent.

5.8.4 Apatite composition

Apatite S-Cl contents

The compositions of igneous apatite from the Côte Gold, Flavrian-St-Jude, and Clifford igneous suites are listed in Table A5.5 and illustrated in Fig. 5.13A. The average chlorite concentration of zircon-hosted apatite inclusion from the Côte Gold tonalite is 0.07 ± 0.05 wt. % (1σ , $n = 9$), whereas the S contents of the said inclusions are below the detection limit (i.e., 0.01 wt. %). The S concentrations of groundmass apatite grains from Côte Gold diorite are below the EPMA detection limit, whereas the average Cl concentration is 0.04 ± 0.01 wt. % (1σ , $n = 43$), which are significantly lower than the Cl contents reported for apatite micro-phenocrysts in Phanerozoic arc-related plutonic and volcanic rocks (e.g., Streck & Dilles, 1998, Imai, 2004, Scott *et al.*, 2015).

The S contents of all of the analyses ($n = 17$) from the Flavrian-St-Jude trondhjemite samples are below the EPMA detection limit. For the apatite from ore-unrelated trondhjemite samples (FLV-22 and FLV-28), the average Cl concentration is 0.07 ± 0.02 wt. % (1σ , $n = 5$) excluding analyses below the detection limit and a single value of 1.10 wt. %. In contrast, the ore-related trondhjemite samples (SJ-04 and FLV-04) have much higher apatite Cl contents of 0.75 ± 0.44 wt. % (1σ , $n = 4$) with four analyses below detection limit excluded. The altered apatite grains hosted in amphibole from sample FLV-32 (diorite) yielded S contents below the detection limit ($n = 6$; except one analysis of 0.01 wt. % S) and Cl contents of 0.37 ± 0.11 wt. % (1σ , $n = 7$).

The primary and altered apatite grains from the Clifford tonalite and plagioclase-phyric porphyry yielded distinctly different S and Cl contents. Two zircon-hosted primary apatite grains from the Clifford tonalite (sample CS-20) yielded S and Cl contents of 0.05 ± 0.03 and 1.86 ± 0.48 wt. %, respectively ($n = 5$), whereas four analyses of apatite hosted in the Amp-I phenocryst in the plagioclase-phyric porphyry (sample CS-22) yielded S and Cl contents of 0.09 ± 0.02 and 0.90 ± 0.03 wt. % (1σ , $n = 4$), respectively. In contrast, the altered apatite grains (samples CS-20 and CS-22) yielded similar compositions with S contents of 0.017 ± 0.003 wt. % (1σ , $n = 5$, but excluding 17 analyses below the detection limit) and Cl contents of 0.16 ± 0.08 wt. % (1σ , $n = 22$), respectively. A single, altered zircon-hosted apatite inclusion (cut by a fracture; [Fig. 5.7I](#)) was also analyzed and yielded similarly low S (0.018 wt. % for one analysis and the second analysis yielding S content below the detection limit) and Cl (0.16 ± 0.06 wt. %; 1σ , $n = 2$) contents. The noticeable decreases of S and Cl contents from primary to altered apatite in these samples are interpreted to reflect the effect of metamorphism and alteration.

Geochemical discrimination of primary versus altered apatites

To evaluate whether the studied apatite grains crystallized in a volatile-undersaturated or water-saturated environment, we followed the thermodynamic models in [Stock *et al.* \(2018\)](#) and accordingly plotted the X_{Cl}/X_{OH} versus X_F/X_{Cl} and X_{Cl}/X_{OH} versus X_F/X_{OH} ratios for analyses yielding halogen contents above the detection limits ([Fig. 5.13B–F](#)). Based on experimental results that demonstrate higher fluid-melt partition coefficients for Cl than for F ([Webster *et al.*, 2009](#)), the models predict that the apatite X_F/X_{Cl} ratio decreases or remains constant with variable X_{Cl}/X_{OH} ratios under volatile-undersaturated conditions. In contrast, for water-saturated conditions the apatite X_F/X_{Cl} ratio increases and is commensurate with a decrease in its X_{Cl}/X_{OH} ratio and, in addition, the apatite X_{Cl}/X_{OH} ratio rapidly decreases with increasing X_F/X_{OH} ratio.

Following the thermodynamic models, we only plotted EMPA analyses obtained using a 5 μm beam or for a 2 μm beam where the apatite was oriented perpendicular to its c -axis so as to limit the effects of beam damage (Webster et al., 2009; Meng et al., 2021). Thus, having taken the data screening criteria into account, the observed correlations between ratios of $X_{\text{Cl}}/X_{\text{OH}}$ and $X_{\text{F}}/X_{\text{Cl}}$ in the plots (Fig. 5.13B–F) are interpreted to represent primary signatures. These results suggest most of the apatite analyses for the Côte Gold tonalite and the Flavrian-St-Jude trondhjemite evolved along water-saturated and volatile-undersaturated trajectories, respectively. The low S contents of apatite grains from the Flavrian-St-Jude trondhjemite samples are consistent with primary compositions unaffected by magmatic degassing and hydrothermal alteration. In comparison, the altered apatite grains hosted in amphibole grains in sample FLV-32 indicate evolution along a water-saturated trajectory (Fig. 5.13B, Fig. A5.2), consistent with hydrothermal alteration of the apatite grains.

Most of the analyses for the Cl-rich primary and Cl-poor altered apatite grains from the Clifford tonalite and plagioclase-phyric porphyry evolve along volatile-undersaturated and water-saturated trajectories, respectively, of which the water-saturated trajectory for the Cl-poor altered apatite analyses support hydrothermal alteration associated with metamorphism. Five analyses of the Cl-poor apatite grains hosted in amphibole from the tonalite evolve along a volatile-undersaturated trajectory (Fig. 5.13E), possibly reflecting selective preservation of pre-degassed apatite in the matrix. Nevertheless, the Cl-rich primary apatite grains are interpreted to have formed prior to magma degassing and also record the primary composition.

Preliminary evaluation of pre-degassed melt S content

The S contents of the silicate melt from which apatite crystallized in each of the three mineral systems was estimated based on the S concentration of apatite in conjunction with published apatite/melt S partition coefficients with the knowledge that the S content of apatite is controlled by S content of the melt, temperature, and oxidation state (Peng *et al.*, 1997, Parat *et al.*, 2011, Webster & Piccoli, 2015, Konecke *et al.*, 2017, 2019). The apatite S concentration for the Côte Gold diorite and tonalite and the Flavrian-St-Jude trondhjemites are below the detection limit, which precludes such evaluation. However, we note that their S contents (below detection limit) are significantly lower than that for apatite micro-phenocrysts from Phanerozoic arc-related magmas (Streck & Dilles, 1998, Imai, 2004, Scott *et al.*, 2015), which are interpreted to reflect either low magmatic S content or a relatively reduced environment based on fO_2 estimation.

In contrast to the Côte Gold and Flavrian-St-Jude igneous suites, the primary apatite grains crystallized from the Clifford magmas yielded a relatively high pre-degassed S content (0.06 ± 0.03 wt. %; 1σ , $n = 9$) at the *model* AST of 869 ± 5 °C (1σ , $n = 2$) and a magmatic fO_2 of $\Delta FMQ \sim +1.5$. If considering the fO_2 -T parameters are comparable to many Phanerozoic arc magmas, the lower apatite S contents for the Clifford rocks compared to that for Phanerozoic arc magmas (0.15 ± 0.07 wt. %, 1σ , $n = 349$; see compilation in Meng *et al.*, 2021) suggest that the S content of the Clifford stock magma was slightly lower than the Phanerozoic arc magmas. In support of that interpretation, we used the method proposed in Meng *et al.* (2021) that combines the apatite/melt partition coefficient for S ($D_S^{\text{apatite/melt}}$) as a function of fO_2 (Konecke *et al.*, 2019) and temperature (Parat & Holtz, 2004) to calculate the S content of the melt. This approach yielded a calculated $D_S^{\text{apatite/melt}}$ of 1.2 and a model melt S content of 0.039

± 0.018 wt. % (1σ) for the Clifford tonalitic magmas, which is similar to the lower limit of the average S content of 0.09 ± 0.07 wt. % (1σ , $n = 69$) for many Phanerozoic arc magmas (see compilation in [Meng *et al.*, 2021](#)).

5.8.4 Estimation of magmatic fO_2

Zircon

Zircon trace element data for representative samples collected from the study areas are illustrated in [Figure 5.14](#) with the full database reported in [Table A5.2](#). To minimize the effects of hydrothermal alteration and contamination from xenocrystic cores and subsurface mineral/melt inclusions on the calculations and related interpretations, we filtered our data using geochemical criteria as follows: (1) La content < 1 ppm; (2) Light REE Index (LREE-I) = (Dy/Nd) + (Dy/Sm) > 10 ([Bell *et al.*, 2016](#)); (3) Ti content < 50 ppm; and (4) age discordance $< 10\%$. Based on these criteria, 32 of 294 analyses (i.e., 11%) were excluded for the following interpretation. The geochemical features of the zircons support a magmatic origin, based on the criteria in [Hoskin & Schaltegger \(2003\)](#), which includes: 1) a lack of compositional variation for each sample; 2) positive Ce_{CN} anomalies; 3) moderate- to significant negative Eu_{CN} anomalies ([Fig. 5.14](#)); and 4) Th/U ratios > 0.4 (rarely between 0.3 to 0.4 for the St-Jude trondhjemite).

The Hf contents and Zr/Hf ratios, which are generally used to indicate magmatic fractionation ([Claiborne *et al.*, 2006](#)), are not observed to correlate with T_{Ti-Zr} for most of the samples ([Fig. A5.3](#)). This suggests that insignificant fractionation had occurred at the time of zircon crystallization, although the slight negative correlations between Hf and Zr/Hf for the Côte Gold samples are the exception. Furthermore, the T_{Ti-Zr} versus Y contents and Th/U ratios do not define well-developed trends ([Fig. A5.3](#)). We therefore infer that the analyzed zircons

crystallized in a narrow interval of magmatic evolution and therefore presumably record homogenous compositions.

Following the above interpretation, the methods of [Loucks *et al.* \(2020\)](#) and [Ferry & Watson \(2007\)](#) are used to quantify the fO_2 and temperatures for the igneous rocks. The standard error for each analysis is propagated based on standard errors of the calibrated equations and the abundances of related elements (i.e., Ce, U, and Ti). The results are reported in the [Table A5.2](#) and illustrated in [Figure 5.15](#). The single analysis results of fO_2 and temperature for each sample overlap with each other within 2 standard errors and yielded p -values >0.05 (most of them are above 0.80), suggesting statistically significant similarities ([Fig. A5.4](#)). We report the average values with standard deviations (1σ) below with results summarized in [Table 5.2](#).

The Côté Gold tonalite (sample Z10993) and diorite (sample Z10896) yielded fO_2 values of $\Delta FMQ -0.8 \pm 0.4$ (1σ , $n = 31$) and 0.7 ± 0.4 (1σ , $n = 35$), respectively. Zircons from the four Flavrian-St-Jude trondhjemite samples yielded similar fO_2 values of $\Delta FMQ +0.07 \pm 0.6$ (1σ , $n = 35$; sample FLV-22), 0.4 ± 1.0 (1σ , $n = 31$; sample FLV-28), -0.0 ± 0.6 (1σ , $n = 43$; sample FLV-04), and -0.3 ± 0.6 (1σ , $n = 22$; sample SJ-04), respectively. Two xenocrystic zircons of ~ 2.85 Ga from sample SJ-04 yielded similar fO_2 values with $\Delta FMQ -0.3 \pm 0.1$ (1σ , $n = 2$). The Clifford tonalite and plagioclase-phyric porphyry yielded $\Delta FMQ +1.2 \pm 0.4$ (1σ , $n = 37$) and $\Delta FMQ +0.2 \pm 0.2$ (1σ , $n = 28$), respectively. The lower fO_2 value of the Clifford plagioclase-phyric porphyry dike versus the coeval Clifford tonalite is interpreted to reflect assimilation of the tonalitic magmas with the surrounding volcanic rocks of the Blake River Group during magma ascent, which is presumed to be as reduced as the coeval Flavrian-St-Jude intrusion (i.e., fO_2 values of $\Delta FMQ -0.3$ and 0.4 above).

Zircons from each sample yielded narrow variations of $T_{\text{Ti-Zr}}$ with 815 ± 30 °C (1σ , $n = 35$) and 773 ± 34 °C (1σ , $n = 31$) for the Côté Gold diorite and tonalite, 736 ± 33 °C (1σ , $n = 109$) for Flavrian trondhjemite samples, and 809 ± 30 °C (1σ , $n = 37$) and 810 ± 27 °C (1σ , $n = 28$) for the Clifford tonalite and plagioclase-phyric porphyry, respectively. Compared to the Flavrian trondhjemite samples, the St-Jude trondhjemite yielded the lowest $T_{\text{Ti-Zr}}$ of 692 ± 33 °C (1σ , $n = 22$; Fig. 5.15B).

Amphibole

The amphibole composition data for the Flavrian trondhjemite, and Clifford tonalite and plagioclase-phyric porphyry, as well as those reported for Côté Gold quartz diorite in a previous study (Katz *et al.*, 2017), are compiled in Table A5.5. We filtered out amphibole data with $\text{TiO}_2 < 0.95$ wt. % that may reflect crystallization under sub-solidus conditions (Houston and Dilles, 2013). Three analyses of amphibole from the Côté Gold quartz diorite are classified as magnesio-hornblende and yielded an average crystallization temperature and $f\text{O}_2$ of 762 ± 4 °C (1σ , $n = 3$) and $\Delta\text{FMQ} +1.6 \pm 0.3$ (1σ , $n = 3$), respectively (Fig. 5.16). Ten analyses of amphiboles from the Flavrian trondhjemite are classified as ferro-edenite, and the $f\text{O}_2$ -T estimations are therefore not applicable.

The forty-four amphibole analyses for the Clifford tonalite and plagioclase-phyric porphyry are classified as magnesio-hornblende. Sixteen amphibole analyses from the tonalite (after excluding six analyses with $\text{TiO}_2 < 0.95$ wt. %) yielded average values for crystallization temperature, pressure, and $f\text{O}_2$ of 806 ± 18 °C (1σ , $n = 16$), 172 ± 22 MPa (1σ , $n = 16$), and $\Delta\text{FMQ} +2.9 \pm 0.2$ (1σ , $n = 16$), respectively (Fig. 5.16). All of the twenty-two analyses for Amp-I and Amp-II phenocrysts in the Clifford plagioclase-phyric porphyry yielded tight clustering of compositional

data that are indistinguishable and are treated as a single population. The average values for crystallization temperature, pressure, and fO_2 are 850 ± 14 °C (1σ , $n = 22$), 259 ± 7 MPa (1σ , $n = 22$), and $\Delta FMQ +2.6 \pm 0.1$ (1σ , $n = 22$), respectively. In comparison, the broadly elevated crystallization temperatures and pressures for the amphibole phenocrysts compared to those in the tonalite suggest an earlier crystallization history for the amphibole phenocrysts (Fig. 5.16).

Sulfur-in-apatite μ -XANES spectra

The S contents of apatite grains from the Côté Gold diorite were too low to yield detectable μ -XANES at S K -edge spectra. Thus, data are only presented for samples from the St-Jude trondhjemite in the Flavrian intrusion and Clifford tonalite and plagioclase-phyric porphyry.

The μ -XANES spectra for two zircon-hosted apatite inclusions from the St-Jude trondhjemite yielded relatively broad and discernible S^{6+} peaks that reflect relatively noisy spectra due to their low S contents (i.e., below the detection limit). The μ -XANES spectra yielded an integrated $S^{6+}/\Sigma S$ peak area ratio of 0.98 ± 0.02 (1σ , $n = 2$; Fig. 5.17), suggesting that the minor amount of S incorporated into the apatite structure is dominated by S^{6+} . The dominance of S^{6+} in the apatite is interpreted to indicate a relatively oxidized redox state of S at the time of apatite crystallization.

The μ -XANES spectra for two analyses of zircon-hosted apatite inclusions from the Clifford tonalite (sample CS-20) yielded an integrated $S^{6+}/\Sigma S$ peak area ratio of 0.97 ± 0.03 (1σ , $n = 2$; Fig. 5.17). Another apatite inclusion in a zircon grain (cut by a fracture) from the sample CS-20 has an internal texture seen in its CL image that was previously interpreted (see above) to reflect the effect of metamorphism (Fig. 5.7I), and yielded a slightly lower $S^{6+}/\Sigma S$ peak area ratio of 0.92 ($n = 1$, Fig. 5.17). For the plagioclase-phyric porphyry (sample CS-22) from the Clifford,

four analyses of primary apatite hosted in the Amp-I phenocryst (Fig. 5.7C) yielded an integrated $S^{6+}/\Sigma S$ peak area ratio of 0.86 ± 0.07 (1σ , $n = 4$; Fig. 5.17). In contrast, three analyses of altered apatite in the Amp-II phenocryst of the same sample yielded a lower integrated $S^{6+}/\Sigma S$ peak area ratio of 0.72 ± 0.09 (1σ , $n = 3$; Fig. 5.17).

The μ -XANES spectra for zircon-hosted apatite inclusions from sample CS-22 acquired at the Swiss Light Source suggest the presence of S^{1+} peak (cf. Sadove et al., 2019), whereas μ -XANES spectra for apatite inclusions from the same sample acquired at the APS did not reveal the presence of S^{1+} (Fig. 5.17). We interpret the S^{1+} peak in the data from the SLS either as an artifact or reflecting different detection capabilities for the two beamlines. More work is required to address this issue. We highlight that the μ -XANES spectra from both beamlines reveal that S incorporated in the apatite is mainly S^{6+} , consistent with a relatively oxidized environment when the apatite crystallized. The primary and altered apatite grains yielded integrated $S^{6+}/\Sigma S$ peak area ratios of 0.83 ± 0.05 (1σ , $n = 3$) and 0.73 ($n = 1$) at SLS, and 0.96 ($n = 1$) and 0.72 ± 0.13 (1σ , $n = 2$) at APS, respectively (Fig. 5.17). These results suggest that the S^{1+} peak can narrow down the discrepancy of $S^{6+}/\Sigma S$ ratios between primary and altered grains, but the decrease in the integrated $S^{6+}/\Sigma S$ peak area ratios for the altered versus primary apatite crystals strongly indicates reduction of S by metamorphism and/or alteration. Instead, the altered apatite in the fractured zircon (Fig. 5.7I) from sample CS-20 only yielded a slightly lower $S^{6+}/\Sigma S$ ratio of 0.92 (Fig. 5.17) compared to 0.97 ± 0.03 for the texturally primary grains, which indicates limited modification of the S oxidation state owing to enclosure in the zircon.

Using the oxybarometer of Konecke et al. (2019), the $S^{6+}/\Sigma S$ peak area ratios of the zircon-hosted primary apatite inclusions from the St-Jude trondhjemite yield fO_2 values $\geq \Delta FMQ + 1.2$.

Relevant in this regard is that the sulfide-sulfate transition in fO_2 space for Fe-poor or Fe-free felsic melts (i.e., soda-lime, $K_2Si_4O_9$, haplo-trondhjemite liquid at 1000–850 °C and 200 MPa; Klimm *et al.*, 2012) is reported to be 1.5 log units lower than that for the Fe-rich basaltic and andesitic melts (Jugo *et al.*, 2010; Botcharnikov *et al.*, 2011). If we consider that sample SJ-08 has a Fe-poor trondhjemitic composition with a *model* AST of 859 °C and an estimated emplacement pressure of ~90–150 MPa (Feng & Kerrich, 1990) that are comparable to those for the melts in Klimm *et al.* (2012), and assuming the effect of the composition of the silicate glasses is proportional to the effect of sulfur incorporation into apatite, the corrected fO_2 values from the $S^{6+}/\Sigma S$ peak area ratios are approximated to be $\geq \Delta FMQ -0.3$.

For the Clifford stock samples, the integrated $S^{6+}/\Sigma S$ peak area ratios for the primary apatite crystals from the samples CS-20 and CS-22 (andesitic compositions) yielded fO_2 values of $\geq \Delta FMQ +1.2$ and $\Delta FMQ +0.83 \pm 0.10$ (1σ), respectively. One analysis without the S^{1+} peak for sample CS-22 yielded fO_2 value of $\Delta FMQ +1.48$, similar to that for sample CS-20. Please note that the sulfide-sulfate transition in fO_2 space is not sensitive to changing melt composition from basalt to andesite (Jugo *et al.*, 2010), but has a narrower transition from $\sim \Delta FMQ +1.5$ to $\sim \Delta FMQ +2.0$ for dacitic melt (Kleinsasser *et al.*, 2022), and is suggested to shift towards more oxidizing or reducing conditions with decreasing temperature or pressure ($\Delta FMQ +0.5$ and $+0.2$ log units per 100 °C and 300 MPa), respectively (Matjuschkin *et al.*, 2016, Nash *et al.*, 2019). Sample CS-20 yielded a *model* AST of 866 °C and emplacement pressure of 172 ± 22 MPa (1σ), hence the P-T-corrected fO_2 value is estimated to be above $\Delta FMQ +1.78 \pm 0.02$ (1σ ; Fig. 5.18). For sample CS-22, which yielded a *model* AST of 893 °C (consistent with the calculated 850 ± 14 °C for the host amphibole phenocryst) and pressure condition of 259 ± 7 MPa (1σ), the P-T-

corrected fO_2 value is estimated at $\Delta FMQ +1.34 \pm 0.10$ (1σ ; Fig. 5.18). We interpret these results to constrain the pre-degassed redox state of the Clifford tonalitic magma to $\sim \Delta FMQ +1.4$ – 1.8 .

Magnetite-ilmenite mineral pairs

Primary magnetite-ilmenite mineral pairs are not present in the studied samples from Côté Gold, Flavrian, and St-Jude. However, sixteen analyses on two representative primary magnetite-ilmenite pairs (Fig. 5.8C–F) hosted in a tonalite from the Clifford intrusion yielded equilibrium temperatures of 619–648°C and fO_2 values of $\Delta FMQ +2.3$ – 4.2 (3.3 ± 1.3 on average; 1σ , $n = 2$; Fig. 5.18). The result is interpreted to record the redox state during the latter stage of magma crystallization.

5.9 Discussion

5.9.1 Geochronology and igneous petrogenesis

The new and previously published geochronological results constrain the emplacement ages of the Côté Gold, Flavrian-St-Jude, and Clifford igneous rocks to ~ 2.74 to 2.69 Ga (Figs. 5.3, 5.11). Formation of the Côté Gold and St-Jude deposits coincides with a period of plume-arc interaction or intermittent melting of the base of the thickened basaltic crust during ~ 2.75 – 2.70 Ga (Benn & Moyen, 2008, Bédard *et al.*, 2013), whereas the Croxall deposit formed during a mountain-building stage in the Neoproterozoic southern AGB when subduction or equivalent processes are interpreted to have been in operation (Feng & Kerrich, 1992, Daigneault *et al.*, 2002, Wyman *et al.*, 2002). The rocks associated with the three studied deposits differ in litho-geochemical features which suggest variable petrogenesis (Galley, 2003, Piercey *et al.*, 2008, Katz *et al.*, 2017).

The Côte Gold diorite/quartz diorite samples are enriched in Cs, Rb, Ba, and light REE contents with concave to listric REE patterns, and have slight negative Eu anomalies and low to moderate Sr/Y ratios (up to 20; Figs. 5.9, 5.10A) that are consistent with a shallow magmatic source. Zircons from the diorite and tonalite yielded comparable positive $\varepsilon_{\text{Hf}}(t)$ and mantle-like $\delta^{18}\text{O}$ values (Fig. 5.12), which are consistent with the interpretation of Katz *et al.* (2017) that the magmas are derived from a differentiated lithospheric mantle or lower-crust mafic source. In addition, our results indicate the sources for these magmas have not been contaminated by a crustal component that was previously altered by low-temperature or high-temperature hydrothermal seawater or meteoric fluids.

In the Flavrian-St-Jude area, the trondhjemitic samples yielded relatively flat mantle-normalized trace-element patterns except for significant depletion of Sr, P, and Ti relative to the tholeiitic diorite (Fig. 5.9C). The depletion of Sr, P, and Ti indicates fractionation of plagioclase, apatite, and Fe-Ti oxides during magma evolution. These features combined with the significant Eu anomalies (Fig. 5.9D) indicate the magmas were sourced from a low-pressure basaltic source reservoir where plagioclase was stable. The geochemistry of the suite, together with their juvenile zircon $\varepsilon_{\text{Hf}}(t)$ signature, support previous arguments that the diorite-trondhjemite magma originated from a primitive mantle source (Galley, 2003).

The low zircon $\delta^{18}\text{O}$ values for the Flavrian-St-Jude trondhjemite samples relative to mantle values (Fig. 5.12) suggests the magma chamber may have extensively interacted with a low- ^{18}O reservoir, such as seawater or meteoric fluids at high temperatures (Valley, 2003), which is consistent with a cauldron subsidence or inferred rifted setting in the area (Hannington *et al.*, 2003). Furthermore, the fact that addition of aqueous fluids can lower the solidus temperature of magmas plausibly explains the apparently lower $T_{\text{Ti-Zr}}$ values for these samples (Fig. 5.15B). The

broadly reduced zircon $\delta^{18}\text{O}$ values and $T_{\text{Ti-Zr}}$ for the Flavrian trondhjemite relative to St-Jude trondhjemite (Figs. 5.12, 5.15B) plausibly reflects enhanced interaction of high-temperature seawater or meteoric fluids with the magma chamber during formation of the St-Jude deposit.

Whole-rock trace element compositions of the Clifford tonalite and plagioclase-phyric porphyry are consistent with typical subduction zone magmas (Kelemen *et al.*, 2007, Mohan *et al.*, 2008, Piercey *et al.*, 2008). The presence of amphibole phenocrysts (Fig. 5.6H), weakly negative to slightly positive Eu anomalies (Fig. 5.9F), and high Sr/Y ratios (Fig. 5.10A) together support suppression of plagioclase fractionation in a relatively hydrous magma. Petrologic modeling indicates garnet residue in the source region for the Clifford intrusive rocks (Piercey *et al.*, 2008). However, garnet incorporates heavy REEs over light REEs and its fractionation can thus decrease the residual melts of Dy/Yb ratios (Macpherson *et al.*, 2006) which is not consistent with the increasing trend of Dy/Yb ratios with SiO_2 (Fig. 5.10B). Amphibole incorporates the middle REEs relative to heavy REEs, the broadly decreasing Dy/Yb ratios versus SiO_2 instead support amphibole fractionation during magma evolution (Macpherson *et al.*, 2006). We therefore interpret the new and published results to suggest amphibole-dominated fractionation with a minor amount of garnet residue in the source region. The slightly lower but homogenous zircon $\delta^{18}\text{O}$ values for the tonalite relative to the mantle values (Fig. 5.12) support a minor degree of high-temperature hydrothermal alteration of the source region (e.g., subducted basaltic oceanic crust or basaltic lower crust) or the magma chamber.

5.9.2 Oxidation state of the magmas

Measuring oxidation state of the ore-related magmas for the Côté Gold, Flavrian-St-Jude, Croxall deposits has to date been hindered by modification of primary minerals by extensive

alteration, deformation, and metamorphism. To address this issue, we restricted our analyses to primary minerals that preserved igneous features or to mineral inclusions protected by the primary zircon, amphibole, and plagioclase.

Zircons from the Côté Gold pre-mineralization tonalite and syn-mineralization diorite yielded fO_2 results of $\Delta FMQ -0.7 \pm 0.4$ and $\Delta FMQ +0.8 \pm 0.4$, respectively. Estimates from the published amphibole composition for quartz diorite (Katz *et al.*, 2017) yielded an fO_2 value of $\Delta FMQ +1.6 \pm 0.3$. If we consider that amphibole may overestimate magmatic fO_2 by about one log unit for plutonic rocks (Wang *et al.*, 2014), the result from amphibole is therefore consistent with the fO_2 estimated from zircon geochemistry, which together indicate an oxidation state of the ore-related Côté Gold diorite/quartz diorite of $\sim \Delta FMQ +0.6-0.7$.

The presence of ilmenite in zircon from the St-Jude trondhjemite indicates a relatively reduced redox state of the magma (Bell *et al.*, 2018). The Ce-Ti-U-in-zircon and S-in-apatite oxybarometers are applicable for the Flavrian-St-Jude trondhjemite rocks and yielded internally consistent results. Zircons from the four trondhjemite samples (FLV-22, FLV-28, FLV-04, and SJ-04) yielded fO_2 values of $\Delta FMQ +0.07 \pm 0.6$, 0.4 ± 1.0 , -0.0 ± 0.6 , and -0.3 ± 0.6 , respectively. The S-poor apatite grains crystallized in the Fe-poor trondhjemitic melt yielded fO_2 values of $> \Delta FMQ -0.3$ at the time of apatite crystallization. These results overlap within uncertainty and are interpreted to constrain the primary fO_2 of the trondhjemite samples to around $\Delta FMQ +0$.

Multiple oxybarometers have been employed for the Croxall tonalitic magmas because primary barometric minerals in the tonalite and plagioclase-phyric porphyry are demonstrated to have locally survived the low-grade prehnite-pumpellyite metamorphism. Zircon grains from the

tonalite yielded $\Delta\text{FMQ} +1.2 \pm 0.4$, consistent with the $f\text{O}_2$ result of $\Delta\text{FMQ} +1.4\text{--}1.8$ from the S-in-apatite oxybarometer for the primary apatite grains hosted in zircon and amphibole.

Amphibole grains from the Clifford stock record oxidation states ranging from $\Delta\text{FMQ} +2.5 \pm 0.1$ (for amphibole phenocrysts in plagioclase-phyric porphyry) to $\Delta\text{FMQ} +2.9 \pm 0.2$ (for amphibole in tonalite). We interpret the $f\text{O}_2$ result of $\Delta\text{FMQ} +2.5 \pm 0.1$ to reflect oxidation state of the less evolved Clifford magma chamber, which again exceeds the result from other oxybarometers by about one log unit, consistent with Wang *et al.* (2014). These results collectively indicate that the Croxall magmas were moderately oxidized at $\sim\Delta\text{FMQ} +1.5$, which is similar to many Phanerozoic arc-related magmas (Richards, 2015). Magnetite-ilmenite pairs hosted in plagioclase from the tonalite yielded significantly higher $f\text{O}_2$ value of $+3.3 \pm 1.3$ at an equilibrium temperature of 634 ± 21 °C, reflecting increased $f\text{O}_2$ values during the late stage of magma crystallization (Lee *et al.*, 2005) or subsolidus re-equilibration.

These results reveal that the Croxall tonalitic magmas are more oxidized than those for the Côte Gold diorite and Flavrian-St-Jude trondhjemite, which together span a broad spectrum of $\Delta\text{FMQ} +0$ to $\Delta\text{FMQ} +1.5$ (Fig. 5.18) that equates to $f\text{O}_2$ values for MORB and Phanerozoic arc magmas (Kadoya *et al.*, 2020). The $f\text{O}_2$ values reported here are consistent with lower apatite S contents of Côte Gold diorite and Flavrian-St-Jude trondhjemite than the relatively oxidized Clifford tonalitic magmas. These results together lead us to conclude that there were variable $f\text{O}_2$ controls on TTG-related porphyry-type Cu \pm Au deposit formation in the Archean.

5.9.3 Metallogenic implications

Phanerozoic porphyry Cu \pm Au deposits commonly form from magmatic-hydrothermal fluid(s) evolved from oxidized, sulfur-rich, hydrous, causative arc-related magmas that are interpreted

to reflect metasomatism of the mantle wedge by slab-derived fluids (Kelley & Cottrell, 2009, Richards, 2011). Magmatic redox state is a primary control on the solubilities of Cu and Au in silicate melts (Holzheid & Lodders, 2001, Botcharnikov *et al.*, 2011, Zajacz *et al.*, 2012) and thus it is generally thought that under relatively reduced conditions ($<\Delta\text{FMQ} + 1$), voluminous sulfide saturation will deplete the silicate melt of Cu and Au during magma ascent (Richards & Şengör, 2017) or in residual sulfides in the mantle or deep crustal cumulates (Richards, 2011, 2015, Audétat & Simon, 2012, Lee *et al.*, 2012, Chiaradia, 2013). If it is the case, then the derivative magmas would have limited fertility to form porphyry Cu \pm Au deposits commensurate with fluid exsolution. Such conditions are hypothesized to have limited the ore-forming potential of sodic granitoids in the Archean as a consequence of recycling of the sulfate-poor seawater and reduced submarine basalts via slab descent into mantle (Jagoutz, 2013, Stolper & Keller, 2018, Stolper & Bucholz, 2019). However, the $f\text{O}_2$ constraints reported here for the causative magmas for the three porphyry-type Cu \pm Au deposits are contrary to that hypothesis in two ways: (1) porphyry-type Cu \pm Au deposits can form from magmas with $f\text{O}_2$ values covering a broad range from $\Delta\text{FMQ} + 0$ to $\Delta\text{FMQ} + 1.5$; and (2) relatively oxidized sulfurous sodic melts did form, at least locally, in the Neoproterozoic.

Case 1 (Relatively reduced and sulfur-poor magmatic conditions): The St-Jude deposit formed from a relatively reduced ($\sim\Delta\text{FMQ} + 0$) trondhjemitic melt derived from a basaltic source at ~ 2.70 Ga. However, such reduced and sulfur-poor characteristics likely reduced the ore-forming potential of the Cu-poor trondhjemitic magmas (Cu content of 11 ± 9 ppm; $n = 14$). As such, an external process is considered to have contributed to its metal fertility. Because this trondhjemite originated from a magma chamber that underwent significant modification due to interaction with hydrothermal fluids (i.e., see interpretation based on zircon O isotope data; Fig. 5.12), the

most plausible control for the mineralization may be the addition of Cu, and possibly other metals, via ingress of heated seawater to the magma chamber that previously circulated through mafic volcanic rocks in the Rouyn-Noranda VMS deposit camp. Such a scenario has also been suggested to explain the presence of modern submarine magmatic-hydrothermal Cu \pm Au deposits in VMS-type camp (Keith *et al.*, 2018).

Case 2 (Mildly oxidized condition): The Côté Gold Cu \pm Au deposit formed from dioritic/quartz dioritic magmas with an fO_2 value of $\sim\Delta FMQ +0.6-0.7$ that were derived from a mildly enriched mantle source at ~ 2.74 Ga. Enrichment of Au in the system is consistent with experimental results showing an apex of Au solubility in silicate melt over a narrow range of redox conditions ($\Delta FMQ < 1$) characterized by the sulfide-sulfate transition and indicating Au can be complexed with bisulfide in silicate melts (Botcharnikov *et al.*, 2011, Jégo & Pichavant, 2012, Zajacz *et al.*, 2012). In addition, the moderate Cu content of 39 ± 21 ppm ($n = 22$) for the least altered diorite/quartz diorite samples is consistent with a minor degree of Cu depletion in the magmas. We interpret these results to indicate that Cu can be transported in the mildly oxidized melts, or voluminous sulfide saturation may have been delayed in the less evolved melts.

Case 3 (Moderately oxidized condition): The Croxall Cu \pm Au deposit formed from moderately oxidized ($\sim\Delta FMQ +1.5$), arc-type tonalitic magmas at ~ 2.69 Ga. The oxidized features of the tonalitic rocks are comparable to those of Phanerozoic island arc magmas (Wallace, 2005, Kelley & Cottrell, 2009, Brounce *et al.*, 2014, Richards, 2015), which supports models that favor subduction processes operating at least locally in the Neoproterozoic due to Earth cooling (Laurent *et al.*, 2014). The results lead us to suggest that the Croxall deposit formed from similar metallogenic processes that typify Phanerozoic porphyry Cu \pm Au deposits. In the

oxidized source magma, voluminous sulfide saturation may have been prevented, which is consistent with the relatively high Cu content of 48 ppm for the least altered tonalite sample.

We note, however, that the presence of oxidized, sulfurous tonalitic magmas in the Clifford stock appears to contradict the hypothesis or experimental results that suggest sodic magmas in the Archean are either reduced or sulfur-poor (Prouteau & Scaillet, 2012, Jagoutz *et al.*, 2013). Formation of oxidized, sulfurous tonalite magmas at Clifford can plausibly be explained however by two recently proposed models: (1) recycling of local sulfate-rich seawater into the mantle (Ohmoto, 2020); or (2) the sufficiently effective oxidizing agent of aqueous fluid to the sub-arc mantle (Lacovino *et al.*, 2020). However, our results themselves are not sufficient to resolve this issue.

Nevertheless, these cases taken together reflect variable fO_2 controls and metallogenic processes for TTG-related porphyry-type Cu-Au deposits in the Archean. However, it is worthwhile to note that: (1) less evolved sodic plutonic rocks (e.g., diorite in the Côté Gold deposit) are minor in the upper crust of Archean cratons such as in the AGB (Matthieu *et al.*, 2020); (2) magmas with low zircon $\delta^{18}O$ values, such as the St-Jude trondhjemite, are sparse in the Archean, which has been interpreted to reflect a preservation bias (Valley *et al.*, 2005; Hammerli *et al.*, 2018); and (3) the formation and extent of oxidized and sulfurous sodic magmas remains poorly constrained. These factors together lead us to conclude that the rarity of TTG-related porphyry Cu \pm Au deposits may be attributed to either local restriction of the identified favorable metallogenic conditions, exploration bias, or a preservation bias towards destruction facilitated by vertical tectonics, which is a process favored in the Archean.

5.10 Conclusion

In contrast to the exclusive association of porphyry Cu \pm Au deposits with moderately oxidized, sulfur-rich calc-alkaline magmas in Phanerozoic arc-related settings, porphyry-type Cu \pm Au deposits in the Neoproterozoic can form from sodic magmas with fO_2 conditions ranging from $\Delta FMQ +0$ to $\Delta FMQ +1.5$ under variable tectonic settings. The Côté Gold and Croxall deposits formed from mildly to moderately oxidized magmas in which early sulfide saturation is interpreted to have been variably limited. The trondhjemitic magmas in Flavrian-St-Jude yielded fO_2 values of $\sim \Delta FMQ +0$ that would have favored early sulfide saturation that likely depleted the magmas of chalcophile metals (e.g., Cu) and hence reduced its fertility. However, that heated seawater leached metals (e.g., Cu and Au) from the regional metalliferous volcanic strata, and altered the Flavrian St-Jude magma, may have contributed to form the unique St-Jude porphyry-type Cu \pm Au deposit.

Constraining the magmatic redox state for old rocks (e.g., Precambrian) is challenging due to the almost ubiquitous pervasive deformation, metamorphism, and alteration as part of Earth's protracted tectonic history. Our detailed petrographic study demonstrates however that primary barometric minerals protected as inclusions in other mineral phases, such as zircon, plagioclase, and mineral phenocrysts, can in fact survive from prehnite-pumpellyite to greenschist facies metamorphism. As such, the scope of this study, as well as methods and derivative information presented, are valuable in the context of guiding future relevant research directed at magmatic processes, metallogensis, plate tectonics and the geochemical evolution of early Earth.

5.11 Acknowledgments

Field assistance provided by a visiting professor, Dr. H. D. Zhang, and Ph.D. student D. McKevitt at Laurentian University are appreciated. We acknowledge the help of D. Crabtree at Ontario GeoLabs, G. Poirier at the University of Ottawa, and M. Kelvin and T. Gore at XPS for EMPA analyses. We acknowledge the Paul Scherrer Institut, Villigen, Switzerland for provision of synchrotron radiation beamtime at beamline X07MB and the Advanced Photon Source, a U.S. Department of Energy (DOE) Office of Science User Facility operated for the DOE Office of Science by Argonne National Laboratory under Contract No. DE-AC02-06CH11357 for beamtime at Sector 13-ID-E. We thank Drs. Thomas Huthwelker and Camelia Borca of SLS and Drs. Antonio Lanzirotti and Matthew Newville of APS. We also thank Drs. R. Sherlock and H. Gibson for valued discussion.

5.12 Funding

The research was funded by Canada First Research Excellence Fund through a Metal Earth thematic project to J. P. Richards. X. Y. Meng was funded by a Chinese Scholarship Council award from China. This is contribution from the Mineral Exploration Research Centre, Harquail School of Earth Sciences.

5.13 References

- Anderson, J. L., Barth, A. P., Wooden, J. L., and Mazdab, F., 2008, Thermometers and Thermobarometers in Granitic Systems: Reviews in Mineralogy and Geochemistry, v. 69, p. 121–142.
- Anderson, J. L., and Thomas, W. M., 1985, Proterozoic anorogenic two-mica granites: Silver Plume and St. Vrain batholiths of Colorado: *Geology*, v. 13, p. 177–180.
- Audétat, A., and Simon, A., 2012, Magmatic controls on porphyry copper genesis: Society of

Economic Geologists Special Publication, v. 16, p. 553–572.

Ayer, J., Amelin, Y., Corfu, F., Kamo, S., Ketchum, J., Kwok, K., and Trowell, N., 2002, Evolution of the southern Abitibi greenstone belt based on U–Pb geochronology: autochthonous volcanic construction followed by plutonism, regional deformation and sedimentation: *Precambrian Research*, v. 115, p. 63–95.

Ayer, J. A., Thurston, P. C., Bateman, R., Dubé, B., Gibson, H. L., Hamilton, M. A., Hathway, B., Hocker, S. M., Houlié, M. G., Hudak, G., Ispolatov, V. O., Lafrance, B., Leshner, C. M., MacDonald, P. J., Péloquin, A. S., Piercey, S. J., Reed, L. E., and Thompson, P. H., 2005, Overview of results from the greenstone architecture project: discover Abitibi initiative, Ontario Geological Survey.

Barker, F., and Arth, J. G., 1976, Generation of trondhjemitic-tonalitic liquids and Archean bimodal trondhjemite-basalt suites: *Geology*, v. 4, p. 596–600.

Bateman, D., Ayer, J. A., Dubé, B., and Hamilton, M. A., 2005, The Timmins-Porcupine Gold Camp, Northern Ontario: The Anatomy of an Archean Greenstone Belt and Its Gold Mineralization, Discover Abitibi Initiative, Open File Report 6158, Ontario Geological Survey, p. 1–90.

Beakhouse, G. P., 2011, The Abitibi Subprovince plutonic record: Tectonic and metallogenic implications: Ontario Geological Survey, Open File, v. 6268, p. 1–161.

Bédard, J. H., 2018, Stagnant lids and mantle overturns: Implications for Archean tectonics, magmagenesis, crustal growth, mantle evolution, and the start of plate tectonics: *Geoscience Frontiers*, v. 9, p. 19–49.

Bédard, J. H., Harris, L. B., and Thurston, P. C., 2013, The hunting of the snArc: *Precambrian Research*, v. 229, p. 20–48.

Bell, E. A., 2016, Preservation of primary mineral inclusions and secondary mineralization in igneous zircon: a case study in orthogneiss from the Blue Ridge, Virginia: *Contributions to Mineralogy and Petrology*, v. 171, p. 26.

Bell, E. A., Boehnke, P., and Harrison, T. M., 2016, Recovering the primary geochemistry of Jack Hills zircons through quantitative estimates of chemical alteration: *Geochimica et Cosmochimica Acta*, v. 191, p. 187–202.

Bell, E. A., Boehnke, P., Harrison, T. M., and Wielicki, M. M., 2018, Mineral inclusion assemblage and detrital zircon provenance: *Chemical Geology*, v. 477, p. 151–160.

Benn, K., and Moyen, J. F., 2008, The Late Archean Abitibi-Opatca terrane, Superior Province: A modified oceanic plateau: When Did Plate Tectonics Begin on Planet Earth?, v. 440, p. 173–197.

Black, L. P., Kamo, S. L., Allen, C. M., Davis, D. W., Aleinikoff, J. N., Valley, J. W., Mundil, R., Campbell, I. H., Korsch, R. J., and Williams, I. S., 2004, Improved $^{206}\text{Pb}/^{238}\text{U}$ microprobe

geochronology by the monitoring of a trace-element-related matrix effect; SHRIMP, ID-TIMS, ELA-ICP-MS and oxygen isotope documentation for a series of zircon standards: *Chemical Geology*, v. 205, p. 115–140.

Bleeker, W., 2015, Synorogenic gold mineralization in granite-greenstone terranes: the deep connection between extension, major faults, synorogenic clastic basins, magmatism, thrust inversion, and long-term preservation: *Targeted Geoscience Initiative*, v. 4, p. 25–47.

Bindeman, I. N., and Simakin, A. G., 2014, Rhyolites—Hard to produce, but easy to recycle and sequester: Integrating microgeochemical observations and numerical models: *Geosphere*, v. 10, p. 930–957.

Bigot, L., and Jébrak, M., 2015, Gold Mineralization at the Syenite-Hosted Beattie Gold Deposit, Duparquet, Neoproterozoic Abitibi Belt, Canada: *Economic Geology*, v. 110, p. 315–335.

Botcharnikov, R. E., Linnen, R. L., Wilke, M., Holtz, F., Jugo, P. J., and Berndt, J., 2011, High gold concentrations in sulphide-bearing magma under oxidizing conditions: *Nature Geoscience*, v. 4, p. 112–115.

Bouvier, A., Vervoort, J. D., and Patchett, P. J., 2008, The Lu–Hf and Sm–Nd isotopic composition of CHUR: Constraints from unequilibrated chondrites and implications for the bulk composition of terrestrial planets: *Earth and Planetary Science Letters*, v. 273, p. 48–57.

Brounce, M. N., Kelley, K. A., and Cottrell, E., 2014, Variations in $\text{Fe}^{3+}/\Sigma\text{Fe}$ of Mariana Arc Basalts and Mantle Wedge $f\text{O}_2$: *Journal of Petrology*, v. 55, p. 2513–2536.

Buddington, A. F., and Lindsley, D. H., 1964, Iron-titanium oxide minerals and synthetic equivalents: *Journal of petrology*, v. 5, p. 310–357.

Calvert, A. J., and Ludden, J. N., 1999, Archean continental assembly in the southeastern Superior Province of Canada: *Tectonics*, v. 18, p. 412–429.

Candela, P. A., and Holland, H. D., 1984, The partitioning of copper and molybdenum between silicate melts and aqueous fluids: *Geochimica et Cosmochimica Acta*, v. 48, p. 373–380.

Cathles, L. M., 1993, Oxygen isotope alteration in the Noranda mining district, Abitibi greenstone belt, Quebec: *Economic Geology*, v. 88, p. 1483–1511.

Cawood, P. A., 2020, Earth Matters: A tempo to our planet's evolution: *Geology*, v. 48, p. 525–526.

Claiborne, L. L., Miller, C. F., Walker, B. A., Wooden, J. L., Mazdab, F. K., and Bea, F., 2006, Tracking magmatic processes through Zr/Hf ratios in rocks and Hf and Ti zoning in zircons: An example from the Spirit Mountain batholith, Nevada: *Mineralogical Magazine*, v. 70, p. 517–543.

Chaloux, E. C., 2005, The Croxall Breccia Pipe: Geological and Geochemical Study of an Archean Porphyry Cu-Mo-Au System. *Applied M. Sc. thesis, Laurentian University ON*, 1–71.

- Chiaradia, M., 2013, Copper enrichment in arc magmas controlled by overriding plate thickness: *Nature Geoscience*, p. 43–46.
- Corfu, F., Hanchar, J. M., Hoskin, P. W., and Kinny, P., 2003, Atlas of zircon textures: *Reviews in mineralogy and geochemistry*, v. 53, p. 469–500.
- Crowe, S. A., Paris, G., Katsev, S., Jones, C., Kim, S.-T., Zerkle, A. L., Nomosatryo, S., Fowle, D. A., Adkins, J. F., and Sessions, A. L., 2014, Sulfate was a trace constituent of Archean seawater: *Science*, v. 346, p. 735–739.
- Daigneault, R., Mueller, W. U., and Chown, E. H., 2002, Oblique Archean subduction: accretion and exhumation of an oceanic arc during dextral transpression, Southern Volcanic Zone, Abitibi Subprovince Canada: *Precambrian Research*, v. 115, p. 261–290.
- D'Angelo, M., Miguel, A., Hollings, P., Byrne, K., Piercey, S., and Creaser, R. A., 2017, Petrogenesis and magmatic evolution of the Guichon Creek batholith: Highland Valley porphyry Cu±(Mo) district, south-central British Columbia: *Economic Geology*, v. 112, p. 1857–1888.
- Davidson, J., Turner, S., Handley, H., Macpherson, C., and Dosseto, A., 2007, Amphibole “sponge” in arc crust?: *Geology*, v. 35, p. 787–790.
- Defant, M. J., and Drummond, M. S., 1990, Derivation of some modern arc magmas by melting of young subducted lithosphere: *Nature*, v. 347, p. 662–665.
- Dhuime, B., Hawkesworth, C., and Cawood, P. A., 2011, When Continents Formed: *Science*, v. 331, p. 154–155.
- Evans, K. A., and Tomkins, A. G., 2011, The relationship between subduction zone redox budget and arc magma fertility: *Earth and Planetary Science Letters*, v. 308, p. 401–409.
- Feng, R., and Kerrich, R., 1990, Geobarometry, differential block movements, and crustal structure of the southwestern Abitibi greenstone belt, Canada: *Geology*, v. 18, p. 870–873.
- Feng, R., and Kerrich, R., 1992, Geodynamic evolution of the southern Abitibi and Pontiac terranes: evidence from geochemistry of granitoid magma series (2700–2630Ma): *Canadian Journal of Earth Sciences*, v. 29, p. 2266–2286.
- Ferry, J. M., and Watson, E. B., 2007, New thermodynamic models and revised calibrations for the Ti-in-zircon and Zr-in-rutile thermometers: *Contributions to Mineralogy and Petrology*, v. 154, p. 429–437.
- Fisher, C. M., Vervoort, J. D., and DuFrane, S. A., 2014, Accurate Hf isotope determinations of complex zircons using the “laser ablation split stream” method: *Geochemistry, Geophysics, Geosystems*, v. 15, p. 121–139.
- Frieman, B. M., Kuiper, Y. D., Kelly, N. M., Monecke, T., and Kylander-Clark, A., 2017, Constraints on the geodynamic evolution of the southern Superior Province: U-Pb LA-ICP-MS analysis of detrital zircon in successor basins of the Archean Abitibi and Pontiac subprovinces of

Ontario and Quebec, Canada: *Precambrian Research*, v. 292, p. 398–416.

Galley, A. G., 2003, Composite synvolcanic intrusions associated with Precambrian VMS-related hydrothermal systems: *Mineralium Deposita*, v. 38, p. 443–473.

Galley, A. G., and Van Breemen, O., 2002, Timing of Synvolcanic Magmatism in Relation to Base-metal Mineralization, Rouyn-Noranda, Abitibi, Volcanic Belt, Quebec, Natural Resources Canada, Geological Survey of Canada.

Ghiorso, M. S., and Evans, B. W., 2008, Thermodynamics of rhombohedral oxide solid solutions and a revision of the Fe-Ti two-oxide geothermometer and oxygen-barometer: *American Journal of Science*, v. 308, p. 957–1039.

Ghiorso, M. S., and Sack, O., 1991, Fe-Ti oxide geothermometry: thermodynamic formulation and the estimation of intensive variables in silicic magmas: *Contributions to Mineralogy and Petrology*, v. 108, p. 485–510.

Goldie, R., Kotila, B., and Seward, D., 1979, The Don Rouyn Mine: an Archean porphyry copper deposit near Noranda, Quebec: *Economic Geology*, v. 74, p. 1680–1684.

Grondahl, C., and Zajacz, Z., 2017, Magmatic controls on the genesis of porphyry Cu–Mo–Au deposits: The Bingham Canyon example: *Earth and Planetary Science Letters*, v. 480, p. 53–65.

Groves, D. I., Condie, K. C., Goldfarb, R. J., Hronsky, J. M. A., and Vielreicher, R. M., 2005, 100th Anniversary Special Paper: Secular changes in global tectonic processes and their influence on the temporal distribution of gold-bearing mineral deposits: *Economic Geology*, v. 100, p. 203–224.

Habicht, K. S., Gade, M., Thamdrup, B., Berg, P., and Canfield, D. E., 2002, Calibration of Sulfate Levels in the Archean Ocean: *Science*, v. 298, p. 2372–2374.

Hammerli, J., Kemp, A. I., and Jeon, H., 2018, An Archean Yellowstone? Evidence from extremely low $\delta^{18}\text{O}$ in zircons preserved in granulites of the Yilgarn Craton, Western Australia: *Geology*, v. 46, p. 411–414.

Hannington, M. D., Santaguida, F., Kjarsgaard, I. M., and Cathles, L. M., 2003, Regional-scale hydrothermal alteration in the Central Blake River Group, western Abitibi subprovince, Canada: implications for VMS prospectivity: *Mineralium Deposita*, v. 38, p. 393–422.

Hart, C. J. R., 2007, Reduced intrusion-related gold systems: *Mineral Deposits of Canada: A synthesis of Major deposit types, district metallogeny, the Evolution of geological provinces, and exploration methods*: Geological Association of Canada, Mineral Deposits Division, Special Publication, v. 5, p. 95–112.

Hastie, A. R., Fitton, J. G., Bromiley, G. D., Butler, I. B., and Odling, N. W. A., 2016, The origin of Earth's first continents and the onset of plate tectonics: *Geology*, v. 44, p. 855–858.

Holland, H. D., 2002, Volcanic gases, black smokers, and the Great Oxidation Event:

Geochimica et Cosmochimica Acta, v. 66, p. 3811–3826.

Holzheid, A., and Lodders, K., 2001, Solubility of copper in silicate melts as function of oxygen and sulfur fugacities, temperature, and silicate composition: *Geochimica et Cosmochimica Acta*, v. 65, p. 1933–1951.

Hou, Z. Q., Pan, X. F., Li, Q. Y., Yang, Z. M., and Song, Y. C., 2013, The giant Dexing porphyry Cu–Mo–Au deposit in east China: product of melting of juvenile lower crust in an intracontinental setting: *Mineralium Deposita*, v. 48, p. 1019–1045.

Hoskin, P. W. O., and Schaltegger, U., 2003, The composition of zircon and igneous and metamorphic petrogenesis. In: Hanchar, J. M. & Hoskin, P. W. O. (eds) *Zircon: Reviews in Mineralogy and Geochemistry*, p. 27–62.

Imai, A., 2004, Variation of Cl and SO₃ contents of microphenocrystic apatite in intermediate to silicic igneous rocks of Cenozoic Japanese island arcs: Implications for porphyry Cu metallogenesis in the Western Pacific Island arcs: *Resource Geology*, v. 54, p. 357–372.

Jagoutz, O., 2013, Were ancient granitoid compositions influenced by contemporaneous atmospheric and hydrosphere oxidation states?: *Terra Nova*, v. 25, p. 95–101.

Jagoutz, O., Schmidt, M. W., Enggist, A., Burg, J. P., Hamid, D., and Hussain, S., 2013, TTG-type plutonic rocks formed in a modern arc batholith by hydrous fractionation in the lower arc crust: *Contributions to Mineralogy and Petrology*, v. 166, p. 1099–1118.

Jamieson, J. W., Wing, B. A., Farquhar, J., and Hannington, M. D., 2013, Neoproterozoic seawater sulphate concentrations from sulphur isotopes in massive sulphide ore: *Nature Geoscience*, v. 6, p. 61–64.

Johnson, T. E., Brown, M., Gardiner, N. J., Kirkland, C. L., and Smithies, R. H., 2017, Earth's first stable continents did not form by subduction: *Nature*, v. 543, p. 239–242.

Johnson, T. E., Kirkland, C. L., Gardiner, N. J., Brown, M., Smithies, R. H., and Santosh, M., 2019, Secular change in TTG compositions: Implications for the evolution of Archaean geodynamics: *Earth and Planetary Science Letters*, v. 505, p. 65–75.

Jugo, P. J., Wilke, M., and Botcharnikov, R. E., 2010, Sulfur K-edge XANES analysis of natural and synthetic basaltic glasses: Implications for S speciation and S content as function of oxygen fugacity: *Geochimica et Cosmochimica Acta*, v. 74, p. 5926–5938.

Kadoya, S., Catling, D. C., Nicklas, R. W., Puchtel, I. S., and Anbar, A. D., 2020, Mantle data imply a decline of oxidizable volcanic gases could have triggered the Great Oxidation: *Nature Communications*, v. 11, p. 2774.

Katz, L. R., 2016, Geology of the Archean Côté Gold Au (-Cu) intrusion-related deposit, Swayze greenstone belt, Ontario, Laurentian University of Sudbury, 1–328 p.

Katz, L. R., Kontak, D. J., Dubé, B., and McNicoll, V., 2017, The geology, petrology, and

geochronology of the Archean Côté Gold large-tonnage, low-grade intrusion-related Au(-Cu) deposit, Swayze greenstone belt, Ontario, Canada: *Canadian Journal of Earth Sciences*, v. 54, p. 173–202.

Katz, L. R., Kontak, D. J., Dubé, B., McNicoll, V., Creaser, R., and Petrus, J. A., 2021, An Archean Porphyry-Type Gold Deposit: The Côté Gold Au(-Cu) Deposit, Swayze Greenstone Belt, Superior Province, Ontario, Canada: *Economic Geology*, v. 116, p. 47-89.

Keith, M., Haase, K. M., Klemd, R., Smith, D. J., Schwarz-Schampera, U., and Bach, W., 2018, Constraints on the source of Cu in a submarine magmatic-hydrothermal system, Brothers volcano, Kermadec island arc: *Contributions to Mineralogy and Petrology*, v. 173, p. 40.

Kelemen, P. B., Hanghøj, K., and Greene, A. R., 2007, 3.18 - One View of the Geochemistry of Subduction-Related Magmatic Arcs, with an Emphasis on Primitive Andesite and Lower Crust, in Holland, H. D., and Turekian, K. K., eds., *Treatise on Geochemistry*: Oxford, Pergamon, p. 1–70.

Kelley, K. A., and Cottrell, E., 2009, Water and the oxidation state of subduction zone magmas: *Science*, v. 325, p. 605–607.

Kemp, A. I. S., Vervoort, J. D., Bjorkman, K. E., and Iaccheri, L. M., 2017, Hafnium Isotope Characteristics of Palaeoarchean Zircon OG1/OGC from the Owens Gully Diorite, Pilbara Craton, Western Australia: *Geostandards and Geoanalytical Research*, v. 41, p. 659–673.

Kerrick, R., Goldfarb, R. J., and Richards, J. P., 2005, Metallogenic provinces in an evolving geodynamic framework: *Economic geology*, v. 100, p. 1097–1136.

Kleinsasser, J., Simon, A. C., Konecke, B., Beckmann, P. & Holtz, F. Sulfide and sulfate saturation of dacitic melts as a function of oxygen fugacity. *Geochimica et Cosmochimica Acta*, accepted pending revision.

Klimm, K., Kohn, S. C., and Botcharnikov, R. E., 2012, The dissolution mechanism of sulphur in hydrous silicate melts. II: Solubility and speciation of sulphur in hydrous silicate melts as a function of fO₂: *Chemical Geology*, v. 322, p. 250–267.

Kim, Y., Konecke, B., Fiege, A., Simon, A., and Becker, U., 2017, An ab-initio study of the energetics and geometry of sulfide, sulfite, and sulfate incorporation into apatite: The thermodynamic basis for using this system as an oxybarometer: *American Mineralogist*, v. 102, p. 1646–1656.

Kleinhanns, I. C., Kramers, J. D., and Kamber, B. S., 2003, Importance of water for Archaean granitoid petrology: a comparative study of TTG and potassic granitoids from Barberton Mountain Land, South Africa: *Contributions to Mineralogy and Petrology*, v. 145, p. 377–389.

Konecke, B. A., Fiege, A., Simon, A. C., Linsler, S., and Holtz, F., 2019, An experimental calibration of a sulfur-in-apatite oxybarometer for mafic systems: *Geochimica et Cosmochimica Acta*, v. 265, p. 242–258.

Konecke, B. A., Fiege, A., Simon, A. C., Parat, F., and Stechern, A., 2017, Co-variability of S^{6+} , S^{4+} , and S^{2-} in apatite as a function of oxidation state: Implications for a new oxybarometer: *American Mineralogist*, v. 102, p. 548–557.

Kontak, D. J., Creaser, R. A., and Hamilton, M. A., 2013, Geological and geochemical studies of the Côté Lake Au (-Cu) deposit Area, Chester Township, northern Ontario: Results from the Shining Tree, Chester Township and Matachewan Gold Projects and the Northern Cobalt Embayment Polymetallic Vein Project. Edited by JA Ayer, DJ Kontak, RL Linnen, and S. Lin. Ontario Geological Survey, Miscellaneous Release Data, v. 294.

Lacovino, K., Guild, M. R., and Till, C. B., 2020, Aqueous fluids are effective oxidizing agents of the mantle in subduction zones: *Contributions to Mineralogy and Petrology*, v. 175, p. 36.

Lafliche, M. R., Dupuy, C., and Dostal, J., 1992, Tholeiitic volcanic rocks of the Late Archean Blake River Group, southern Abitibi greenstone belt: origin and geodynamic implications: *Canadian Journal of Earth Sciences*, v. 29, p. 1448–1458.

Laurent, O., Björnsen, J., Wotzlaw, J. F., Bretscher, S., Pimenta Silva, M., Moyon, J. F., Ulmer, P., and Bachmann, O., 2020, Earth's earliest granitoids are crystal-rich magma reservoirs tapped by silicic eruptions: *Nature Geoscience*, p. 163–169.

Laurent, O., Martin, H., Moyon, J. F., and Doucelance, R., 2014, The diversity and evolution of late-Archean granitoids: Evidence for the onset of “modern-style” plate tectonics between 3.0 and 2.5Ga: *Lithos*, v. 205, p. 208–235.

Leclerc, F., Harris, L. B., Bédard, J. H., van Breemen, O., and Goulet, N., 2012, Structural and Stratigraphic Controls on Magmatic, Volcanogenic, and Shear Zone-Hosted Mineralization in the Chapais-Chibougamau Mining Camp, Northeastern Abitibi, Canada: *Economic Geology*, v. 107, p. 963–989.

Lee, C. T. A., Leeman, W. P., Canil, D., and Li, Z. X. A., 2005, Similar V/Sc systematics in MORB and arc basalts: implications for the oxygen fugacities of their mantle source regions: *Journal of Petrology*, v. 46, p. 2313–2336.

Lee, C. T., Luffi, P., Chin, E. J., Bouchet, R., Dasgupta, R., Morton, D. M., Le Roux, V., Yin, Q. Z., and Jin, D., 2012, Copper systematics in arc magmas and implications for crust-mantle differentiation: *Science*, v. 336, p. 64–68.

Lepage, L. D., 2003, ILMAT: an Excel worksheet for ilmenite–magnetite geothermometry and geobarometry: *Computers & Geosciences*, v. 29, p. 673–678.

Loucks, R. R., Fiorentini, M. L., and Henríquez, G. J., 2020, New magmatic oxybarometer using trace elements in zircon: *Journal of Petrology*, v. 61, p. 1–30.

Ludwig, K. R., 2011, Isoplot/Ex, Version 4.15: A geochronological toolkit for Microsoft Excel: *Geochronology Center Berkeley*, v. 4.

Lyons, T. W., and Gill, B. C., 2010, Ancient Sulfur Cycling and Oxygenation of the Early

Biosphere: Elements, v. 6, p. 93–99.

Jégo, S., and Pichavant, M., 2012, Gold solubility in arc magmas: Experimental determination of the effect of sulfur at 1000°C and 0.4GPa: *Geochimica et Cosmochimica Acta*, v. 84, p. 560–592.

MacDonald, P. J., and Piercey, S. J., 2019, Geology, lithogeochemistry, and significance of porphyry intrusions associated with gold mineralization within the Timmins–Porcupine gold camp, Canada: *Canadian Journal of Earth Sciences*, v. 56, p. 399–418.

Macpherson, C. G., Dreher, S. T., and Thirlwall, M. F., 2006, Adakites without slab melting: High pressure differentiation of island arc magma, Mindanao, the Philippines: *Earth and Planetary Science Letters*, v. 243, p. 581–593.

Madon, B., Mathieu, L., and Marsh, J. H., 2020, Oxygen Fugacity and Volatile Content of Syntectonic Magmatism in the Neoproterozoic Abitibi Greenstone Belt, Superior Province, Canada: *Minerals*, v. 10, p. 966.

Martin, H., Moyen, J. F., Guitreau, M., Blichert-Toft, J., and Le Pennec, J. L., 2014, Why Archean TTG cannot be generated by MORB melting in subduction zones: *Lithos*, v. 198, p. 1–13.

Mathieu, L., Crépon, A., and Kontak, D. J., 2020, Tonalite-Dominated Magmatism in the Abitibi Subprovince, Canada, and Significance for Cu-Au Magmatic-Hydrothermal Systems: *Minerals*, v. 10, p. 242.

Matjuschkin, V., Blundy, J. D., and Brooker, R. A., 2016, The effect of pressure on sulphur speciation in mid- to deep-crustal arc magmas and implications for the formation of porphyry copper deposits: *Contributions to Mineralogy and Petrology*, v. 171, p. 66.

Meng, X., Kleinsasser, J., Richards, J., Tapster, S., Jugo, P., Simon, A., Kontak, D., Robb, L., Bybee, G., Marsh, J., and Stern, R., 2021, Oxidized sulfur-rich arc magmas formed porphyry Cu deposits by 1.88 Ga. *Nature Communications* 12, 2189.

Mohan, M. R., Kamber, B. S., and Piercey, S. J., 2008, Boron and arsenic in highly evolved Archean felsic rocks: Implications for Archean subduction processes: *Earth and Planetary Science Letters*, v. 274, p. 479–488.

Mole, D. R., Thurston, P. C., Marsh, J. H., Stern, R. A., Ayer, J. A., Martin, L. A. J., and Lu, Y. J., 2021, The formation of Neoproterozoic continental crust in the south-east Superior Craton by two distinct geodynamic processes: *Precambrian Research*, v. 356, p. 106104.

Monecke, T., Mercier-Langevin, P., Dubé, B., and Frieman, B., 2017, Geology of the Abitibi greenstone belt: Archean base and precious metal deposits, Southern Abitibi greenstone belt, Canada. *Reviews in Economic Geology*, v. 19, p. 7–49.

Moyen, J. F., and van Hunen, J., 2012, Short-term episodicity of Archean plate tectonics: *Geology*, v. 40, p. 451–454.

- Mutch, E. J. F., Blundy, J. D., Tattitch, B. C., Cooper, F. J., and Brooker, R. A., 2016, An experimental study of amphibole stability in low-pressure granitic magmas and a revised Al-in-hornblende geobarometer: *Contributions to Mineralogy and Petrology*, v. 171, p. 85.
- Nagel, T. J., Hoffmann, J. E., and Münker, C., 2012, Generation of Eoarchean tonalite-trondhjemite-granodiorite series from thickened mafic arc crust: *Geology*, v. 40, p. 375–378.
- Nash, W. M., Smythe, D. J., and Wood, B. J., 2019, Compositional and temperature effects on sulfur speciation and solubility in silicate melts: *Earth and Planetary Science Letters*, v. 507, p. 187–198.
- Ohmoto, H., 2020, A seawater-sulfate origin for early Earth's volcanic sulfur: *Nature Geoscience*, p. 1–8.
- Parat, F., and Holtz, F., 2004, Sulfur partitioning between apatite and melt and effect of sulfur on apatite solubility at oxidizing conditions: *Contributions to Mineralogy and Petrology*, v. 147, p. 201–212.
- Parat, F., Holtz, F., and Streck, M. J., 2011, Sulfur-bearing Magmatic Accessory Minerals: Sulfur in Magmas and Melts: Its Importance for Natural and Technical Processes, v. 73, p. 285–314.
- Peng, G. Y., Luhr, J. F., and McGee, J. J., 1997, Factors controlling sulfur concentrations in volcanic apatite: *American Mineralogist*, v. 82, p. 1210–1224.
- Péloquin, A. S., Piercey, S. J., and Hamilton, M. A., 2008, The Ben Nevis volcanic complex, Ontario, Canada: part of the late volcanic phase of the Blake River Group, Abitibi Subprovince: *Economic Geology*, v. 103, p. 1219–1241.
- Piccoli, P., and Candela, P., 1994, Apatite in felsic rocks: a model for the estimation of initial halogen concentrations in the Bishop Tuff (Long Valley) and Tuolumne Intrusive Suite (Sierra Nevada Batholith) magmas: *American Journal of Science*, v. 294, p. 92–135.
- Piercey, S. J., Chaloux, E. C., Péloquin, A. S., Hamilton, M. A., and Creaser, R. A., 2008, Synvolcanic and younger plutonic rocks from the Blake River Group: implications for regional metallogenesis: *Economic Geology*, v. 103, p. 1243–1268.
- Planavsky, N. J., Bekker, A., Hofmann, A., Owens, J. D., and Lyons, T. W., 2012, Sulfur record of rising and falling marine oxygen and sulfate levels during the Lomagundi event: *Proc Natl Acad Sci U S A*, v. 109, p. 18300–18305.
- Powell, W. G., Carmichael, D. M., and Hodgson, C. J., 1995, Conditions and timing of metamorphism in the southern Abitibi greenstone belt, Quebec: *Canadian Journal of Earth Sciences*, v. 32, p. 787–805.
- Prouteau, G., and Scaillet, B., 2012, Experimental constraints on sulphur behaviour in subduction zones: implications for TTG and adakite production and the global sulphur cycle since the Archean: *Journal of Petrology*, v. 54, p. 183–213.

- Richards, J. P., 2011, Magmatic to hydrothermal metal fluxes in convergent and collided margins: *Ore Geology Reviews*, v. 40, p. 1–26.
- Richards, J. P., 2015, The oxidation state, and sulfur and Cu contents of arc magmas: implications for metallogeny: *Lithos*, v. 233, p. 27–45.
- Richards, J. P., Boyce, A. J., and Pringle, M. S., 2001, Geologic evolution of the Escondida area, northern Chile: A model for spatial and temporal localization of porphyry Cu mineralization: *Economic Geology and the Bulletin of the Society of Economic Geologists*, v. 96, p. 271–305.
- Richards, J. P., López, G. P., Zhu, J. J., Creaser, R. A., Locock, A. J., and Mumin, A. H., 2017, Contrasting Tectonic Settings and Sulfur Contents of Magmas Associated with Cretaceous Porphyry Cu ± Mo ± Au and Intrusion-Related Iron Oxide Cu-Au Deposits in Northern Chile: *Economic Geology*, v. 112, p. 295–318.
- Richards, J. P., and Kerrich, R., 2007, Special paper: adakite-like rocks: their diverse origins and questionable role in metallogenesis: *Economic Geology*, v. 102, p. 537–576.
- Richards, J. P., and Mumin, A. H., 2013, Magmatic-hydrothermal processes within an evolving Earth: Iron oxide-copper-gold and porphyry Cu ± Mo ± Au deposits: *Geology*, v. 41, p. 767–770.
- Richards, J. P., López, G. P., Zhu, J. J., Creaser, R. A., Locock, A. J., and Mumin, A. H., 2017, Contrasting Tectonic Settings and Sulfur Contents of Magmas Associated with Cretaceous Porphyry Cu ± Mo ± Au and Intrusion-Related Iron Oxide Cu-Au Deposits in Northern Chile: *Economic Geology*, v. 112, p. 295–318.
- Richards, J. P., and Şengör, A. M. C., 2017, Did Paleo-Tethyan anoxia kill arc magma fertility for porphyry copper formation?: *Geology*, v. 45, p. 591–594.
- Richards, J. P., Spell, T., Rameh, E., Razique, A., and Fletcher, T., 2012, High Sr/Y Magmas Reflect Arc Maturity, High Magmatic Water Content, and Porphyry Cu ± Mo ± Au Potential: Examples from the Tethyan Arcs of Central and Eastern Iran and Western Pakistan: *Economic Geology*, v. 107, p. 295–332.
- Ridolfi, F., Renzulli, A., and Puerini, M., 2010, Stability and chemical equilibrium of amphibole in calc-alkaline magmas: an overview, new thermobarometric formulations and application to subduction-related volcanoes: *Contributions to Mineralogy and Petrology*, v. 160, p. 45–66.
- Robert, F., 2001, Syenite-associated disseminated gold deposits in the Abitibi greenstone belt, Canada: *Mineralium Deposita*, v. 36, p. 503–516.
- Sadove, G., Konecke, B. A., Fiege, A., and Simon, A. C., 2019, Structurally bound S²⁻, S¹⁻, S⁴⁺, S⁶⁺ in terrestrial apatite: The redox evolution of hydrothermal fluids at the Phillips mine, New York, USA: *Ore Geology Reviews*, v. 107, p. 1084–1096.
- Sack, R. O., and Ghiorso, M. S., 1991, Chromian spinels as petrogenetic indicators - thermodynamics and petrological applications: *American Mineralogist*, v. 76, p. 827–847.

- Schiller, D., and Finger, F., 2019, Application of Ti-in-zircon thermometry to granite studies: problems and possible solutions: *Contributions to Mineralogy and Petrology*, v. 174, p. 51.
- Scott, J. A. J., Humphreys, M. C. S., Mather, T. A., Pyle, D. M., and Stock, M. J., 2015, Insights into the behaviour of S, F, and Cl at Santiaguito Volcano, Guatemala, from apatite and glass: *Lithos*, v. 232, p. 375–394.
- Sillitoe, R. H., 2010, Porphyry Copper Systems: *Economic Geology*, v. 105, p. 3–41.
- Simon, A. C., and Ripley, E. M., 2011, The Role of Magmatic Sulfur in the Formation of Ore Deposits: *Reviews in Mineralogy and Geochemistry*, v. 73, p. 513–578.
- Singer, D. A., Berger, V. I., and Moring, B. C., 2008, Porphyry copper deposits of the world: Database and grade and tonnage models: USGS Open-File Report 2008-1155: USGS: Reston, VA, USA.
- Smythe, D. J., and Brenan, J. M., 2016, Magmatic oxygen fugacity estimated using zircon-melt partitioning of cerium: *Earth and Planetary Science Letters*, v. 453, p. 260–266.
- Söderlund, U., Patchett, P. J., Vervoort, J. D., and Isachsen, C. E., 2004, The ^{176}Lu decay constant determined by Lu–Hf and U–Pb isotope systematics of Precambrian mafic intrusions: *Earth and Planetary Science Letters*, v. 219, p. 311–324.
- Spencer, K. J., and Lindsley, D. H., 1981, A solution model for coexisting iron–titanium oxides: *American mineralogist*, v. 66, p. 1189–1201..
- Sproule, R. A., Leshner, C. M., Ayer, J. A., Thurston, P. C., and Herzberg, C. T., 2002, Spatial and temporal variations in the geochemistry of komatiites and komatiitic basalts in the Abitibi greenstone belt: *Precambrian Research*, v. 115, p. 153–186.
- Stock, M. J., Humphreys, M. C. S., Smith, V. C., Isaia, R., Brooker, R. A., and Pyle, D. M., 2018, Tracking Volatile Behaviour in Sub-volcanic Plumbing Systems Using Apatite and Glass: Insights into Pre-eruptive Processes at Campi Flegrei, Italy: *Journal of Petrology*, v. 59, p. 2463–2492.
- Stolper, D. A., and Bucholz, C. E., 2019, Neoproterozoic to early Phanerozoic rise in island arc redox state due to deep ocean oxygenation and increased marine sulfate levels: *Proceedings of the National Academy of Sciences*, v. 116, p. 8746–8755.
- Stolper, D. A., and Keller, C. B., 2018, A record of deep-ocean dissolved O_2 from the oxidation state of iron in submarine basalts: *Nature*, v. 553, p. 323–327.
- Streck, M. J., and Dilles, J. H., 1998, Sulfur evolution of oxidized arc magmas as recorded in apatite from a porphyry copper batholith: *Geology*, v. 26, p. 523–526.
- Sun, S. S., and McDonough, W. F., 1989, Chemical and isotopic systematics of oceanic basalts: implications for mantle composition and processes: Geological Society, London, Special Publications, v. 42, p. 313–345.

Sutcliffe, R., Barrie, C. T., Burrows, D., and Beakhouse, G., 1993, Plutonism in the southern Abitibi Subprovince; a tectonic and petrogenetic framework: *Economic Geology*, v. 88, p. 1359–1375.

Tepper, J. H., and Kuehner, S. M., 1999, Complex zoning in apatite from the Idaho batholith: A record of magma mixing and intracrystalline trace element diffusion: *American Mineralogist*, v. 84, p. 581–595.

Thompson, J. F. H., Sillitoe, R. H., Baker, T., Lang, J. R., and Mortensen, J. K., 1999, Intrusion related gold deposits associated with tungsten-tin provinces: *Mineralium Deposita*, v. 34, p. 323–334.

Thurston, P. C., Ayer, J. A., Goutier, J., and Hamilton, M. A., 2008, Depositional Gaps in Abitibi Greenstone Belt Stratigraphy: A Key to Exploration for Syngenetic Mineralization: *Economic Geology*, v. 103, p. 1097–1134.

Valley, J. W., 2003, Oxygen Isotopes in Zircon: Reviews in Mineralogy and Geochemistry, v. 53, p. 343–385.

Valley, J. W., Lackey, J. S., Cavosie, A. J., Clechenko, C. C., Spicuzza, M. J., Basei, M. A. S., Bindeman, I. N., Ferreira, V. P., Sial, A. N., King, E. M., Peck, W. H., Sinha, A. K., and Wei, C. S., 2005, 4.4 billion years of crustal maturation: oxygen isotope ratios of magmatic zircon: *Contributions to Mineralogy and Petrology*, v. 150, p. 561–580.

Valley, J. W., Kinny, P. D., Schulze, D. J., and Spicuzza, M. J., 1998, Zircon megacrysts from kimberlite: oxygen isotope variability among mantle melts: *Contributions to Mineralogy and Petrology*, v. 133, p. 1–11.

Wainwright, A. J., Tosdal, R. M., Wooden, J. L., Mazdab, F. K., and Friedman, R. M., 2011, U–Pb (zircon) and geochemical constraints on the age, origin, and evolution of Paleozoic arc magmas in the Oyu Tolgoi porphyry Cu–Au district, southern Mongolia: *Gondwana Research*, v. 19, p. 764–787.

Wallace, P. J., 2005, Volatiles in subduction zone magmas: concentrations and fluxes based on melt inclusion and volcanic gas data: *Journal of Volcanology and Geothermal Research*, v. 140, p. 217–240.

Wang, R., Richards, J. P., Hou, Z. Q., Yang, Z. M., Gou, Z. B., and Dufrane, A., 2014, Increasing magmatic oxidation state from Paleocene to Miocene in the Eastern Gangdese belt, Tibet: Implication for Collision-related porphyry Cu–Mo±Au Mineralization: *Economic Geology*, v. 109, p. 1943–1965.

Webster, J. D., and Piccoli, P. M., 2015, Magmatic Apatite: A Powerful, Yet Deceptive, Mineral: *Elements*, v. 11, p. 177–182.

Webster, J. D., Tappen, C. M., and Mandeville, C. W., 2009, Partitioning behavior of chlorine and fluorine in the system apatite–melt–fluid. II: Felsic silicate systems at 200MPa: *Geochimica et Cosmochimica Acta*, v. 73, p. 559–581.

Wiedenbeck, M., Alle, P., Corfu, F., Griffin, W. L., Meier, M., Oberli, F., Von Quadt, A., Roddick, J. C., and Spiegel, W., 1995, Three natural zircon standards for U-Th-Pb, Lu-Hf, trace element and REE analyses: *Geostandards newsletter*, v. 19, p. 1–23.

Wilkinson, B. H., and Kesler, S. E., 2007, Tectonism and Exhumation in Convergent Margin Orogens: Insights from Ore Deposits: *The Journal of Geology*, v. 115, p. 611–627.

Wyman, D. A., Kerrich, R., and Polat, A., 2002, Assembly of Archean cratonic mantle lithosphere and crust: plume–arc interaction in the Abitibi–Wawa subduction–accretion complex: *Precambrian Research*, v. 115, p. 37–62.

Yang, X. Z., Gaillard, F., and Scaillet, B., 2014, A relatively reduced Hadean continental crust and implications for the early atmosphere and crustal rheology: *Earth and Planetary Science Letters*, v. 393, p. 210–219.

Zajacz, Z., Candela, P. A., Piccoli, P. M., Wälle, M., and Sanchez-Valle, C., 2012, Gold and copper in volatile saturated mafic to intermediate magmas: Solubilities, partitioning, and implications for ore deposit formation: *Geochimica et Cosmochimica Acta*, v. 91, p. 140–159.

Zhang, C., Holtz, F., Ma, C. Q., Wolff, P. E., and Li, X. Y., 2012, Tracing the evolution and distribution of F and Cl in plutonic systems from volatile-bearing minerals: a case study from the Liujiawa pluton (Dabie orogen, China): *Contributions to Mineralogy and Petrology*, v. 164, p. 859–879.

Zhu, J. J., Richards, J. P., Rees, C., Creaser, R., DuFrane, S. A., Locock, A., Petrus, J. A., and Lang, J., 2018, Elevated Magmatic Sulfur and Chlorine Contents in Ore-Forming Magmas at the Red Chris Porphyry Cu-Au Deposit, Northern British Columbia, Canada: *Economic Geology*, v. 113, p. 1047–1075.

5.14 Figures

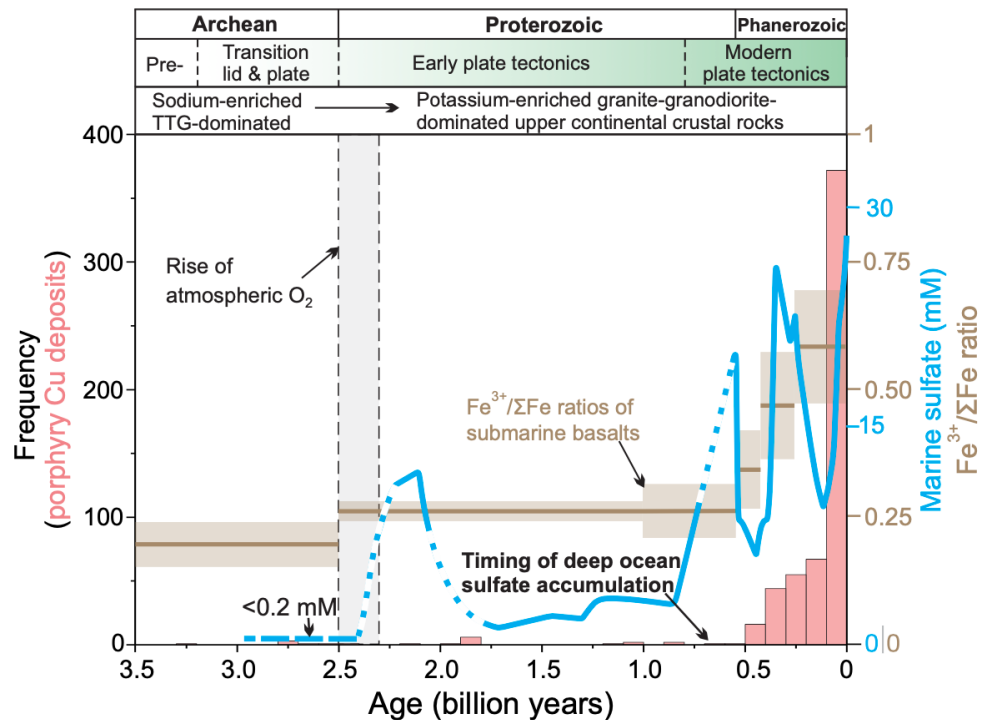


Figure 5.1. Temporal correlation between global porphyry Cu deposits, Earth's tectonic regimes, lithologic transition, and ocean-atmospheric evolution through geological time since 3.5 Ga. The temporal distribution of global porphyry Cu deposits based on the database from [Singer *et al.* \(2008\)](#) is illustrated in the pink histogram. The interpretation of tectonic regimes is from [Cawood \(2020\)](#). The lithological transition from sodic tonalite-trondhjemite-granodiorite- to potassic granite-granodiorite-dominated upper continental crust is from [Jagoutz \(2013\)](#). The timing of the rise of the atmospheric O₂ during the Great Oxygenation Event (GOE; in grey) is from [Holland \(2002\)](#). The Fe³⁺/ΣFe ratios (in light gold) of the submarine basalts are from [Stolper and Keller \(2018\)](#). Marine sulfate contents on average (in blue; uncertainty not marked for simplification) are compiled in previous studies ([Lyons & Gill, 2010](#), [Planavsky *et al.*, 2012](#)), where data are not reported, we speculate marine sulfate contents along the blue dashed line.

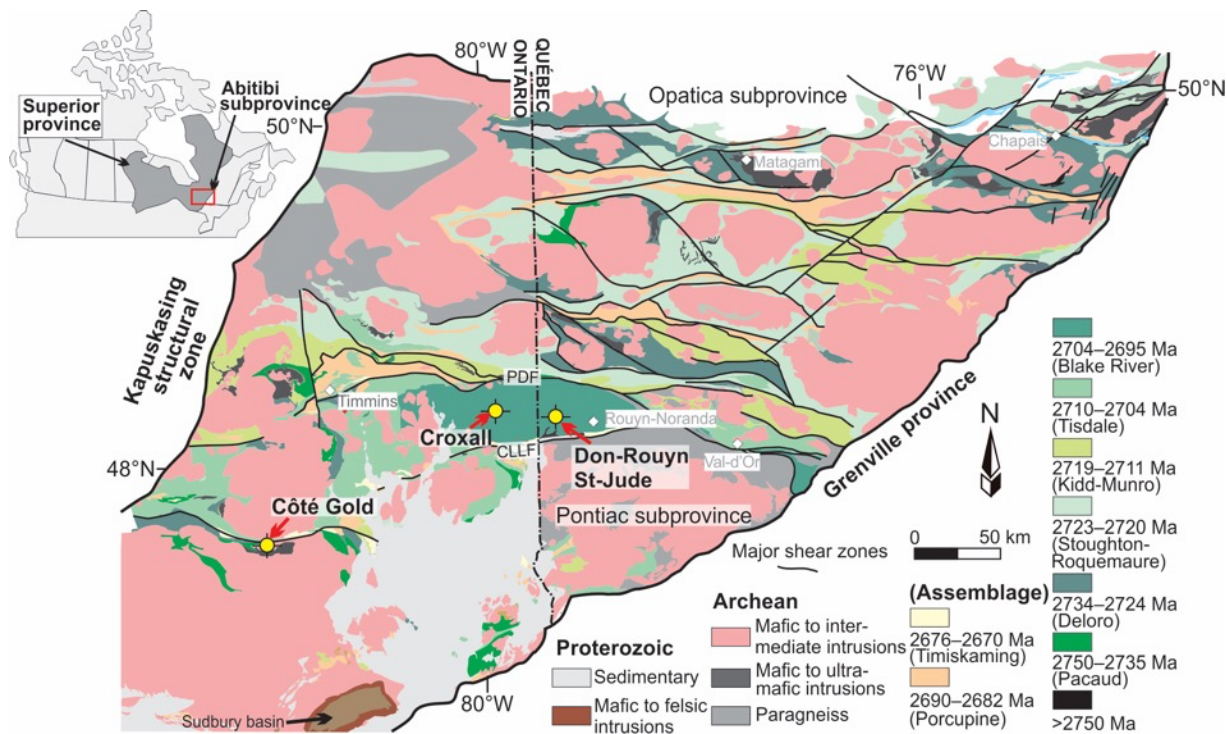


Figure 5.2. Simplified geologic map of the Abitibi and Pontiac subprovinces, modified from Thurston *et al.* (2008) and Leclerc *et al.* (2012). Inset in upper-left showing the location of Figure 4.2 in the Superior province. Abbreviations: PDF = Destor–Porcupine Fault Zone, LLCF = Larder Lake–Cadillac Fault Zone.

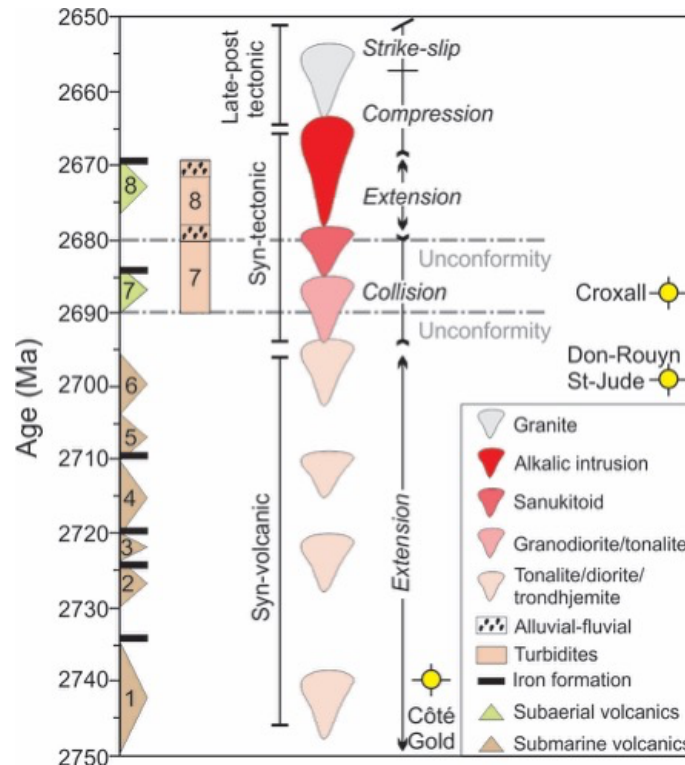


Figure 5.3. Geological framework of the southern Abitibi subprovince over geological time. Submarine volcanic assemblages include (1) Pacaud, (2) Deloro, (3) Stoughton-Roquemaure, (4) Kidd Munro, (5) Tisdale, and (6) Blake River succeeded by minor volcanic rocks hosted in (7) Porcupine and (8) Timiskaming sedimentary assemblages (Ayer *et al.*, 2002, Thurston *et al.*, 2008). The timing of evolving plutonic rock phases from syn-volcanic tonalite-diorite-trondhjemite, early syn-tectonic granodiorite, syn-tectonic sanukitoid (mainly quartz syenite-quartz monzonite-granite), and late-tectonic alkalic intrusion, to crust-derived granite, are based on data compiled in Ayer *et al.* (2005) and Beakhouse (2011). Deformation events are adapted from Bateman *et al.* (2005). The timing of the Côté Gold, Don-Rouyn, St-Jude, and Croxall deposits are marked, see text for the new and published geochronological results.

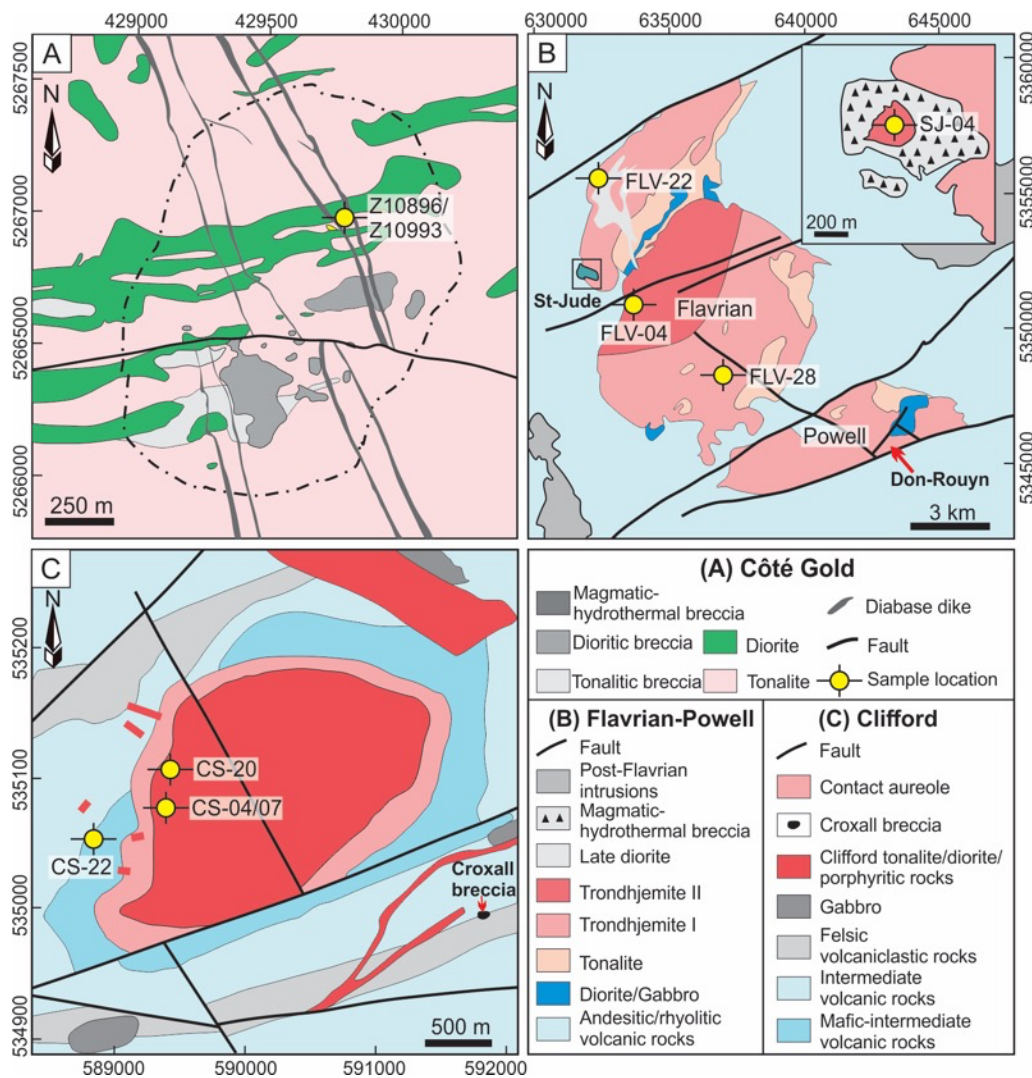


Figure 5.4. Simplified geologic maps of the (a) Côté Gold, (b) Flavrian-St-Jude, and (c) Clifford area, modified from [Katz *et al.* \(2021\)](#), [Galley \(2003\)](#), and [Piercey *et al.* \(2008\)](#).

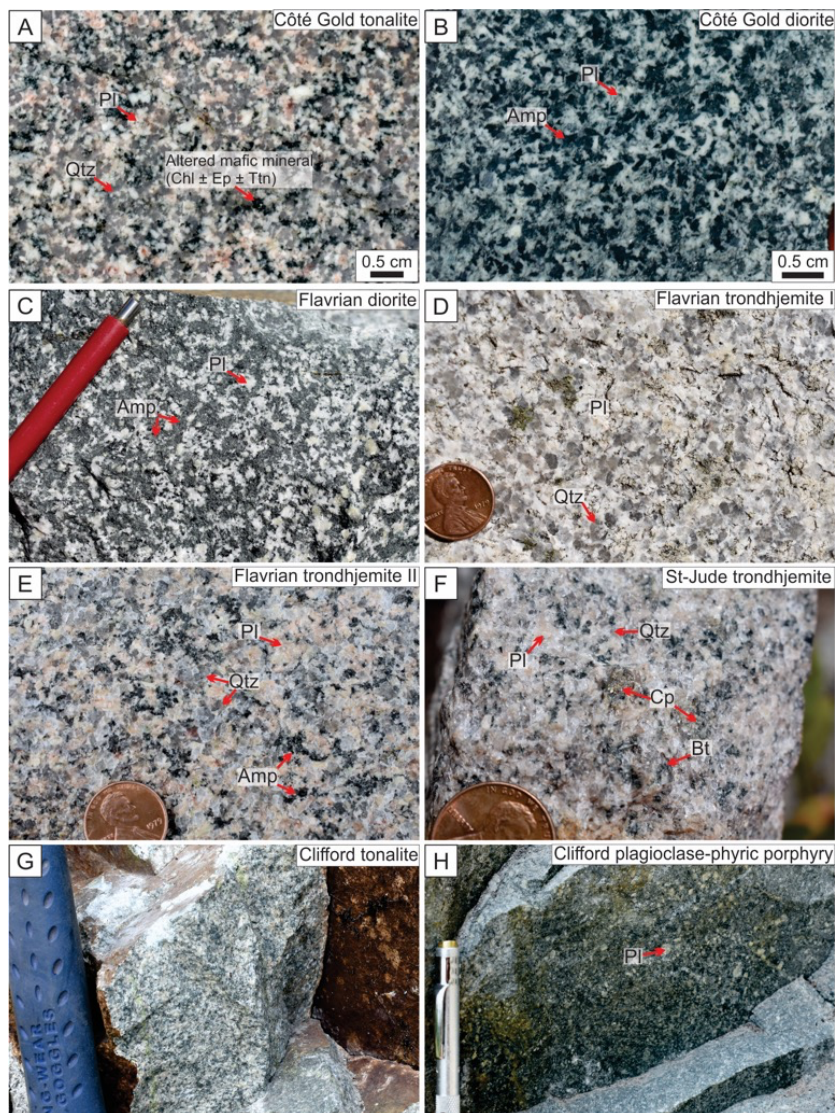


Figure 5.5. Field photographs for main lithological units from the Côté Gold, Flavrian-St-Jude, and Clifford areas in the southern Abitibi subprovince. (A) Côté Gold tonalite (UTM 17U 429714E, 5266923N, 387 m), (B) Côté Gold diorite (UTM 17U 429717E, 5266928N, 387 m), (C) Flavrian diorite (UTM 17U 634297E, 5346583N, 322 m; WGS84 datum), (D) Flavrian trondhjemite phase I (UTM 17U 636535E, 5348252N, 311 m), (E) Flavrian trondhjemite phase II (UTM 17U 633312E, 5350516N, 339 m), (F) St-Jude trondhjemite (UTM 17U 631709E, 5352100N, 330 m), (G) Clifford tonalite (UTM 17U 589288E, 5351012N, 321 m), and (H) Clifford plagioclase-phyric porphyry (UTM 17U 588929E, 5350439N, 323 m). Abbreviations: Amp = amphibole, Bt = biotite, Cp = chalcopyrite, Pl = plagioclase, Qtz = quartz.

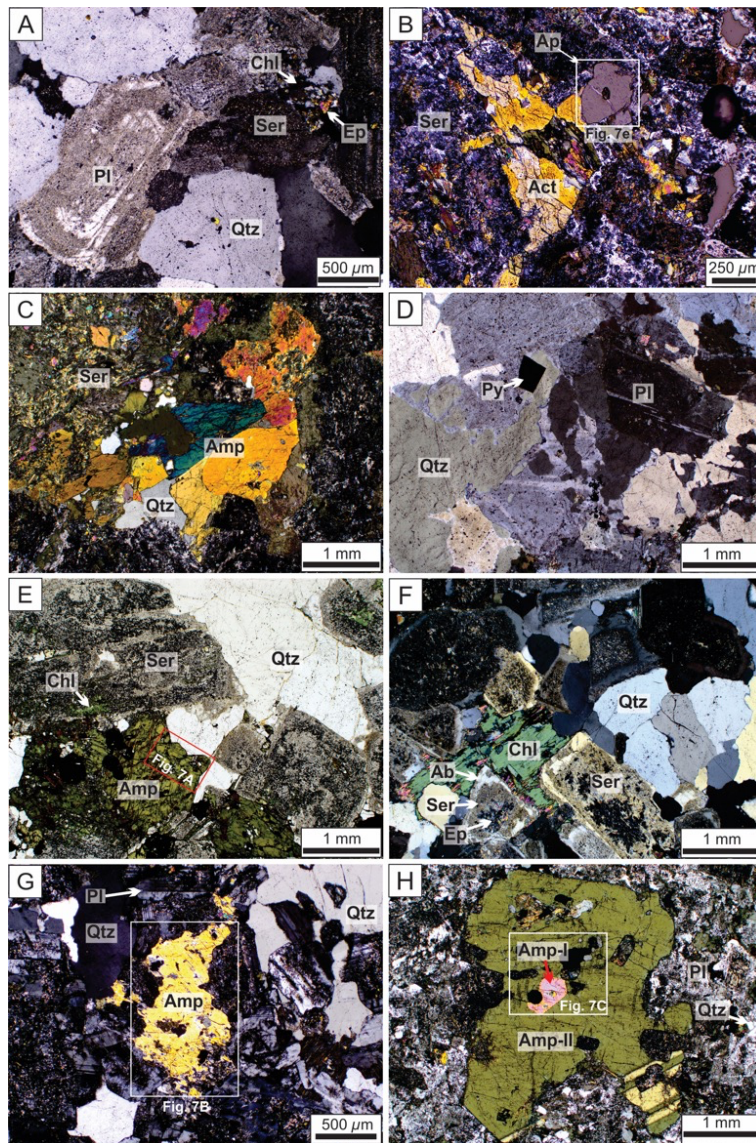


Figure 5.6. Microphotographs for the main igneous rock phases from the Côte Gold, Flavrian-St-Jude, and Clifford areas in the southern Abitibi subprovince. (A) tonalite and (B) diorite/quartz diorite from Côte Gold; cross-polarized light. (C) Flavrian diorite (sample FLV-32); cross-polarized light. (D) Flavrian trondhjemite-I; cross-polarized light. (E) Flavrian trondhjemite-II (sample FLV-04); plane-polarized light. (F) St-Jude trondhjemite (sample SJ-08); plane-polarized light. (G) Clifford tonalite (sample CS-07); cross-polarized light. (H) Clifford plagioclase-phyric porphyry (sample CS-22); cross-polarized light. Abbreviations: Ab = albite, Act = actinolite, Amp = amphibole, Ap = apatite, Chl = chlorite, Ep = epidote, Pl = plagioclase, Py = pyrite, Qtz = quartz, Ser = sericite. See [Table 5.1](#) for sample locations and descriptions.

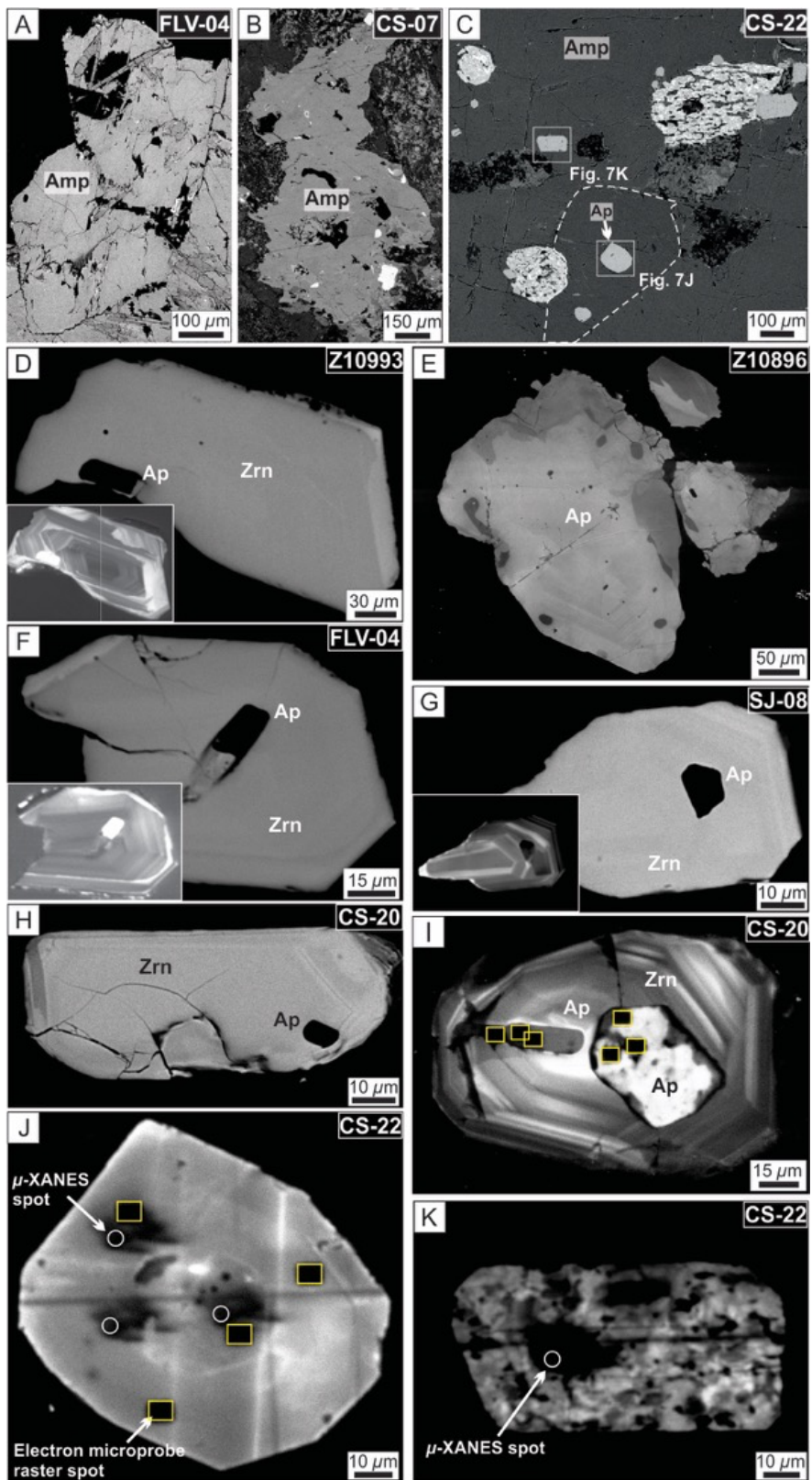


Figure 5.7. Representative amphibole and apatite crystals from the main lithological units from Côté Gold, Flavrian-St-Jude, and Clifford in the southern Abitibi subprovince.

(A) Amphibole in the Flavrian trondhjemite-II (sample FLV-04); backscattered electron (BSE) image. (B) Amphibole in the Clifford tonalite (sample CS-07); BSE. (C) Amphibole phenocryst with core (Amp-I) and rim (Amp-II) zones in the Clifford plagioclase-phyric porphyry (sample CS-22); BSE. (D) Apatite inclusion wholly enclosed in zircon from Côté Gold tonalite (sample Z10993); BSE. Inset is cathodoluminescence (CL) image for the zircon grain. (E) Apatite with the sector and oscillatory zonings in the matrix of the Côté Gold diorite (sample Z10896); CL image. (F–G) Apatite inclusions wholly enclosed in zircons from the St-Jude trondhjemite (sample SJ-04) and Flavrian trondhjemite (sample FLV-04); BSE. Insets are CL images for the host zircon grains. (H) Zircon and the wholly hosted apatite grain from the Clifford tonalite (sample CS-20); BSE. (I) Primary (left) and altered (right) apatite grains in zircon with oscillatory zoning from sample CS-20; CL. (J) Primary and (K) altered apatite grains in amphibole phenocryst of sample CS-22; CL. The black-filled yellow squares in (I) and (J) represent electron microprobe raster beam spots. White-circles in (J) and (K) represent μ -XANES spot. Abbreviations: Amp = amphibole, Ap = apatite, Zrn = zircon; μ -XANES = micro X-ray absorption near edge structure. See [Table 5.1](#) for sample locations and descriptions.

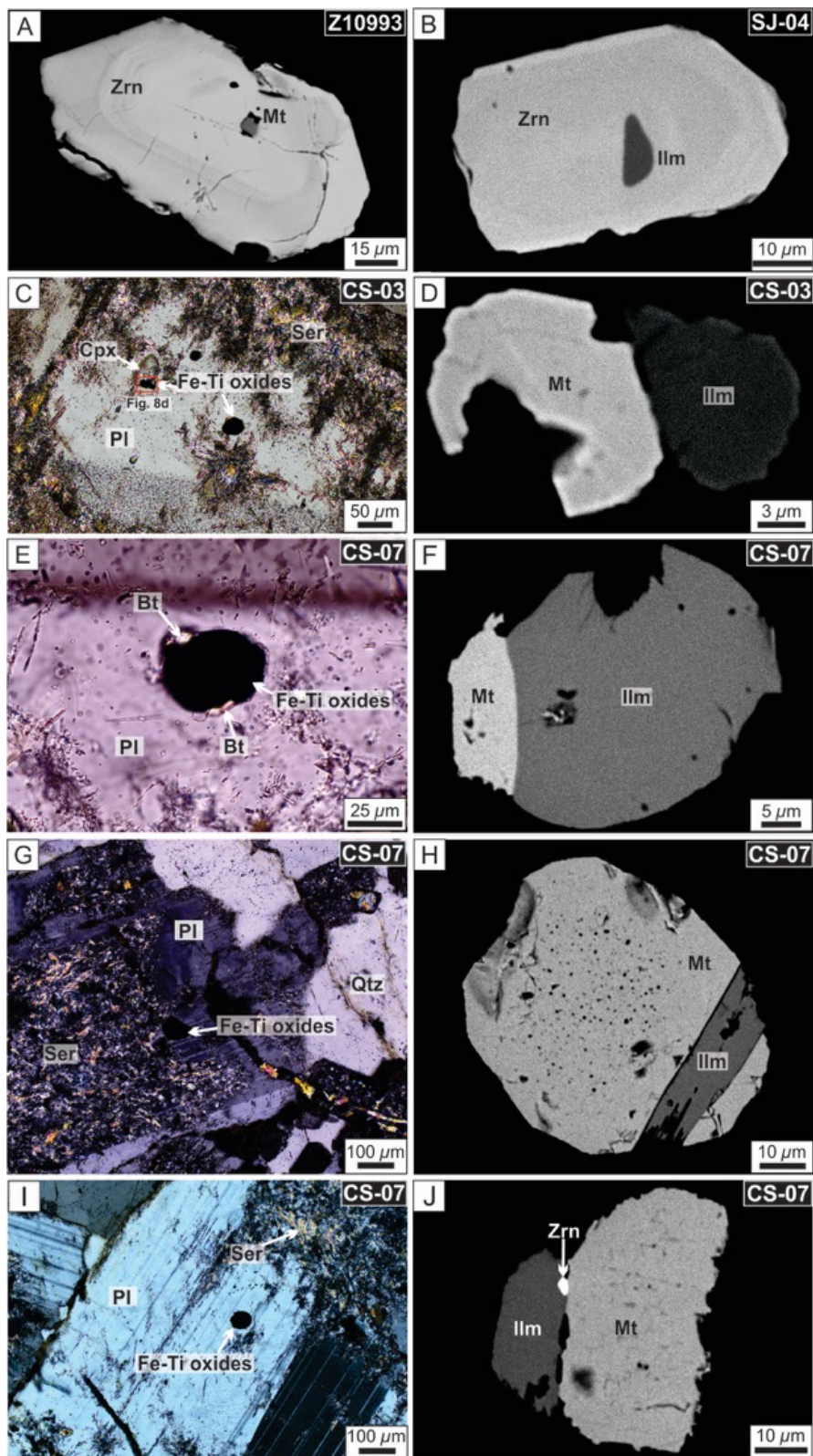


Figure 5.8. Representative magnetite and ilmenite from the main lithologies from Côte Gold, Flavrian-St-Jude, and Clifford in the southern Abitibi subprovince. (A) Magnetite in zircon from the Côte Gold tonalite (sample Z10993); BSE. (B) Ilmenite in zircon from the St-Jude trondhjemite (sample SJ-04); BSE. (C–F) Primary magnetite-ilmenite mineral pairs hosted in plagioclase in the Clifford tonalite (samples CS-03 and CS-07); cross-polarized light in (C, E) and BSE in (D, F). (G–J) Partially altered magnetite-ilmenite mineral pair hosted in plagioclase in sample CS-07; cross-polarized light in (G, I), and BSE in (H, J). The magnetite in (H) has partially been altered with rim retaining primary composition, whereas the magnetite in (J) has been altered. Abbreviations: Bt = biotite, Cpx = clinopyroxene, Ilm = ilmenite, Mt = magnetite, Pl = plagioclase, Ser = sericite, Zrn = zircon. See [Table 5.1](#) for sample locations and descriptions.

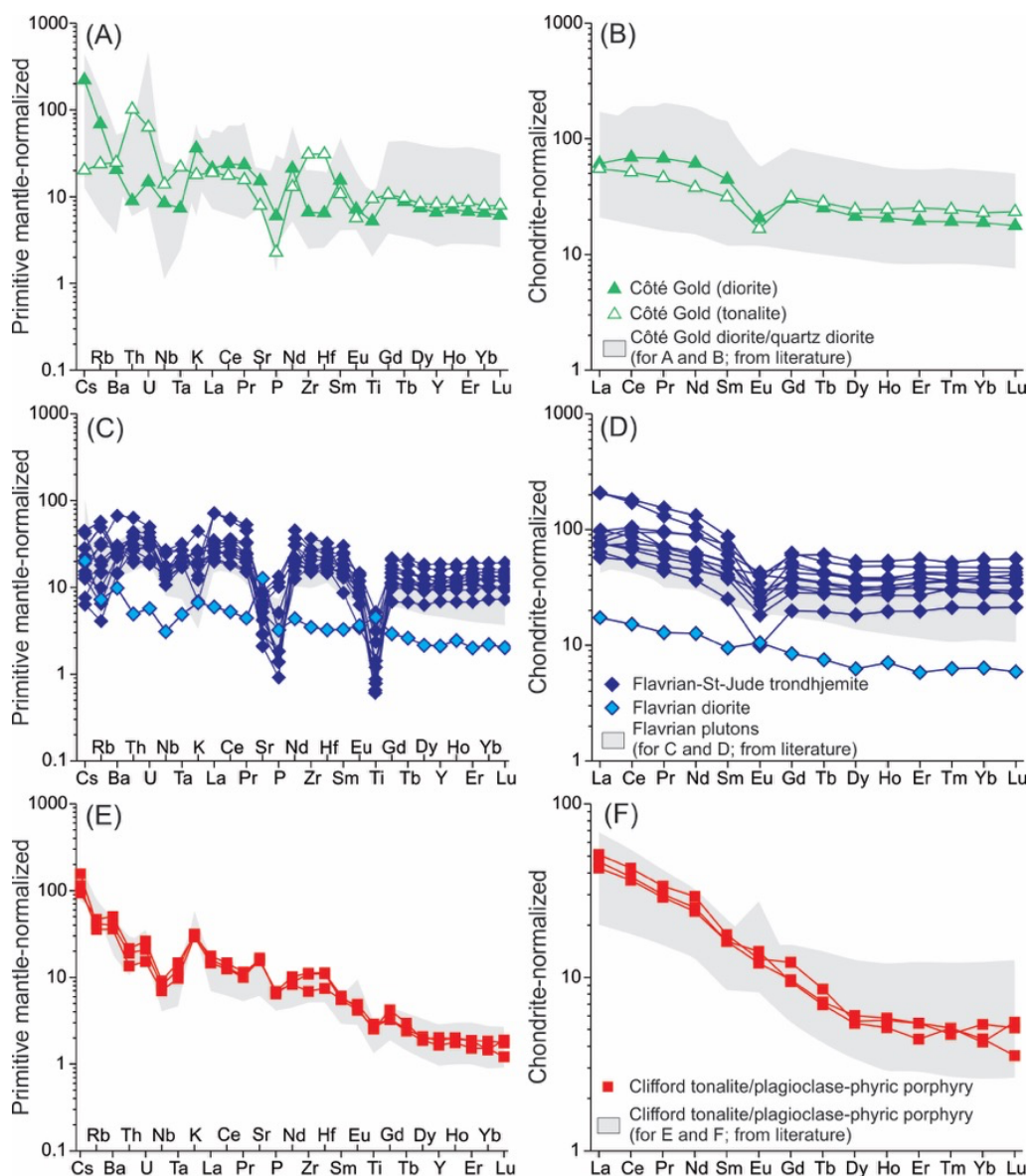


Figure 5.9. Primitive mantle-normalized trace element and chondrite-normalized rare earth element diagrams for the major igneous lithologies from Côté Gold, Flavrian-St-Jude, and Clifford in the southern Abitibi subprovince. (A, B) Côté Gold diorite (filled green triangle) compared with data for diorite and quartz diorite (in grey) from literature (Katz, 2016). One sample of tonalite is white-filled green triangle. (C, D) Flavrian-St-Jude diorite and trondhjemite compared with data (in grey) from literature (Galley, 2003). (E, F) Clifford tonalite and plagioclase-phyric porphyry (in red) compared with data (in grey) from literature (Piercey et al., 2008). Normalization values are from Sun and McDonough (1989).

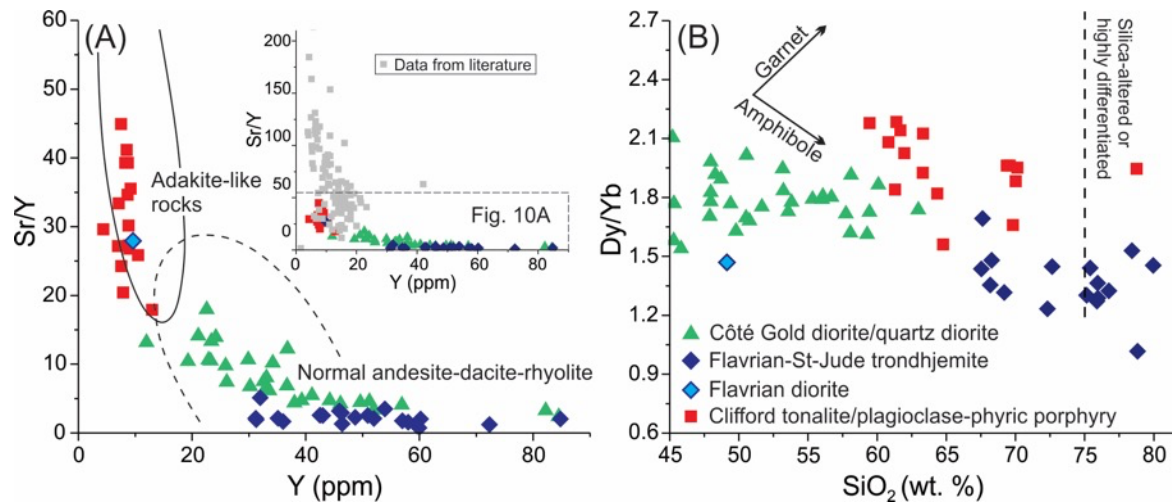


Figure 5.10. Trace element concentration and ratios for the major igneous lithologies from Côté Gold, Flavrian-St-Jude, and Clifford in the southern Abitibi subprovince.

(A) Sr/Y ratios versus Y (ppm) diagram. The compiled data are for igneous rocks associated with representative Phanerozoic porphyry Cu systems, including Bingham, Dexing, Escondida, Highland Valley, Red Chris, Red Diq, Oyu Tolgoi, and deposits in Chile (Richards et al., 2001; Wainwright et al., 2011; Richards et al., 2012; Hou et al., 2013; Richards et al., 2017; D'Angelo et al., 2017; Grondahl and Zajacz, 2017; Zhu et al., 2018).

(B) Dy/Yb ratios versus SiO₂ (wt. %) diagram. The 'adakite-like rocks' and 'normal andesite-dacite-rhyolite' zones in (A) are from Defant and Drummond (1990). The fractionation trends of garnet and amphibole during magma evolution in (B) are from Davidson et al. (2007).

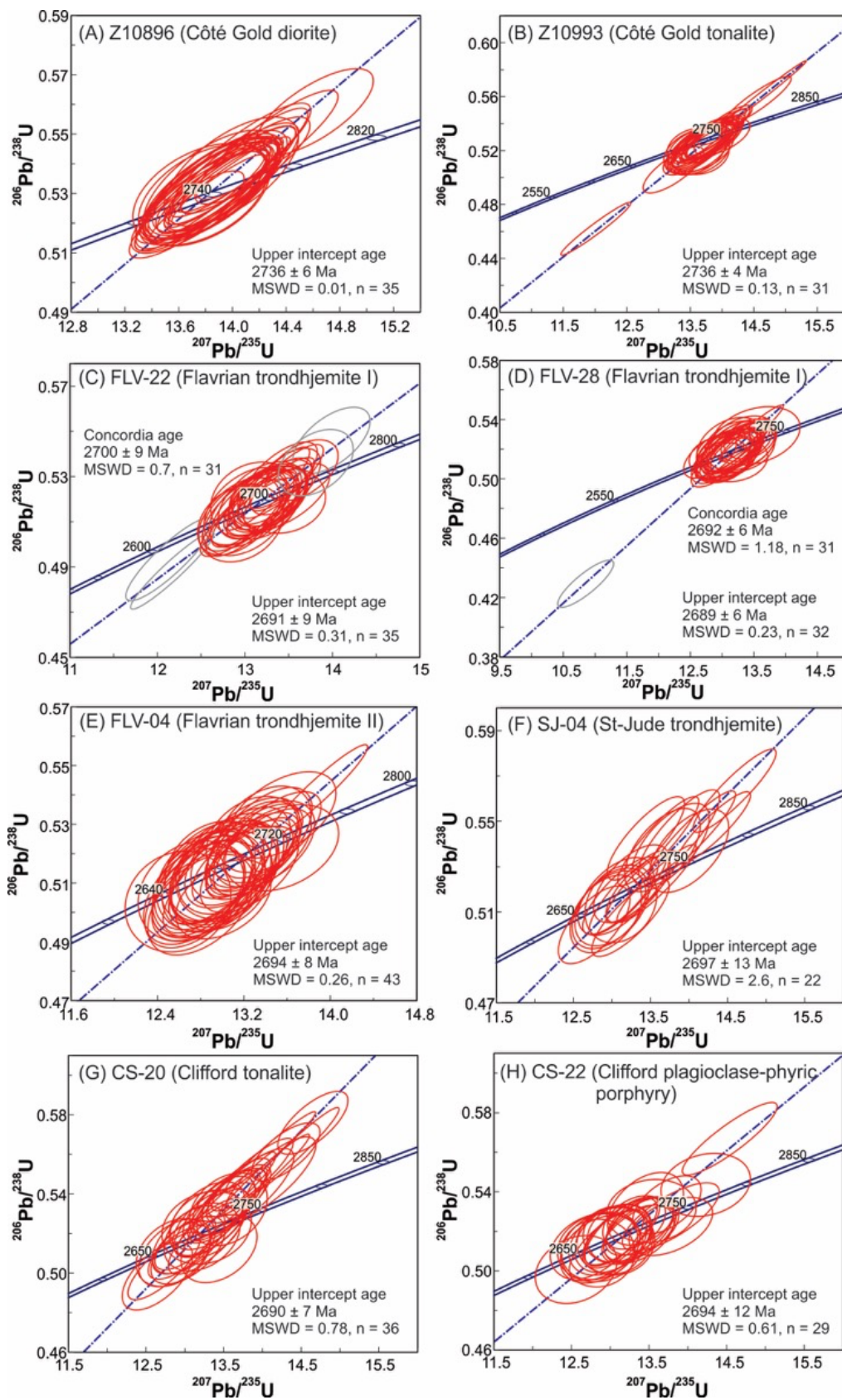


Figure 5.11. Zircon U-Pb concordia diagrams for the major igneous rock phases from Côte Gold, Flavrian-St-Jude, and Clifford in the southern Abitibi subprovince. Error ellipses are shown at 2σ . Upper concordia intercept or concordia ages are calculated to represent the crystallization ages of these rocks. (A) Côte Gold diorite (sample Z10896). (B) Côte Gold tonalite (sample Z10993). (C) Flavrian trondhjemite phase I (sample FLV-22). Four Pb-loss and reversely discordant analyses excluded for concordia age determination are indicated in grey ellipses. (D) Flavrian trondhjemite phase I (sample FLV-28). One Pb-loss analysis excluded for concordia age determination is indicated in a grey ellipse. (E) Flavrian trondhjemite phase II (sample FLV-04). (F) St-Jude trondhjemite (sample SJ-04). (G) Clifford tonalite (sample CS-20). (H) Clifford plagioclase-phyric porphyry (CS-22). Cathodoluminescence images of representative zircon grains are shown in [Figure A5.1](#). See [Table 5.1](#) for sample locations and descriptions.

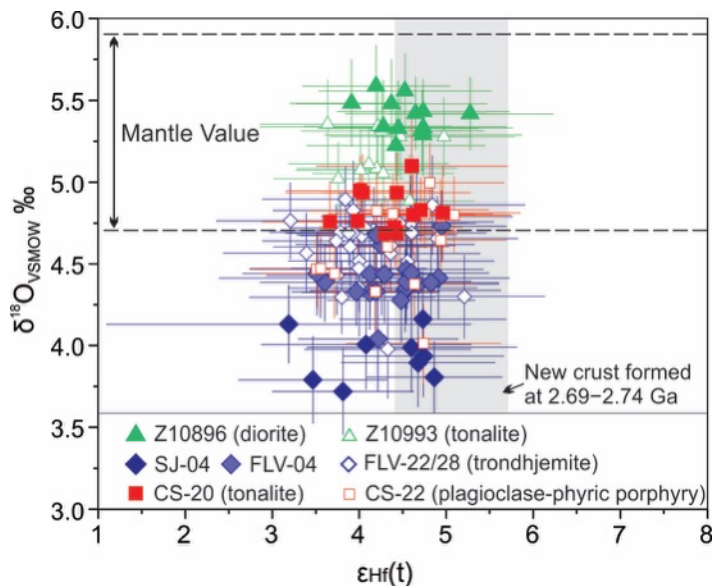


Figure 5.12. Zircon Hf-O isotopes for the major igneous rock phases from Côté Gold, Flavrian-St-Jude, and Clifford in the southern Abitibi subprovince. Error bars represent 2 standard errors. The zircon $\epsilon_{\text{Hf}}(t)$ value range for new crust formed at 2.69–2.74 Ga is calculated based on [Dhuime *et al.* \(2011\)](#). Oxygen isotope ratios are reported in the standard per mil (‰) relative to standard mean ocean water (VSMOW). The $\delta^{18}\text{O}$ isotope value range (5.3 ± 0.6 ‰, 2σ) for zircon in equilibrium with mantle is from [Valley *et al.* \(1998\)](#). See [Table 5.1](#) for sample locations and descriptions. Cathodoluminescence images of representative zircon grains are shown in [Figure A5.1](#).

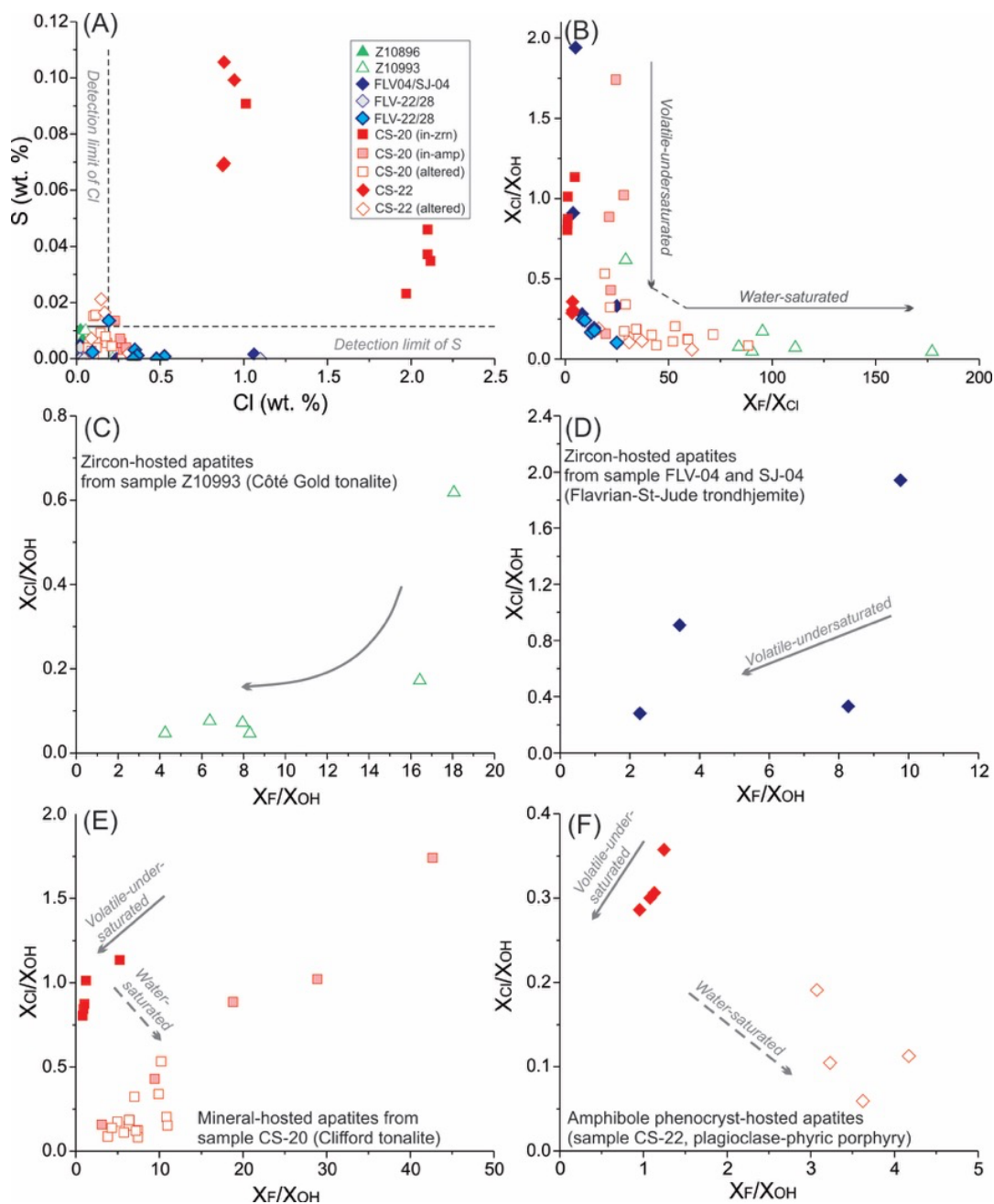


Figure 5.13. Plots of apatite volatile compositions for the major igneous rock phases from Côte Gold, Flavrian-St-Jude, and Clifford in the southern Abitibi subprovince. (A) S versus Cl abundances (wt. %). (B) X_{Cl}/X_{OH} versus X_F/X_{Cl} ratios. (C–F) X_{Cl}/X_{OH} versus X_F/X_{OH} ratios. The X_F , X_{Cl} , and X_{OH} represent mole fractions of F, Cl, and OH in apatite, respectively. The *volatile-undersaturated* and *water-saturated* trajectories in (b–f) are adapted from [Stock *et al.* \(2018\)](#). See [Table 5.1](#) for sample locations and descriptions.

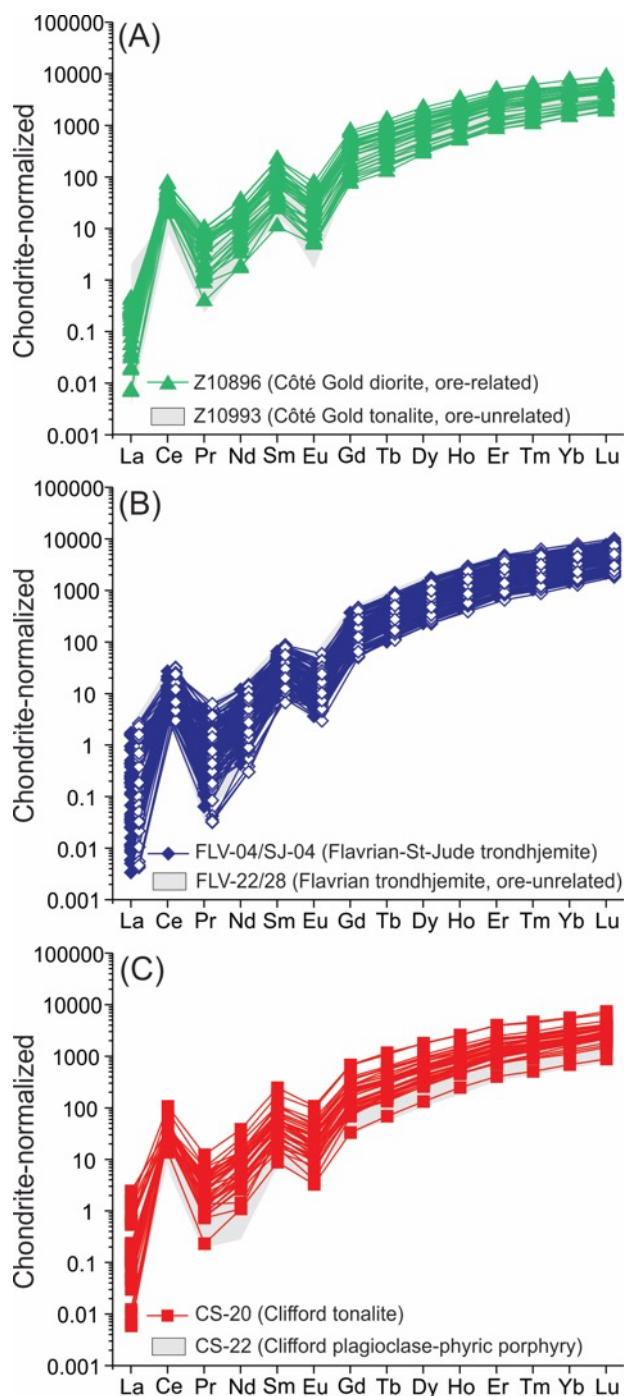


Figure 5.14. Chondrite-normalized rare earth elements for zircons from the major igneous rock phases from the study areas in the southern Abitibi subprovince. (A) Côté Gold diorite and tonalite; (B) Ore-related and ore-unrelated trondhjemites from Flavrian-St-Jude; (C) Clifford tonalite and plagioclase-phyric porphyry. Normalization values are from [Sun and McDonough \(1989\)](#).

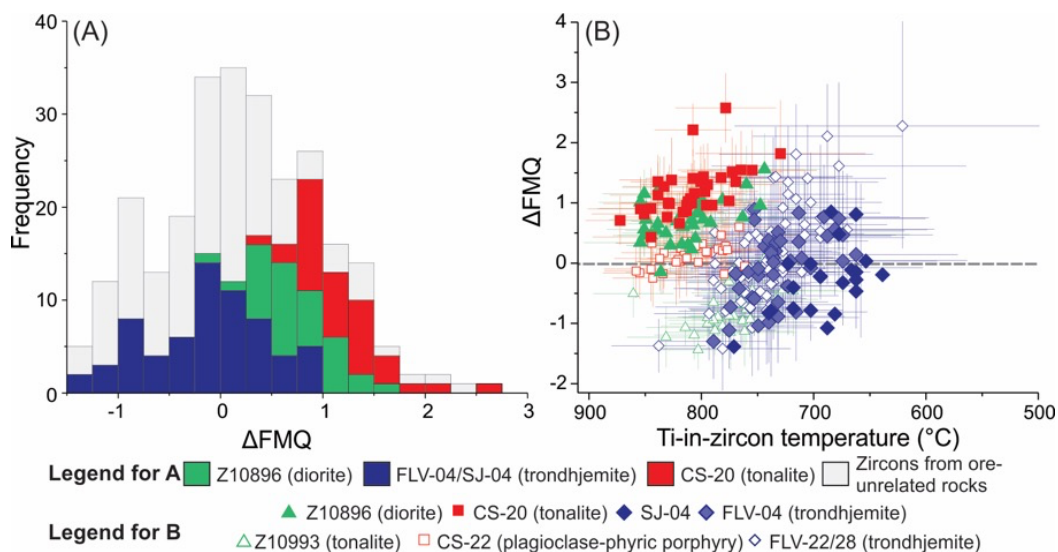


Figure 5.15. Histogram and plot of $T\text{-}f\text{O}_2$ values estimated from zircon geochemistry for the major igneous phases in Côté Gold, Flavrian-St-Jude, and Clifford in the southern Abitibi subprovince. (A) ΔFMQ histogram. (B) ΔFMQ versus Ti-in-zircon temperature ($T_{\text{Ti-Zr}}$). The ΔFMQ values and $T_{\text{Ti-Zr}}$ are calculated using methods of Loucks *et al.* (2020) and Ferry & Watson (2007), respectively. Error bars in (B) represent standard errors.

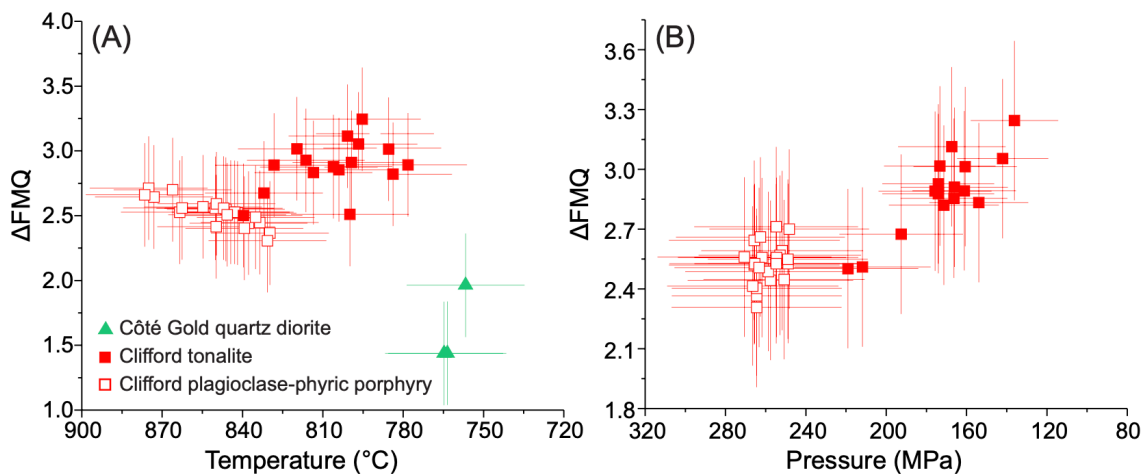


Figure 5.16. Plots for ΔFMQ values versus temperatures and/or pressures, as estimated from amphibole for the major igneous rock phases from Côte Gold and Clifford in the southern Abitibi subprovince. (A) ΔFMQ versus temperature. (B) ΔFMQ versus pressure. Error bars represent standard errors. The data for Côte Gold quartz diorite is from [Katz *et al.* \(2017\)](#). The ΔFMQ values and temperatures are calculated using the method of [Ridolfi *et al.* \(2010\)](#). Pressures are estimated using the method of [Mutch *et al.* \(2016\)](#).

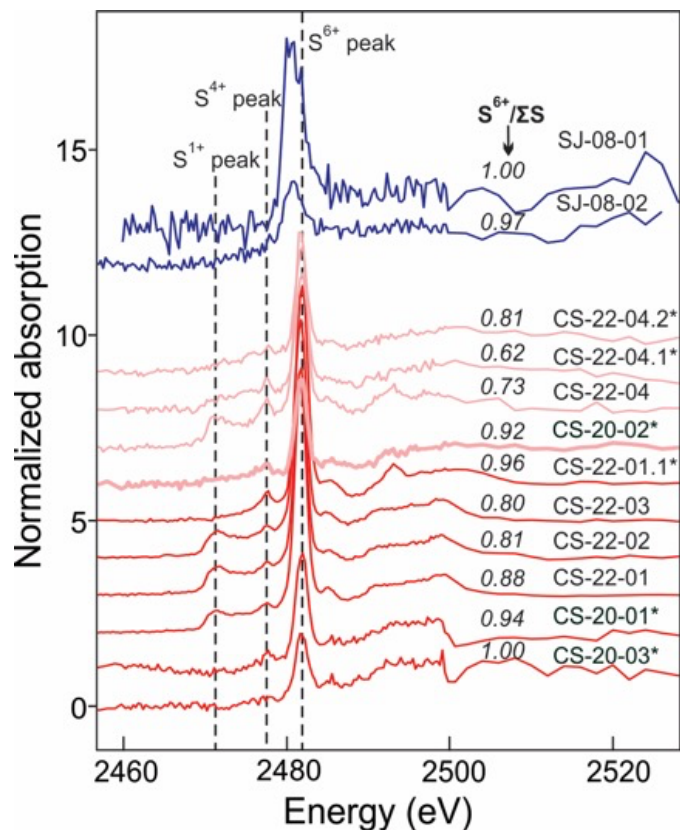


Figure 5.17. Apatite μ -XANES spectra at S K-edge for St-Jude trondhjemite (SJ-08), Clifford tonalite (sample CS-20) and plagioclase-phyric porphyry (sample CS-22). See Table 5.1 for sample locations and descriptions. The asterisks against the sample numbers indicate analyses conducted at APS, whereas the other analyses were conducted at SLS.

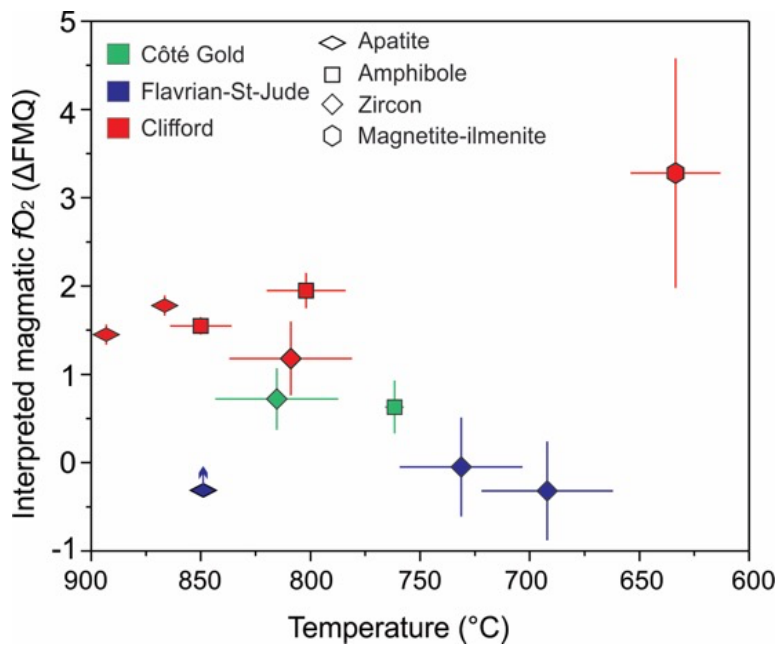


Figure 5.18. Summary of the interpreted fO_2 -T estimates using zircon, amphibole, apatite, and magnetite-ilmenite oxybarometers for the major igneous rock phases from Côte Gold, Flavrian-St-Jude, and Clifford in the southern Abitibi subprovince. The interpreted fO_2 result for amphibole is lower than the calculated value by one log unit. Error bars represent 1σ uncertainty.

5.15 Tables

Table 5.1. Locations and descriptions of representative igneous rock samples from the Côté Gold, Flavrian-St-Jude, and Clifford areas in the southern Abitibi subprovince

Sample	UTM (17U) and elevation	Rock type	Texture and dominant mineralogy (approximated volume percentage)	Zircon inclusion mineralogy
Z10896	429713E, 5266923N, 386 m	Diorite	Equigranular. Amp (~45 %, Act-altered), Pl (~50 %, Ser-altered), Ttn (~5 %), and minor Qtz.	No inclusions.
Z10993	429711E, 5266917N, 386 m	Tonalite	Equigranular. Pl (~50 %, partially Ser-altered), Qtz (~45–50 %), mafic mineral (Chl-Ep-Ttn-altered; ~5 %).	Ap, Qtz, Kfs, Ab, Mt.
FLV-32	634297E, 5346583N, 322 m	Gabbro	Equigranular. Amp (~60 %), Pl (~35 %; Ser-altered), and minor quartz (<5 %).	
FLV-22	631930E, 5355035N, 326 m	Trondhjemite-I	Equigranular. Qtz (~50 %), Pl (~50 %), minor Py.	Ap, Ab, Kfs, Qtz.
FLV-28	636535E, 5348252N, 311 m	Trondhjemite-I	Equigranular. Qtz (~50 %), Pl (~50 %), minor Chl.	Ap, Qtz, Ab, Kfs.
FLV-04	633312E, 5350516N, 339 m	Trondhjemite-II	Equigranular. Amp (~15 %), Qtz (~50 %), and Pl (~35 %, Ser-Ab-altered).	Ap, Qtz, Ab, Kfs, Pl, Cp.
SJ-04	631709E, 5352100N, 330 m	Trondhjemite	Equigranular. Pl (~60 %; Ser-Ep-Ab-altered), Qtz (25–30 %), minor Bt, Ep, Chl, and Cp (~2 %).	Ap, Qtz, Kfs, Ab, Ilm.
SJ-08	631727E, 5352149N, 327 m	Trondhjemite	Equigranular. Pl (~60 %; Ser-Ep-Ab-altered), Qtz (25–30 %), Chl (~10 %).	Ap, Qtz, Ttn.
CS-03	589354E, 5350566N, 364 m	Tonalite	Equigranular. Pl (~35 %), Qtz (~30 %), Amp (~30 %), Kfs (2–5 %).	
CS-07	589502E, 5350664N, 384 m	Tonalite	Equigranular. Pl (~30 %, partially Ser-altered), Qtz (30–35 %), Amp (~30 %), Kfs (2–5 %).	
CS-20	589295E, 5350924N, 326 m	Tonalite	Equigranular. Pl (~35 %, Ser-altered), Qtz (~30 %), Amp (~20–30 %, partially Chl-altered), Kfs (2–5 %), and Bt (<1%).	Qtz, Ab, Kfs, Ap.
CS-22	588929E, 5350439N, 323 m	Plagioclase-phyric porphyry	Porphyritic. Pl and rare Amp phenocrysts in groundmass of plagioclase (partially Ser-altered) with minor quartz.	Bt, Cpx, Kfs, Ttn, Ab, Qtz, Ap.

Abbreviations: Ab = albite, Act = actinolite, Amp = amphibole, Bt = biotite, Cp = chalcopyrite, Cpx = clinopyroxene, Ep = epidote, Ilm = ilmenite, Kfs = K-feldspar, Pl = plagioclase, Py = pyrite, Qtz = quartz, Ser = sericite, Ttn = titanite.

Table 5.2. Summary of zircon U-Pb-Hf-O isotopic and fO_2 -T estimation results for the Côté Gold, Flavrian-St-Jude, and Clifford rocks in the southern Abitibi subprovince

Sample	Location	Rock type	Zircon U-Pb-Hf-O isotopes			Mineral crystallization temperatures (°C, 1 σ)				Magmatic fO_2 values (ΔFMQ , 1 σ)			
			Age (Ma, 2 σ)	$\epsilon_{Hf}(t)$ (1 σ)	$\delta^{18}O$ (1 σ)	Zircon	Amphibole	Apatite	Magnetite-ilmenite	Zircon	Amphibole	Apatite	Magnetite-ilmenite
Z10896	Côté Gold	Diorite	2736 \pm 6	4.54 \pm 0.33	5.40 \pm 0.11	815 \pm 30		682			0.8 \pm 0.4		
Z10993	Côté Gold	Tonalite	2736 \pm 4	4.23 \pm 0.37	5.16 \pm 0.16	773 \pm 34		900			-0.7 \pm 0.4		
FLV-22	Flavrian	Trondhjemite-I	2700 \pm 9	4.16 \pm 0.45	4.70 \pm 0.10	746 \pm 33		854			0.07 \pm 0.6		
FLV-28	Flavrian	Trondhjemite-I	2692 \pm 6	4.10 \pm 0.48	4.41 \pm 0.18	730 \pm 37		900			0.4 \pm 1.0		
FLV-04	Flavrian	Trondhjemite-II	2694 \pm 8	4.35 \pm 0.39	4.41 \pm 0.15	731 \pm 30		926			-0.0 \pm 0.6		
SJ-04	St-Jude	Trondhjemite	2697 \pm 13	4.18 \pm 0.64	3.91 \pm 0.13	692 \pm 33		852			-0.3 \pm 0.6	>0.3	
CS-03	Clifford	Tonalite								634 \pm 21			3.3 \pm 1.3
CS-07	Clifford	Tonalite					802 \pm 18	850			2.9 \pm 0.2		
CS-20	Clifford	Tonalite	2690 \pm 7	4.35 \pm 0.37	4.83 \pm 0.12	809 \pm 30		866			1.2 \pm 0.4		1.78 \pm 0.02
CS-22	Clifford	Plagioclase-phyric porphyry	2694 \pm 12	4.41 \pm 0.49	4.61 \pm 0.25	810 \pm 27	850 \pm 14	893			0.2 \pm 0.2	2.6 \pm 0.1	1.34 \pm 0.10

Concluding Statements

6.1 Conclusions

Most known porphyry Cu \pm Au deposits formed in Phanerozoic arc-related settings, and older analogues in Precambrian terranes are rarely reported. This study focuses on documenting the rare reported porphyry Cu \pm Au deposits, constraining the nature of the causative magmas of selected mineralized settings, and resolving some relevant issues with respect to whether the metallogenic processes that typify Phanerozoic porphyry Cu \pm Au deposits also occurred in the Precambrian. The results of the deposit settings presented in this thesis have: (1) resolved the debate regarding the genesis of the ca. 2.1 Ga Tongkuangyu Cu deposit, China (porphyry-type versus sediment-hosted stratiform type), which indicate a causative magma chamber and related dikes or stocks need not always be apparent; (2) revealed that similar metallogenic processes that typify Phanerozoic porphyry Cu deposits have operated in late Paleoproterozoic based on investigating the ca. 1.88 Ga Haib setting in Namibia; and (3) suggested that formation of porphyry Cu \pm Au deposits in the Neoarchean Abitibi subprovince (Canada) did not necessarily require relatively oxidized sulfur-rich arc-type magmas.

The Tongkuangyu Cu deposit in the Trans-North China Orogen is mainly hosted by a 2181 ± 5 Ma intrusive complex comprising granodiorite and granodiorite porphyry that transects basaltic-andesitic sills and a poorly constrained, but older sequence of rhyolitic tuff. The volcanic and shallow plutonic host rocks, biotite \pm K-feldspar alteration, and chalcopyrite mineralization resemble porphyry Cu deposits, however, the mineralization was constrained to ~ 2.1 Ga, which is significantly younger than the host rocks. We were able to verify a ~ 2.09 Ga basaltic-andesitic

tuff sequence close to the Tongkuangyu deposit in a later study (Chapter 3), which indicates the presence of a presently unexposed causative magma chamber which exsolved hydrothermal fluids to form the Tongkuangyu deposit. Considering the age discordance between the host rocks and mineralization at Tongkuangyu, we consider an adapted model that suggest an exposed causative magma, as represented by immediately subjacent to porphyry stocks and dikes, need not be a prerequisite for all porphyry deposit settings.

The Haib porphyry Cu deposit in the Paleoproterozoic Richtersveld Magmatic Arc, Namibia, is interpreted as a mature island-arc setting. As it only records minimal deformation and relatively low-grade metamorphism, it provides an ideal setting to study ancient metallogenic processes. The absolute timing of emplacement of the causative magmas at Haib was constrained using high-precision zircon U-Pb geochronology to ca. 1886–1881 Ma. Whole-rock geochemistry and zircon Hf-O isotopes show that the magmas are derived from a shallow source dominated by amphibole \pm plagioclase fractionation and minimal crustal assimilation during magma ascent. We used multiple independent oxybarometers based on zircon geochemistry, S μ -XANES spectroscopy of apatite inclusions in zircons, and titanite + magnetite + quartz assemblage to reveal that the magmas were relatively oxidized. Finally, the relatively high S contents of apatite grains analyzed attest to high magmatic sulfur contents. The results are interpreted to indicate that moderately oxidized, sulfur-rich arc magma associated with porphyry Cu mineralization already existed in the late Paleoproterozoic and that the causative magmas were probably sourced from a mantle lithosphere modified by oxidized slab-derived fluids in the Paleoproterozoic.

Compared to the dominance of potassium-enriched granite-granodiorite suites in post-Archean upper continental crusts, the intrusive rocks in the Archean are mainly sodium-enriched tonalite-

trondhjemite-granodiorite-diorite (TTG) suites. It is hypothesized that these sodium-enriched rocks are relatively reduced (i.e., unoxidized) and sulfur-poor which prevented porphyry Cu deposit formation. To test this model, we examined the nature of the causative magmas for Côte Gold, St-Jude, and Croxall porphyry-type Cu \pm Au deposits reported in the Neoproterozoic southern Abitibi greenstone belt. Zircon Hf-O isotopes reveal that the causative sodium-enriched magmas for the mineralization are sourced from mantle with minimal crustal assimilation, although for the St-Jude and Croxall settings the magmas or the sources may have experienced variable modification by high-temperature seawater or meteoric fluids. Whole-rock geochemistry indicates the magmas formed along plagioclase- to amphibole-dominated fractionation trends. To estimate fO_2 values for the causative magmas, we analyzed the compositions of primary barometric minerals (i.e., zircon, amphibole, apatite, and magnetite-ilmenite) which are inferred from petrographic study to have survived metamorphism and alteration. The results suggest that the Côte Gold and Croxall deposits formed from mildly ($\sim\Delta FMQ +0.6-0.7$) to moderately ($\sim\Delta FMQ +1.5$) oxidized magmas, whereas the St-Jude deposit formed from the relatively reduced and metal-poor magma ($\sim\Delta FMQ +0$) and that external high-temperature hydrothermal fluids might develop metal fertility.

Three main conclusions have been made from the above studies: (1) the Tongkuangyu Cu deposit in the Trans-North China Orogen is a porphyry-type deposit. Importantly its formation did not require a causative magma chamber immediately subjacent to the mineralized porphyritic dikes; (2) the metallogenic processes that typify Phanerozoic porphyry Cu deposits, such as their exclusive association with oxidized sulfur-rich arc magmas, have existed since at least the Paleoproterozoic; (3) The porphyry-type Cu \pm Au deposits reported in the Neoproterozoic southern Abitibi subprovince are associated with sodium-rich, tonalite-trondhjemite-granodiorite-dioritic

magmas with variable fO_2 values, therefore demonstrating variable formation modes of these deposits. These variable formation modes of these deposits lead us to conclude that the rarity of porphyry Cu \pm Au deposits in the Archean may be attributed to a more complex factors, such as local restriction of these favorable metallogenic processes, exploration bias, or preservation bias towards vertical tectonics.

6.2 Future Work

One of main objectives of this Ph.D. project was to constrain the nature of the causative magmas (e.g., fO_2 and volatile element abundances) for the porphyry Cu \pm Au deposits reported in the Archean and Paleoproterozoic terranes. The completed studies suggest: (1) similar metallogenic processes typify Phanerozoic porphyry Cu systems operated since at least the late Paleoproterozoic; and (2) there may be variable formation modes for porphyry Cu \pm Au deposits in the Neoproterozoic. However, the extent of magmas favorable for porphyry Cu \pm Au deposit formation in the Precambrian remains unclear. Thus, resolving this issue will greatly improve our understanding as to the exact cause of the apparent rarity of porphyry Cu \pm Au deposits in the Precambrian. In addition, the presented constraints of fO_2 and volatile contents rely mainly on indirect geochemical and mineralogical methods, direct measurements of pre-eruptive compositions using zircon-hosted melt inclusions for the causative magmas are likely a very worthwhile area to be investigated.

Appendix A (Additional Figures)

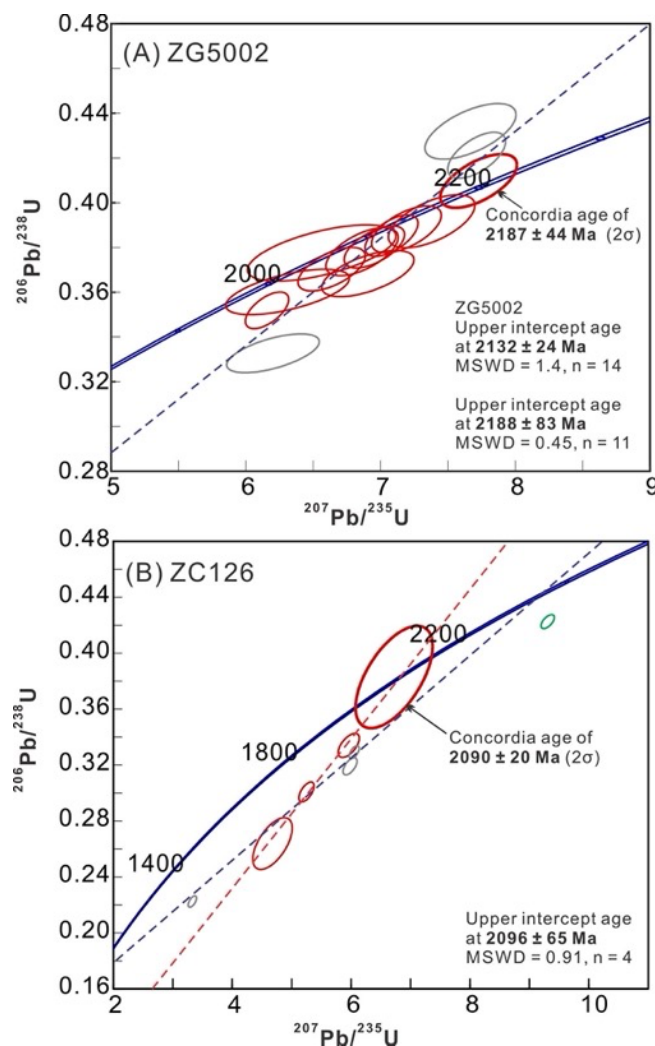


Figure A2.1. Zircon U-Pb data, recalculated from [Sun and Hu \(1993\)](#). (A) sample ZG5002 (meta-rhyolitic tuff from the Jiangxian Group), and (B) sample ZC126 (meta-dacitic tuff from the Zhongtiao Group). Grey ellipse represents the highly discordant or reversely discordant analysis, and blue ellipse represents the analysis of an inherited zircon aliquot. (A–B) Sample R4B5, showing possible tuffaceous bedding textures; cross-polarized and plane-polarized light. (C–D) Sample R4B10, showing possible relict volcanic textures; cross-polarized and plane-polarized light. Abbreviations: Qtz = quartz, Ser = sericite. See [Table A2.2](#) for sample locations and descriptions.

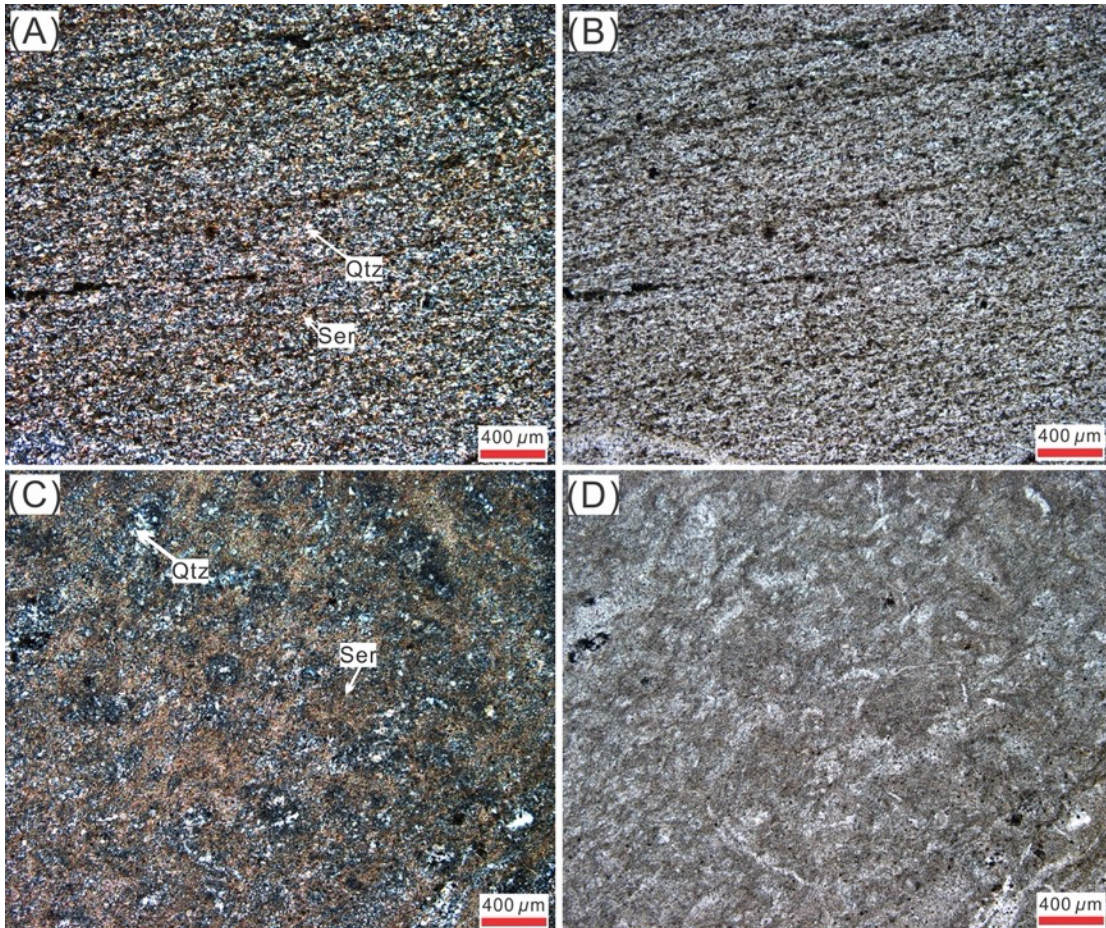


Figure A2.2. Photomicrographs of relatively unaltered quartz-sericite schist collected from outcrops of the Luotuofeng Formation, 5 km northeast of Tongkuangyu.

The minerals in (D) are identified using their elemental components. Abbreviations and colors in (D): Ab = albite (grey), All = allanite (red), Ap = apatite (green), Bt = biotite (turquoise), Cp = chalcopyrite (white), Kfs = K-feldspar (blue), Mt = magnetite (pink), Py = pyrite, Qtz = quartz (dark blue), Ser = sericite. See [Table A2.2](#) for sample locations and descriptions.

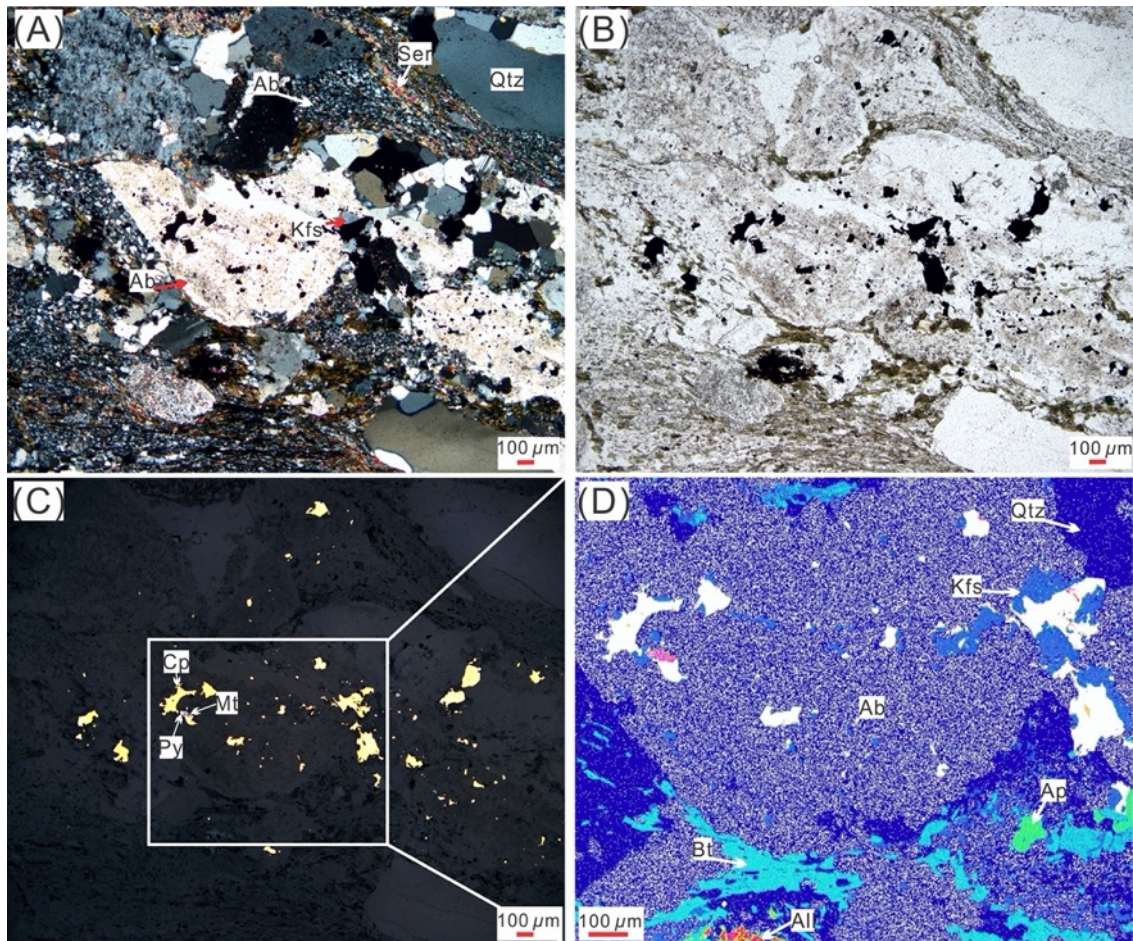


Figure A2.3. Secondary K-feldspar associated with chalcopyrite overprinting on the albite phenocryst in granodiorite porphyry (sample R3B14); (A) cross-polarized light; (B) plane-polarized light; (C) reflected light; (D) false-color SEM image.

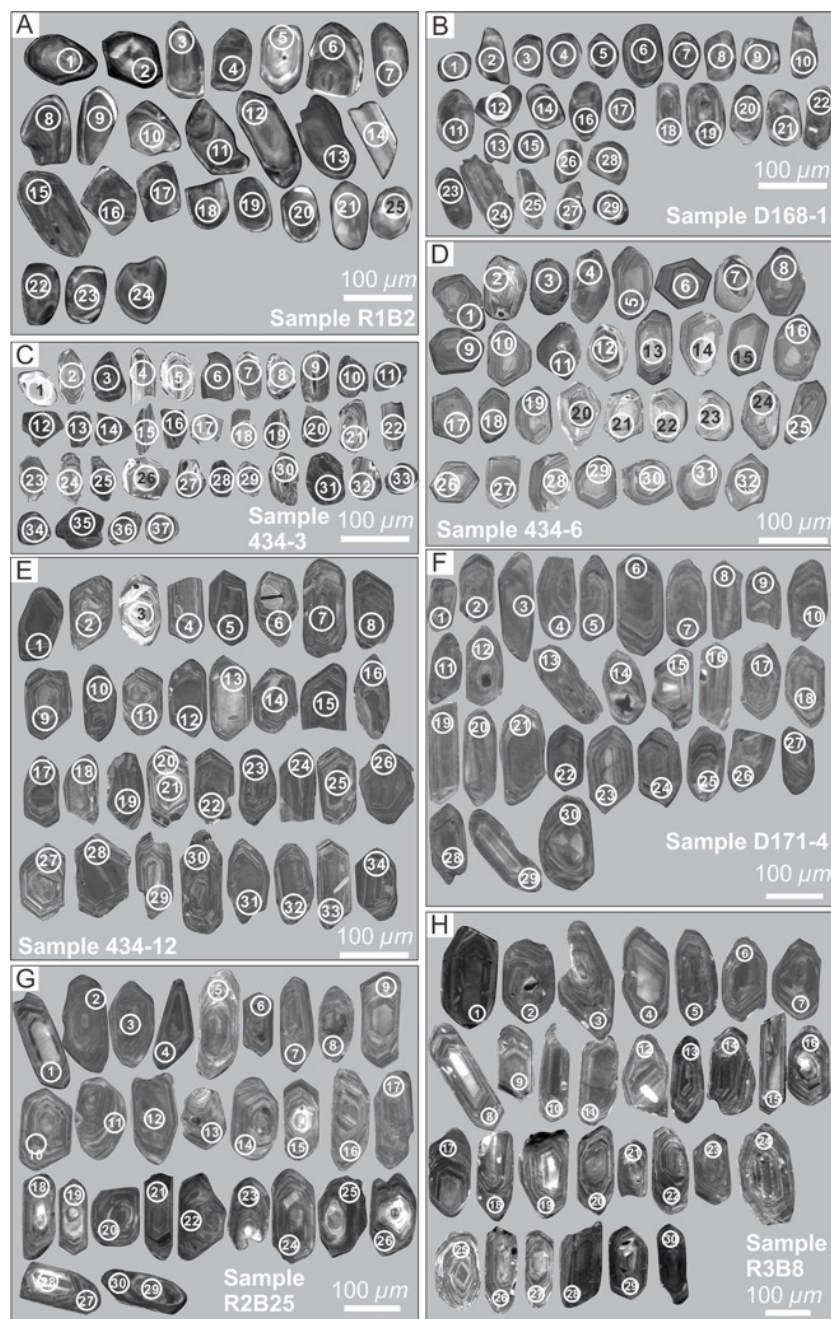


Figure A2.4. Cathodoluminescence images showing zircon grains for U-Pb analyses from (A) quartz-sericite schist (sample R1B2), (B) quartz-rich quartz-sericite schist (sample D168-1), (C) biotite schist (sample 434-3), and (D–H) granodiorite porphyry and granodiorite (samples 434-6, 434-12, D171-4, R2B25, and R3B8-2). White circles represent spot locations for U-Pb analyses, with analysis numbers annotated.

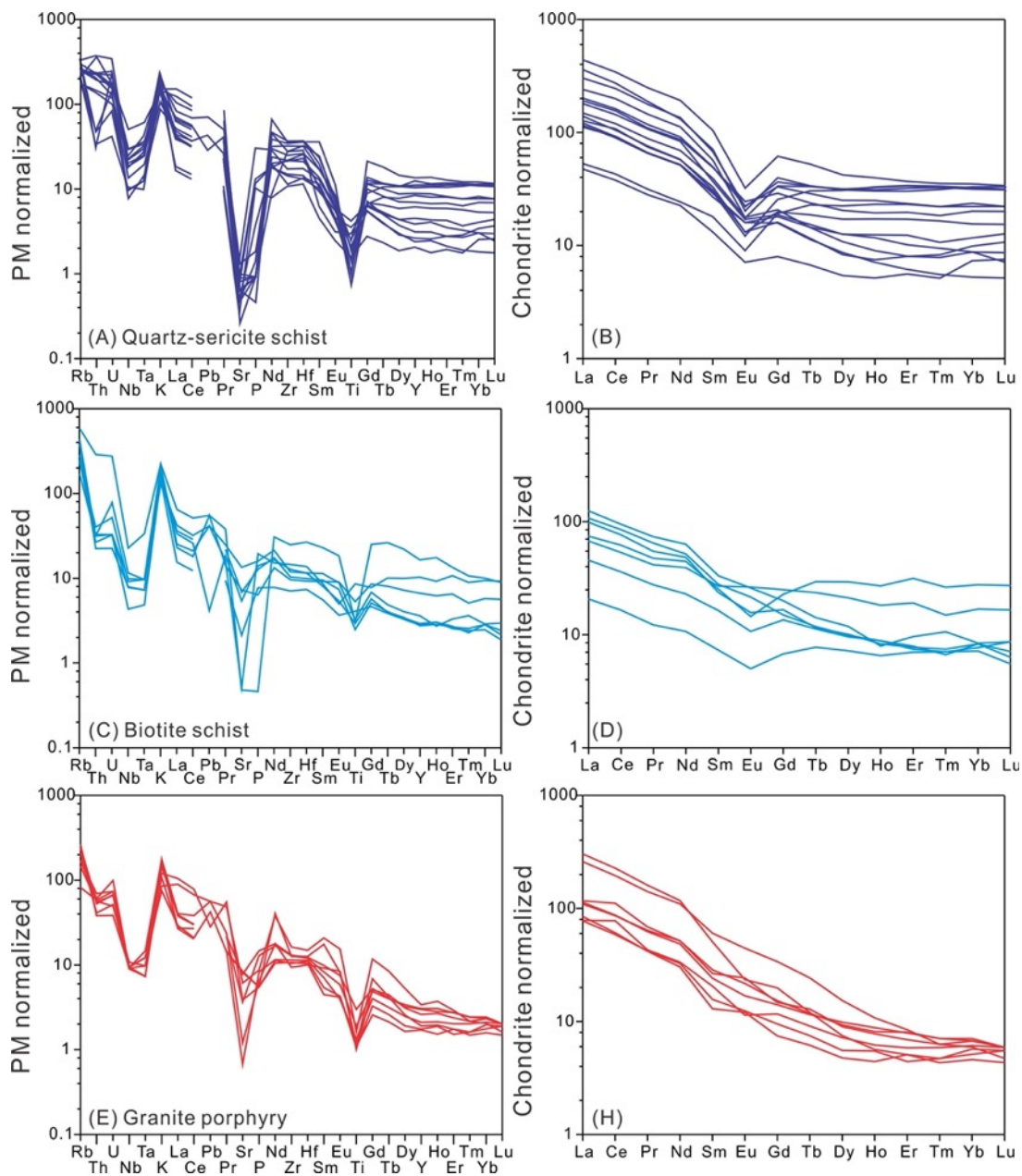


Figure A2.5. Primitive mantle- and chondrite-normalized trace element diagrams for (A–B) quartz-sericite schist, (C–D) biotite schist, and (E–F) granodiorite porphyry. Normalization values are from [Sun and McDonough \(1989\)](#).

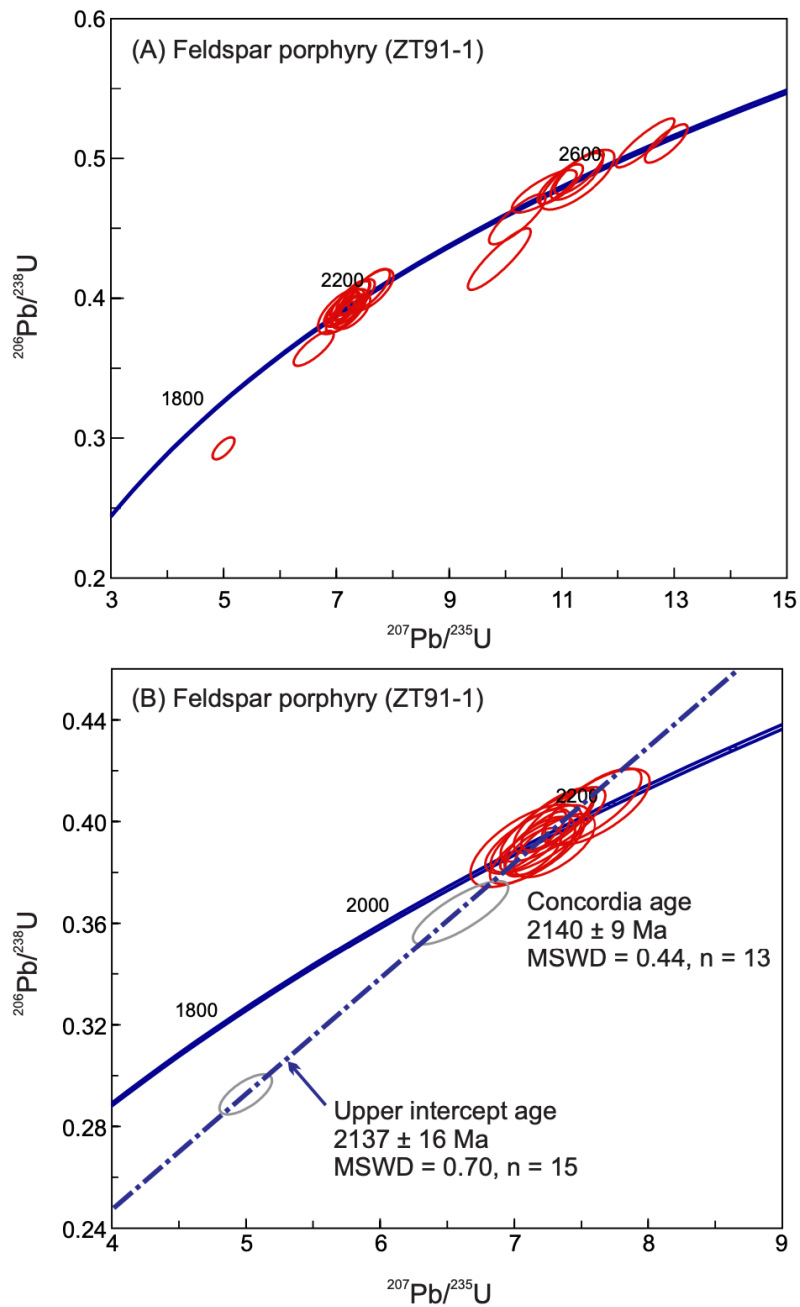


Figure A3.1. Zircon U-Pb concordia diagrams for sample ZT91-1 (feldspar porphyry) from the lower part of the Zhongtiao Group, northern Zhongtiaoshan region. Error ellipses are shown at 2σ . See sample location in [Fig. 3.1B](#).

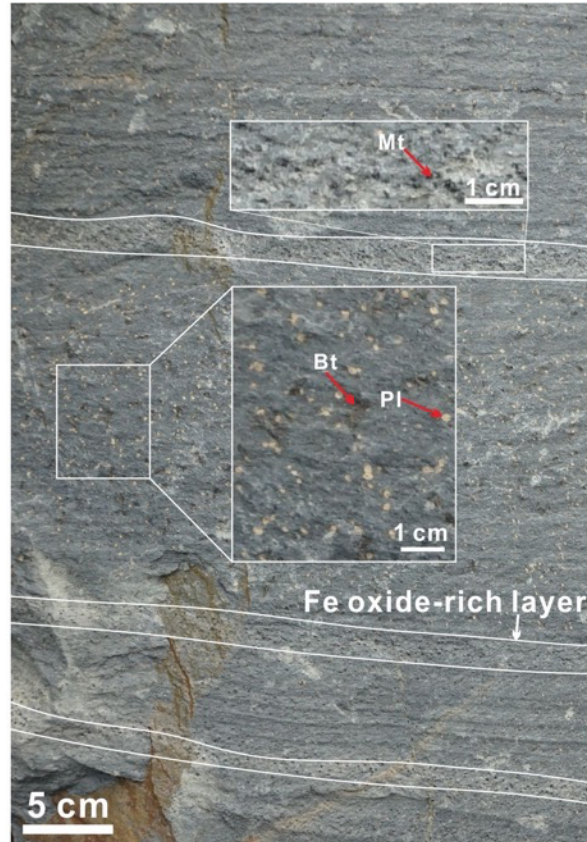


Figure A3.2. Outcrop photograph of layered albite-chlorite-sericite schist rock from the bottom of the Bizigou Formation of the Zhongtiao Group in the northern Zhongtiaoshan region (35°19'37.2''N, 111°37'16.4''E, 700 m). As discussed in the text, these are interpreted as bedded basaltic or andesitic volcanic tuffs. Inset images are enlarged parts of the outcrop.

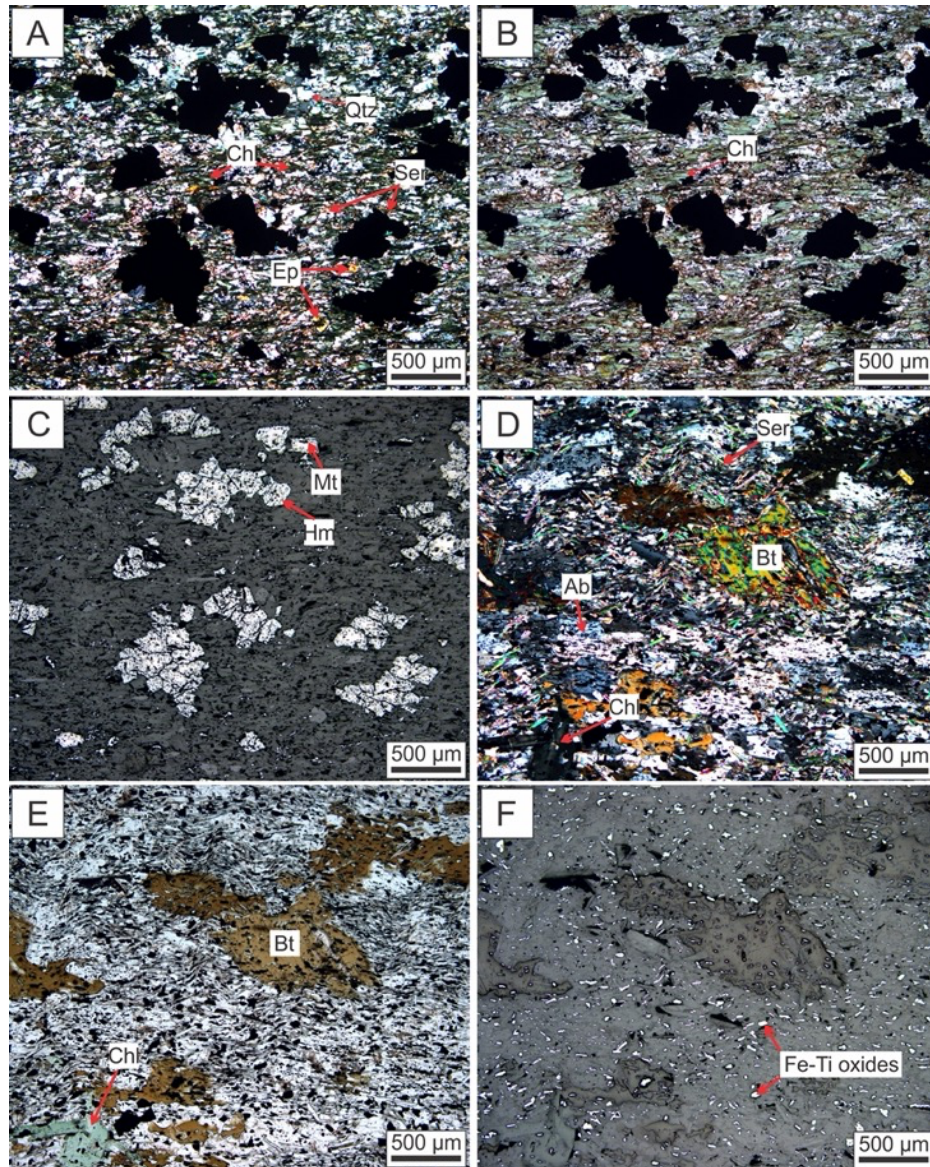


Figure A3.3. Photomicrographs of the albite-chlorite-sericite schist (i.e., basaltic to andesitic volcanic tuffs) samples collected from the bottom of the Bizigou Formation in the northern Zhongtiaoshan region. (A–C) Sample 19V05 with magnetite clasts (note secondary hematite rim); cross-polarized light, plane-polarized light, and reflected light. (D–F) Sample 19V08 with biotite clasts or phenocrysts; cross-polarized light, plane-polarized light, and reflected light. Abbreviations: Ab = albite, Bt = biotite, Chl = chlorite, Ep = epidote, Hm = hematite, Mt = magnetite, Ser = sericite.

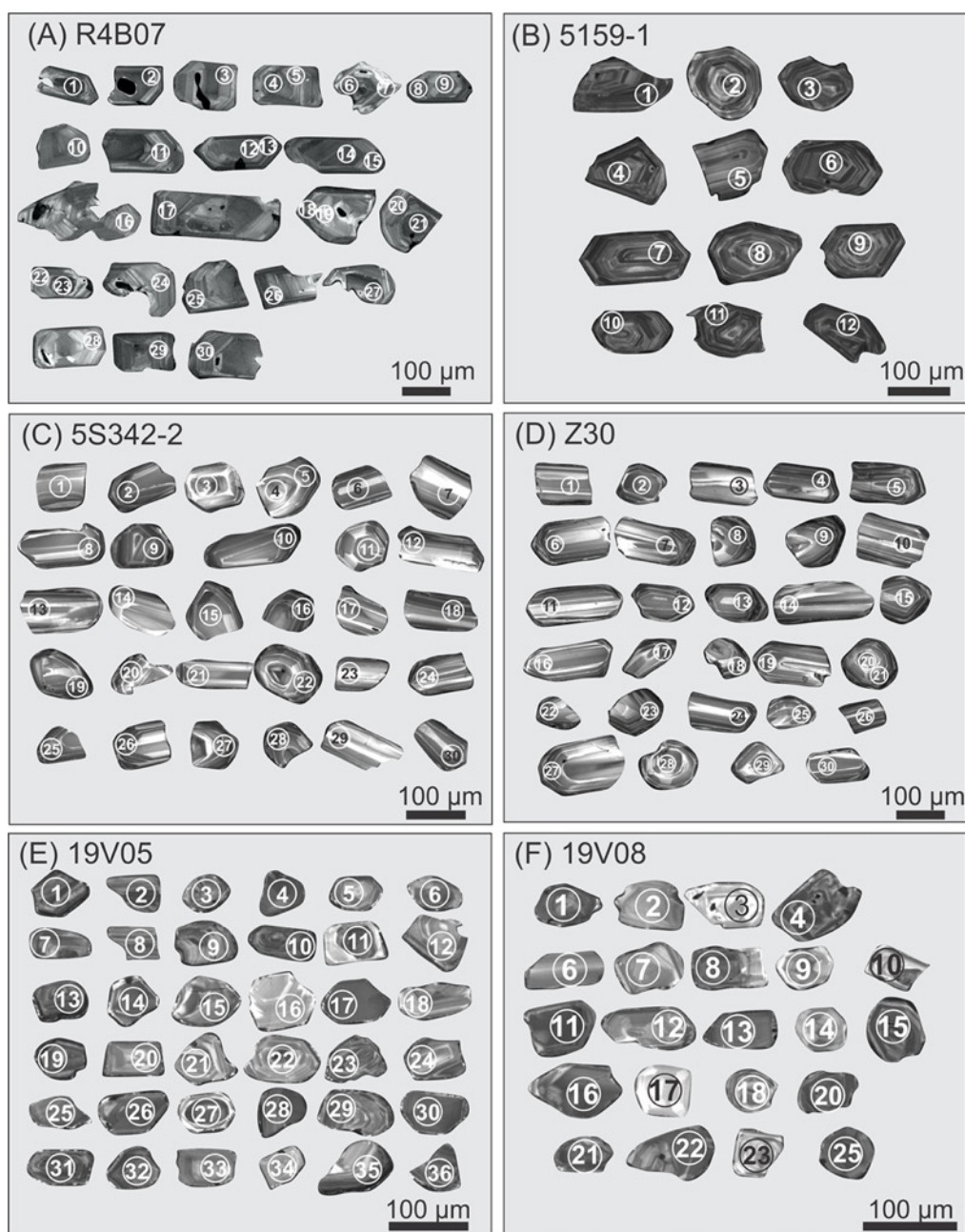


Figure A3.4. Cathodoluminescence (CL) images of the zircon grains analyzed for U-Pb dating from (A) rhyolitic tuff (sample R4B07), (B–D) granodiorite (samples 5159-1, 5S342-2, and Z30), (E, F) albite-chlorite-sericite schist (i.e., basaltic–andesitic volcanic tuffs; samples 19V05 and 19V08). See [Table 3.2](#) for sample locations and descriptions. The circles represent spot locations for U-Pb isotope analyses, with analysis numbers marked.

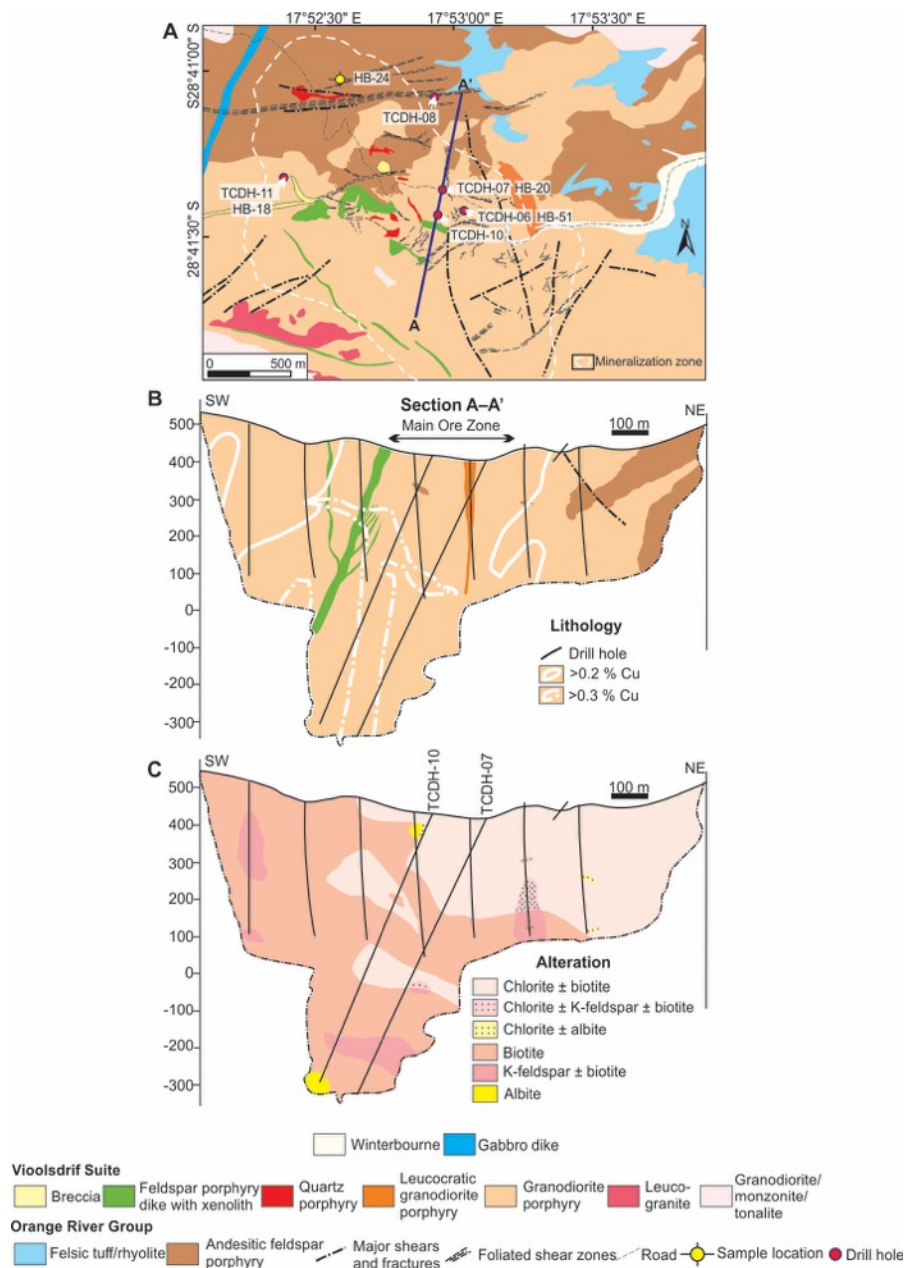


Figure A4.1. Geological map and cross section of the Haib deposit. (A) Geological map of the Haib deposit, showing lithological units and their geometry, modified from Minnitt (1986). The defined mineralization zone is made by Deep South Resources, Inc.. (B) cross section of lithology and Cu-grade contours, (C) cross section of alteration. Location of the section shown in Fig. A4.1A. The cross sections were modified from the Deep South Resources, Inc. (unpublished report).

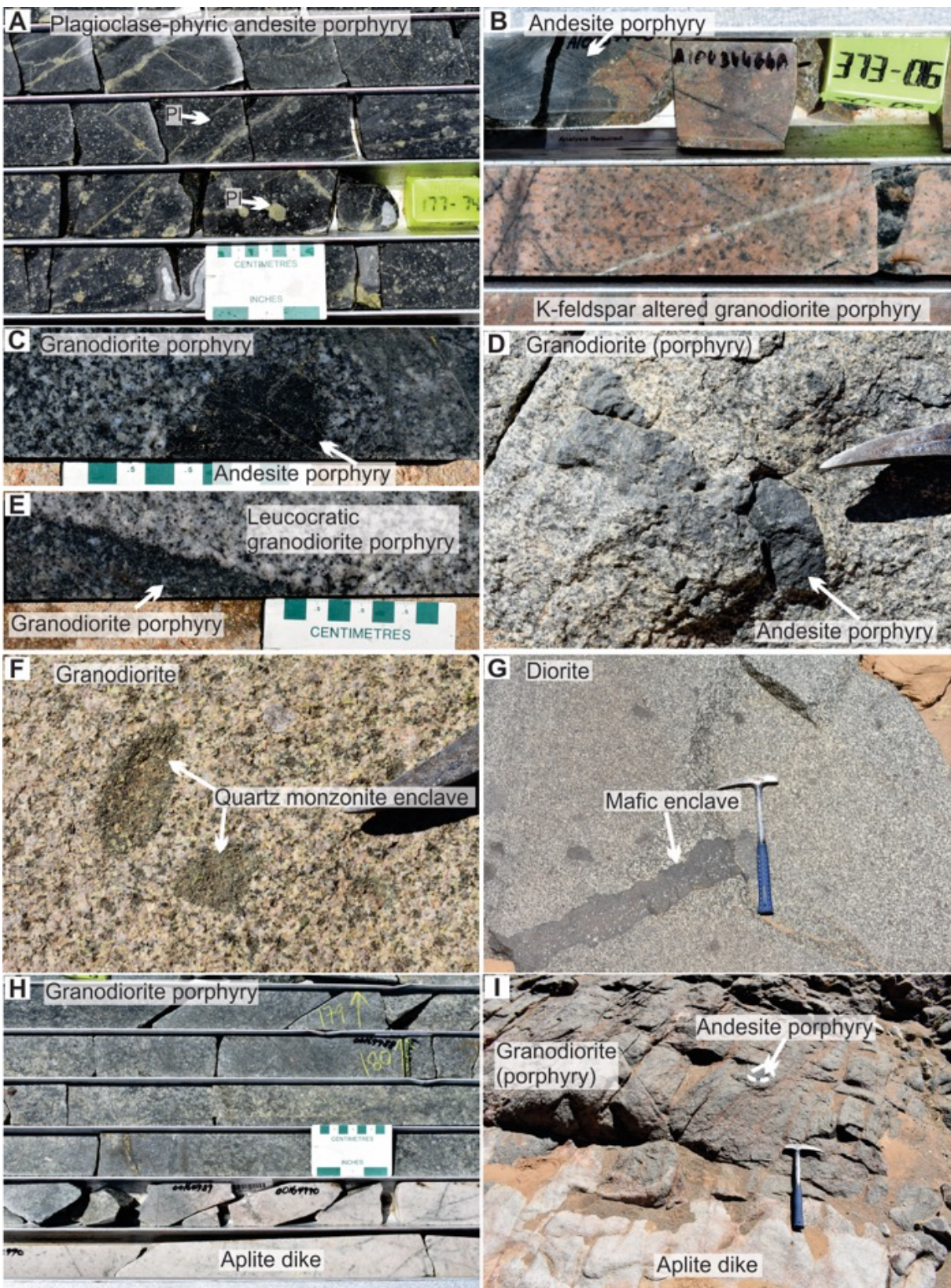


Figure A4.2. Drill core and field photographs of igneous rocks in the Haib area.

(A) Plagioclase-phyric andesite porphyry with epidote-altered plagioclase phenocrysts (TCDH-08, 173.7–180.1 m). (B) Andesite porphyry intruded by granodiorite porphyry with quartz phenocrysts (K-feldspar altered and hematite stained; TCDH-11, 373 m). (C) Granodiorite porphyry with xenolith of andesite porphyry (TCDH-06, 741–741.2 m). (D) Plagioclase-phyric andesite porphyry xenolith in granodiorite porphyry (UTM 33J 0781257 6823338, 452 m, WGS 84 datum). (E) Leucocratic granodiorite porphyry dike in granodiorite porphyry (TCDH-06, 742–742.3 m). (F) Granodiorite in batholith and its quartz monzonite enclave (UTM 33J 0783664 6827781, 369 m). (G) Diorite in the batholith with xenolith of mafic to ultramafic composition (UTM 33J 0785311 6827730, 232 m). (H) Aplite dike cutting the granodiorite porphyry (chlorite-altered; TCDH-07, 182–183 m). (I) Aplite dike cutting the granodiorite (porphyry) with plagioclase-phyric andesite porphyry xenolith (UTM 33J 0781257 6823338, 452 m). Abbreviations: Pl = plagioclase. Drill hole collar locations can be seen in [Table A4.1](#).

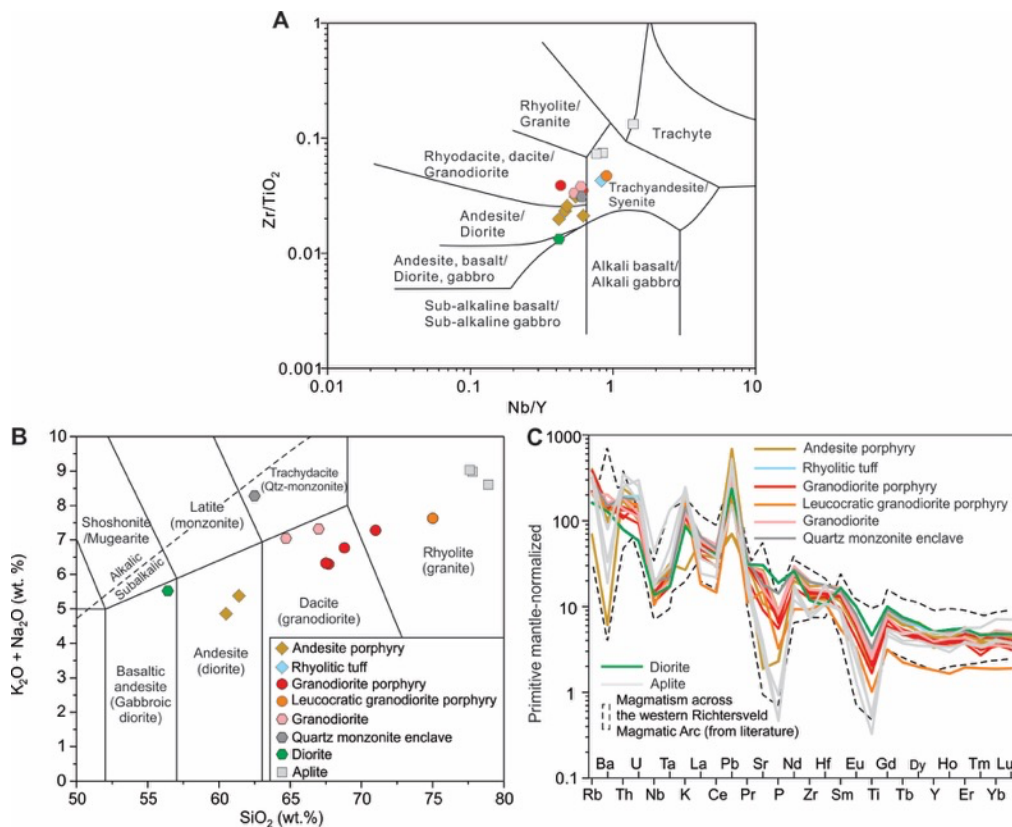


Figure A4.3. Summary of whole-rock geochemistry of the igneous rocks from Haib and the western Richtersveld Magmatic Arc. (A) Zr/TiO_2 versus Nb/Y discrimination diagram (Winchester and Floyd, 1977) for the major rock types from Haib. (B) Total alkali-silica diagram (Le Maitre, 1989) for the major rock types from Haib (samples with LOI > 2 wt. % were excluded). The alkali/subalkalic boundary line is from Irvine and Baragar (1971). (C) Primitive mantle-normalized trace-element spider diagram. The normalization values for (C) are from Sun and McDonough (1989). Data for the igneous rocks from the western Richtersveld Magmatic Arc were compiled in Macey et al. (2017).

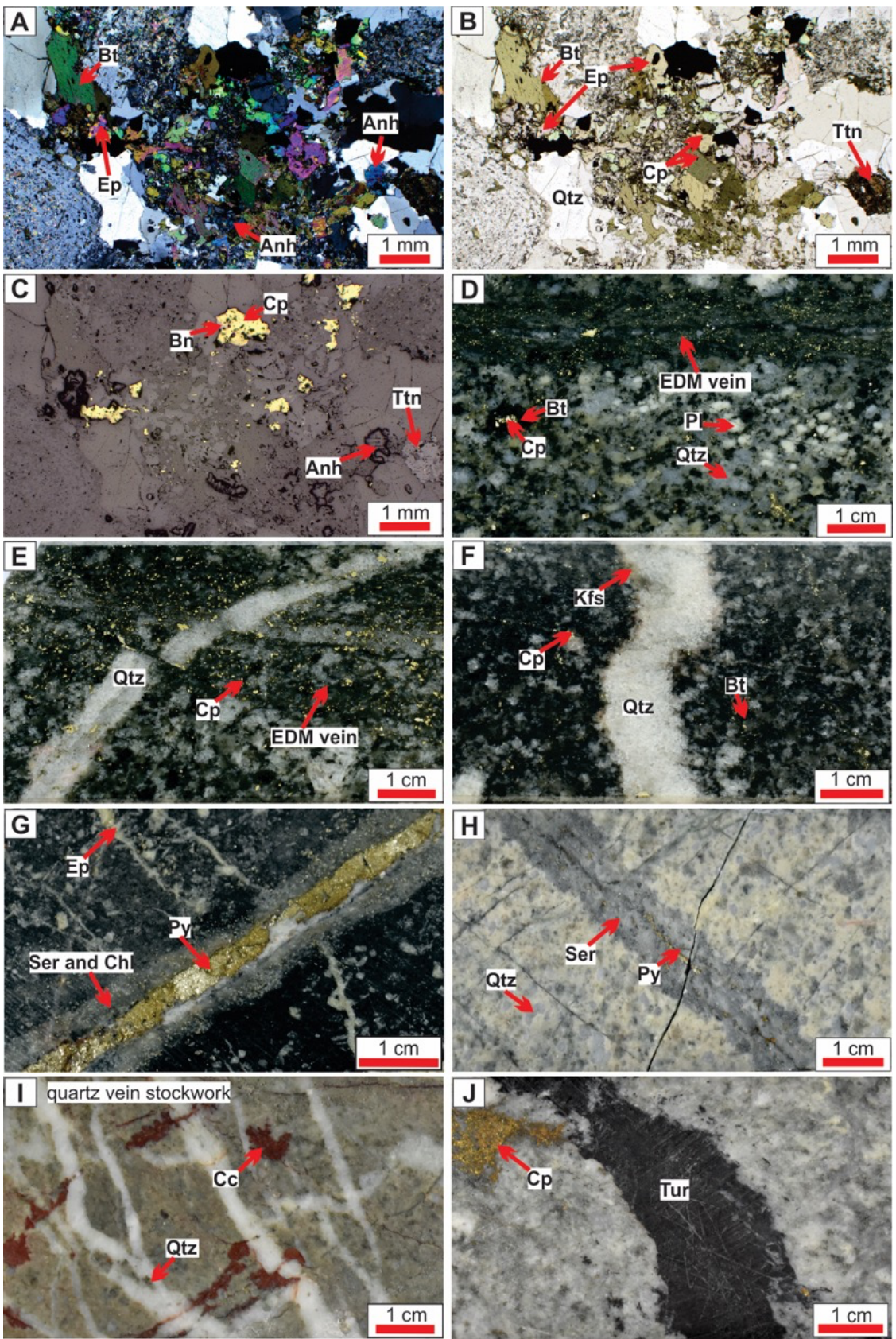


Figure A4.4. Photographs and photomicrographs of alteration and vein types.

(A–C) Biotite ± epidote ± anhydrite ± titanite alteration associated with chalcopyrite ± bornite mineralization in granodiorite porphyry (sample HB-53; TCDH-06, ~749.8 m); (A) thin section cross-polarized, (B) plane-polarized, and (C) reflected light. (D) Granodiorite porphyry with early dark micaceous (EDM) alteration selvage and disseminated chalcopyrite mineralization (sample HB-43, TCDH-10, ~365 m). (E) EDM vein crosscut by A-type quartz vein in the granodiorite porphyry (TCDH-06, ~755 m). The A-type quartz vein is offset by a fracture. (F) Sigmoidal A-type quartz vein with minimal sulfide mineralization and minor K-feldspar along margin in biotite-altered granodiorite porphyry (TCDH-06, below 755 m). (G) Pyritic D-vein with sericite-chlorite alteration halo in the epidote-altered plagioclase-phyric andesite porphyry (TCDH-08, ~175 m). (H) Pyritic D-vein with sericite alteration halo in granodiorite porphyry (TCDH-11, ~377 m). (I) Quartz vein stockwork in granodiorite porphyry (TCDH-06, 762.5–762 m) with high-Cu grade (1.2–1.4 % Cu), possibly reflecting oxidation and formation of secondary chalcocite. (J) Tourmaline vein in sericite-altered granodiorite porphyry (sample HB-49, TCDH-06, ~606 m). Abbreviations: Anh = anhydrite, Bn = bornite, Bt = biotite, Cc = chalcocite, Chl = chlorite, Cp = chalcopyrite, Ep = epidote, Kfs = K-feldspar, Py = pyrite, Qtz = quartz, Ser = sericite, Ttn = titanite, Tur = tourmaline. See drill hole collar location in [Table A4.1](#) and [Fig. A4.1](#).

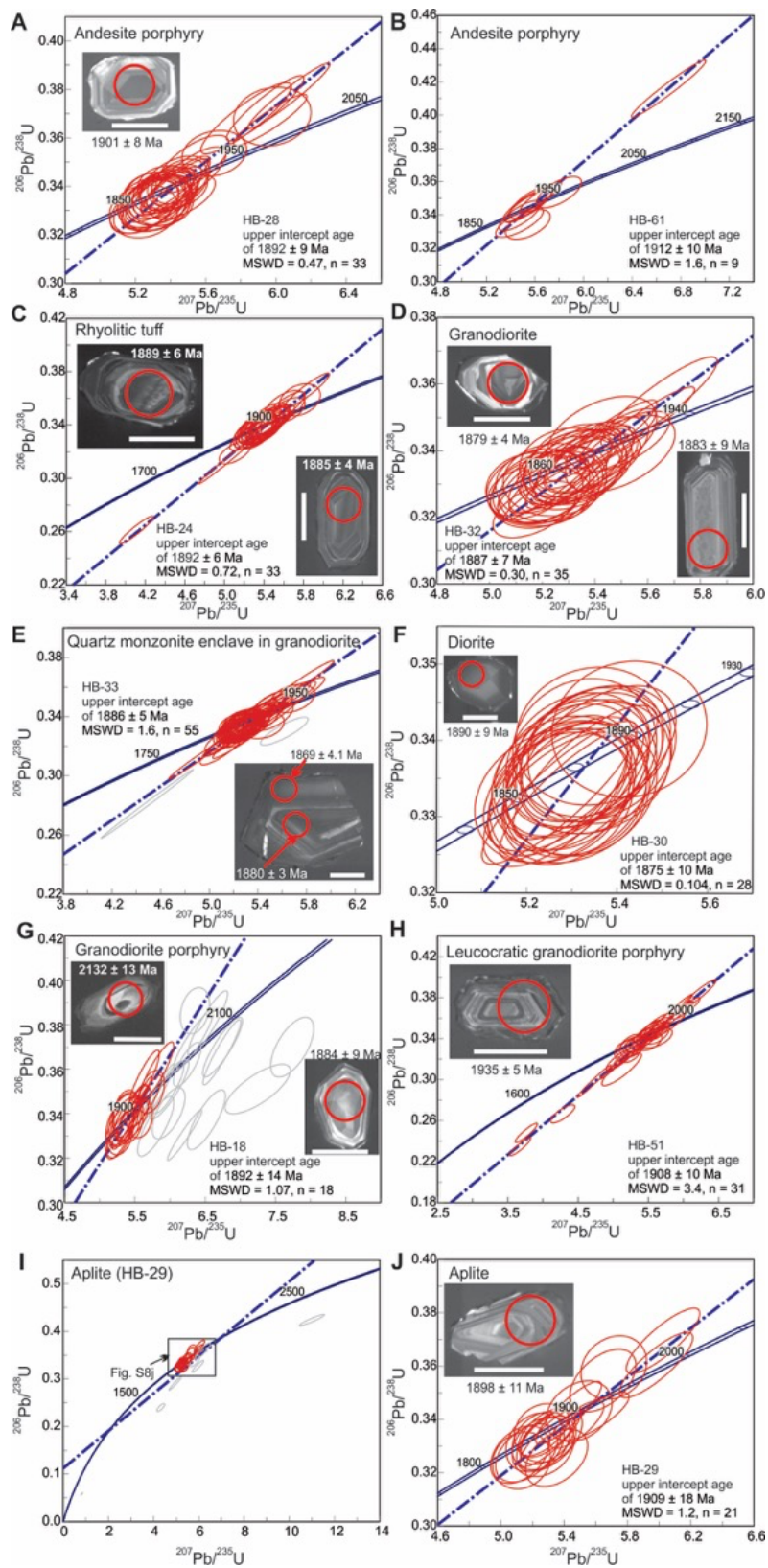


Figure A4.5. Zircon U-Pb concordia diagrams for the major rock units from Haib. MSWD represents the mean square of weighted deviates. For these samples, upper intercept concordia ages were calculated using Isoplot v. 4.5 to define the crystallization ages. Uranium decay constant uncertainties are not considered. (A and B) Plagioclase-phyric andesite porphyry (samples HB-28 and HB-61). (C) Rhyolitic tuff (sample HB-24). (D) Granodiorite (sample HB-32). (E) Quartz monzonite xenolith in granodiorite (sample HB-33, two discordant analyses excluded are indicated in grey ellipses). (F) Diorite (sample HB-30). (G) Granodiorite porphyry (sample HB-18; analyses with common lead excluded from the regression are indicated in grey error ellipses). The common lead may come from subsurface phosphate-rich inclusions, such as apatite, as demonstrated by high P content (thousands of ppm; [Table A4.4](#)). (H) Leucocratic granodiorite porphyry (sample HB-51). (I) Aplite (sample HB-29). (J) Aplite (sample HB-29; with six discordant analyses excluded from the upper concordia age determination as indicated in grey ellipses in [Fig. A4.5I](#)). Insets are CL images of representative zircons with $^{207}\text{Pb}/^{206}\text{Pb}$ ages (2σ uncertainty) reported. The red circles indicate the spots for laser ablation. The white bars beneath the CL images are 50 μm scale bars. See [Table A4.1](#) for sample locations and descriptions.

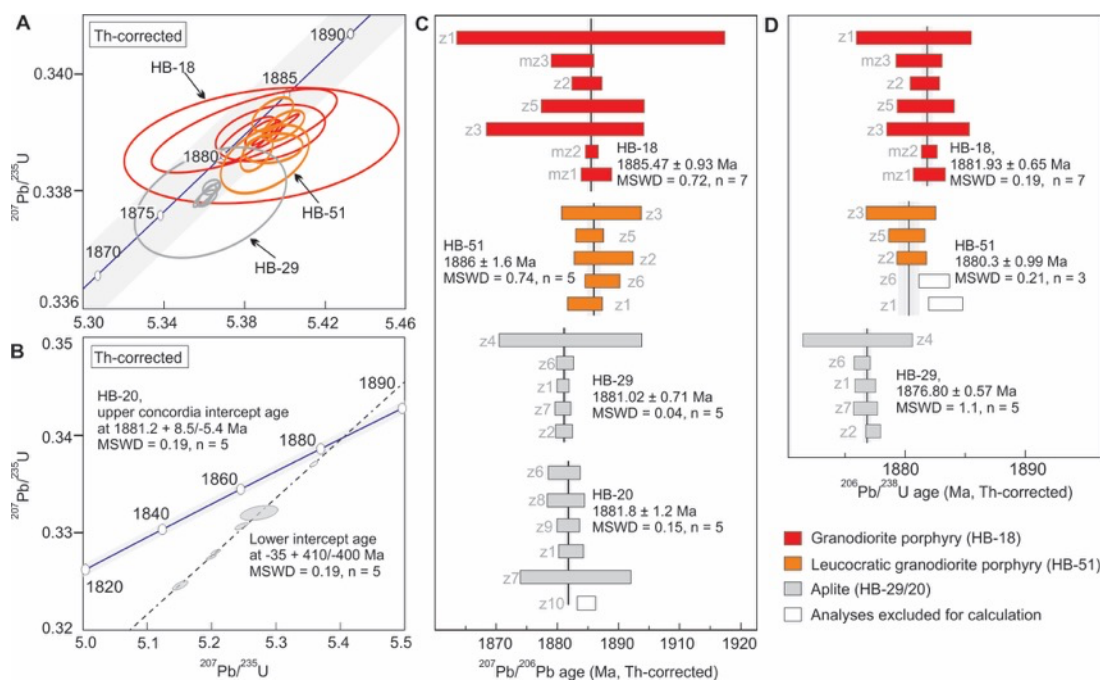


Figure A4.6. CA-ID-TIMS zircon U-Pb dating results for representative igneous rocks from the Haib deposit. (A and B) Wetherill concordia diagram of CA-ID-TIMS U-Pb isotope analyses. I plot of zircon $^{207}\text{Pb}/^{206}\text{Pb}$ dates for samples HB-18, HB-51, HB-29, and HB-20. (D) Plot of zircon $^{206}\text{Pb}/^{238}\text{U}$ dates for samples HB-18, HB-51, and HB-29. The grey bands along the concordia lines in (A) and (B) indicate uranium decay constant uncertainties.

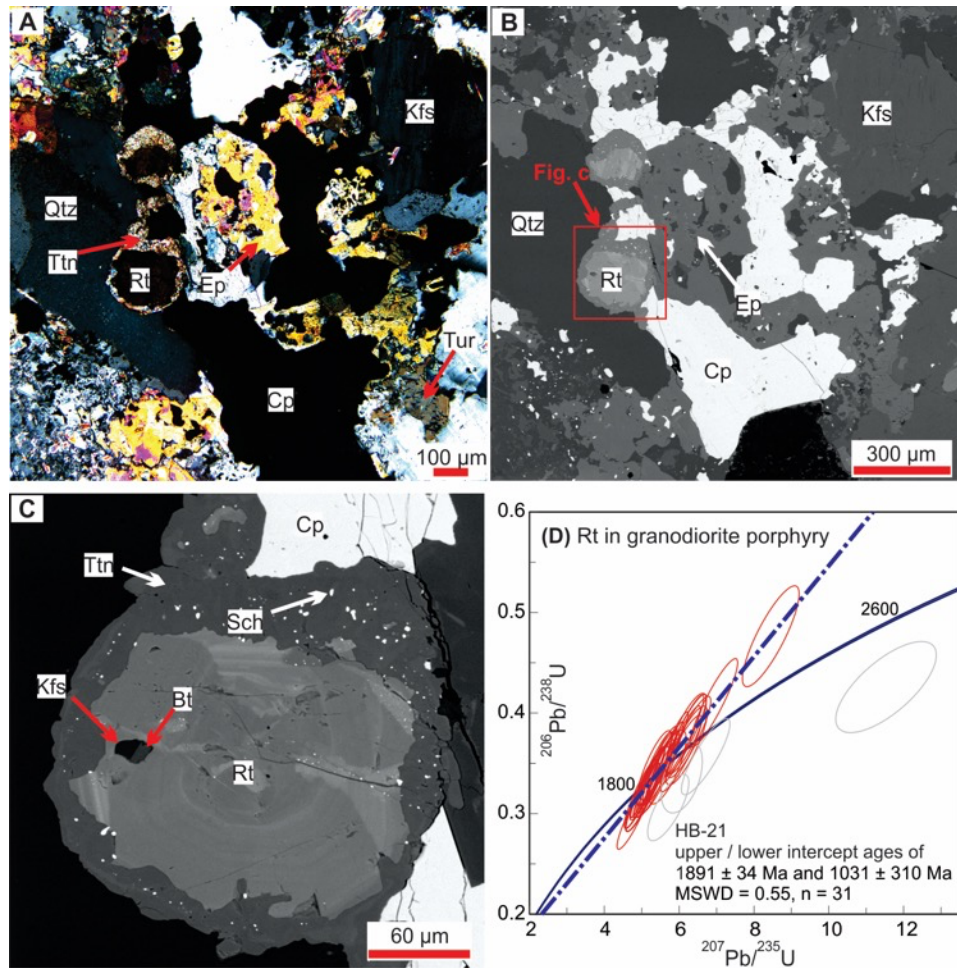


Figure A4.7. LA-ICP-MS U-Pb dating of hydrothermal rutile intergrown with chalcopyrite. (A and B) Subhedral hydrothermal rutile with sector and oscillatory zoning intergrown with epidote, K-feldspar, and chalcopyrite in the granodiorite porphyry (sample HB-21); cross-polarized light and BSE. (C) The zoned rutile replaced by titanite in the granodiorite porphyry (sample HB-21); BSE. (D) U-Pb concordia diagram for rutile sample HB-21; four analyses excluded from the upper intercept concordia age determination are indicated in grey ellipses. All uncertainties are reported at 2σ . MSWD represents the mean square of weighted deviates. Abbreviations: Anh = anhydrite, Bt = biotite, Cp = chalcopyrite, Ep = epidote, Kfs = K-feldspar, Rt = rutile, Sch = scheelite, Ttn = titanite. See [Table A4.1](#) for sample locations and descriptions.

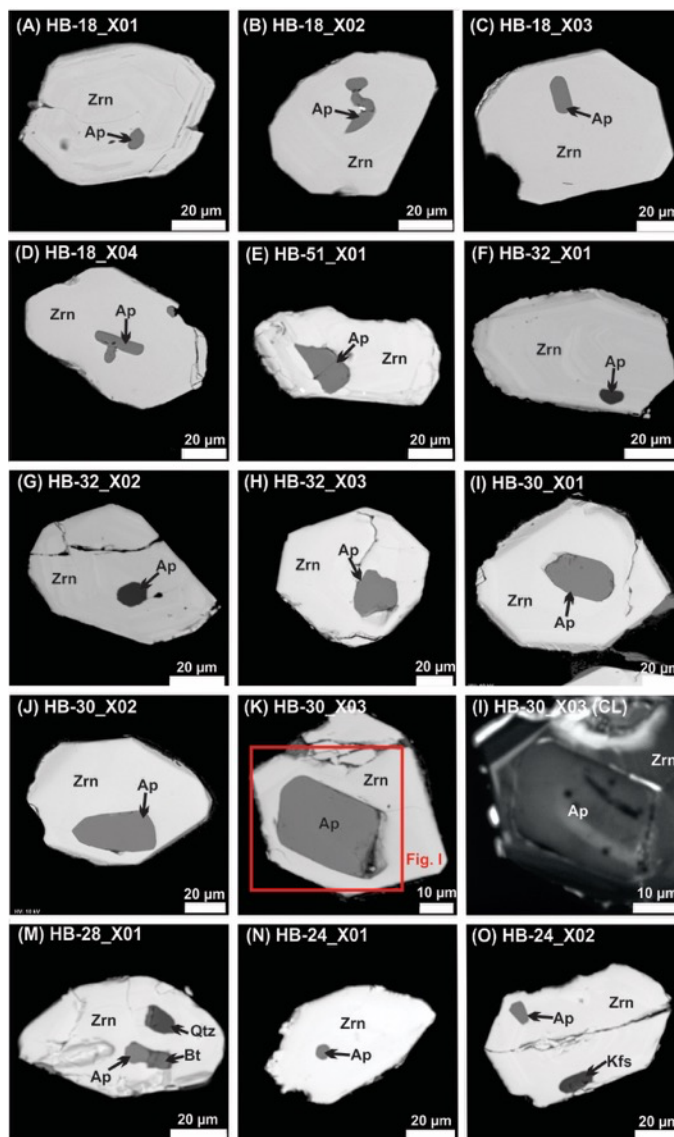


Figure A4.8. Backscattered electron images of zircons and the apatite inclusions for μ -XANES analyses from Haib, except for image I which is in cathodoluminescence. All of these apatite inclusions are wholly enclosed in zircon and isolated from fractures. (A–D) Sample HB-18, granodiorite porphyry. I Sample HB-51, leucocratic granodiorite porphyry. (F–H) Sample HB-32, granodiorite. (I–L) sample HB-30, diorite. (M) Sample HB-28, plagioclase-phyric andesite porphyry. (N and O) Sample HB-24, rhyolitic tuff; BSE. Abbreviations: Ap = apatite, Bt = biotite, Kfs = K-feldspar, Qtz = quartz, Zrn = zircon. See [Table A4.1](#) for sample locations and descriptions.

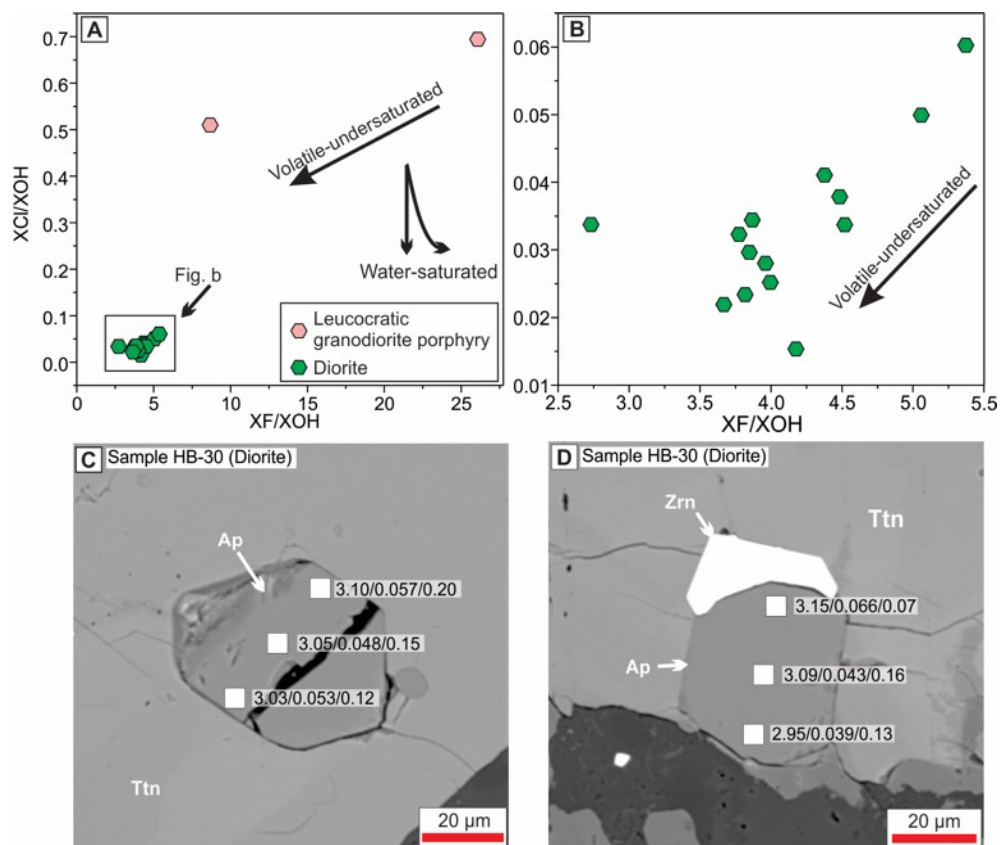


Figure A4.9. Titanite- and zircon-hosted apatite halogen contents. (A and B) Plots of X_{Cl}/X_{OH} versus X_F/X_{OH} ratios of apatite inclusions in zircon and titanite from Haib (mainly for samples HB-30 and HB-51, diorite and leucocratic granodiorite porphyry). The water-saturated and volatile-undersaturated trajectories are modified from [Stock et al. \(2018\)](#). (C and D) Backscattered electron images of apatite inclusions in titanite from sample HB-30 (diorite). Concentrations of F, Cl, S in these two apatite inclusions are shown in wt. % (F/Cl/S). White-filled squares represent raster beam spots. No zoning has been identified. Abbreviations: Ap = apatite, Ttn = titanite, Zrn = zircon.

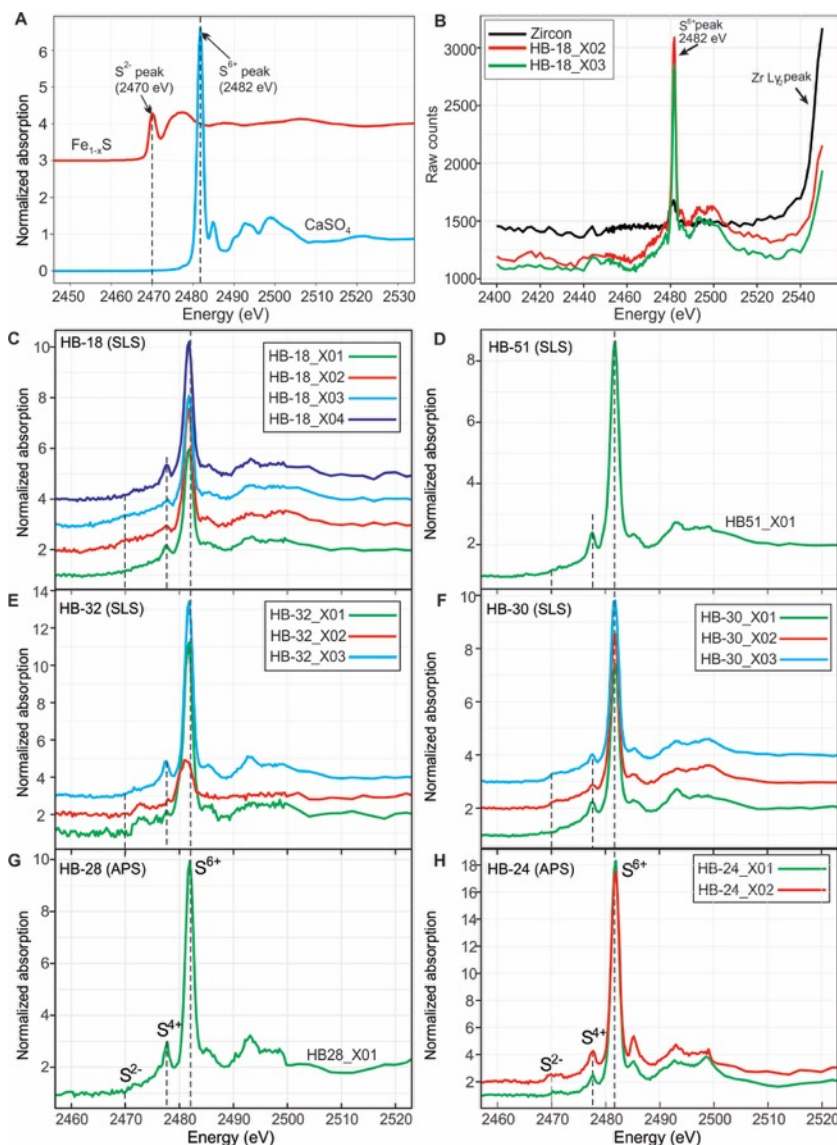


Figure A4.10. Sulfur μ -XANES spectra of apatites and zircon from the main igneous phases in Haib, as well as reference materials. (A) Reference materials pyrrhotite (Fe_{1-x}S) and powdered anhydrite (CaSiO_4). (B) Raw counts of zircon and apatites from sample HB-18. (C) Sample HB-18, granodiorite porphyry. (D) Sample HB-51, leucocratic granodiorite porphyry. (E) Sample HB-32, granodiorite. (F) Sample HB-30, diorite. (G) Sample HB-28, plagioclase-phyric andesite porphyry. (H) Sample HB-24, rhyolitic tuff. The apatite spectra numbers are consistent with the apatite grain numbers in Fig. A4.8. Abbreviations for laboratories: SLS = Swiss Light Source, APS = Advanced Photon Source. See Table A4.1 for sample locations and descriptions.

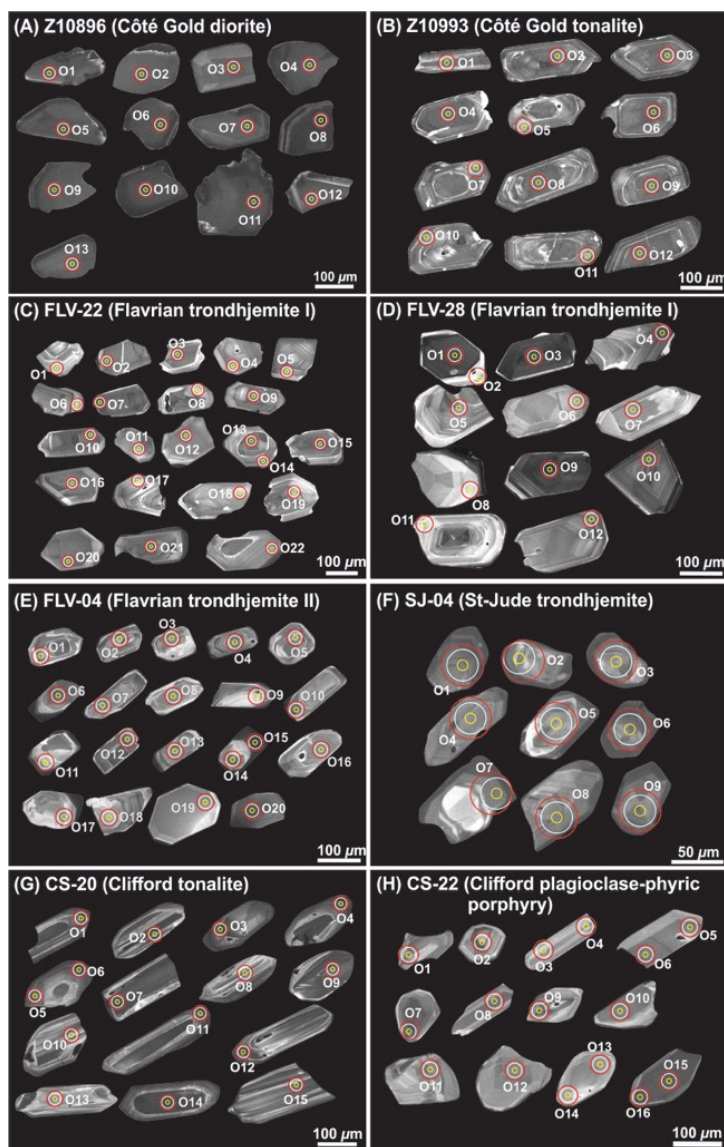


Figure A5.1. Cathodoluminescence (CL) images of representative zircon grains analyzed for U-Pb-Hf-O isotopes from (A) Côte Gold diorite (sample Z10896), (B) Côte Gold tonalite (sample Z10993), (C–D) Flavrian trondhjemite phase I (samples FLV-22 and FLV-28), (E) Flavrian trondhjemite phase II (sample FLV-04), (F) St-Jude trondhjemite (sample SJ-04), (G) Clifford tonalite (sample CS-20), and (H) Clifford plagioclase-phyric porphyry (sample CS-22). The circles represent spot locations for analyses of O isotopes (in yellow), U-Pb isotopes and trace elements (in white), and Lu-Hf isotopes (in red). Analysis numbers are marked, with the corresponding dataset listed in [Tables A5.2–5.4](#). See [Table 5.1](#) for sample locations and descriptions.

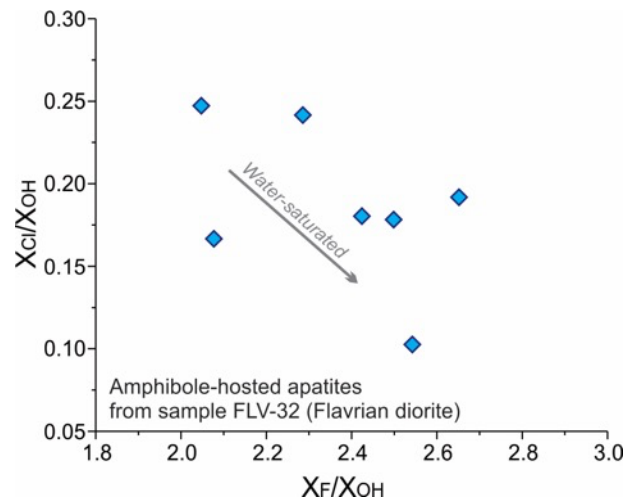


Figure A5.2. X_{Cl}/X_{OH} versus X_F/X_{OH} ratios for altered apatite inclusions in amphibole in sample FLV-32 (Flavrian diorite). The water-saturated trajectory is adapted from [Stocks *et al.* \(2018\)](#). See [Table 5.1](#) for sample locations and descriptions.

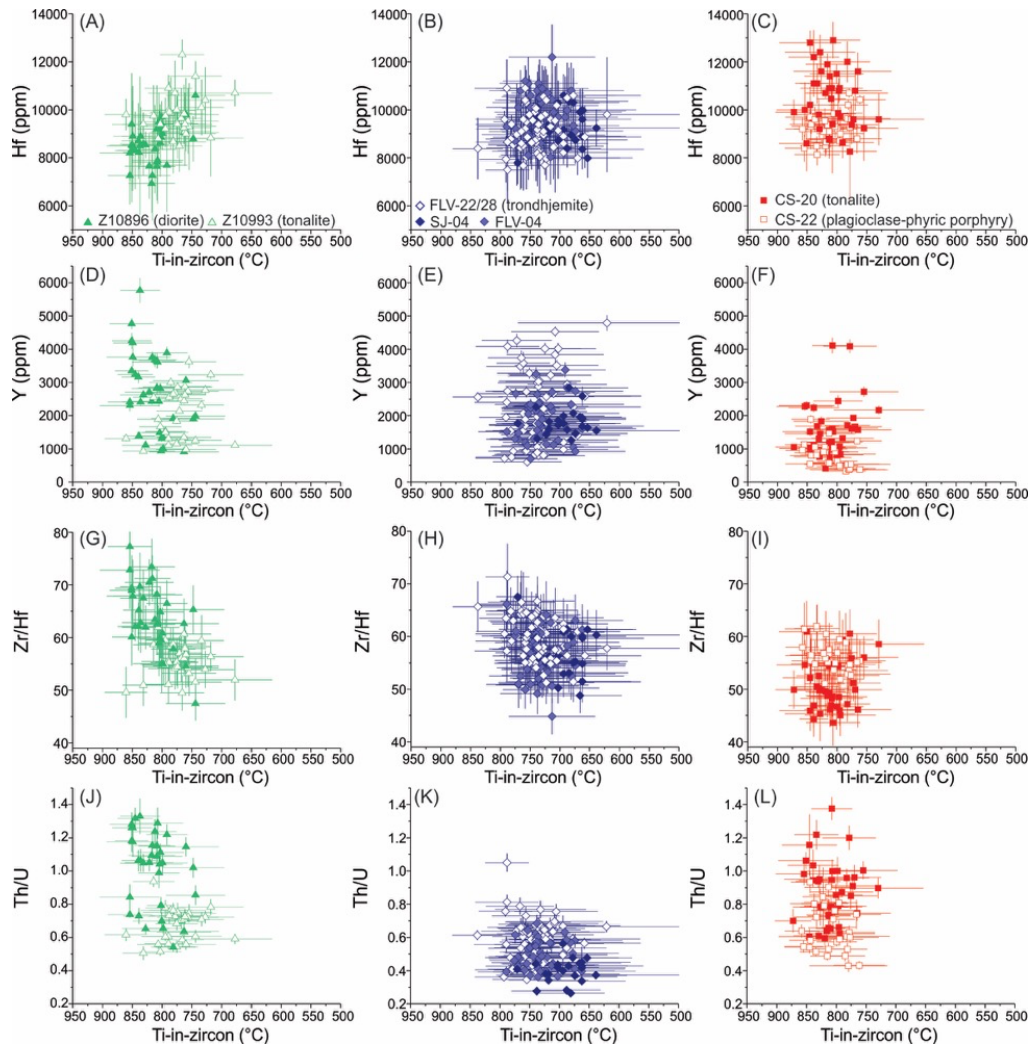


Figure A5.3. Zircon Hf and Y contents, and Zr/Hf and Th/U ratios for samples from the Côte Gold, Flavrian-St-Jude, and Clifford intrusions. (A–C) Zircon Hf contents versus T_{Ti-zircon} temperatures for (A) Côte Gold diorite and tonalite, (B) Flavrian-St-Jude trondhjemite, and (C) Clifford tonalite and plagioclase-phyric porphyry. (D–F) Zircon Y contents versus T_{Ti-Zr} for (D) Côte Gold diorite and tonalite, (E) Flavrian-St-Jude trondhjemite, and (F) Clifford tonalite and plagioclase-phyric porphyry. (G–I) Zircon Zr/Hf ratios versus T_{Ti-Zr} for (G) Côte Gold diorite and tonalite, (H) Flavrian-St-Jude trondhjemite, and (I) Clifford tonalite and plagioclase-phyric porphyry. (J–L) Zircon Th/U ratios versus T_{Ti-Zr} for (J) Côte Gold diorite and tonalite, (K) Flavrian-St-Jude trondhjemite, and (L) Clifford tonalite and plagioclase-phyric porphyry. Error bars represent standard errors.

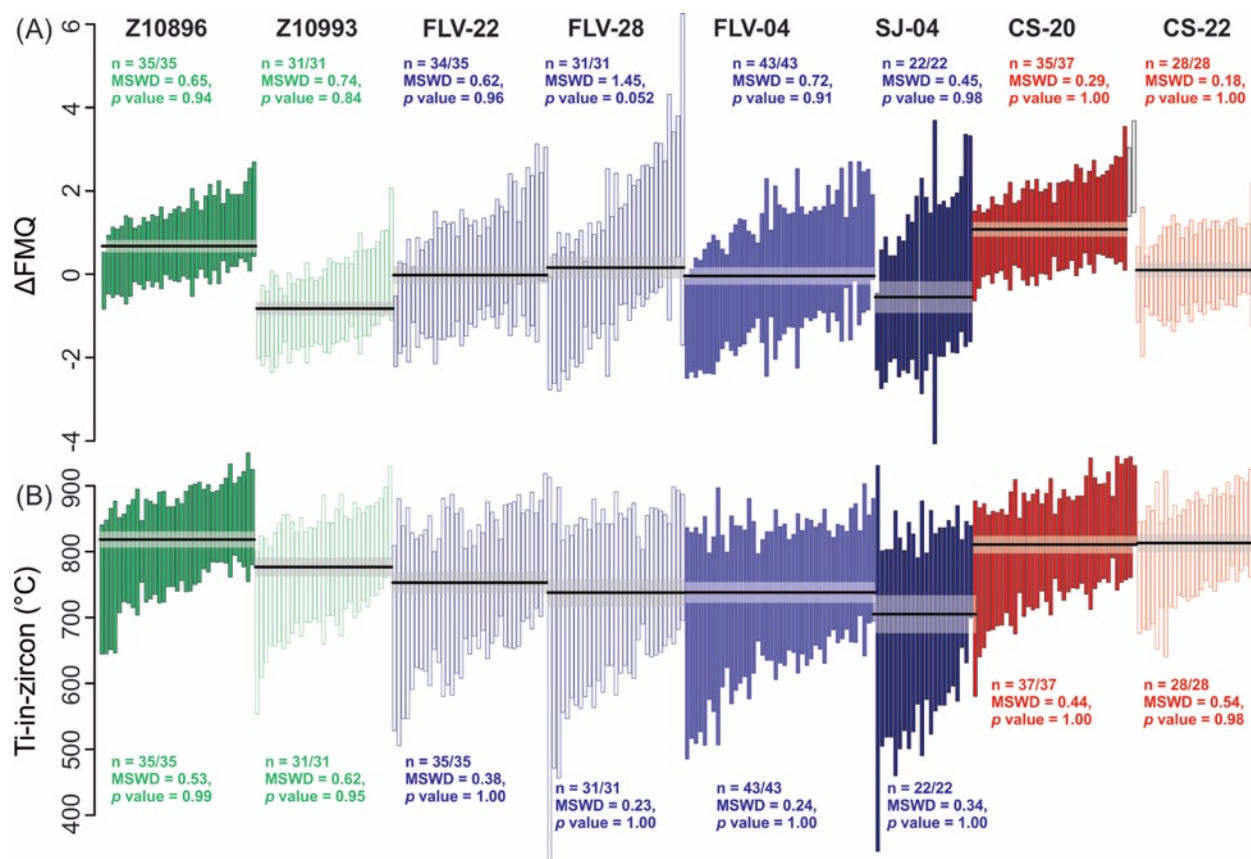


Figure A5.4. Plots of (A) fO_2 (ΔFMQ , from zircon oxybarometers) and (B) Ti-in-zircon temperatures for representative igneous rocks from the study areas. Error bars represent 2 standard errors. MSWD represents mean squares of weighted deviates. The plots and associated calculation (MSWD and p values) are for supporting homogeneity of the fO_2 and T_{Ti-Zr} values for each sample within analytical and calibration errors. The weighted mean average values are not reported. In the main text, we choose to report the average values and standard deviation (1σ).